Microphysical modelling of aerosols in the ORAC retrieval

Andrew John Alexander Smith

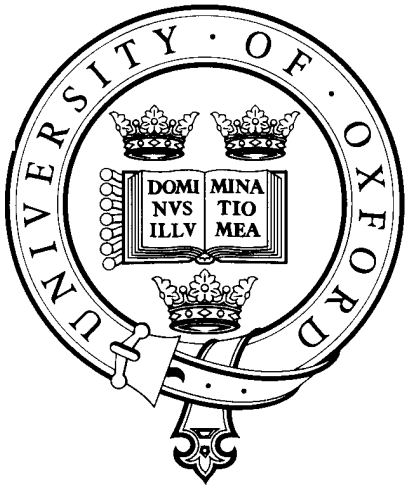

Submitted for the Degree of Doctor of Philosophy
Trinity Term 2011

Atmospheric, Oceanic and Planetary Physics
Department of Physics
University of Oxford

Abstract

Microphysical modelling of aerosols in the ORAC retrieval

Andrew John Alexander Smith, St. Hugh's College

Submitted for the degree of Doctor of Philosophy in Physics, Trinity Term 2011

This thesis describes an investigation of, and improvements to, the microphysical modelling of aerosols in the **O**xford-**R**utherford Appleton Laboratory **A**erosol and **C**louds retrieval (ORAC), which is used to obtain aerosol properties from measurements by the **A**dvanced **A**long **T**rack **S**canning **R**adiometer (AATSR). Modelling decisions determine the light scattering properties of the aerosol classes which in turn alter the retrieved aerosol properties: aerosol optical depth, and effective radius.

The maritime, mineral dust, urban, and biomass burning aerosol classes were first investigated, and then improvements implemented. Major additions to the scheme include the ability to model non-spherical dust as spheroids, soot as fractal aggregates, and to coat spherical particles with an extra layer of differing refractive index (whose thickness can be modified by ambient relative humidity where necessary). Output from aerosol retrievals containing these new models is presented.

Modelling of marine aerosol was found to be adequate, but an improvement in the relative humidity assumptions led to an average 5 % increase in aerosol optical depth (AOD). Modelling of mineral dust aerosols has been dramatically altered by the addition of non-spherical dust and hygroscopic particles, leading to increases in measured AOD of over 100 % during dust events, compared to the previous model. Measurement of biomass burning aerosol has been tested with an "ageing" aerosol scheme, leading to increases in over-land measured AOD of 0.14 ($\sim$ 50 % increase). With such significant changes in AOD, representation of aerosol light scattering properties is seen to be important factor in the accuracy of the ORAC scheme.

Finally, a method of optimising the placement of detectors in an aerosol measurement device is presented.

Contents

List of Figures

List of Tables

Chapter 1

Introduction

Since the beginning of the industrial revolution, the increase in atmospheric greenhouse gas concentrations has been accompanied by an increase in the concentration of atmospheric aerosols. This latter increase has reduced the warming effect that would have resulted from industrial emissions that produced only the gaseous pollutants. Aerosols can prevent solar radiation from reaching the Earth's surface that could otherwise warm the planet, and are indirectly responsible for brighter, more persistent clouds. However, confidence in quantitative values of radiative forcing due to aerosols is the largest source of uncertainty in the modelling of future climate change [Solomon et al., 2007].

Knowledge of worldwide aerosol concentrations and aerosol types is required to constrain and test aerosol models. Certain satellite instruments are uniquely suited to this task: specifically those that measure with high spatial and temporal frequency, and at wavelengths where light scattering is sensitive to the presence of aerosol. Significant difficulties are inherent in the retrieval of aerosol properties from satellites, since a full description of an aerosol distribution is under-constrained by the available measurements. As such, assumptions about the aerosols being observing must be made in order to obtain the most important information. Improving these assumptions, and demonstrating this improvement is the purpose of this work.

Representation of the three most prevalent aerosol types[1], maritime, mineral dust, and carbon-

[1]Those aerosols with the largest annual mean atmospheric loadings

aceous are investigated, and specific attention is paid to improvements to the Oxford-RAL Aerosol Clouds (ORAC) retrieval from the Advanced Along Track Scanning Radiometer (AATSR). Current ORAC modelling approaches are compared to in situ measurements, and to methods employed by other satellite retrievals. Sensitivity of aerosol optical properties to modelling changes are calculated, and the effect of new models on the ORAC retrieval are tested.

1.1 What are aerosols?

An aerosol is a suspension of solid or liquid particles in a gas, with dimensions on length scales of several nanometres to tens of microns. Aerosols arise from natural sources such as sand (mineral dusts), sea spray, emissions from volcanoes, and from anthropogenic sources. This final category mainly consists of the many products of fuel combustion and biomass burning (although this can also occur naturally).

Primary aerosol is composed of particles emitted into the atmosphere. Secondary aerosol are those particles formed in the atmosphere by gas-to-particle conversion processes [Seinfeld and Pandis, 2006]. Concentrations can reach as high as several thousand per cubic centimetre for small particles ($< 1\ \mu$m), whereas bigger particles usually have number densities less than 1 part. cm^{-3}.

Removal of the particles from the atmosphere occurs through two principal mechanisms: dry deposition where the particles return to the Earth's surface due to gravitational settling, and wet deposition where the particles are incorporated into water droplets (in or below clouds) and are deposited on the Earth's surface during precipitation.

Distribution

Aerosols found in the troposphere and stratosphere are very different. Tropospheric content varies in size, shape (from spherical to extremely non-spherical), homogeneity, and refractive index. By contrast, stratospheric aerosol is, for the most part, aqueous sulphuric acid of varying concentrations. Volcanic eruptions can be a large source of SO_2 which is injected directly into the stratosphere at

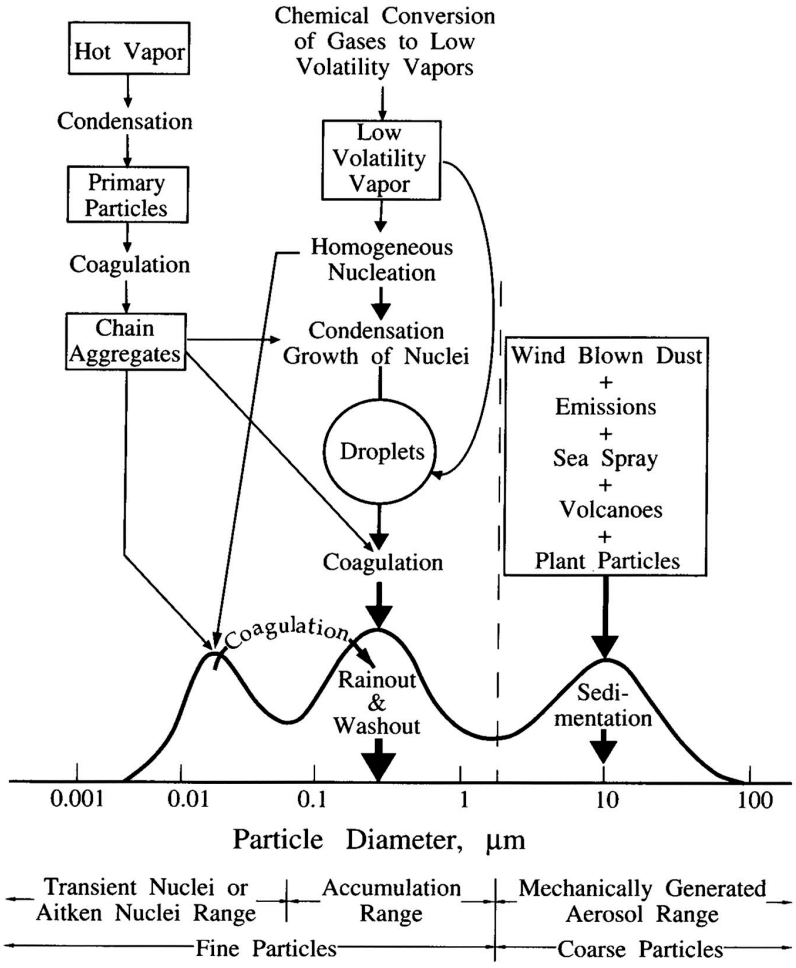

Figure 1.1: Idealised schematic of the distribution of particle surface area of atmospheric aerosol, including sources and sinks for the modes. From Seinfeld and Pandis [2006], based on Whitby and Cantrell [1976], reproduced with permission.

high velocity. After these events, stratospheric concentrations of sulphate gradually decrease back to a background level with a half-life of months [Mergenthaler et al., 1995].

Particle sizes can normally be well characterised by log-normal distributions with three principal modes. The smallest mode (with length scales of 5 nm to 0.1 μm) is nucleation, where particles are formed from atmospheric species in gas-to-particle conversion either on existing particles (heterogeneous nucleation), or through condensation (homogeneous nucleation) [Colbeck, 1998].

The second, and generally most populous mode is the accumulation mode with particle diameters

of 0.1 to 2.5 μm. Here are particles which arise from the condensation of low-volatility vapours, and from coagulation of nucleation mode particles. Particles in this range are subject to the least number of removal mechanisms, so numbers accumulate here. The nucleation and accumulation modes are collectively named the fine mode.

The coarse mode ($> 2.5\,\mu$m) consists of large particles, formed by mechanical processes such as weathering and wind erosion. Due to their larger mass, they have high sedimentation velocities (which increase roughly quadratically with size) and settle out of the atmosphere by dry deposition. There is little conversion between fine and coarse modes because the sources and sinks are different.

Fig. 1.1 shows the three principal modes and their methods of growth and decay. Notice the one-way increase in the accumulation mode from the nucleation mode and the lack of exchange between fine and coarse particles.

1.2 Sources

Unlike most atmospheric gases, many aerosols have mixing times which are shorter then their atmospheric lifetimes. This leads to spatially inhomogeneous distributions of individual species, often in specific regions. For example, Fig. 1.2 shows time-averaged total aerosol optical depth for two periods in 2001. Certain areas of the globe have generally higher concentrations of aerosol (for which optical depth is a good marker). Increased optical depth marks a clear plume of desert dust extending into the Atlantic ocean from Saharan Africa. Biomass emissions can be seen over the Amazon, tropical African, and Indonesian rainforests. Industrial pollution can be seen from the east and west coasts of the USA, Europe, India, and China.

This section gives a brief outline of aerosol sources, divided into those that are natural and those of anthropogenic origin. Particles that are the focus of later chapters will be given additional, more detailed attention there. Although the categories “natural” and “anthropogenic” are not strictly accurate (e.g. biomass aerosol can also be due to natural wild fires; mineral dust aerosol can be through desertification of the Sahel region due to overgrazing), most species are created predominantly by

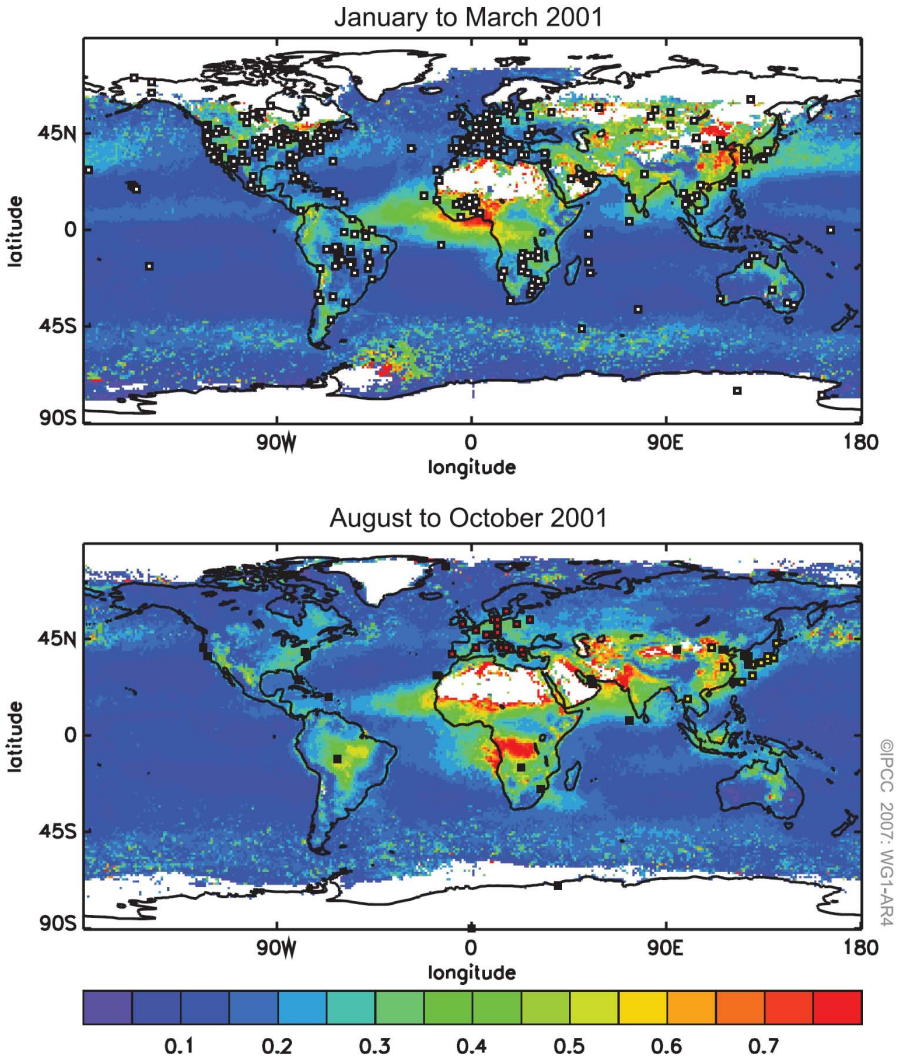

Figure 1.2: Total aerosol optical depth determined from satellite measurements, showing seasonal and geographical changes in aerosol concentration. In white areas, no values are available due to the high reflectivity of mineral dust (in the Sahara) and snow (in the Arctic and Antarctic regions). Dots show locations of ground based measurements, complementing the satellite data (for the top figure, AERONET measurement stations; for the bottom, aerosol lidar networks. This plot is Fig. TS.4. from IPCC WG1 report [Solomon et al., 2007], reproduced with permission.

one mechanism. A type of particle that is mainly in the atmosphere due to human activity will be termed anthropogenic.

1.2.1 Natural aerosols

The sources of natural aerosols are controlled by local environmental conditions. Wind, temperature and humidity all play a part in affecting the rate of emission. Many of the particles are "kicked up" into the atmosphere so wind speed is the main factor determining population, and large temporal variation in natural aerosol is seen. Of the natural aerosols, the significant non-spherical component is mineral dust, and the largest component by number is marine aerosol.

Salt

Maritime aerosol is mainly composed of sea-salt. At the surface of the ocean, air bubbles burst, spraying droplets which either fall back to the surface of the water (if they are too large) or are carried higher, forming aerosol as evaporation brings them into equilibrium with atmospheric relative humidity. Depending on the wind speed, the aerosol will or will not be able to escape the surface layer (the faster the wind, the more likely). Concentration varies roughly linearly with wind speed [Colbeck, 1998].

The main components of sea salt are NaCl, KCl, $CaSO_4$ and Na_2SO_4. Atmospheric emission is estimated at 1300 Tg yr^{-1} [Colbeck, 1998, Table 7.2]. This is a large proportion of the natural tropospheric aerosol but concentrations rapidly decrease when travelling inland. Salt aerosol can be considered spherical as it will generally be dissolved in water droplets. A full description of marine aerosol is the subject of Chapter 2.

Mineral dust

Mineral dust from desert and semi-arid regions is a major source of tropospheric aerosol. About 50 % of this is subject to long-range transport and will turn up all over the world. Fig. 1.3 shows a dust

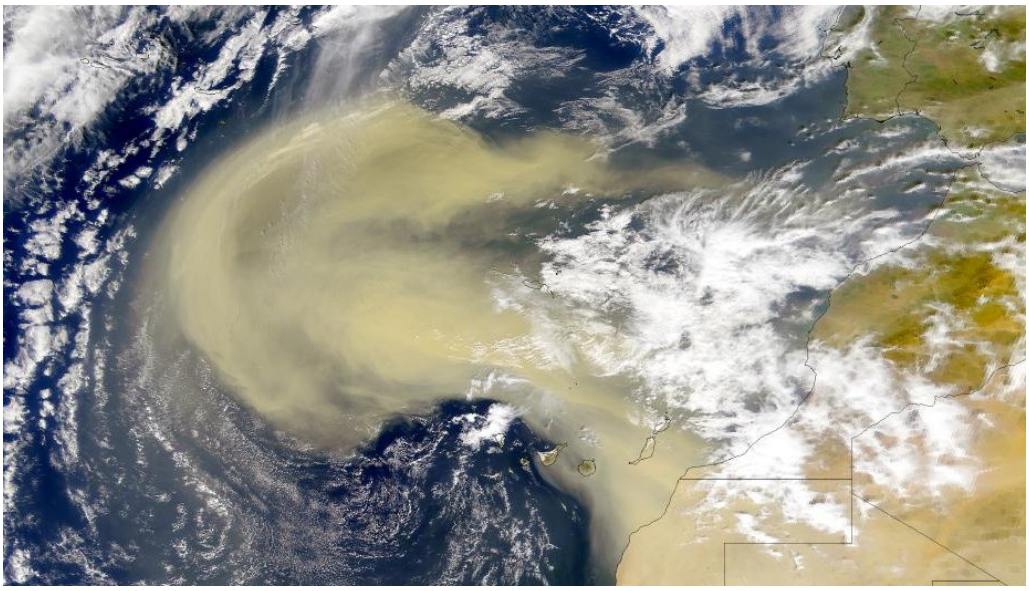

Figure 1.3: Sand storm event off the West African coast, 26th February, 2000. From http://earthobservatory.nasa.gov/Newsroom/NewImages/images.php3?img_id=1520, accessed on 3/7/2008. Image is in the public domain.

plume extending out over the Atlantic ocean from the west coast of Africa; an example of the huge enhancement of optical depth that airborne mineral constituents can cause. Saharan mineral dust is thought to play a vital role in the support of vegetation in the Amazon basin and provides nutrient iron to the biogeochemical cycle of the ocean systems [Solomon et al., 2007].

Apart from the Sahara, the other major world source of mineral dust is the Gobi desert, with the US South West and the Saudi Arabian peninsula providing local sources that do not have the same global reach. However, these lesser sources can still significantly modify weather and climate e.g. Saudi Arabian dust outbreaks have been linked to weakening of the monsoon trough over India [Ackerman and Cox, 1989]. Although the mineral dust aerosol is mainly from desert regions, other types of soil can enter the atmosphere in a similar way. They are generally prevented from leaving the ground by increased moisture of the surface, and vegetation cover.

The size of mineral dust in the atmosphere is around 1 μm and varies hugely in shape. Fig. 1.4 shows scanning electron microscopy of sample Saharan mineral dust, demonstrating the sharp corners and varying shape which make these particles most certainly not spheres.

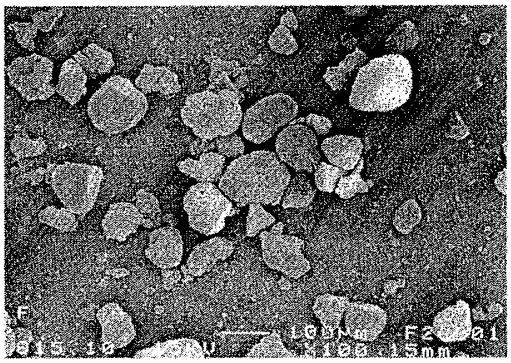

Figure 1.4: Scanning electron microscope photograph of Saharan mineral dust. This is Fig. 2(g) from Volten et al. [2001], reproduced with permission. It is highly likely that the sample was collected at ground level, since the sizes are too large to be representative of dust in the troposphere.

Principal constituents of mineral dust are oxides and carbonates of silicon, aluminium, calcium and iron. A full description of mineral dust aerosol is given in Chapter 3.

Volcanic emissions

Solid and gaseous material is injected into the atmosphere sporadically with the eruption of volcanoes. The larger solids are heavy and mostly deposited in the local area due to gravity, but huge amounts of ash, SO_2 and HCl are left in the atmosphere. Ash principally consists of SiO_2, Al_2O_3 and Fe_2O_3 and is in the coarse aerosol mode, mostly impacting on the regional scale. Generally, in periods not directly after an eruption there is little ash in the atmosphere due to rapid sedimentation.

Globally, the main result of volcanoes is the creation of sulphate aerosol in the stratosphere. The explosive nature of eruptions means that SO_2 can be injected buoyantly into the stratosphere where it is oxidised and condensed forming H_2SO_4 aerosol. Small particle size, and lack of precipitation lead to long lifetimes. Residence times for stratospheric aerosols are estimated at 6–9 months [Colbeck, 1998]. Since the aerosol is a liquid, it can be assumed to be spherical.

The eruption of Mount Pinatubo on Luzon Island, Philippines in 1991 was the largest in recent times. Satellite measurements of column SO_2 estimated 20–30 Tg was released, and had encircled the Earth within 22 days [Bluth et al., 1992; Seinfeld and Pandis, 2006]. As a result, 1991–92 saw a sudden drop in global mean air temperature. This was attributed to the spread of scattering aerosols in the stratosphere from the Pinatubo eruption [Bhutiyani et al., 2007], and was one of the most significant deviations from the upward trend of global mean temperature that has been observed over

the past century. It took more than two years for aerosol loading in the stratosphere to decay back to "normal" levels. Eruptions that modify the stratosphere "significantly" occur with a frequency of $5\frac{1}{2}$ years [Grainger and Highwood, 2003].

1.2.2 Anthropogenic aerosols

Anthropogenic aerosols come from particulate emissions from industry, transport and farming. They contain a higher fraction of fine mode aerosols than natural emissions [Seinfeld and Pandis, 2006].

Activities such as mining and stone crushing in quarries are the main contributers to coarse mode mineral dust particles [Colbeck, 1998]. Combustion of fuels leads to both primary fine-mode smoke aerosols, and secondary material from the chemical reactions of burning products. The main precursors to the secondary aerosol are SO_2 and the various nitrous oxides (NO_x) which oxidise to H_2SO_4 and HNO_3. Sulphuric acid has low vapour pressure, and condenses, becoming aerosol mass. Nitric acid is split between gas and aerosol phases.

Carbon

Aerosols formed from burning are mostly black carbon (BC) and organic carbon (OC) particles. The BC aerosol products are often described as having a fractal shape when first produced [Helble et al., 1988; Sorensen, 2001], but over the course of a few hours "fold" into densely packed clusters and, it is hypothesised, become coated by organics [Abel et al., 2003]. Hoffer et al. [2006a] and Capes et al. [2008] both show an increase in the fraction of organic material with the aging of biomass burning aerosol. Black carbon is highly absorbing in the visible. Organic carbon particles are more spherical, more soluble, and less absorbing. They form by gas-to-particle conversion on any available nucleation sites close to combustion [Jacobson et al., 2000]. Additional OC particles are formed from degrading plant matter, but a large majority of emissions are due to burning. A full description of carbonaceous aerosol is provided in Chapter 4.

1.3 The influence of aerosols on the atmosphere

The radiative forcing (RF) associated with a process that alters the atmosphere is a measure of how that process has changed the global radiative balance. It is often defined as the net change in irradiance at the tropopause. A positive value implies that there is more incoming then outgoing radiation. The best known example is the positive RF due to increase in greenhouse gas concentrations that trap the outgoing long-wave radiation while not impeding incoming shortwave radiation. Since the Intergovernmental Panel on Climate Change [IPCC, see Solomon et al., 2007] are interested in the net effect of human industrial activity, they define RF slightly differently as the "rate of energy change per unit area of the globe as measured at the top of the atmosphere" since 1750 (the beginning of the industrial era).

Aerosol direct and indirect influences on the atmosphere are, at the time of writing, the largest unknown in estimates of net radiative forcing. Fig. 1.5 shows the IPCC's best estimate for global mean radiative forcings in 2005, with their 90 % confidence intervals marked. By far the widest confidence intervals are for the aerosol effects. There is also a low level of scientific understanding.

Aerosols reflect light back into space and act as cloud condensation nuclei (CCN), increasing the albedo. They also act as surfaces for other chemical reactions in the atmosphere to take place, for example the destruction of ozone in the troposphere and the night-time formation of nitric acid. Their temporal variability, speciation, emission and deposition rates, and the number of different effects and reactions they influence makes them extremely difficult to model in climate studies.

1.3.1 Direct radiative influence

The direct effect is the radiative forcing caused by aerosols scattering and absorbing light, altering the Earth's radiative balance. If the aerosols are purely scattering, the effect is always a negative RF, since some of the light destined to pass through an atmospheric layer is now reflected and will pass back into space. For absorbing aerosols, the effect is more variable. Haywood and Shine [1995], using a simplified formula, show that radiative forcing will be negative only if the single scatter

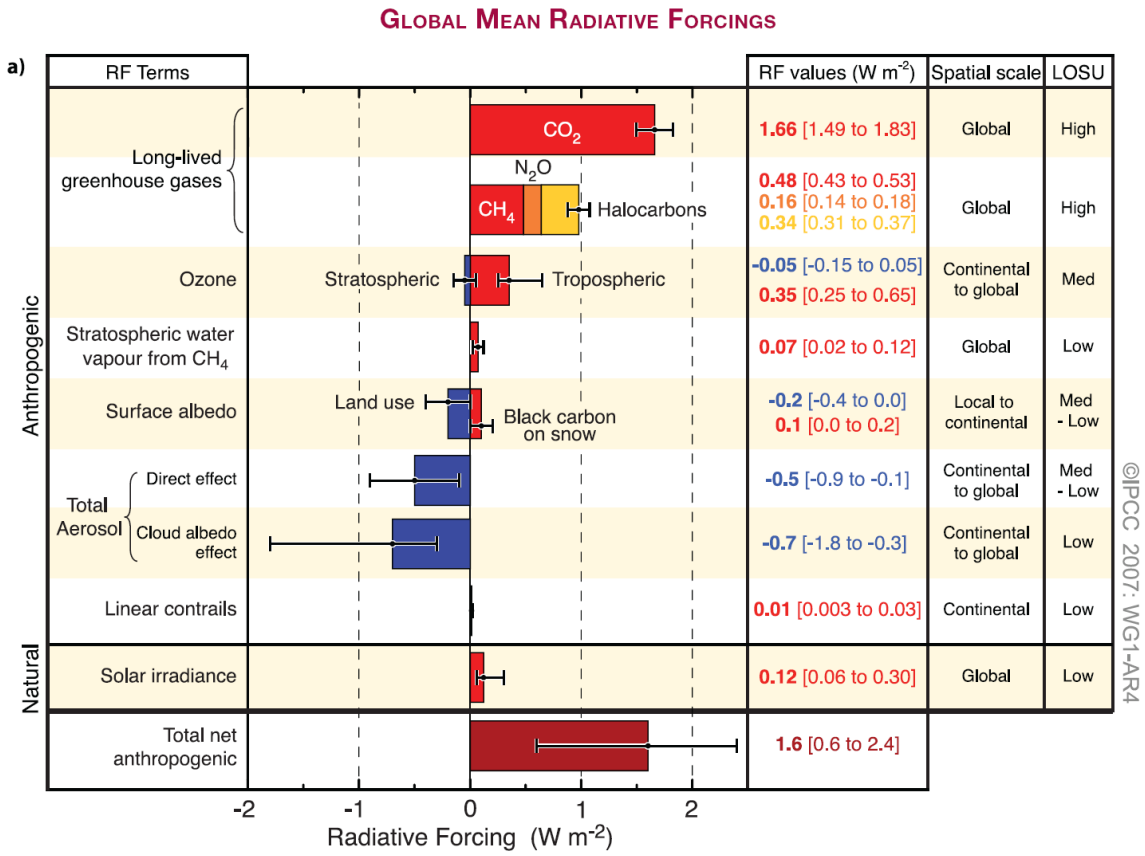

Figure 1.5: The estimates for global mean radiative forcings, presented by Working Group One of the IPCC. LOSU is the level of scientific understanding. Notice that the two largest error bars are those on the estimates of the aerosol direct and indirect effects. This is Fig. TS.5 in Solomon et al. [2007], reproduced with permission.

albedo, $\bar{\omega}_0$ satisfies:

$$\bar{\omega}_0 > \frac{2R_s}{\bar{\beta}(1-R_s)^2 + 2R_s}, \tag{1.1}$$

where R_s is the surface reflectance and $\bar{\beta}$ is the backscatter fraction, the ratio of backscattered to forward scattered light, obtained from the phase function [Wiscombe and Grams, 1976]. Hence over dark surfaces (forests or oceans), the effect is still negative while over bright surfaces (desert or snow or if the aerosol is above a cloud), there can be a positive RF.

1.3.2 Chemical influence

Heterogeneous reactions involve the reaction of a gas molecule with a solid or liquid surface. This makes aerosols ideal atmospheric reactants in these cases.

In the troposphere for example, dry sea-salt acts to liberate hydrogen chloride when it comes into contact with gaseous nitric acid. Ozone destruction can also take place on the surface of carbon based aerosol, generating CO and CO_2. Hazes in the troposphere offer wet surfaces for heterogeneous reactions, for example the night-time formation of nitric acid.

In the stratosphere, polar stratospheric clouds, consisting of frozen or liquid sulphuric and nitric aerosol, are responsible for heterogeneous chlorine activation reactions which have a heavy role in polar ozone depletion [Colbeck, 1998]. Ozone depletion is also reported within desert dust plumes [Nicolas et al., 2009, and references therein].

1.3.3 Clouds

The indirect aerosol effect is the collective name for the RF caused by several aerosol-cloud interactions which change the microphysical properties of clouds. Aerosols are vital in cloud formation, acting as cloud condensation nuclei (CCN). Since clouds are a big influence on the Earth's albedo due to their high reflectivity, changes in atmospheric aerosol concentration inevitably have an effect on RF (although, as Fig. 1.5 shows, an understanding of the subtleties is in no way complete).

The first indirect effect, or Twomey effect [Twomey, 1977b], is a direct consequence of increased particulate in the atmosphere: more CCN mean that there are more sites where droplets can form in developing clouds. This leads to greater numbers of droplets, but of a smaller size than in an unperturbed cloud (leading to an increase in the surface area of water droplets in the cloud). The end result for the radiative properties of the cloud is an increase in light reflected back into space and thus a negative radiative forcing.

Secondary effects (not accounted for in Fig. 1.5) include the suppression of drizzle with greater numbers of CCN and other factors [Albrecht, 1989; Yia et al., 2008] which increase the liquid water

content of the cloud. The cloud height can also increase, which leads to emission of radiation as the clouds rise and cool [Pincus and Baker, 1994]. The lifetime of the cloud is also increased since the reduced drizzle stops the cloud from breaking up [Albrecht, 1989]. A good overview of cloud effects can be found in Solomon et al. [2007, §2.4.1].

Finally, there is the semi-direct effect [Hansen et al., 1997; Cook and Highwood, 2004]. Here, short wave absorbing aerosols reduce cloud cover by warming the atmosphere so that relative humidity decreases.

1.4 Aerosol characteristics

It is possible to describe a broad range of atmospheric aerosol using only a few parameters. The lognormal distribution is almost universally used by aerosol scientists to parameterise aerosol size distributions. Internal mixtures (where various components are combined within single particles), and external mixtures (where various components are combined, each as individual particles) describe almost all situations when more than one type of aerosol is present. In the past decade, the pragmatic description of all particles being spherical (for the purposes of light scattering calculations) has been changed as computing power has increased.

1.4.1 The lognormal distribution

A lognormal distribution is a normal distribution in log-space. Assuming the number distribution of aerosol radii, $n(r)$, is lognormal, we require only the median radius, r_g, and σ (the standard deviation of $\ln r$) to fully compute the ensemble's light scattering properties. A normalised lognormal number distribution is defined as:

$$n(r) = \frac{1}{\sigma r \sqrt{2\pi}} \exp\left[-\frac{1}{2}\left(\frac{\ln r - \ln r_g}{\sigma}\right)^2\right]. \tag{1.2}$$

The effective radius of an aerosol distribution, r_{eff}, is defined as

$$r_{\text{eff}} = \frac{\int_0^\infty r^3 n(r)\,\mathrm{d}r}{\int_0^\infty r^2 n(r)\,\mathrm{d}r}, \tag{1.3}$$

and for a sum of lognormal distributions, can be calculated as

$$r_{\text{eff}} = \frac{\sum_i m_{\text{rat},i} \exp\left[3\ln r_{g,i} + \frac{9}{2}\sigma_i^2\right]}{\sum_i m_{\text{rat},i} \exp\left[2\ln r_{g,i} + 2\sigma_i^2\right]} \quad \text{[for a lognormal distribution]}. \tag{1.4}$$

The mixing ratios $m_{\text{rat},i}$ are the relative amounts of each mode and so $\sum_i m_{\text{rat},i} = 1$, although in (1.4), this requirement does not actually matter. The standard deviation of $\ln r$, σ is sometimes expressed as S, where $\sigma = \ln S$.

Manipulating the lognormal distribution

If a measured distribution appears to be lognormal, a good fit can be obtained by using the apparent mode and median radii to calculate the spread. Differentiating (1.2) w.r.t. r to find the turning point, it follows that $r_{\text{mode}} = \exp\left[\ln r_g - \sigma^2\right] = r_g e^{-\sigma^2}$, which can be rearranged to give

$$\sigma = \sqrt{\ln\left[\frac{r_g}{r_{\text{mode}}}\right]}. \tag{1.5}$$

Particularly with measurements from optical particle counters, lognormal distributions of volume w.r.t. r can be provided, i.e. $\frac{dV}{dr}$. Since (assuming spherical particles) $V = \frac{4}{3}\pi r^3 n(r)$, the equivalent number distribution can be found. Given r_V and σ_V, the median and spread in volume space, the

number distribution is given by [Seinfeld and Pandis, 2006]:

$$\ln r_n = \ln r_V - 3\sigma_V^2 \quad ; \quad \sigma_n = \sigma_V, \tag{1.6}$$

and similarly for surface area distributions

$$\ln r_n = \ln r_S - 2\sigma_S^2 \quad ; \quad \sigma_n = \sigma_S. \tag{1.7}$$

From a lognormal distribution of the number of spherical particles, $Nn(r)$ (where N is the total number of particles, and $n(r)$ is normalised), given particle density ρ, the total mass of aerosol is

$$M = \rho \int_0^\infty \frac{dV}{dr}\, dr = \frac{4}{3}\pi\rho N r_n^3 \exp\left[\frac{9}{2}\sigma^2\right]. \tag{1.8}$$

1.4.2 Refractive index

For light travelling between two different media, the relative refractive index, $m(\lambda)$, describes the phase speed and attenuation differences between the two.

$$m = \frac{v_{1,\text{ phase}}}{v_{2,\text{ phase}}} = \sqrt{\frac{\varepsilon_2\mu_2}{\varepsilon_1\mu_1}}, \tag{1.9}$$

where ε_i and μ_i are the permittivity and permeability respectively of the two media. When the first medium is a vacuum, $v_1 = c$, and m is the absolute refractive index. For non-magnetic media, such as those to be dealt with in the remainder of this work, the relative permeability is unity ($\mu_i = \mu_0$) and so we can assume that $m \simeq \sqrt{\varepsilon_r}$, where $\varepsilon_r = \varepsilon/\varepsilon_0$ is the relative permittivity.

Consider a plane wave with wavelength in free space λ travelling along the x-axis through a medium:

$$\mathbf{E} = \mathbf{E}_0 \exp\left[\frac{2\pi i}{\lambda}\left(m(\lambda)x - ct\right)\right]. \tag{1.10}$$

Separating m into its real and imaginary components ($m = n + ik$) [2], it is clear that the imaginary part

[2] Depending on the setup of the equations, we can also define m so that we have $m = n + jk$ where k is negative.

leads to the attenuation of the field amplitude, while the real part corresponds to the motion of the waves along the x-axis. All mediums have absorption bands at some frequency, and the Kramers–Kronig relations require that $n(\lambda)$ is some function of an integral transform of k over the entire spectrum [Bohren and Huffman, 1983; Clapp et al., 1995], so m must be wavelength dependent (or dispersive).

At a flat boundary, the conditions requiring continuity lead to Snell's law, $\sin\theta_i = m \sin\theta_t$ where θ_i and θ_t are the incident and transmitted angles of the light between the normal to the boundary surface and direction of travel. The reflection and transmission coefficients can also easily be calculated, giving the Fresnel equations [Hecht, 2002].

1.4.3 Properties related to non-sphericity

If the assumption of spherical, homogeneous particles is discarded, additional aerosol properties are required in order to describe an aerosol microphysical model. Most analysis of aerosol particle shape is only partially quantitative in that a sample of particulate is generally inspected under an electron microscope, and the shape properties of these few are manually measured [e.g. Kalashnikova and Sokolik, 2004; Gwaze et al., 2006]. As such, one is only looking at a two dimensional image of the aerosol. Various parameters are used to characterise shape.

Aspect ratio (AR) The first is the AR, defined as the ratio of length along maximum projection of the shape and the width (perpendicular to that projection). This is very similar to the parameter ε given in the definition of a spheroid. It gives the ratio of a/b, the major and minor axes, about one of which, the ellipse will be rotated to form a spheroid. For $\varepsilon = 1$ we have a sphere; $\varepsilon < 1$ implies a prolate spheroid (e.g. rugby ball); $\varepsilon > 1$ implies an oblate spheroid (e.g. a disk).

Circularity (CIR) This gives a measure of how a particle's projected perimeter compares to its projected area. It is usually defined as CIR $=\text{perimeter}^2/(4\pi A)$ [e.g. Kalashnikova and Sokolik, 2004] or the reciprocal of this expression so that as with AR, CIR will be unity for a sphere.

Fractal dimension When looking at aggregate particles (such as fresh products of combustion), it is often true that their shapes are scale invariant over several orders of magnitude [Sorensen, 2001]. In this case, a fractal dimension D_f is a useful quantity. A similar quantity to circularity, it is a measure of how a particle's length relates to its mass. For aggregate particles of N_p equally sized spherules, $N_p \propto \left(\frac{R_g}{r_p}\right)^{D_f}$, where R_g is the radius of gyration, describing overall size, and r_p is the radius of an individual spherule within the whole [Wentzel et al., 2003].

1.5 Optical theory

1.5.1 Methods of calculating light scattering

Mie theory

Mie theory was developed by Gustav Mie [Mie, 1908] in order to understand the colours that resulted from light scattering by gold particles suspended in water. Although it is exact, only with the emergence of computing has it become practical to calculate the scattering values. An excellent introduction to the theory is provided in Bohren and Huffman [1983], whose notation and outline have been used here. Code to calculate Mie scattering properties and their derivatives with respect to size and refractive index in the IDL programming language can be found on the AOPP, Oxford website[3].

An incident, electromagnetic, x-polarised plane wave is expressed in **v**ector **s**pherical **w**ave **f**unctions (VSWF), $\mathbf{M}_{mn}(kr,\theta,\phi)$ and $\mathbf{N}_{mn}(kr,\theta,\phi)$, which are solutions to $\nabla^2\mathbf{E}+k^2\mathbf{E}=0$, in spherical coordinates. The incident electric field is shown to be

$$\mathbf{E}_i = E_0 \sum_{n=1}^{\infty} i^n \frac{2n+1}{n(n+1)} \left(\mathbf{M}^{(1)}_{o1n} - i\mathbf{N}^{(1)}_{e1n}\right), \tag{1.11}$$

the subscripts e and o [4] meaning only the even, and only the odd solutions respectively of $\mathbf{M}_{mn}(k\mathbf{r})$ and $\mathbf{N}_{mn}(kr,\theta,\phi)$ are wanted. The magnetic field can be simply obtained from $\nabla\times\mathbf{H} = -i\omega\varepsilon\mathbf{E}$ where

[3] `http://www-atm.physics.ox.ac.uk/code/mie/` Details of the code are given in Grainger et al. [2004].
[4] which are not indices of the VSWFs.

ε is the electric permittivity and ω the angular frequency. Applying boundary conditions at the sphere radius, r_0,

$$(\mathbf{E}_i + \mathbf{E}_s - \mathbf{E}_I) \times \hat{\mathbf{e}}_r = (\mathbf{H}_i + \mathbf{H}_s - \mathbf{H}_I) \times \hat{\mathbf{e}}_r = 0 \qquad (\text{for } r = r_0), \tag{1.12}$$

and writing the scattered field, $\mathbf{E}_s$, and internal field, $\mathbf{E}_I$, as a similar sum of VSWFs to the incident field, the scattered field solution is found, which turns out to be a sum of Riccati-Bessel functions and associated Legendre functions.

Coated spheres

For coated spheres, one only needs to extend the theory of the previous section. Boundary conditions are imposed at the boundary between 1st and 2nd media as well as between the 2nd medium and the containing medium. After these are satisfied, there is a very similar solution to the Mie case. Details of this can be found in Bohren and Huffman [1983, p181–183].

T-matrix method

The T-matrix method, originally developed by Waterman [1969, 1973, 1976, 1979], is another method capable of analytically solving Maxwell's equations, but it is also applicable to non-spherical particles. While any shape can in principle be used, the method is particularly efficient for particles with axial symmetry, which allows simplification of the T-matrix calculations.

The incident field is written as a sum of VSWFs,

$$\mathbf{E}_i(\mathbf{r}) = \sum_{n=1}^{\infty} \sum_{m=-n}^{n} \left[a_{mn}\, \mathbf{M}_{mn}^{(1)}(k\mathbf{r}) + b_{mn}\, \mathbf{N}_{mn}^{(1)}(k\mathbf{r}) \right], \tag{1.13}$$

the scattered field similarly,

$$\mathbf{E}_s(\mathbf{r}) = \sum_{n=1}^{\infty} \sum_{m=-n}^{n} \left[p_{mn}\, \mathbf{M}_{mn}^{(3)}(k\mathbf{r}) + q_{mn}\, \mathbf{N}_{mn}^{(3)}(k\mathbf{r}) \right], \tag{1.14}$$

and the field on the surface of the scattering object as

$$\hat{\mathbf{n}}\times\mathbf{E}(mk\mathbf{r}) = \hat{\mathbf{n}}\times\sum_{n=1}^{\infty}\sum_{m=-n}^{n}\left[c_{mn}\,\mathbf{M}_{mn}^{(1)}(mk\mathbf{r}) + d_{mn}\,\mathbf{N}_{mn}^{(1)}(mk\mathbf{r})\right], \tag{1.15}$$

where m is the relative refractive index and bracketed superscripts on the VSWFs denote specific solutions [Mishchenko et al., 2000]. The orthogonality properties of VSWFs can be used to obtain relationships between just a_{mn} and b_{mn} or just p_{mn} and q_{mn} and the surface fields on the scattering object. These relationships can be written:

$$\begin{bmatrix}\mathbf{a}\\ \mathbf{b}\end{bmatrix} = \mathbf{Q_1}\begin{bmatrix}\mathbf{c}\\ \mathbf{d}\end{bmatrix}, \qquad \begin{bmatrix}\mathbf{p}\\ \mathbf{q}\end{bmatrix} = \mathbf{Q_2}\begin{bmatrix}\mathbf{c}\\ \mathbf{d}\end{bmatrix}, \tag{1.16}$$

and the unknown scattering coefficients ($\mathbf{p}$, $\mathbf{q}$) can be related to the known incident field coefficients ($\mathbf{a}$, $\mathbf{b}$) by

$$\begin{bmatrix}\mathbf{p}\\ \mathbf{q}\end{bmatrix} = \mathbf{Q_2}\mathbf{Q_1}^{-1}\begin{bmatrix}\mathbf{a}\\ \mathbf{b}\end{bmatrix}, \tag{1.17}$$

where the T-matrix, $\mathbf{T} = \mathbf{Q_2}\mathbf{Q_1}^{-1}$. The matrices $\mathbf{Q_1}$ and $\mathbf{Q_2}$ are to be found by integrating over the surface of the scattering particle [as described in Tsang et al., 1985, Chapter 3].

1.5.2 Additional modelling methods

The discrete dipole approximation (DDA) [Draine and Flatau, 1994; Yurkin and Hoekstra, 2007] can in theory calculate the light scattering characteristics of almost any shape, at the price of much greater computational complexity. It also suffers from the disadvantage (not present in T-matrix or layered sphere methods) that for each incoming and outgoing light direction incident on the particle, the entire calculation must be repeated. In contrast, techniques which solve the wave equation as an expansion of VSWFs, such as Mie theory or the T-matrix method, do not need to recalculate when re-

orientating their particles. In a system such as the atmosphere, where a huge distribution of randomly orientated particles are involved, this problem makes DDA cumbersome while other methods are still computationally viable.

There are several options available for scattering of light from aggregate particles (which DDA can also deal with). Most use addition theorems for VSWF with axes that are not co-located [Cruzan, 1962]. The RDG approximation (Rayleigh-Debye-Gans) ignores any interaction between the spheres, assuming that they do not interact, summing the single scattering waves in the far field. More complex methods, such as the Generalised Multi-particle Mie method (GMM) by Xu and Å. S. Gustafson [2001] deal with the multiple scattering.

1.5.3 Relevant optical properties

Size parameter

When looking at how light will scatter from a particle, the most important question is how comparable is the wavelength of light to the particle's size. If the wavelength is much greater than the size of the scattering object, the object won't be able to deflect the light in any significant way. If it is much smaller, it will come across the boundary of the scattering object as something relatively flat, and calculations will be in the domain of geometrical optics. As a result, the size parameter, x, is a clearer measure of the size regime of interest than an absolute measure of the particle.

$$x = \frac{2\pi}{\lambda} r_0 = k r_0, \tag{1.18}$$

where λ is the wavelength of light and r_0 is the characteristic length of a particle and k is the circular wavenumber. For a sphere, r_0 is the radius of the particle but for non-spherical particles the choice of r_0 is not so clear. Mishchenko and Travis [1998] have written T-matrix code which gives users the option of defining r_0 as the radius of a sphere of either equal volume or equal surface area to that of the scattering object.

The amplitude matrix

The amplitude matrix relates the scattered amplitude, $\mathbf{E}_s$, to the incident amplitude of the electric field, $\mathbf{E}_i$, where the light is split into light polarised parallel and perpendicular to the plane of scattering.

$$\begin{aligned} \mathbf{E}_s &= \frac{e^{ikr}}{kr}\,\mathbf{S}\mathbf{E}_i, \\ \begin{pmatrix} E_{\parallel s} \\ E_{\perp s} \end{pmatrix} &= \frac{e^{ikr}}{kr} \begin{pmatrix} S_2 & S_3 \\ S_4 & S_1 \end{pmatrix} \begin{pmatrix} E_{\parallel i} \\ E_{\perp i} \end{pmatrix}. \end{aligned} \tag{1.19}$$

Definitions vary slightly between texts. For example, Bohren and Huffman [1983] multiply the prefactor by i, or Mishchenko et al. [2000] by k (as well as using $E_\theta = E_\parallel$ and $E_\phi = -E_\perp$). Note the somewhat odd choice of element numbering in (1.19) which is due to convention in solving for the spherical case. This is a far field solution where it can be assumed that the scattered field is transverse ($\mathbf{E}_s \cdot \hat{\mathbf{e}}_r \simeq 0$). The elements of $\mathbf{S}$ will be complex.

Stokes parameters

Stokes parameters are closely linked to the electric field, but have been chosen to mirror easily measurable scattering quantities. From van de Hulst [1957]:

$$\mathbf{I} = \begin{pmatrix} I \\ Q \\ U \\ V \end{pmatrix} \quad \text{where} \quad \begin{aligned} I &= E_\parallel E_\parallel^* + E_\perp E_\perp^*, & Q &= E_\parallel E_\parallel^* - E_\perp E_\perp^*, \\ U &= E_\parallel E_\perp^* + E_\parallel^* E_\perp, & V &= i(E_\parallel E_\perp^* - E_\parallel^* E_\perp). \end{aligned} \tag{1.20}$$

The intensity is I and the other elements measure the various amounts of polarisation. For a completely polarised beam, we have $I^2 = Q^2 + U^2 + V^2$ and for partially polarised beams, $I^2 \geq Q^2 + U^2 + V^2$. The degree of linear polarisation is given by Q and U and circular polarisation by V, as shown in

Direction of polarisation for unit intensity ($I = 1$)		Stokes parameter		
		Q	U	V
Unpolarised		0	0	0
$\hat{\mathbf{e}}_{\parallel}$	$0°$	1	0	0
$\hat{\mathbf{e}}_{\parallel}$	$90°$	-1	0	0
$(\hat{\mathbf{e}}_{\parallel} + \hat{\mathbf{e}}_{\perp})/\sqrt{2}$	$45°$	0	1	0
$(\hat{\mathbf{e}}_{\parallel} - \hat{\mathbf{e}}_{\perp})/\sqrt{2}$	$-45°$	0	-1	0
Right circular	↻	0	0	1
Left circular	↺	0	0	-1

Table 1.1: Showing the meaning of the values of different Stokes parameters for polarised light. Adapted from Bohren and Huffman [1983].

Table 1.1.

Scattered parameters can be calculated from the incident parameters using the phase matrix, $\mathbf{Z}$:

$$\begin{pmatrix} I_s \\ Q_s \\ U_s \\ V_s \end{pmatrix} = \frac{1}{k^2 r^2} \begin{pmatrix} Z_{11} & Z_{12} & Z_{13} & Z_{14} \\ Z_{21} & Z_{22} & Z_{23} & Z_{24} \\ Z_{31} & Z_{32} & Z_{33} & Z_{34} \\ Z_{41} & Z_{42} & Z_{43} & Z_{44} \end{pmatrix} \begin{pmatrix} I_i \\ Q_i \\ U_i \\ V_i \end{pmatrix}. \tag{1.21}$$

The values for elements Z_{ij} (as a function of the amplitude matrix) are given as eqn (3.16) in Bohren and Huffman [1983] and eqns (13–29) in Chapter 1 of Mishchenko et al. [2000]. As with the definition of the amplitude matrix, slight differences occur. Mishchenko et al. [2000] multiply (1.21) by k^2 and have differing signs for some off diagonal elements, due to the use of unit vector $\hat{\mathbf{e}}_{\phi}$ instead of $\hat{\mathbf{e}}_{\perp}$.

Cross-sections and efficiencies

Cross-sections tell us how much of an incident beam's intensity is taken away[5] in terms of the area of the beam. If the power taken away by a certain process is W_x, then the cross-section for this process,

[5]The cross section is taken in a plane perpendicular to the direction of incident beam.

C_x, is:

$$C_x = \frac{W_x}{\frac{1}{2}\sqrt{\frac{\varepsilon}{\mu}}|\mathbf{E}_{i0}|^2}.$$

For example, scattering cross-section, C_{sca}, tells us what area of the incident beam becomes scattered light. The extinction cross-section, C_{ext}, tells us how much of the incident light is removed from the incident beam by scattering and absorption.

$$C_{\text{sca}} = \frac{1}{I_i}\int_{4\pi} I_s(\mathbf{n}_s)\, d\mathbf{n}_s, \tag{1.22}$$

$$C_{\text{ext}} = \frac{2\pi}{k}\,\Im\{Z_{11} + Z_{22}\} \tag{1.23}$$

$$C_{\text{abs}} = C_{\text{ext}} - C_{\text{sca}} \tag{1.24}$$

where $I_s = Z_{11} I_i + Z_{12} Q_i + Z_{13} U_i + Z_{14} V_i$ and Z_{ij} can be obtained from the Stokes parameters defined in (1.21).

Efficiencies are closely linked to cross-sections, but tell us what *proportion* of the beam incident on a particle is diverted to a certain process. As such, we define efficiencies, Q, as:

$$Q_{\text{ext}} = \frac{C_{\text{ext}}}{G}, \qquad Q_{\text{sca}} = \frac{C_{\text{sca}}}{G}, \qquad Q_{\text{abs}} = \frac{C_{\text{abs}}}{G}, \tag{1.25}$$

where G is the cross sectional area of a particle, projected onto a plane perpendicular to the direction of incident light. In the case of a sphere of radius r_0, $G = \pi r_0^2$. Naïvely, we could guess that the extinction cross-section would be equal to G, but since the influence of the particle outside the limits of its physical shape is non-zero, this is not the case.

Single scatter albedo

The single scatter albedo tells us the probability that a photon incident on a volume element will be scattered.

$$\bar{\omega}_0 = \frac{C_{\text{sca}}}{C_{\text{ext}}} \quad \left(= \frac{Q_{\text{sca}}}{Q_{\text{ext}}} \right). \tag{1.26}$$

The range of values is $0 \leq \bar{\omega}_0 \leq 1$, since $0 \leq C_{\text{sca}} \leq C_{\text{ext}}$.

Optical depth

Aerosol optical depth (AOD), also known as aerosol optical thickness (AOT), and given the symbol τ, gives the amount by which light is attenuated when travelling through an aerosol field. High optical depths imply a rapid reduction in signal. Specifically, transmitted intensity is related to incident intensity, I_0 by $I = I_0 e^{-\tau}$.

Using terms already given above, we can calculate τ saying [Thomas et al., 2011]

$$\tau(\lambda) = \int_0^\infty \beta^{\text{ext}}(z,\lambda)\, dz, \tag{1.27}$$

where this is the integral over the path of the light, and the extinction coefficient, β^{ext}, is defined from properties above as:

$$\beta^{\text{ext}}(z,\lambda) = \int_0^\infty C_{\text{ext}}(r,\lambda)\, n(r,z)\, dr. \tag{1.28}$$

The extinction coefficient gives a path-dependent measure of how a size distribution of particles, $n(r,z)$, causes extinction of light from a beam. It has dimensions of L^{-1}, making τ dimensionless, as we would expect. While clouds have very large optical depths ($\gg 1$), atmospheric aerosols generally have $\tau < 1$. They will be clearly visible from space when $\tau > 1$.

The phase function

The phase function is a normalised measure of how the intensity of scattered light varies with scattering angle. For a single, spherical particle, irradiated with unpolarised incident light, this is defined

as [van de Hulst, 1957; Bohren and Huffman, 1983]:

$$P(\theta) = \frac{2}{C_{\text{sca}}\, k^2\, r^2} \left(|S_1(\theta)|^2 + |S_2(\theta)|^2 \right), \qquad \text{[for spherical particles]} \tag{1.29}$$

where C_{sca} is the scattering cross-section and S_1 and S_2 are the amplitude functions for perpendicular and parallel components of the electric field. If we know the incident irradiance, I_0, the scattered intensity can be calculated as

$$I = I_0 C_{\text{sca}} P(\theta). \tag{1.30}$$

Due to the spherical symmetry (all incident angles can be considered identical), all that matters is the relative angle of scattering. This is not true for non-spherical particles, and more generally, we would have to define $P(\theta, \phi)$, dependent upon $S_1(\theta, \phi)$ and $S_2(\theta, \phi)$. Since the phase function is normalised, we find:

$$\int_{4\pi} P \, d\Omega = 1. \tag{1.31}$$

Asymmetry parameter

The asymmetry parameter (or anisotropy factor) is calculated from the phase function and tells us whether more light scatters in the forward or backwards direction.

$$g = \langle \cos\theta \rangle = \int_{4\pi} P(\theta, \phi) \cos\theta \, d\Omega. \tag{1.32}$$

Positive values indicate more forwards scattering. If $g = 0$ then light scatters equally in forward and backwards directions.

In earlier works on remote measurements of particles, $\langle \cos\theta \rangle$ was used in the Henyey-Greenstein function [Henyey and Greenstein, 1941], a low order approximation to the phase function which is easier to calculate:

$$P_{\text{H-G}}(\theta) = \frac{1}{4\pi} \frac{1 - g^2}{[1 + g^2 - 2\cos\theta]^{3/2}}. \tag{1.33}$$

Using this approximation, the phase function is imitated well on the large scale, but with none of the fine structure one would expect to see.

1.6 Satellites and retrievals

1.6.1 AATSR

The **A**dvanced **A**long **T**rack **S**canning **R**adiometer (AATSR) is the most recent in a set of instruments designed to measure sea surface temperature (SST) with very high accuracy (0.3 K). Previous instruments were ATSR-1 which was operational from 1991–2000, and ATSR-2 from 1995–2008. AATSR was launched in March 2002 on the Envisat platform, a sun-synchronous polar orbiting satellite. Due to the extended overlap between the missions, extensive calibration has been available allowing the collection of a long term data series of SST.

The design of all three instruments includes the measurement of light at two different viewing angles, almost simultaneously (2 minute difference), using a rotating mirror. The forward view looks ahead of the satellite with an angle of $\sim 55^{\circ}$ to the vertical; the nadir view looks directly down (see Fig. 1.6). Since the two views have different atmospheric path lengths, but expect to see the same surface (particularly over water), simplistically we could say that differences between the two views can be attributed to the differing atmospheric path length, and these could then be easily removed to obtain the SST measurements.

AATSR takes measurements at channels given in Table 1.2. The visible channels are ideal for the measuring of aerosols, since they are at wavelengths similar to the sizes of accumulation mode aerosol, and are in atmospheric viewing windows.

1.6.2 Retrieval theory

The retrieval method used by **O**xford-**R**AL **A**erosol and **C**loud retrieval (ORAC) is optimal estimation as described clearly and rigorously by Rodgers [2000]. This section is a very brief overview that

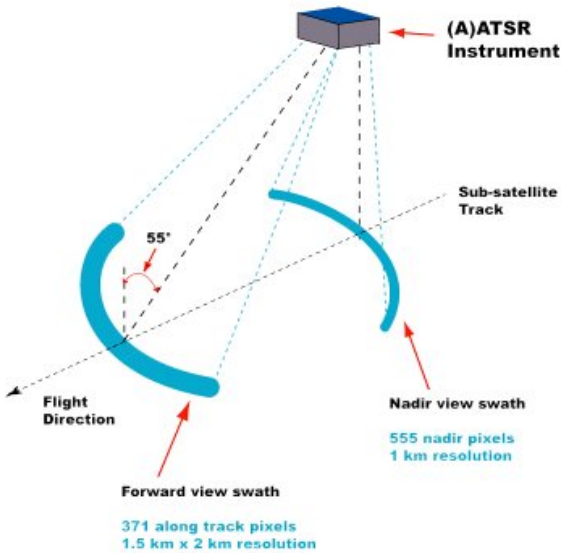

Figure 1.6: Showing the viewing swath taken by AATSR. From `http://www.leos.le.ac.uk/AATSR/whatis/instrument.html`, accessed on 5/8/2011. Reproduced with permission of C. Mutlow, STFC Rutherford Appleton Laboratory.

Channel	Central wavelength	Bandwidth
0.55	0.560	0.021
0.66	0.660	0.020
0.87	0.863	0.020
1.6	1.59	0.061
3.75	3.74	0.34
11	10.86	0.73
12	12.05	0.92

Table 1.2: AATSR channel locations and bandwidths. All values are given in μm.

borrows heavily from that text.

Consider a system that can be described by a number of quantities, collectively called the state vector, $\mathbf{x}$. Measurements of this system, $\mathbf{y}$, are related to $\mathbf{x}$ by a forward function, $\mathbf{y} = \mathbf{f}(\mathbf{x})$. The forward function can be approximated by a forward model, $\mathbf{y} = \mathbf{F}(\mathbf{x})$ which we hope to invert to obtain the state of our system, given the measurements: $\mathbf{x} = \mathbf{F}^{-1}(\mathbf{y})$.

Optimal estimation includes a framework for dealing with errors in such an inversion, allowing measurement errors and uncertainties in our forward model to propagate through the equations to give an uncertainty in the retrieved state, $\mathbf{x}$. The actual relationship between measurement and state used is

$$\mathbf{y} = \mathbf{F}(\mathbf{x}) + \varepsilon, \tag{1.34}$$

where ε is the error. Errors in the measurements are given in a covariance matrix, $\mathbf{S_y}$, which includes uncertainty in the measurement, uncertainties in the forward model, and the numerical precision of the forward model [Sayer, 2008].

Prior constraints are required to make the inverse problem well posed [Rodgers, 2000, Chapter 10]. These constraints are used in the form of an *a priori* state vector $\mathbf{x}_a$ with associated covariance $\mathbf{S_x}$ that collectively describe the state limits within which we expect our system to exist.

Cost and the retrieved state

Goodness of fit is measured by defining a cost, J, which measures the deviation of forward model measurement from actual measurement and deviation of state from the *a priori*. Both are weighted by how uncertain we are in the elements of $\mathbf{x}_a$ and $\mathbf{y}$:

$$J = \left(\mathbf{f}(\mathbf{x}) - \mathbf{y}\right) \mathbf{S}_\mathbf{y}^{-1} \left(\mathbf{f}(\mathbf{x}) - \mathbf{y}\right)^T + \left(\mathbf{x} - \mathbf{x}_a\right) \mathbf{S}_\mathbf{x}^{-1} \left(\mathbf{x} - \mathbf{x}_a\right)^T. \tag{1.35}$$

This is not the most general definition of cost, which can also include terms that take account of model parameters, $\mathbf{b}$, but for the purposes of this work can be assumed to have been assimilated into

estimates of error in $\mathbf{y}$. The object of the retrieval is to minimise J.

The retrieved state vector, $\hat{\mathbf{x}}$, at the minimum cost is written as:

$$\hat{\mathbf{x}} = \left(\mathbf{S}_{\mathbf{x}}^{-1} + \mathbf{K}_{\mathbf{x}}^{T}\mathbf{S}_{\mathbf{y}}^{-1}\mathbf{K}_{\mathbf{x}}\right)^{-1}\left(\mathbf{S}_{\mathbf{x}}^{-1}\mathbf{x}_{a} + \mathbf{K}_{\mathbf{x}}^{T}\mathbf{S}_{\mathbf{y}}^{-1}\mathbf{y}\right), \tag{1.36}$$

where $\mathbf{K}_{\mathbf{x}}$ is the weighting function, the partial derivatives of the forward model with respect to the state:

$$\mathbf{K}_{\mathbf{x}} = \frac{\partial \mathbf{F}(\mathbf{x})}{\partial \mathbf{x}}, \tag{1.37}$$

which shows the sensitivity of measurements to various regions of state space. In this form, we see $\hat{\mathbf{x}}$ as a combination of the *a priori* state and the linearised forward model, each weighted by their relative merits.

Averaging kernel

Just as $\mathbf{K}_{\mathbf{x}}$ shows the sensitivity of forward model to state, the gain matrix, $\mathbf{G}_{\mathbf{y}}$, shows sensitivity of the retrieval to measurement and measurement error [Rodgers, 2000, Chapter 3] and is defined as:

$$\mathbf{G}_{\mathbf{y}} = \left(\mathbf{S}_{\mathbf{x}}^{-1} + \mathbf{K}_{\mathbf{x}}^{T}\mathbf{S}_{\mathbf{y}}^{-1}\mathbf{K}_{\mathbf{x}}\right)^{-1}\mathbf{K}_{\mathbf{x}}^{T}\mathbf{S}_{\mathbf{y}}^{-1}. \tag{1.38}$$

Expanding the second bracket in (1.36), we see that the term in $\mathbf{y}$ is equal to $\mathbf{G}_{\mathbf{y}}\mathbf{y}$.

From this, we move to the averaging kernel, $\mathbf{A}$, that tells us the sensitivity of the retrieval to the state and is defined as:

$$\mathbf{A} = \mathbf{G}_{\mathbf{y}}\mathbf{K}_{\mathbf{x}}. \tag{1.39}$$

1.6.3 The current ORAC aerosol forward model

The aerosol forward model used by ORAC AATSR retrievals takes the four shortest wavelength channels (given in Table 1.2), and uses both the forward and nadir views. This means that there are

Value	No. of points	Min. value	Max value
$\log_{10}(\tau_{550})$	20	-2.0	0.75
$\log_{10}(r_{\text{eff}})$	20	-2.0	1.0
θ_0	10	0°	90°
θ_v	10	0°	81°
ϕ	11	0°	180°

Table 1.3: Dimensions of ORAC LUTs. Taken from Thomas et al. [2011]. The angles θ_0, θ_v, and ϕ are the solar zenith, viewing zenith, and azimuth angles respectively.

up to eight measurements available, from which the retrieval obtains a six element state vector:

$$\mathbf{x} = [\tau_{550},\ r_{\text{eff}},\ R_{550},\ R_{660},\ R_{870},\ R_{1600}]. \tag{1.40}$$

The first two elements, aerosol optical depth at 550 nm, and effective radius, are properties of the aerosol size distribution. The final elements, R_{550}, R_{660}, R_{870}, and R_{1600} are surface reflectances at the four shortest wavelength AATSR channels.

Due to the high computational cost of both aerosol light scattering calculations, and the radiative transfer calculations that obtain the top-of-atmosphere (TOA) reflectances, this code is run off-line and the data stored in look-up tables (LUTs) which are consulted at run-time. The tables have five dimensions which are given in Table 1.3.

Aerosol properties

When the ORAC retrieval was first developed over a decade ago, an ad hoc decision was made to use the microphysical descriptions of aerosol provided in the **O**ptical **P**roperties of **A**erosol and **C**louds package (OPAC) [Hess et al., 1998]. In this, typical aerosol distributions are called “classes”; the maritime class represents natural, ocean aerosol for example. Classes are built up by combinations of various aerosol modes and might have a nucleation, accumulation, and coarse mode. Various standard OPAC modes and classes are given in Table 1.4.

The individual aerosol modes making a class are defined as lognormal number distributions of

Aerosol mode	Aerosol class								
	Continental (clean)	Continental (average)	Continental (polluted)	Urban	Desert	Maritime (clean)	Maritime (polluted)	Maritime (tropical)	Arctic
Insoluble	x	x	x	x					x
Water soluble	x	x	x	x	x	x	x	x	x
Soot		x	x	x			x		x
Sea salt (acc.)						x	x	x	x
Sea salt (coarse)						x	x	x	
Dust (nuc.)					x				
Dust (acc.)					x				
Dust (coarse)					x				

Table 1.4: The constituent components of aerosol classes defined by Hess et al. [1998] for OPAC. This is a adaption of Table 4. Although some classes appear to be identical in this table, the relative mixing of the aerosol modes will be different, leading to different size distributions.

spherical particles. The particles are homogeneous, with constant refractive indices as a function of size (although RI varies with scattering wavelength). Any mode is thus defined by three values: a median radius r_g, a radius spread $\sigma = \ln S$, and a refractive index m, all of which are provided by OPAC. The biomass burning class is the exception to the rule. It takes its size and RI information from AERONET retrievals of cerrado burning aerosol by Dubovik et al. [2002].

The lookup tables require aerosol distributions with specific r_{eff} and AOD values. To obtain the required r_{eff}, the relative mixing of the component modes is changed. For smaller r_{eff}, the number concentration of small modes relative to large modes increases, and vice versa. If r_{eff} is smaller than that of the smallest aerosol component mode, then this smallest mode becomes the only aerosol in the distribution. Its median radius is then reduced, while holding its width constant. An example aerosol class, varying as a function of r_{eff} is shown in Fig. 1.7. In order to obtain the correct AOD, the total number concentration of the entire aerosol distribution is changed.

The uncertainty in the AOD *a priori* is not strongly constrained, since values are expected to vary

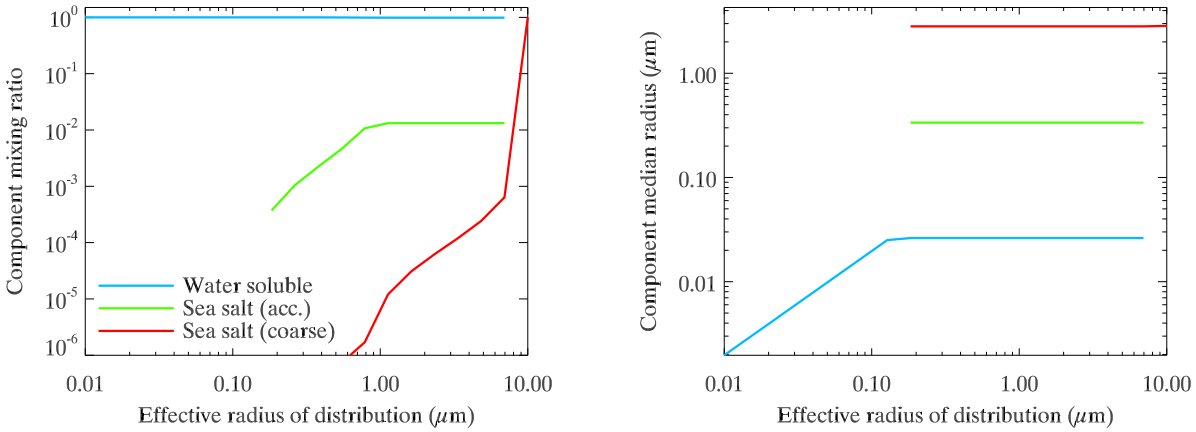

Mode	r_g (μm)	S	Refractive index	Number conc.
Water soluble mode	0.0262	2.24	$1.437+0.003i$	98.7 %
Sea salt accumulation mode	0.336	2.03	$1.373+0.000i$	1.32 %
Sea salt coarse mode	2.82	2.03	$1.373+0.000i$	0.00021 %

Figure 1.7: An example size distribution as a function of r_{eff} for the "marine (clean)" class as defined by Hess et al. [1998]. The relative humidity is 50 %. As r_{eff} becomes lower than the effective radius of the smallest mode, then this mode is reduced in size to obtain the correct value. Similarly, for the largest particles the smaller modes are no longer used, and the remaining particles are increased in size.

greatly between areas with high and low aerosol loading. Conversely, since r_{eff} is not expected to vary greatly, its *a priori* uncertainty is more tightly constrained.

Surface reflectance

The modelling of surface reflectance proceeds differently depending on whether a retrieval is over land or water. The surface is described by a bidirectional reflectance distribution function (BRDF) [Thomas et al., 2011] which means that if the surface appears to be different from the AATSR forward and nadir views, this change will not be attributed by the retrieval to aerosol effects .

Over water, a sea surface reflectance model developed by Sayer et al. [2010] is used as the *a priori* reflectance. Using ECMWF reanalysis wind speeds, and the GlobCOLOUR chlorophyll-A product, the model takes account of whitecaps, under-lighting, and sun glint. Over land, the MODIS BRDF product is used to determine the reflectance *a priori* [Thomas et al., 2011].

Calculations of top-of-atmosphere reflectance

The DISORT radiative transfer package [Stamnes et al., 1988] is used to calculate atmospheric transmission. Atmospheric gas absorption is included, along with aerosol scattering and absorption calculated in advance, and described above. Transmission calculations are stored in LUTs that are generated using a mid-latitude summer atmosphere. In the visible, aerosol optical depths are far higher than gas absorption, so changes in atmospheric profiles will not change transmissions significantly. In the operational retrieval, the aerosols are placed in the bottom two layers of the modelled atmosphere. This might not always be the most physically reasonable position, but since AATSR is looking down, and since there is not enough information to retrieve aerosol height, this is a suitable generalisation. At retrieval run time, the atmospheric transmission is combined with the BRDF to obtain TOA reflectance.

Class selection

The aerosol class is not obtained by the retrieval. When the algorithm is run, a specific aerosol class must be chosen. In order to obtain information about the type of aerosol, the retrieval can be run repeatedly using various classes. The retrieval cost function can then be compared between the various retrievals to see which has best fitted the measurements.

Chapter 2

Marine aerosol microphysical model

2.1 Background

As one might expect, given the amount of Earth which is covered by sea and ocean, maritime aerosols (those formed naturally over ocean) are some of the most commonly found atmospheric particulate on Earth [Lewis and Schwartz, 2004] and as a result contribute over 40 % to the global aerosol optical depth [O'Dowd and de Leeuw, 2007]. They are also a major source of CCN over oceans [Charlson et al., 1987].

Background values of AOD at 550 nm are around 0.1 [Smirnov et al., 2002], but can get much higher when surface wind speed increases [e.g. Moorthy and Satheesh, 2000]. Background values of effective radius are less than 1 μm, and increase with wind speed. The full size distribution ranges over 5 orders of magnitude, from nucleation mode sulphates with sizes as small as $r \simeq 2$ nm [O'Dowd and de Leeuw, 2007] to sea salt particles of $r \leq 150$ μm [Katoshevski et al., 1999].

2.1.1 Production and deposition mechanisms

The following section is a summary of current marine aerosol knowledge. The majority of this information is a synthesis of the reviews by Fitzgerald [1991], O'Dowd et al. [1997], Katoshevski et al. [1999], Lewis and Schwartz [2004], and O'Dowd and de Leeuw [2007]. The works by Fitzgerald

[1991], and Lewis and Schwartz [2004] are particularly recommended.

Non-sea salt particles

The smaller particles in the maritime atmosphere do not generally consist of sea salt but of sulphate[1]. It has been known for decades that almost all marine aerosol below $\sim$0.2 μm is sulphate (generally ammonium sulphate or similar) [Gras and Ayers, 1983], except that after periods of sustained high wind speed, small salt particles can become a significant presence below 0.3 μm [O'Dowd and Smith, 1993]. Studies also show that organic matter can contribute to the non-sea salt (NSS) aerosol mass fraction when biological activity is high [Vignati et al., 2010; Cavalli et al., 2004; O'Dowd et al., 2004], although those studies involving measurements were mainly carried out in non-remote areas.

Small particles make up about 5 % of the mass of the maritime aerosol, but 95 % of the number concentration [Petters et al., 2006]. The principal formation pathway is by homogeneous gas to particle conversion of oxidised dimethyl sulphide (DMS), a phytoplankton waste product [Charlson et al., 1987], into sulphate aerosol [Clarke et al., 1998]. Major nucleation events occur only after precipitation has washed out the majority of aerosol from the atmosphere, leaving such small quantities of atmospheric particulate that it becomes favourable for H_2SO_4 vapour to nucleate, rather than to accumulate on other particles. The size distribution of the NSS-sulphate is very constant, meaning there is also continuous, slow nucleation as well as these "bursts". The ubiquitous presence of ammonia [Quinn et al., 1992] is an important factor in ensuring that this nucleation can occur, particularly when the amount of ammonium is greater than the amount of sulphate [Katoshevski et al., 1999]. Gradually, particles grow by condensation of gaseous SO_2 and H_2SO_4 and when they are large enough to become activated as cloud condensation nuclei (CCN) can grow more rapidly as they are repeatedly processed by non-precipitating stratus, which at any time covers $\sim$50 % of the ocean. If enough time is allowed between precipitation events this can lead to a second peak in the NSS-sulphate size distribution close to 0.1 μm, as first measured by Hoppel et al. [1989].

It has been postulated by Charlson et al. [1987] that NSS-sulphate processes could form a neg-

[1] Or more accurately, non-sea salt sulphate (NSS-sulphate) since there is a sulphate component of sea salt

ative feedback on increased global temperature, since as ocean temperature increases, we expect an increase in DMS emission and so in NSS-sulphate concentration [Bigg et al., 1984] leading to the 1st indirect aerosol (or Twomey) effect [Twomey, 1977b].

Sea salt particles

Sea salt aerosol particles (SSA) are generally thought to have sizes in the range $0.2\,\mu\text{m} \leq r \leq 150\,\mu\text{m}$. They are created by primary, mechanical processes, removing small drops of water from the sea's surface. One can split the size of SSA into three modes, each characterised by a different method of aerosol production.

The two processes creating the smaller modes are the result of the formation of whitecaps. Wind stress on the ocean causes the surface layer to move faster than the layer underlying it. This forms waves which break, trapping air under the surface. These bubbles of air form white caps as they reach the surface and burst, emitting salt water solution droplets (the precursors to SSA), as shown in Fig. 2.1. The smallest particles are formed as the film of water around the bubble bursts, ejecting

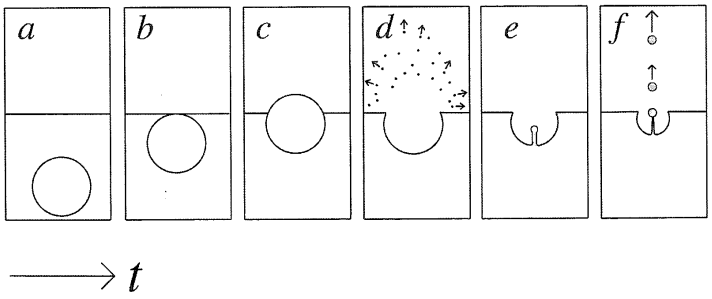

Figure 2.1: Diagram of idealised drop formation. Bursting of the air bubble releases film droplets (d) which form the sub-micron sea salt mode, and jet drops (f) which form the smaller particles of the super-micron mode. From Lewis and Schwartz [2004, Fig. 6], reproduced with permission.

hundreds of droplets in all directions. Larger particles are also created by this method. Next, as the cavity on the surface of the water is refilled, a jet forms which ejects a very small number (6 or less, as the size of the parent bubble increases) of super-micron particles vertically out of the vanishing bubble. The size of the jet particles are generally around one tenth the size of the bursting bubble.

Whitecap formation begins with wind speeds of ~ 3 ms^{-1} and the coverage increases rapidly with additional wind stress. As such, the whitecap cover (and thus the flux of SSA into the atmosphere) are generally parameterised as a function of wind speed and particle radius [Monahan and Muircheartaigh, 1980].

At very high wind speeds, the waves can be "torn", directly removing sea-salt liquid from the crest, and are called spume drops. Particles formed thus are extremely large (can be up to hundreds of microns) and so are very unlikely to be entrained into the atmosphere in great numbers. These spume drops are also formed in much smaller numbers (although they can have a significant mass density).

In fact, while all SSA generally do not make up a large proportion of the number density of maritime aerosol, they contribute overwhelmingly to the mass density. As mentioned above, work by O'Dowd and Smith [1993] suggests that SSA could be found at radii as small as 0.05 μm. This is important, as sodium chloride would preferentially be used for CCN, slowing down cloud processing of NSS-sulphate.

Dry deposition occurs at rates of the order 1 cm s^{-1} [Pham et al., 1995], but the principal removal mechanism is the sporadic wet deposition which removes a large proportion of the particles.

2.1.2 Observations of general marine conditions

Within the marine boundary layer (MBL), numerous experiments have shown that the maritime aerosol is generally consistent in relative size resolved number concentration, decreasing in total number concentration with height [Blanchard et al., 1984; Hoppel et al., 1994; Barnaba and Gobbi, 2001; Lewis and Schwartz, 2004]. Relative humidity is fairly consistent, around 80 %, and wind speeds in non-stormy conditions are around 8 m s^{-1}.

The size distribution over ocean generally contains up to two NSS-sulphate modes, from homogeneous nucleation of oxidised DMS peaking around 0.03 μm and a larger mode around 0.1 μm from cloud processing of the smaller particles. There are up to three sea salt modes present in the

atmosphere, a sub-micron mode, a super-micron mode, and a large mode (with $r > 25$ μm) [Lewis and Schwartz, 2004] although for the purposes of satellite retrieval, only the smaller two are observable. The large, spume drop particles have low production rates, and very high dry deposition rates meaning their atmospheric concentrations are extremely low.

2.1.3 The ORAC microphysical model for maritime aerosol

The pre-existing ORAC model of maritime aerosol follows OPAC's definition for maritime clean aerosol [Hess et al., 1998] with a relative humidity of 50 %. This means there are three lognormal modes, the "water soluble", "sea salt accumulation", and "sea salt coarse" modes. The effective radius is set by modifying the relative mixing ratios between modes, and the AOD is set by modifying the total number concentration, as described in §1.6.3.

2.1.4 Other microphysical models used in satellite retrievals

MODIS

The MODIS operational retrieval [Remer et al., 2005] over ocean splits the aerosol into "small mode particles" and "large mode particles", both with lognormal size distributions. During a retrieval, only one of each mode size can be selected and their relative concentrations are altered to obtain a final bi-modal distribution. Based on the refractive index and sizes of the particles as given by Levy et al. [2003, 2009] and Remer et al. [2005][2], the modes are very similar to certain OPAC modes.

The "small mode particles" closely resemble the OPAC "water soluble" mode at two relative humidities, 50 % and 80 %, each with two possible sizes, giving a median radius range of 0.06 μm $\leq$ $r_{m\,\mathrm{small}} \leq$ 0.10 μm. The "large mode particles" resemble the OPAC "sea salt accumulation mode" at RH=80 % with three possible sizes, 0.4 μm $\leq r_{m\,\mathrm{large}} \leq$ 0.8 μm. There is also the option of the large

[2]The sea salt refractive indices given in Levy et al. [2003, Table 1b] and Remer et al. [2005, Table 2] where modes at RH=80 % (modes 5–7) are a repeat of the refractive indices of the water soluble class at RH=50 % differ from those given in Levy et al. [2009, Table 2a]. This is because the former are values for MODIS collection 4 and the latter are for MODIS collection 5.

mode particles being desert dust.

After calculating ε (the equivalent of cost for ORAC retrievals) for each possible combination of small and large mode distributions, the optical properties of those combinations with $\varepsilon < 3$ % are averaged together to get the final optical properties.

This is an extremely similar setup to the current ORAC aerosol microphysical model, although the MODIS team have chosen a higher relative humidity (which is more consistent with observations).

MISR

The MISR operational retrieval [Diner et al., 2008] over dark ocean uses a model with variable relative humidity and defines a clean maritime class consisting of up to three lognormal modes, "sulphate", "sea salt accumulation" and "sea salt coarse" which are extremely similar to the OPAC modes. The relative abundance of these modes can vary, and the changing relative humidity alters each mode's median radius and refractive index. Different modes also have different height profiles [Diner et al., 1999]. Combining of modes is carried out using a fraction of total optical depth, not number concentration.

2.2 Minor factors altering the marine aerosol mode

2.2.1 External or internal mixing

Since NSS-sulphate and SSA are soluble, it seems very likely that there will be mixed aerosols where there is an internal mixture of the two types. This is not modelled by the ORAC microphysical model, which uses external mixing only. Concerns about changes to the optical properties based on a different aerosol mixing method were shown to be unwarranted for maritime aerosol by Tang [1997], who found that scattering coefficients for internal and external mixtures of various salts were very similar when the relative humidity was above 60 %.

2.2.2 Non-sphericity and efflorescence / deliquescence

The difference between efflorescence and deliquescence points[3] for aqueous salts [Lewis and Schwartz, 2004] means that there is the potential for both solid and aqueous salts, possibly at the same time, if the marine air were ever to get dry enough. This would alter the shape and refractive index of the salt aerosol.

Ambient oceanic relative humidities generally are around 80 %, rarely dropping below the relative humidities at the limit of efflorescence, and sea salt aerosols are created in liquid droplet form [Irshad et al., 2009]. As such, over the open ocean, anything other than aqueous spherical aerosols are not expected.

2.2.3 Refractive index

Changes to the composition of sea salt and concentration of aqueous sea salt water droplets will both change the refractive index of what one would generally assume to be a homogeneous light scatterer. Again, using the work of Tang [1997], it can be argued that the likely biggest change in sea salt composition in an aqueous solution would be due to the the addition of new salts, such as ammonium sulphate, which have been shown to not significantly alter the scattering properties. Additionally, simple 1st order mixing rules can be used to show that realistic changes in the ratios of ions in sea salt result in changes in the real and imaginary part of refractive index of less than 5 %, which would lead to much smaller changes in the light scattering properties of the aerosol and so not be of great concern.

[3] Efflorescence is the dehydration of a soluble salt, and deliquescence the hydration. The change in salt radius as a function of the relative humidity has hysteresis. The radius will sudden flip from dry to wet at a certain RH (the deliquesence point) and vice versa (the efflorescence point).

2.3 Size distribution

2.3.1 Wind speed

Wind speed has two effects that help to selectively change the size distribution of marine aerosol. Firstly, an increase in wind speed increases the whitecap cover [Lewis and Schwartz, 2004] which increases the production of SSA relative to NSS-sulphate aerosol as well as increasing the likelihood of spume SSA forming. Secondly, the increased wind speed means that there will be greater turbulence at sea level [Lewis and Schwartz, 2004] leading to more entrainment of larger particles.

O'Dowd and Smith [1993] found positive correlations between wind speed and SSA concentration while increases in NSS-sulphate were much less pronounced. Nair et al. [2005] found positive correlation for SSA but negative changes in NSS-sulphate with increased wind speed. Moorthy and Satheesh [2000] saw consistent increases in AOD with increased wind speed.

2.3.2 Relative humidity

As the marine aerosol distribution is completely soluble, changes in relative humidity result in changes in the radius of particles, and their refractive indices. Since changes in size with RH are not strongly dependent on the radius of the particles [Hänel, 1976; Shettle and Fenn, 1979] we would expect the growth in the aerosol size distribution to be fairly uniform with increased RH, if all other factors stayed the same.

2.3.3 ACE-1 measurements

The first Aerosol Composition Experiment (ACE-1) campaign took place in the southern hemisphere summer of 1995, and involved measurements of aerosol and ambient conditions taken on board ships and at observation stations throughout the Pacific area, principally south of Australia[4] [Bates et al., 1998]. From the point of view of investigating remote maritime aerosol this is one of the best sets

[4] ACE-1 data can be obtained from the CODIAC system (`http://data.eol.ucar.edu/codiac/projs?ACE-1`).

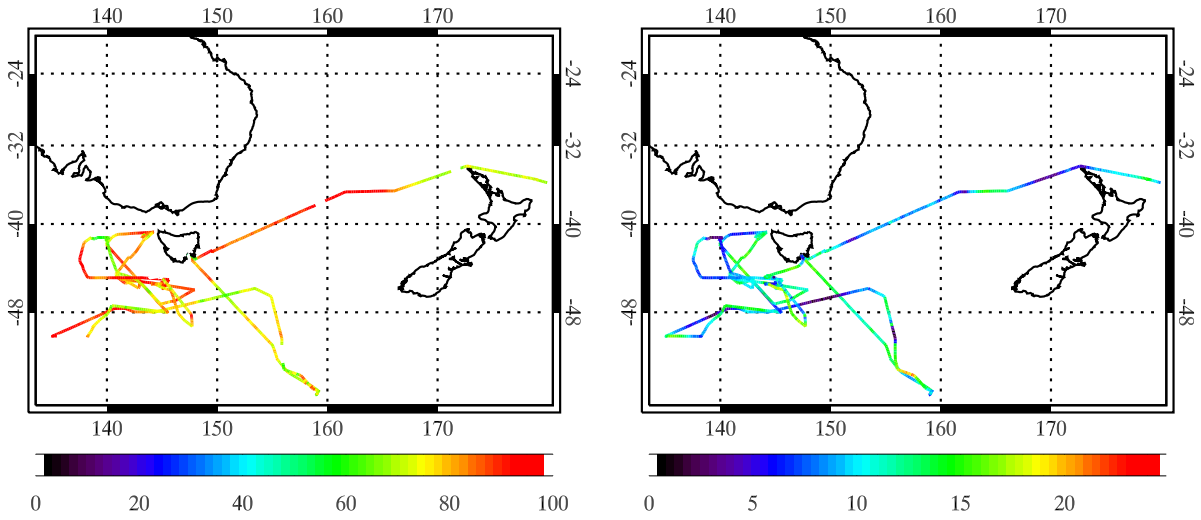

(a) Relative humidity, %

(b) Wind speed, m s^{-1}

Figure 2.2: Measurements of ambient conditions from leg 2 of Discoverer's route.

of measurements that could be used, particularly those taken from the Discoverer ship [Quinn et al., 1998], which travelled between New Zealand and Tasmania during the course of the campaign, as shown in Fig. 2.2.

Advantages of this measurement set are that:

- The southern hemisphere has far fewer shipping routes than the extremely busy North Atlantic and North Pacific [Campmany et al., 2009; Kaluza et al., 2010] although other areas of the southern hemisphere are less busy than the area in which the experiment took place.

- The ship board measurements would not be susceptible to coastal effects such as increased wave breaking, which could alter the local aerosol size distribution [Reid et al., 2001], making it less representative of the ocean in general. In the northern hemisphere, the Mace Head site on the west coast of Ireland has long-term measurements of aerosol size distribution [O'Connor et al., 2008] and work by Rinaldi et al. [2009] has shown that these coastal measurements can be representative of aerosol composition of open ocean measurements taken during the Marine Aerosol Production (MAP) experiment. Since these measurements would be representative of

the North Atlantic, we would not expect pristine natural conditions, due to both transport of continental anthropogenic aerosol [Fischer-Bruns et al., 2010] or ship based aerosol [Campmany et al., 2009].

- Simultaneous measurements of aerosol size distribution and hygroscopicity, relative humidity, wind speed and temperature allowed analysis of potential variation of size distribution with varying ambient conditions [Bates et al., 1998].

Rationale behind analysis

As discussed in §2.3.1 and §2.3.2, increases in wind speed and relative humidity would both lead to increases in the effective radius of an aerosol distribution, but in different ways.

While we would expect an increase in wind speed to change the mixing ratios between aerosol modes, preferentially increasing the quantities of larger particles, we would expect an increase in RH to increase the values of $r_{m,i}$ for the modes while holding the mixing ratios fairly constant.

This could be seen in work by Smirnov et al. [1995] who found that while measuring maritime optical depth over the ocean, wind speed was correlated strongly with changes in AOD at 1.6 μm while RH affected AOD at 550 nm. This shows preferential increasing of the very large SSA particles with wind speed, while the smaller particles were affected by RH.

By analysing how the ACE-1 measurements are correlated with atmospheric conditions, it will be possible to identify whether there is a more physically sensible method of changing the size distribution than that currently employed by the ORAC retrieval.

Measurement method

The Discoverer was brought from Seattle to Hobart in Tasmania for the ACE-1 experiment, and during the journey to the southern hemisphere, measurements were taken (called leg 1). The ACE-1 intensive campaign (leg 2) was entirely carried out in the Southern Ocean south of mainland Australia. Relative humidity, wind speed and temperature were measured along with aerosol properties.

Size distributions were obtained from a Differential Mobility Analyser (DMA) for particles with geometric diameters from 5 nm $\lesssim d_g \lesssim$ 0.57 μm and an Aerosol dynamic Particle Sizer (APS) measuring up to $d_g \lesssim 5$ μm. Prior to measurement by the DMA, the air was dried to an approximate RH of 10 %, and by the APS, to 35-40 %. "Corrected" distributions were provided at a calculated dry diameter equivalent to RH = 10 %, as described in Quinn et al. [1998]. Growth factors at ~35 nm, 50 nm, 75 nm and 165 nm were measured using a humidity-controlled tandem-DMA [Berg et al., 1998].

Data analysis

Since the end purpose of this research is to better represent the modelling of aerosol as seen from space, aerosol as seen in ambient conditions are what we require. The ACE-1 measurements taken from Discoverer are corrected to "dry aerosol" radii (at a relative humidity of 10 %) so will need to be re-grown to the more humid atmospheric conditions.

Using Köhler theory for equilibrium between an aqueous solution drop and humid air [Pruppacher and Klett, 1997], a wet radius at the relative humidity measured by the boat is obtained at the relative humidity measured by the boat. The equation to be solved is

$$\frac{e_a}{e_{\mathrm{sat},w}} = \exp\left[\frac{2M_w\sigma_{s/a}}{\mathcal{R}T\rho_w a} \; - \; \nu\Phi_s(\mathrm{m_B})\;\mathrm{m_B}\right], \tag{2.1}$$

where M_w is the molecular weight of water (= 18.0160 g mol^{-1}), $\mathcal{R}$ is the universal gas constant (= 8.314 J mol^{-1} K^{-1}), a is the wet particle radius, ρ_w is the density of water, ν is the number of ions into which the salt will disassociate in water, $\sigma_{s/a}$ is the surface tension of solute / air boundary, Φ_s is the molal osmotic coefficient of the salt in solution (a measure of a solution's deviation from Raoult's law) and $\mathrm{m_B}$ is the molality of a fully aqueous solution drop (the quantity of solute divided by the mass of solvent). The fraction of solution vapour pressure over the vapour saturation pressure for water ($e_a/e_{\mathrm{sat},w}$) is the relative humidity when the solution drop is in equilibrium with its environment as is assumed. The equation is solved for $\mathrm{m_B}$ (if the ambient relative humidity is above the efflorescence

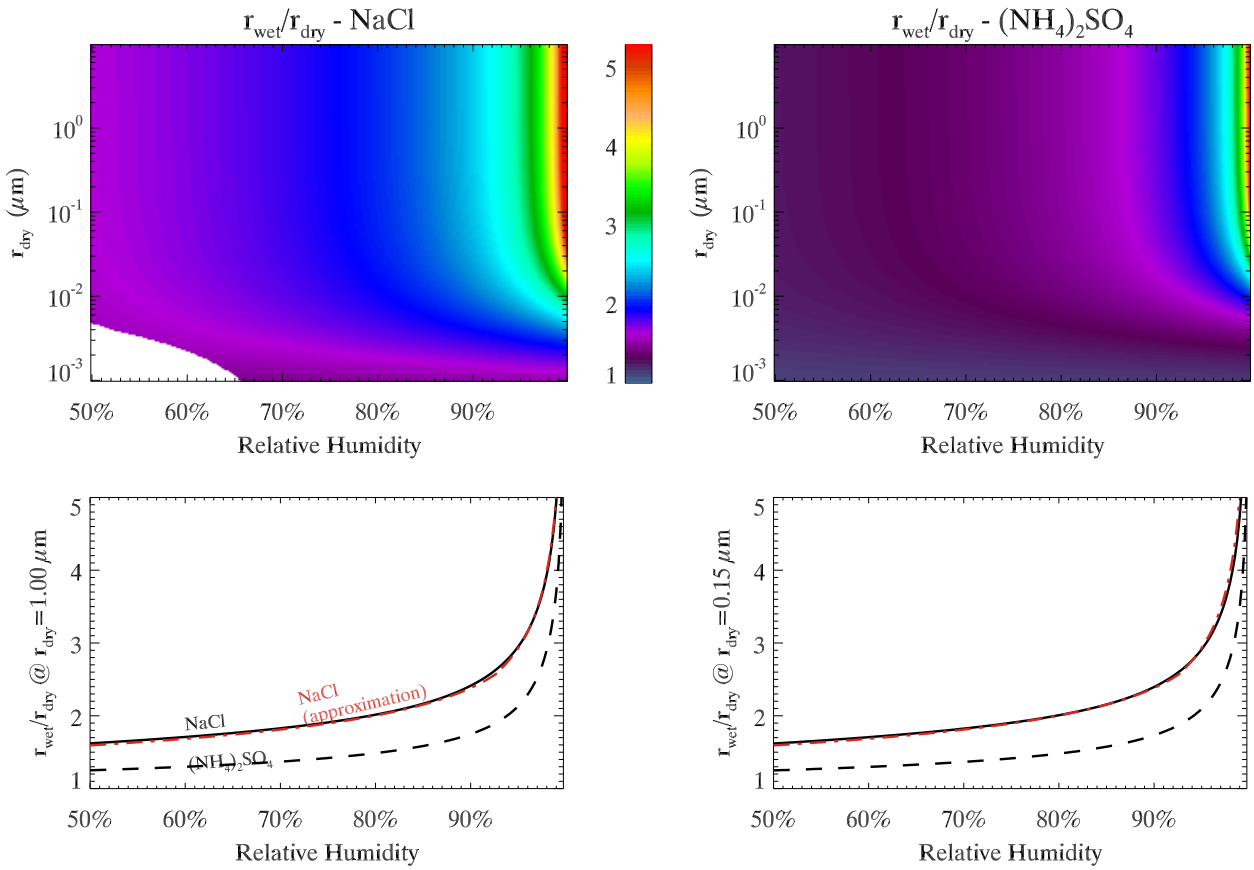

Figure 2.3: Model for aerosol growth factors ($r_{\text{wet}}/r_{\text{dry}}$) for two soluble aerosol types, NaCl and $(NH_4)_2SO_4$ calculated from full Köhler theory for soluble solutions [Pruppacher and Klett, 1997]. Top plots show growth factor as a function of relative humidity and dry particle radius. Missing sections of the plot are where the relative humidity is lower than the efflorescence point as given in Gao et al. [2007]. The lower two plots show transects at constant particle radius. Shown in red is a size-independent approximation for NaCl growth from Lewis and Schwartz [2004, 2006].

point) which can be converted to wet radius using:

$$\mathrm{m_B} = \frac{r_{\text{dry}}^3}{M_s\left(a^3 - r_{\text{dry}}^3\right)} \cdot \frac{\rho_s}{\rho_w}. \tag{2.2}$$

Example of swelling calculations are demonstrated in Fig. 2.3. The growth factors given are ratios of humid to dry particle radius as a function of RH.

The TDMA measurements were used by Berg et al. [1998] to separate out measurements into less-hygroscopic, more-hygroscopic, and sea salt peaks. They then equated more-hygroscopic particles

RH / type		Growth factor Leg 1 ($d = 165$ nm)	Leg 2 ($d = 150$ nm)	Theory ($d = 150$ nm)
50 %	mhp	-	1.19	1.24
	ssp	-	1.41	1.62
90 %	mhp	1.63	1.78	1.71
	ssp	2.01	2.14	2.38

Table 2.1: Measured and calculated growth factors for more-hygroscopic particles (mhp) which were modelled as a $(NH_4)_2SO_4$ solution, and sea salt particles which were modelled as a NaCl solution. Measured values are taken from Berg et al. [1998].

(mhp) with NSS-sulphate aerosol, and the less-hygroscopic particle (lhp) as those aerosols of anthropogenic origin. Each measurement includes the fraction of the three types of particles, since studies show that aerosols of various hygroscopicities form external mixtures in the troposphere [Swietlicki et al., 1999].

Measurements with high proportions of lhp were discarded as being of anthropogenic origin, although in reality, there were few cases where this occurred during leg 1 and fewer in leg 2. In re-growing the sizes, each DMS bin was split into mhp and ssp and grown separately, with the NSS-sulphate assumed to be ammonium sulphate solution, and the sea salt assumed to be sodium chloride solution. Comparison between growth factors calculated with these assumptions and measured growth factors are shown in Table 2.1. Reasonable agreement between the two can be seen as well as with measurements from other campaigns (e.g. Zhou et al. [2001, Table 1] gives growth factors of 1.71 and 2.06 for mhp and ssp respectively at 90 % RH and d=165 nm).

Since there were TDMA measurements at three dry diameters, an appropriate ratio of mhp:ssp was taken for each DMS bin by calculating a linear interpolation of the ratio between the TDMA measurements at different d_{dry}. For the APS measurements (which started at a diameter greater than the largest TDMA measurement), it had been assumed that measurements were entirely of sea salt when calculating dry diameters (a fair approximation [e.g. see Quinn and Coffman, 1998, Fig. 5]), and so were re-grown also with this assumption.

After an ambient relative humidity size distribution was obtained, bi- and tri-modal lognormal size distributions were fitted using the `mpfit` idl routines[5]. It was found that tri-modal distributions could more accurately represent these data due to a consistent peak with $0.05\ \mu\text{m} < r_m < 0.1\ \mu\text{m}$ (previous fits to this data by Heintzenberg et al. [2004] also needed more than two lognormal modes to fit accurately[6] although this was for percentiles of number distribution over the whole campaign, and not individual samples.) Example fits are shown in Fig. 2.4. The effective radius was then calculated from the lognormal parameters using eqn 1.4.

Fits were judged to be successful if the value of the summed squared residuals of the model output were below a threshold value of 15.0 (called "Best norm" in Fig. 2.4). Of the 2167 measurements taken during legs 1 & 2, 1684 were found to be suitable by this method and the following analysis only includes these results.

Fig. 2.5 shows comparisons of the fitted effective radius to relative humidity and wind speed. Clear correlation between r_{eff} and RH can be seen and is as would be expected. Increases in RH cause swelling of the particles, and so swelling of the total r_{eff}. Increases in wind speed (which we would expect to lead to greater aerosol production) also has a positive effect on r_{eff}, but this is less pronounced than in the case of RH. Long residence times, of the order days for sub-micron SSP [Gong et al., 2002; Lewis and Schwartz, 2004], mean that in general, the effect of local wind conditions on aerosol production does not imply a change in total aerosol loading at a certain particle size. However, it could have been hoped that during the ACE-1 campaign, where wet deposition led to regular "flushing" of aerosol [Bates et al., 2000], the relatively fresh distributions would have shown a good correlation. As it is, Fig. 2.5 does not show a clear relationship between wind speed and r_{eff}, compared with the clear increase in r_{eff} as a function of RH.

Analysis of the fits to each individual lognormal mode, as seen in Fig. 2.6, shows 2D histograms of the fitted parameters r_m, S, and m_{rat} as a function of the effective radius, r_{eff}. These are overlaid with lines of best fit, and the statistics of these lines are also shown. From these, it can be seen that

[5] Available from `http://cow.physics.wisc.edu/~craigm/idl/idl.html`

[6] Four modes were fitted, but the number concentration of the smallest mode was 0.0 in two of the three fits [see Heintzenberg et al., 2004, Table 2]

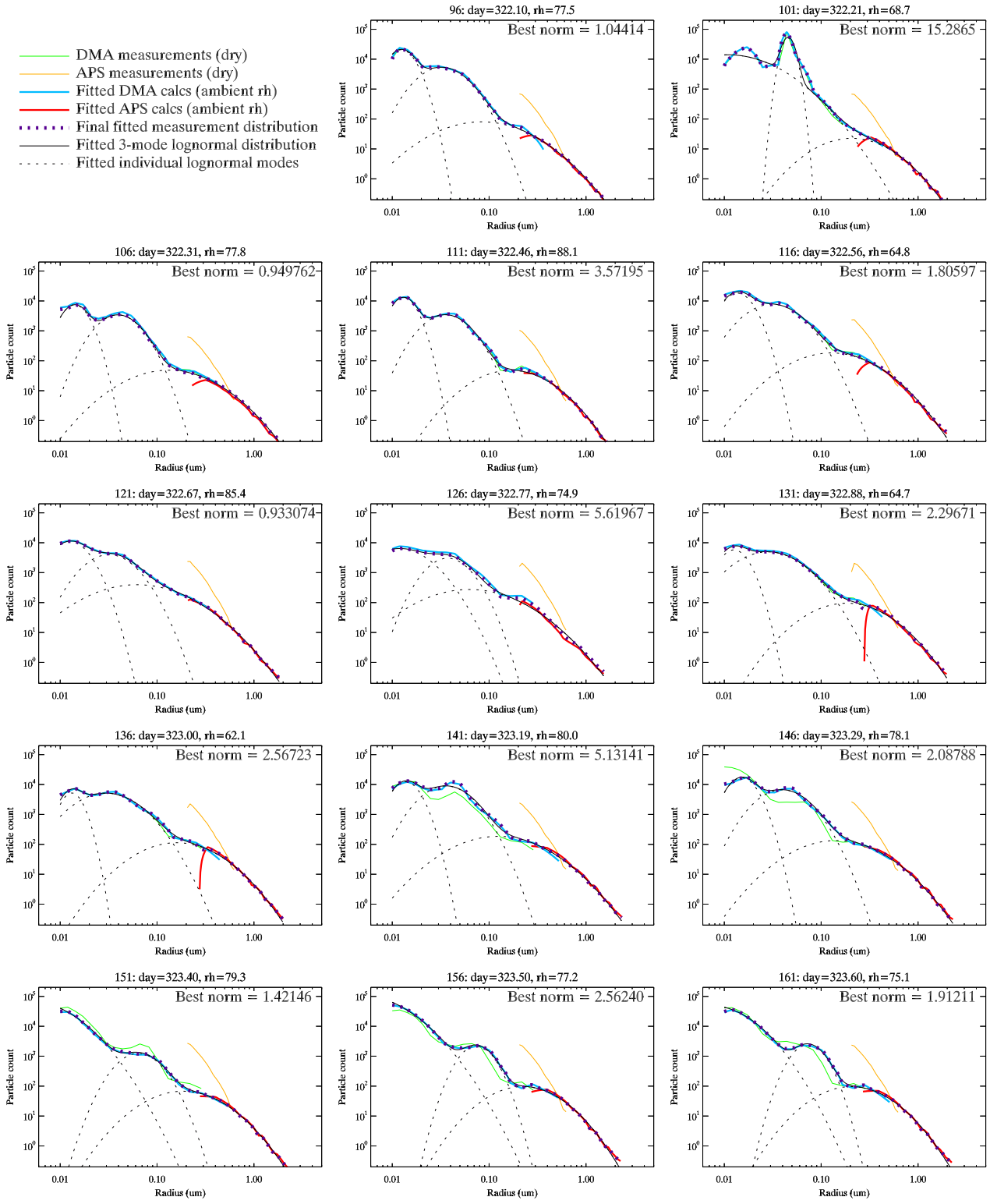

Figure 2.4: Examples of fitted lognormal distributions from ACE-1 Discoverer measurements. Dry measurements (with RH = 10 %) are grown to the ambient RH and then at the crossover between APS and DMA, weighted so that the number concentrations match up giving an ambient measured size distribution (thick dashed purple line). This is fitted with three mode lognormal distribution (purple thin solid line). The second panel, showing the 101st measurement is an example of a badly fitted distribution which would not be included in the final statistics due to poor goodness of fit characteristics.

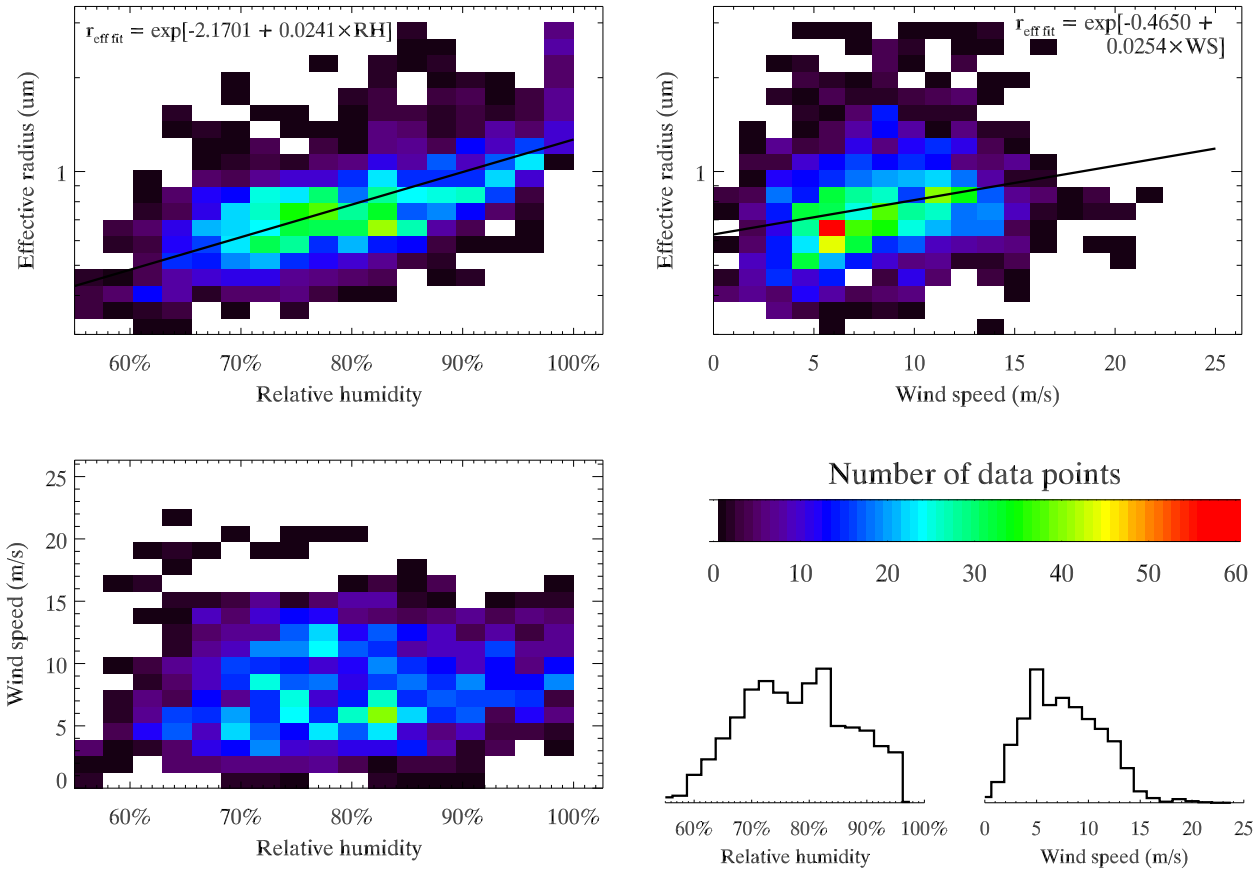

Figure 2.5: Histograms comparing fitted effective radius to ambient relative humidity and wind speed. Measurements were from legs 1 & 2 of the Discoverer's campaign. Linear fit parameters and related χ^2 statistics are also shown. In plots only including RH or wind speed, only measurements that were concurrent with successful lognormal fits have been used.

the median radius of individual modes, $r_{m,i}$, is fairly static as a function of r_{eff} (although there is a slight positive slope in the largest mode), and increases in r_{eff} are changed by altering the mixing ratios ($m_{\text{rat},i}$) between different modes, as is currently done in the ORAC retrieval. This is despite evidence that, in general, as the relative humidity increases $r_{m,i}$ also increases, as can be seen in Fig. 2.7. This could be explained by the lack of variation in RH during the campaign (and in general over water). As the retrieval method uses r_{eff} as its varying parameter on the aerosol microphysical properties, these results appear to confirm that the current method of variation is appropriate for the marine aerosol class.

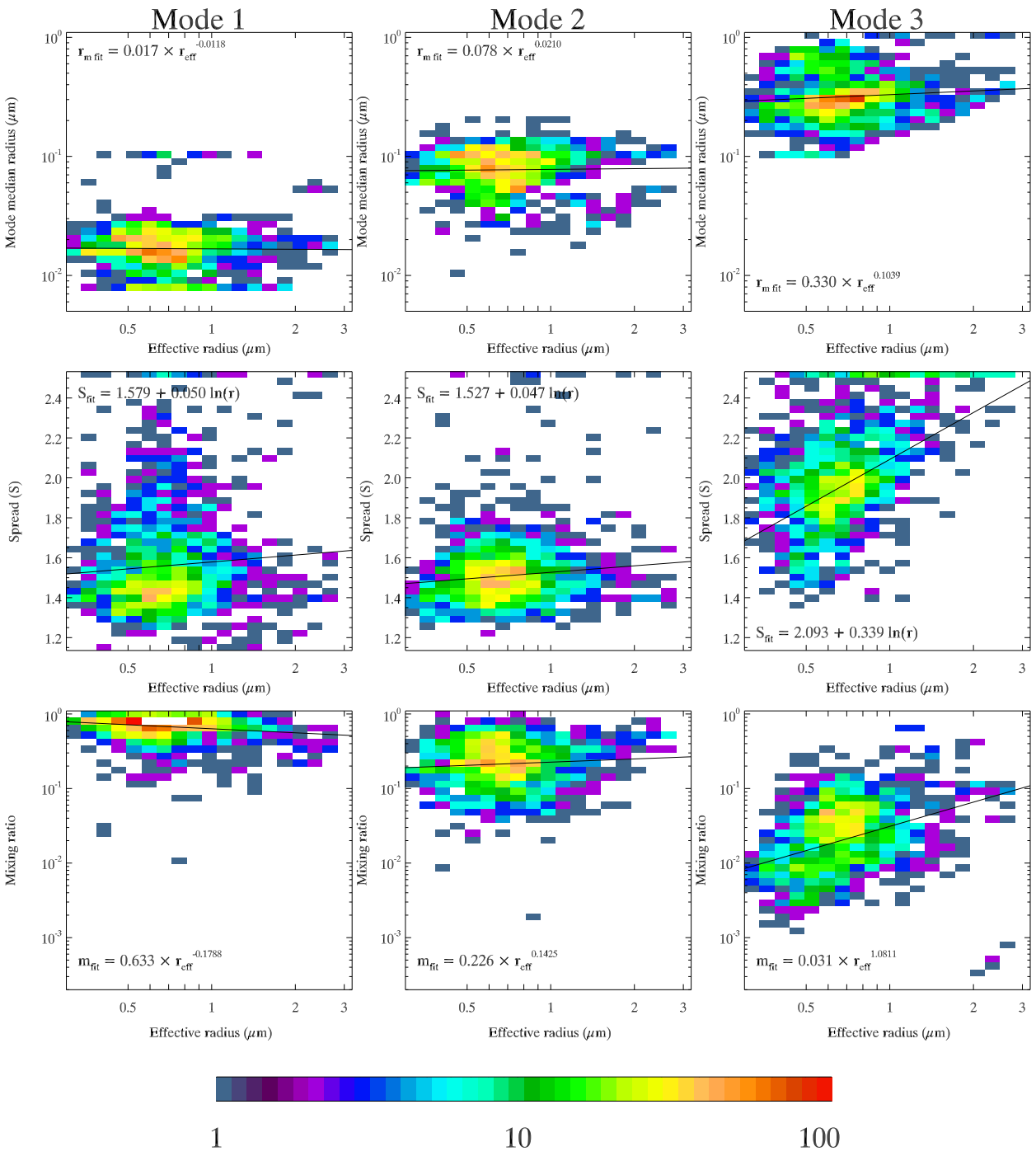

Figure 2.6: 2D histograms of fitted lognormal distribution parameters for ACE-1 aerosol data. The top panels show the fits for r_m, the middle for S, and the bottom for mixing ratio as a function of r_{eff}. The count scale is logarithmic. This figure can be thought of as variant of Fig. 1.7 in which ACE-1 fitted parameters for r_{eff}, r_m, and m_{rat} have replaced the modelled values used by the ORAC forward model.

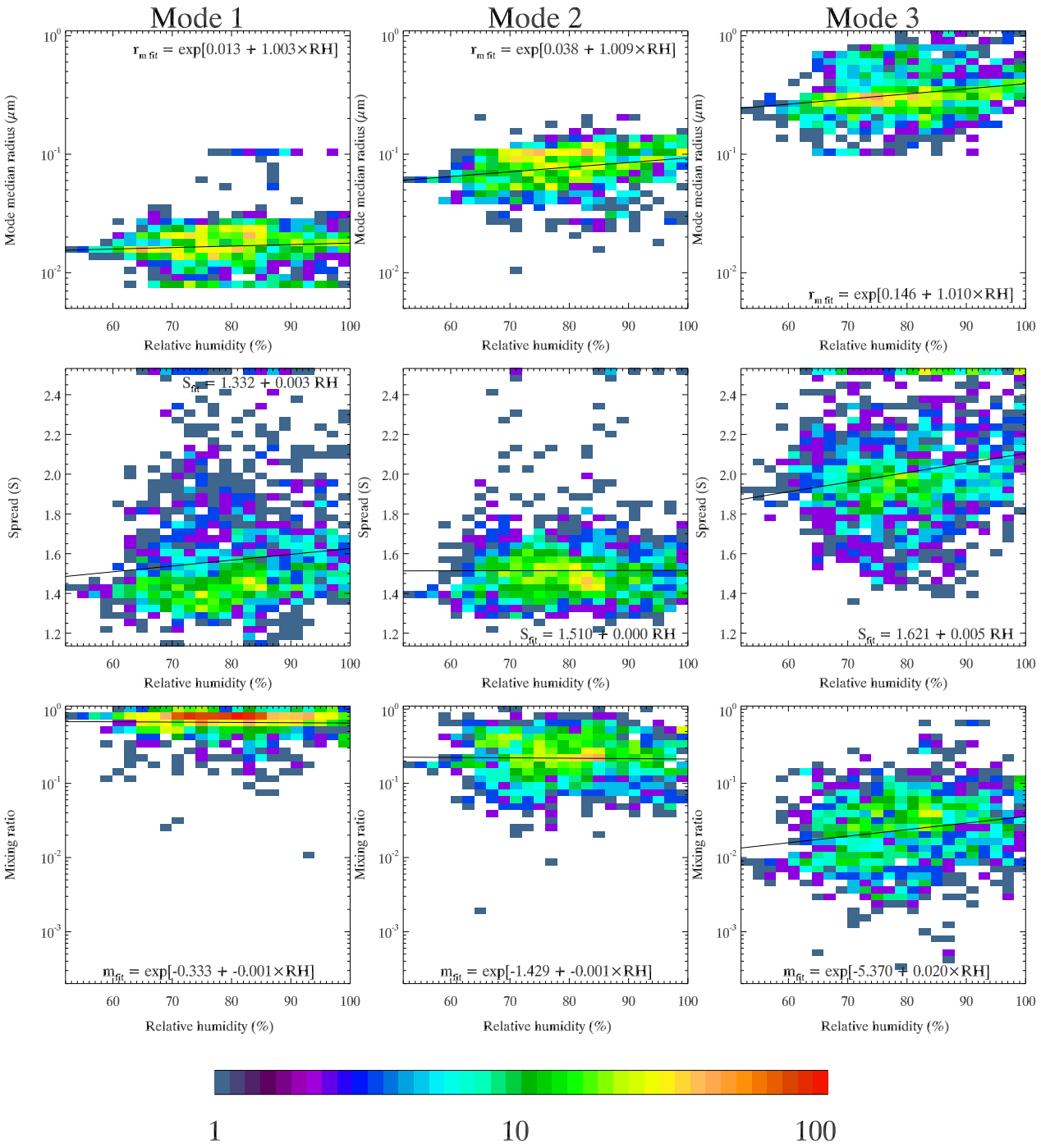

Figure 2.7: 2D histograms of fitted lognormal distribution parameters for ACE-1 aerosol data. The top panels show the fits for r_m, the middle for S, and the bottom for mixing ratio as a function of the relative humidity, RH. The count scale is logarithmic. The only difference between this figure and Fig. 2.6 is the replacement of r_{eff} with RH as the abscissa.

Finally, measurements of relative humidity from ACE-1 clearly confirm that the current ORAC estimate of 50 % is too low and a better choice would be around 80 %. Comparable retrieval schemes (such as the MODIS team's method) choose refractive indices for their water soluble and sea salt components that suggest they are using RH of around this value (see §2.1.4).

2.3.4 Defining a potential new size distribution

Figure 2.8 shows the fitted values of r_m and m_{rat} from ACE-1, plotted along with the current size distribution used by ORAC. The largest, coarse mode sea salt mode is not present in the measurements, as the particle sizers used in ACE-1 did not measure at large enough diameters to fit this. Since an additional mode was still required in order to accurately fit the data, this would suggest that during the ACE-1 campaign there were additional microphysical processes, resulting in a peak between the water soluble mode and the sea salt accumulation mode.

While most studies do not model additional marine aerosol modes below 100 nm, they are often seen in maritime size distributions, from artificially generated marine aerosol measurements [e.g. Sellegri et al., 2006], field campaigns [e.g. Hoppel et al., 1989, 1994; Murphy et al., 1998; O'Dowd et al., 2001; Bates et al., 2002; Clarke and Kapustin, 2002; Heintzenberg et al., 2004; Phinney et al., 2006; Smirnov, 2006], or sectional aerosol models [e.g. Gong and Barrie, 2003]. The mode is referred to as the "cloud residue mode" by Hoppel et al. [1994] and is thought to be the product of cloud processing of the smaller NSS-sulphate which are large enough to be CCN by non-precipitating stratus [Fitzgerald, 1991; Hoppel et al., 1994; Katoshevski et al., 1999].

Fig. 2.9 shows histograms of the scatter-plot data shown in Fig. 2.8. The main point of the two figures is presented in Table 2.2. Namely, adding an additional mode between the water soluble and sea salt accumulation modes could be an appropriate way to improve the microphysical modelling of maritime aerosol. Based on the discussion above, and since aerosol with radius less than 0.1 μm is generally considered too small to contain much sea salt [Fitzgerald, 1991; Murphy et al., 1998], it makes sense that this intermediate mode is classified as water soluble. That Table 2.2 shows the

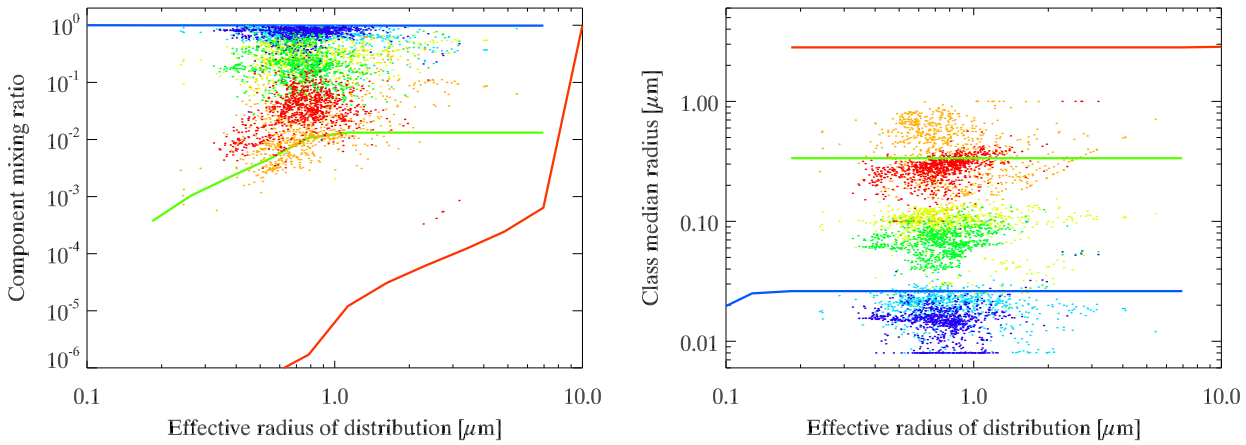

Figure 2.8: Comparing the size distribution currently used by the ORAC retrieval (solid lines) to a fitted three mode distribution which excludes the coarse mode, taken from fits to ACE-1 data. For all three fits, the lighter of the two similar colours (light blue, greenish yellow, orange) indicates fits from the first leg of the experiment (Seattle to Hobart) and the darker shades (dark blue, green, red) indicate fits from the second leg (south of Australia as shown in Fig. 2.2).

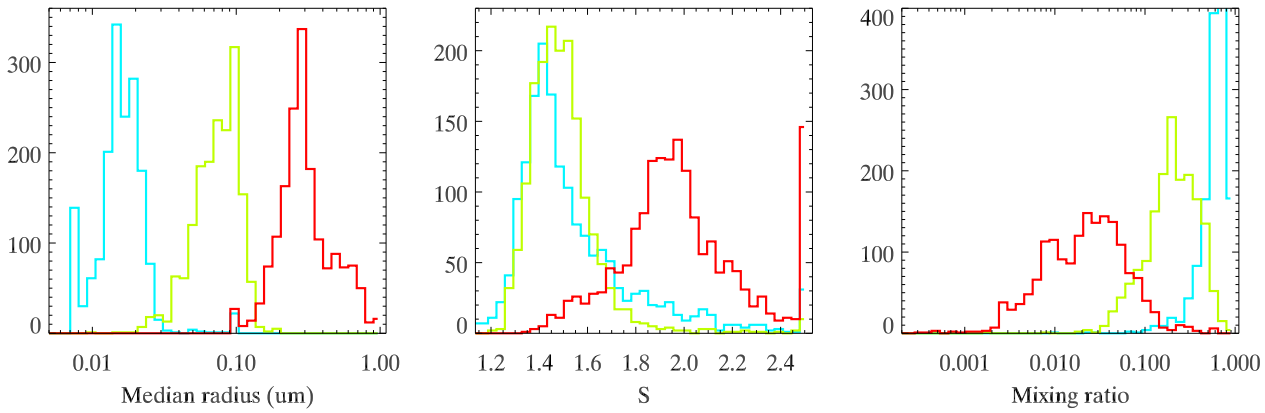

Figure 2.9: Histograms of fitted lognormal distribution parameters for ACE-1 Discoverer aerosol data (both legs).

Mode	Name	r_m / μm			m_{rat}	
		ACE-1	OPAC		ACE-1	OPAC
			50 %	80 %		
1.	Water soluble	0.018	0.0262	0.0306	0.79	0.987
2.	[no name]	0.090	-	-	0.19	-
3.	Sea salt acc.	0.400	0.336	0.416	0.02	0.0132
4.	Sea salt coarse	-	2.82	3.49	-	2.1×10^{-6}

Table 2.2: Size distribution parameters taken from ACE-1 fitted data and the ORAC retrieval's marine aerosol distribution. ACE-1 values were chosen from peaks in histograms as shown in Fig. 2.9. Values of r_m are shown at the current ORAC relative humidities of 50 % and at the more physically realistic 80 %. Names of the mode are taken from the OPAC aerosol modes; the 2nd mode, marked "[no name]" does not have an OPAC equivalent. Mode 4 was too large to be measured by the detectors aboard the Discoverer in ACE-1, so is omitted for those columns.

sum of the number concentrations of the two water soluble modes almost equivalent to the number concentration of the single mode currently used, and that Fig. 2.8 shows the current water soluble mode sitting in between the two fitted modes, adds weight to this decision. The median radius, r_m, of this mode has an equivalent size parameter of $x_m = 1.03$ for the shortest wavelength AATSR channel, so would be expected to have noticeable effect on optical properties.

New optical tables were therefore generated including an additional water soluble mode with $r_m = 0.090$ μm and $m_{\text{rat}} = 0.19$. The relative number of aerosol in the sea salt accumulation and coarse modes was kept the same, and so all of this m_{rat} was taken away from the current water soluble mode.

More important than the size distribution is the relative humidity assumption, which is currently too low at 50 %. Runs where RH was changed to 80 % are also included in the work that follows. So as to not alter two parameters at once, both the additional mode and the RH change were tried separately as well as trying a distribution with both an additional mode and RH = 80 %.

The change in light scattering properties is shown in Fig. 2.10. It can be seen that increasing the relative humidity does not dramatically effect the optical properties, but does lead to slightly less absorbing aerosol (increase in SSA, due to the decrease in imaginary RI), and slightly larger

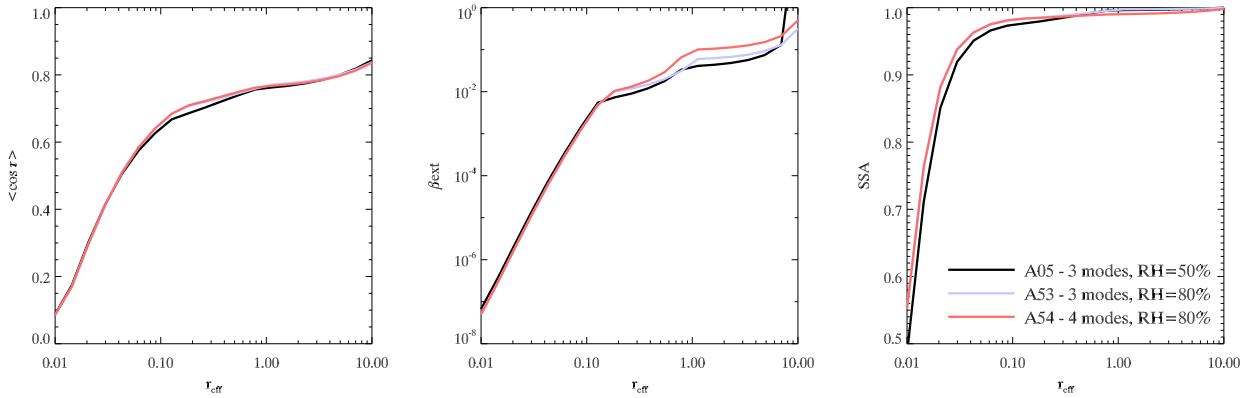

Figure 2.10: Comparing asymmetry parameter ($\langle\cos\theta\rangle$), extinction coefficient (β^{ext}), and single scatter albedo ($\bar{\omega}_0$) at $\lambda = 550$ μm for different marine aerosol models, as described in Table 2.3. The class shown in black is the current operational ORAC maritime aerosol model, labelled A05. The three models will be very similar when $r_{\text{eff}} < 0.10$ μm since at that point they only consist of the water soluble mode with the same size distribution.

extinction (due to the increase in particle size with increased RH).

2.4 Retrieval comparison

AATSR retrievals over water were processed for the month of July 2008. The month was chosen somewhat arbitrarily, due to the availability of data on local servers at the time. Mulcahy et al. [2009] reported that there was "no evidence of any clear seasonal pattern" in AOD over the "northeast Atlantic region" (Mace Head), and generally, maritime aerosol is the most globably consistent aerosol type, due to its globaly consistent methods of production. Changes in the size distributions are likely to be due to changes in wind speed and relative humidity, which are to seasonally dependent, but whose effects we are investigating anyway. As a result, for marine aerosol, the time of year at which we are investigating is unlikely to distort results.

A standard set of aerosol classes was used, alongside several modifications to the standard maritime class, as described in Table 2.3. The additional, non-marine classes were used to check that the currently retrieved pixel could not be better represented by another aerosol class, suggesting that it

Class	RH	Description
A05	50 %	Standard ORAC maritime clean class (as currently used)
A51	50 %	Additional sea salt mode at $r_m = 0.09$ μm
A52	50 %	Additional water soluble mode at $r_m = 0.09$ μm
A53	80 %	Standard ORAC maritime clean class
A54	80 %	Additional water soluble mode at $r_m = 0.09$ μm

Table 2.3: List of the test maritime aerosol classes used in the retrieval. Additional standard aerosol classes were also run. They were "continental clean", "urban". "biomass burning", and a non-standard "non-spherical desert dust" class, described in Chapter 3. These were used to make sure than only cases where a maritime aerosol was the best fitting class were selected.

was not marine aerosol. In these cases, the retrieval results were discarded for the following analysis.

Fig. 2.11 shows (for cases where one of the marine classes was the most likely type) the histograms of the retrieval cost (described in §1.6.2), aerosol optical depth at 550 nm and r_{eff} for the maritime classes. In the lower three figures, the retrieval values from the current class (A05) are compared to the various new models. None of these models are dramatically different and so it is not a great surprise that huge differences between their retrievals are not seen. That being said, the two classes with higher relative humidity (A53 and A54) have the lowest costs on average, and so could be said to be providing a slightly better representation of the true marine aerosol. The changes in optical depth and r_{eff} viewed in this manner are even less significant.

It can be seen more clearly in Fig. 2.12 that generally r_{eff} is retrieved with a larger value when an additional water soluble class is added, particularly in areas where it could be suspected that we were not actually looking at maritime aerosol; for example, off the west coast of North Africa, and in the Arabian sea, west of India. In the Southern Ocean, where we would expect to see high maritime aerosol loading, the cost generally appears to be higher for the A54 class. This suggests that the additional accumulation mode, added as a result of measurements from this region, is not improving the retrieval (although increasing the relative humidity is). One might argue that those measurements were taken during the southern hemisphere summer, whereas the retrievals were obtained for southern

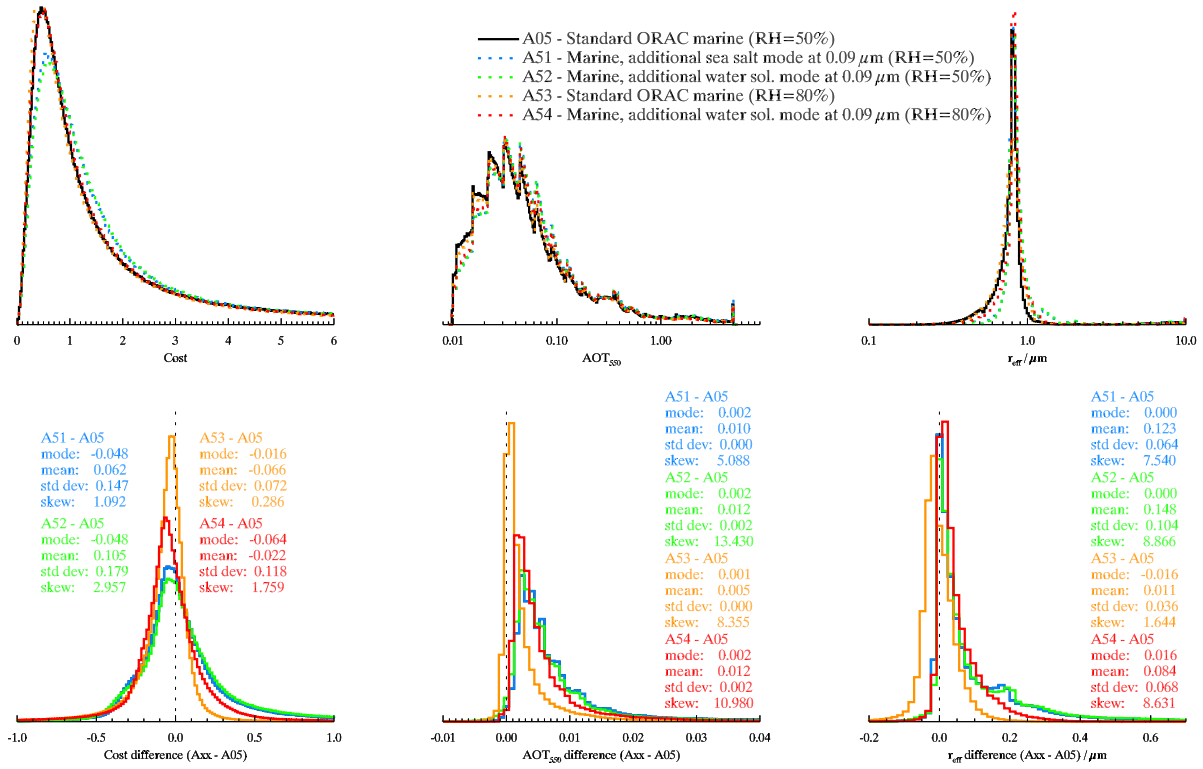

Figure 2.11: Retrieval histograms for various sea salt classes. Cost, aerosol optical thickness and r_{eff} are shown for cases where marine aerosol was the most likely aerosol. The jagged edges to the optical depth and r_{eff} histograms are due to retrievals sticking at lookup table points where the Jacobians suddenly change. The lowest values of AOD ($\tau < 0.011$) have been removed, as these values are so low that there is essentially no aerosol in the scene.

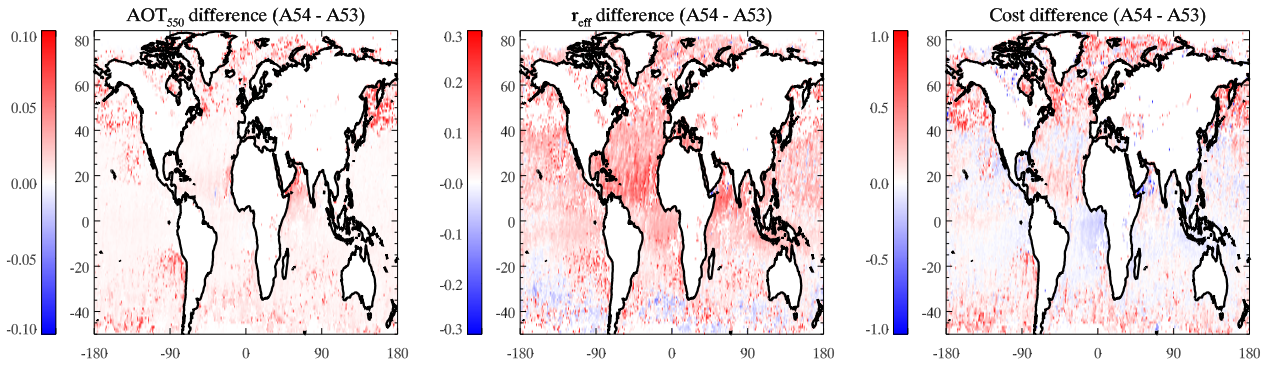

Figure 2.12: Average over the month of differences in cost, AOD, and r_{eff} on a $1^\circ \times 1^\circ$ lat-lon grid between A54 and A53 classes for cases where maritime aerosol was the most preferable. Differences are calculated before the averaging.

hemisphere winter (equivalent latitudes in the northern hemisphere are slightly more ambivalent) but in general it would appear that an additional aerosol mode is neither necessary nor helpful. The increase in relative humidity from 50 % to 80 % has resulted in retrieved optical depths that are approximately 5 % larger on average.

2.4.1 Other measurements

Using the **Ae**rosol **Ro**botic **Net**work (AERONET) [Holben et al., 1998; Dubovik and King, 2000], and the **M**aritime **A**erosol **N**etwork (MAN) [Smirnov et al., 2009], comparisons with the satellite retrievals were attempted. AERONET sites which were in remote locations likely to encounter mainly maritime aerosol, and operational during July 2008, were selected[7]. All available MAN campaigns for July 2008 were inspected[8]. Unfortunately, only 16 AERONET measurements for the whole month were obtained where a satellite passed over within an hour of a measurement. For the MAN, it was even less favourable, with only a single matching measurement for the entire month.

These comparison measurements showed high correlation with satellite retrievals although the AERONET values tended to be systematically higher (see Fig. 2.13). All of the over-plotted linear fits have gradients of ~ 0.7, implying that marine aerosol retrieved by ORAC is reported with 30 % less optical depth than AERONET measurements. There is very little difference between the ORAC marine classes used, which suggests that there are problems other than the microphysical modelling of the marine aerosol affecting the retrieval, such as surface reflectance modelling or retrieval algorithm difficulties.

2.4.2 Retrieval residuals

As with the cost, the residuals from the retrieval (the amount of light in each channel that cannot be accounted for by the forward model) are extremely similar for all of the marine classes. From

[7]These sites were Andenes, Crozet Island, Guam, Hornsund, Izana, Kangerlussuaq, Jey Biscayne la Laguna, La Parguera, Mauna Loa, Midway Island, Reunion St. Denis, Ragged Point, Santa Cruz Tenerife, and Tudor Hill.

[8]Measurements were being collected on three ships at this time: Amundsen, Healy and Islandia.

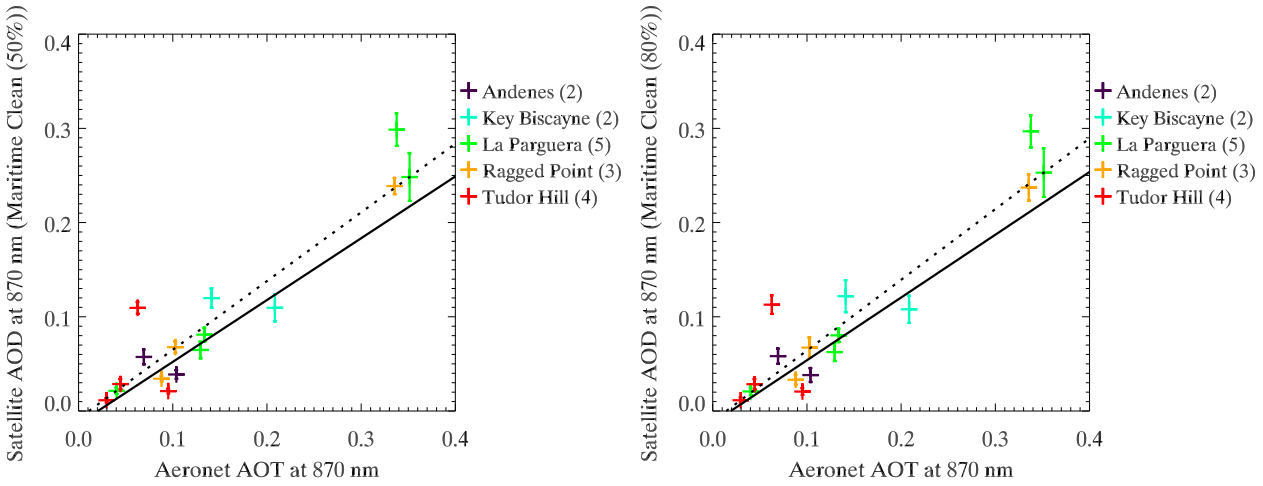

Figure 2.13: Concurrent marine ORAC AOD and AERONET AOD retrievals, both at $\lambda = 870$ nm for the original ORAC marine class (left), and a modified class with an additional nucleation mode, and higher relative humidity (right). Correlation coefficients are $\rho = 0.939$ and $\rho = 0.936$ respectively. The dashed lines show the least absolute deviation linear fits, and the solid lines are minimum χ^2 error statistic linear fits. There is almost no discernible difference between the two plots, due to the lack differences between the two retrievals.

Fig. 2.14, it can be seen that the 0.66 μm and 0.87 μm channels have been fitted well for both detector views, but the 0.55 μm channel has a slight positive bias in the nadir view, and the 1.6 μm channel a slight negative bias in the nadir, and a positive bias in the forward view.

Any systematic offset suggests that something is consistently being misrepresented in the retrieval. As a first order test on whether it is possible to correctly nudge the aerosol microphysics to get better agreement with the residuals, we can look at the light scattering properties of an aerosol distribution on its own before it is sent through the radiative transfer code. Changing any property of the aerosol distribution is likely to affect the different optical channels' extinction by different amounts. Since the residuals for $\lambda = 660$ nm, 870 nm are centred and appear unbiased, it is desirable that the ratio of their light scattering intensities remains the same as a property is changed, while the relative extinctions of biased channels would change. In the case an improvement to the microphysical model would see changes in nadir 550 nm and 1600 nm channels to be in opposite senses.

The residuals include measurements with a multitude of scattering angles, and sample two angles

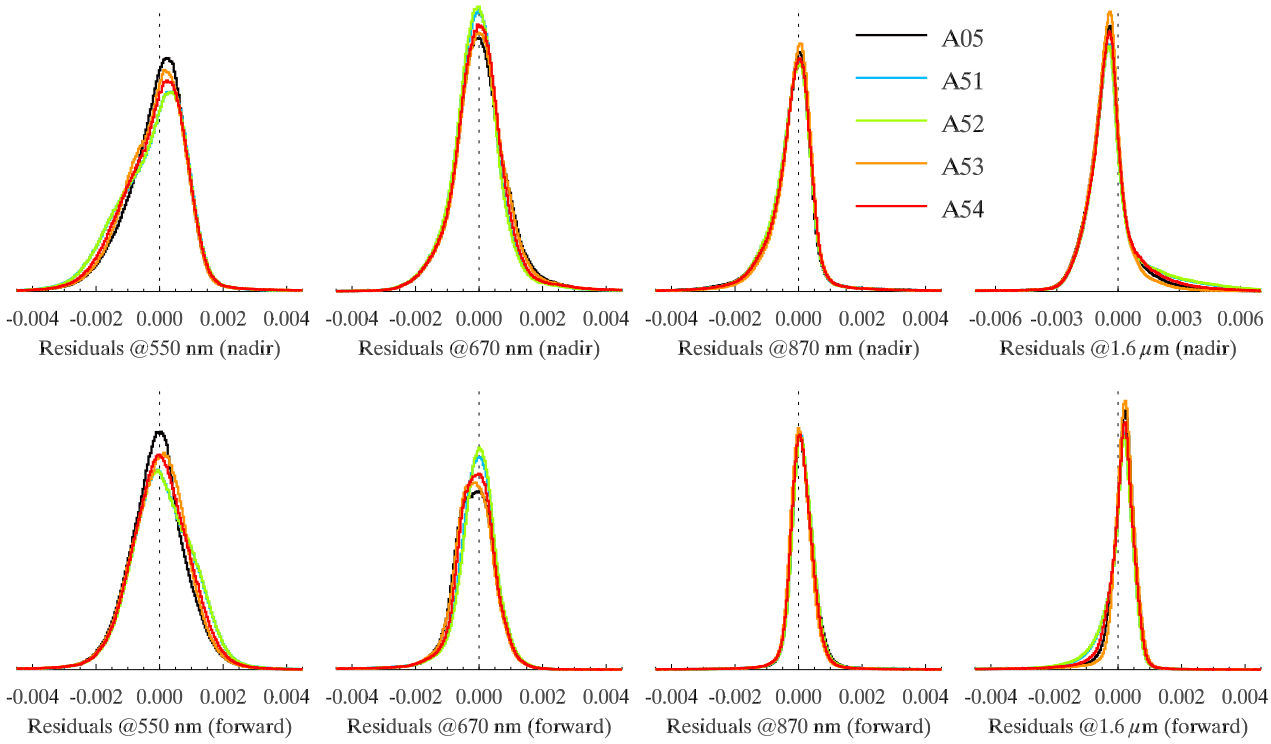

Figure 2.14: Histograms of AATSR ORAC retrieval residuals from July 2008 for various sea salt classes where the marine class was the most likely. The top row is for the nadir view, and the bottom for the forward view.

for each measurement so some measure of the scattered intensity that is representative of the radiance measured by the satellite and provided to the retrievals is desired. For this, a property $\Theta_i(\lambda, r)$, the Averaged Relative Scatter, where $i = \{\text{nadir; forward}\}$ is defined:

$$\Theta_i(\lambda, r) = \iint p(\cos\theta_{\text{nad}}, \cos\theta_{\text{fwd}}) \frac{\beta^{\text{sca}}(\lambda, r)\, P(\lambda, r, \cos\theta_i)}{\beta^{\text{sca}}(\lambda_0, r)\, P(\lambda_0, r, \cos\theta_{\text{nad}})}\, d\cos\theta_{\text{nad}}\, d\cos\theta_{\text{fwd}}. \tag{2.3}$$

where $\beta^{\text{sca}}(\lambda, r)$ is the scattering coefficient, $P(\lambda, r, \cos\theta)$ is the phase function and $p(\cos\theta_{\text{nad}}, \cos\theta_{\text{fwd}})$ is the probability of a randomly selected retrieval from July 2008 having a light scattering angle θ_{nad} as measured by the nadir channel and θ_{fwd} as measured by the forward channel. This probability distribution is plotted in Fig. 2.15a.

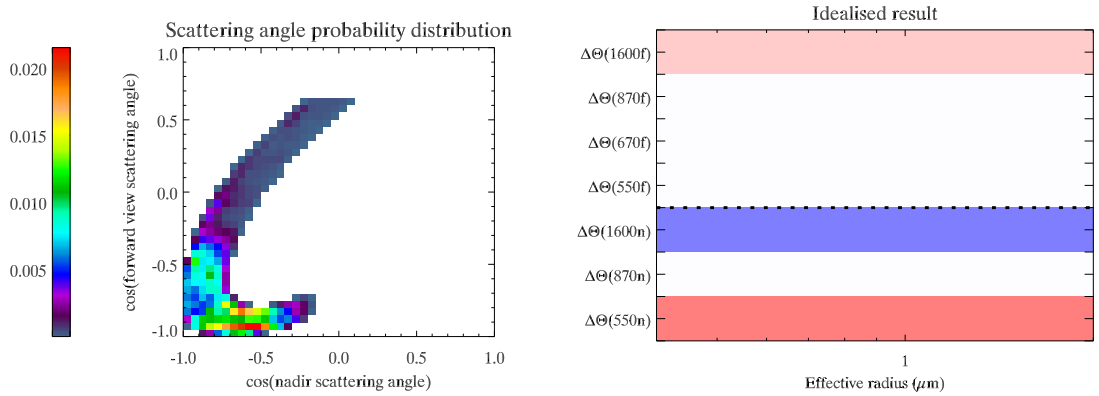

(a) Probability distribution of scattering angles for the AATSR nadir and forward views for cases when the marine aerosol class was selected in the ORAC retrieval.

(b) Ideal outcome for plots of $\Delta\Theta$: changing a microphysical property leads to noticeable relative changes in certain channel's values of $\Delta\Theta$ while holding other relative changes constant.

Figure 2.15: Considerations when calculating $\Delta\Theta$.

The value of Θ_i gives a measure of an average normalised light intensity scattered by an aerosol distribution as a fraction of the average normalised light intensity scattered to the nadir channel at wavelength λ_0 (which is the 670 nm channel). The absolute values of $\beta^{\text{sca}} P(\theta)$ are less important than relative values since the retrieval scheme changes aerosol optical depth to better fit measurements by altering the number concentration of the aerosol, which scales the measurements of all the channels equally, assuming single scattering.

Next, consider nudging a parameter of the aerosol distribution in the hope that this small change could improve the residuals in the retrieval. In this case, the change this causes in light scattering intensity of one channel relative to another would change the offset of the two related residuals. We are hoping that we could find a parameter nudge that pushes the values of Θ for the 550 nm nadir and 1.6 μm forward channels in the same direction, the 1.6 μm nadir channel in the opposite direction, while holding the other channels' values steady.

Defining $\Delta\Theta$ as

$$\Delta\Theta = \ln\left[\frac{\Theta[b+\delta b]}{\Theta[b]}\right], \tag{2.4}$$

where some parameter, b, of the aerosol microphysical model has been modified, if we were to see

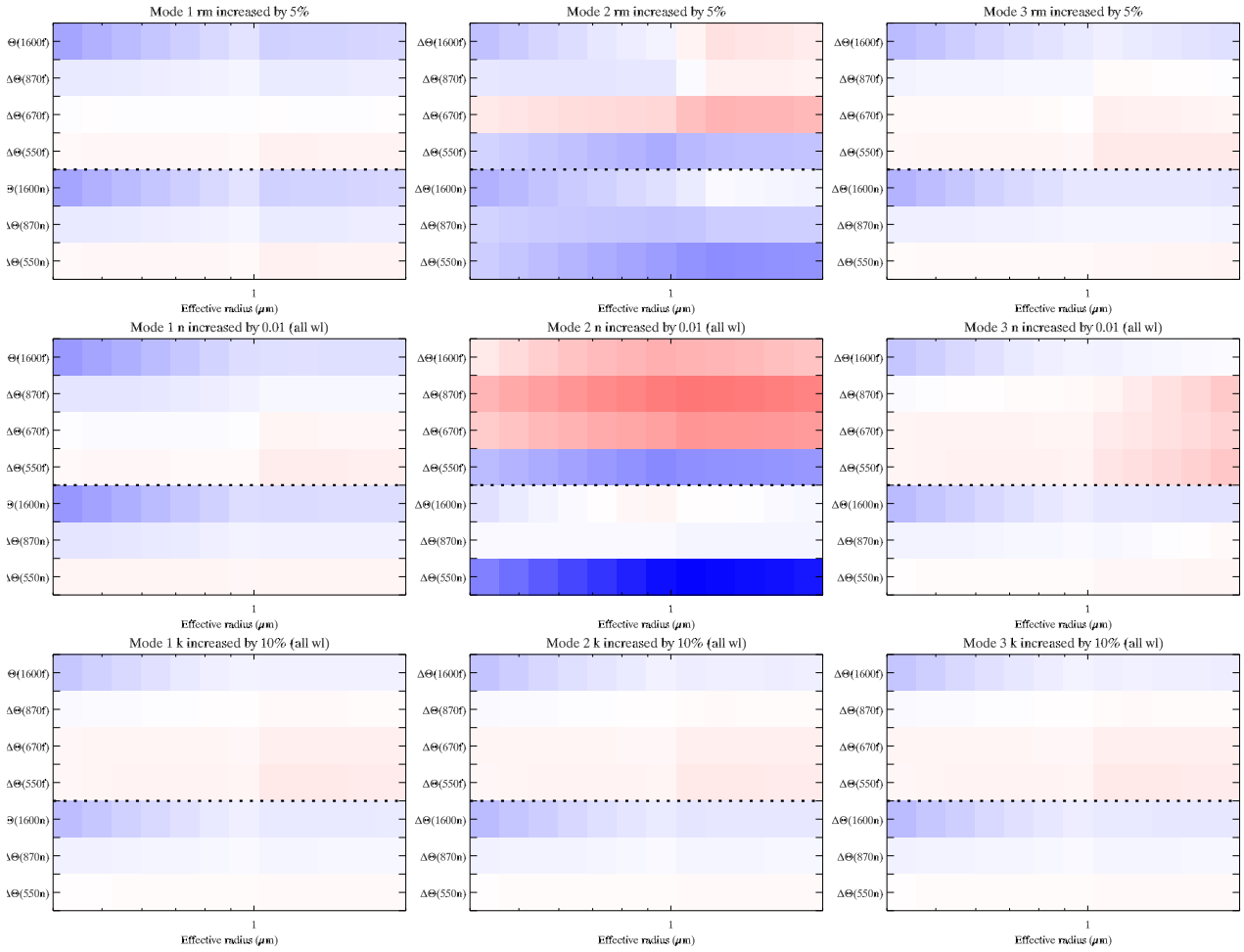

Figure 2.16: How nudging the parameters of marine aerosol at RH= 80 % changes the value of $\Theta_i(\lambda, r_{\text{eff}})$ as defined in (2.3).

something that looked like Fig. 2.15b (or the inverse of this), we would have an indication that a small change in the value of the parameter could nudge our residuals closer to zero.

The values of r_m, n, and k were nudged (by 5 %, 0.01, and 10 % respectively) for each of the three modes in the A53 aerosol distribution and the values of $\Delta\Theta$ obtained are shown in Fig. 2.16. Nudges in n and k were applied simultaneously to all wavelengths. It would appear that nudging the chosen parameters will not be suitable since in all but one case the values of $\Delta\Theta(1.6\ \mu\text{m}, \text{nadir})$ and $\Delta\Theta(1.6\ \mu\text{m}, \text{forward})$ have the same sign, and in the case where this does not happen (increasing $n_{\text{mode 2}}$), values of $\Delta\Theta(870\text{ nm}, \text{forward})$ and $\Delta\Theta(670\text{ nm}, \text{forward})$ are both non-negligible.

The conclusion is thus that a small nudge of the basic aerosol model's properties is not going to help remove biases from the retrieved distribution, and that it may be necessary to look elsewhere; either at the surface reflectance model [Sayer et al., 2010], or the atmospheric model, both of which are outside the scope of this study.

2.5 Conclusions

The principle recommendation of this chapter is that the relative humidity assumed when creating a general purpose maritime aerosol class should be 80 %, as this is a more reasonable base value and gives a marginally better average fit to the data than the 50 % value currently used by ORAC. Beyond that, modifying the microphysical model for marine aerosol is not likely to improve the ORAC retrieval scheme; other sections of the retrieval or forward model must be looked to. In §2.4.2 it was shown that tweaking the modes of the aerosol, either by changing the mode median radii or by altering the refractive index, would not improve the retrievals residuals, and in §2.4 that adding a physically realistic CCN mode at ~ 0.1 μm did not improve the retrieval any more than altering the relative humidity.

As expected, when relative humidity is higher, the individual aerosol mode sizes increased, but since values of relative humidity are so invariant over the ocean, there is little point in modelling this. Especially since wind speed is far more variable, and affects the size distribution in a different manner, i.e. by the selective increase of number concentration in the sea salt modes. This is the method currently used by the ORAC retrieval and seems the most sensible. It was also backed up by the comparison with ACE-1 data set which showed constant $r_{m,i}$ and varying $m_{\mathrm{rat}\,i}$ with increased r_{eff}.

Chapter 3

Desert dust aerosol microphysical model

3.1 Background

Desert dust aerosol is naturally occurring, although desertification caused by anthropogenic factors, such as changes to climate and to land use [e.g. Giannini et al., 2008; Jeong et al., 2011] can be responsible for changes in emissions patterns and quantities.

Dust is brought into the atmosphere by saltation, a jumping motion whereby already detached, larger particles collide with obstructions on the surface bed, projecting smaller particles into the air. Wind on its own is not enough to remove particles from the surface bed. Experiments carried out by Bagnold [1941] found that when a steady stream of air was blown over loosely scattered, fine cement, no particle motion was recorded, even at very high wind speeds. Larger particles, already in motion, were required to lift the particulate. A good description of saltation is provided in Twomey [1977a].

Since fine mineral dust (which is light enough to be lifted into the troposphere) is quickly removed from the surface, most of a desert region will not be a huge source of dust. Generally, the surface mineral dust is very coarse. Specific regions such as the Bodélé Depression in Chad, where annual deposition of mineral dust occurs, along with other preferable circumstances (including strong surface winds and favourable topography), provide the atmosphere with the mineral dust observed,

this in fact being the world's largest dust source [Washington et al., 2006].

While not as prevalent in the global atmosphere as maritime aerosol, local dust events dominate total aerosol optical depth in deserts and the surrounding regions during periods of high wind. Long range transport of the desert dust (particularly the smaller particles) means that the dust can be seen all over the world, deposition over the Atlantic and in the Amazon basin being well known [Kaufman et al., 2005].

Sand composition determines refractive index, with increasing hematite content responsible for increased absorption (and sand with a more reddish hue) [Sokolik and Toon, 1999]. Shapes are decidedly non-spherical, often having sharp edges and aspect ratios (AR) far from unity [e.g. Okada et al., 2001; Kandler et al., 2007].

3.1.1 The ORAC microphysical model for desert dust

The current ORAC desert dust aerosol class is made up of lognormal aerosol modes. The smallest of these modes is the "water soluble" mode, followed by the nucleation, accumulation and coarse mineral dust modes. The mineral modes are hydrophobic and the water soluble mode is assumed to always be present in an atmosphere with 50 % relative humidity. The three mineral dust modes all have identical refractive indices, the only difference between them being the median radii, r_g, and the width, S, of their lognormal size distributions. All of the modes are modelled as homogeneous spheres.

3.1.2 Comparing the ORAC model with field measurements

The size distribution

The desert dust size distribution is shown in Fig. 3.1, along with measurements made in the recent SAMUM campaign in North-West Africa [Weinzierl et al., 2009]. In these measurements, a four mode size distribution of aerosol particles was retrieved from data provided by several particle sizers operating over a wide range of aerosol radii using the method described by Fiebig et al. [2005] to fit

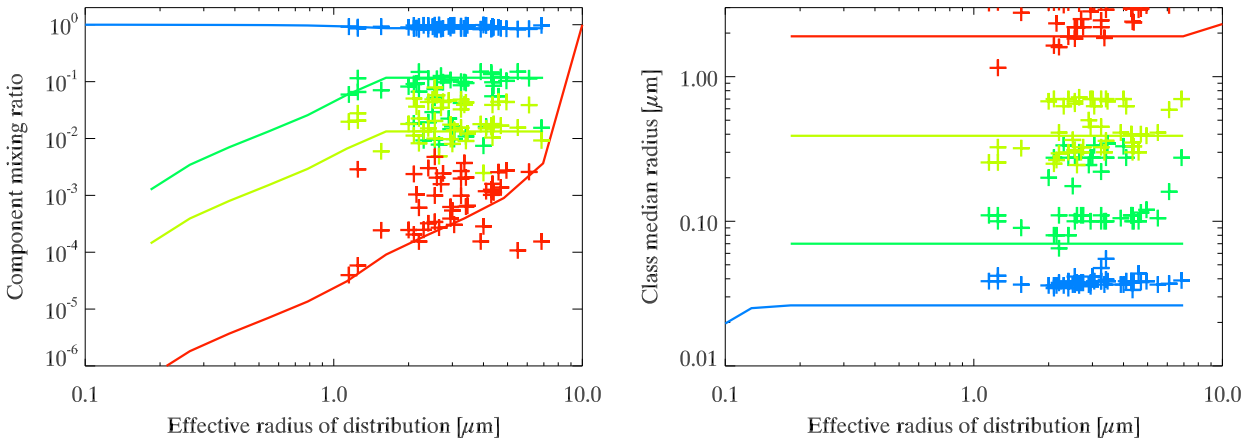

Figure 3.1: Showing how the ORAC scheme generates aerosol distributions with the correct r_{eff}. Each colour represents a log-normal mode (or class). Blue is the "water soluble" class; dark green is the nucleation mode mineral dust; light green the accumulation mode mineral dust; red the coarse mode mineral dust. The left-hand figure shows the component mixing ratio for the four classes as a function of overall r_{eff}. On the right we see the median radius of each class as r_{eff} varies. Overlaid crosses are microphysical measurements taken in the SAMUM campaign between 18th May and 7th June, 2006 in Casablanca, Ouarzazate and Zagora [Weinzierl et al., 2009, Tables 4 & 5].

lognormal distributions. This fit does not make assumptions about the chemical composition of the particles in each mode, so different coloured crosses denote only the size order for each measurement and not an aerosol "type".

The ORAC assumption that changes in r_{eff} are accounted for by variations in the relative mixing ratios of the different modes (see §1.6.3) appears to hold (although the very largest r_{eff} values do see an increase in r_g for all three sand modes). Fine mode measured particles appear to follow the ORAC microphysical scheme relatively well. Mixing ratios between modes are similar, and r_g values are relatively constant with changes in r_{eff} (although larger than the values of r_g used by the ORAC microphysical model). Measurement of the coarse mode r_g, and mixing ratio have less of a clear relationship with r_{eff}, but have comparable values to the ORAC assumptions.

The optical properties

From the ORAC size distribution of desert dust aerosols, we now model their optical properties. In the light scattering calculations, the main assumption made about the ORAC desert dust class is that the scattering particles are spherical and homogeneous. This is certainly not the most realistic shape as any inspection of sand with electron microscopy will reveal [e.g. Fig. 1.4; Buseck et al., 2000; Okada et al., 2001; Reid et al., 2003; Kalashnikova and Sokolik, 2004]. Data have been inspected from several Saharan campaigns: SHADE [Tanré et al., 2003], DABEX [Haywood et al., 2008], DODO [McConnell et al., 2008] and, most recently, SAMUM [Heintzenberg, 2009]. Where values of extinction coefficient (β^{ext}), asymmetry parameter ($\langle\cos\theta\rangle$) and single scatter albedo ($\bar{\omega}_0$) could be obtained or derived, they have been added to Fig. 3.2 which also shows the mineral dust optical properties as they are currently represented by the ORAC forward model.

The values of β^{ext} appear to be underestimated. Similarly, $\bar{\omega}_0$ is underestimated quite dramatically suggesting that the ORAC optical model is too absorbing. The asymettry parameter, $\langle\cos\theta\rangle$, appears to be well represented over the range, although the range of values has a very small spread and this parameter is not actually used in retrievals (only as a single value representation of the phase function).

Certain caveats apply to the use of each set of field measurements for a fair inter-comparison, and these are listed below:

Esselborn et al. [2009]; Weinzierl et al. [2009] The ORAC tables use β^{ext} $\frac{1}{1000}\text{km}^{-1}$ for 1 particle per cm^3. In order to plot like with like, we need to know the number density (by which to divide the measured β^{ext}) and r_{eff} (for the abscissa). These values were taken from Weinzierl et al. [2009, Tables 4 & 5] in both cases (since both papers were from the same campaign flights) while the measurements of β^{ext} appeared to be for the same flights at the same (or similar) locations. Times of β^{ext} measurements could vary by up to an hour from the size distribution measurements, and were obtained by sight from graphs of lidar measurements since data were not requested. Times coincided more closely for the β^{ext} measurements made by Weinzierl

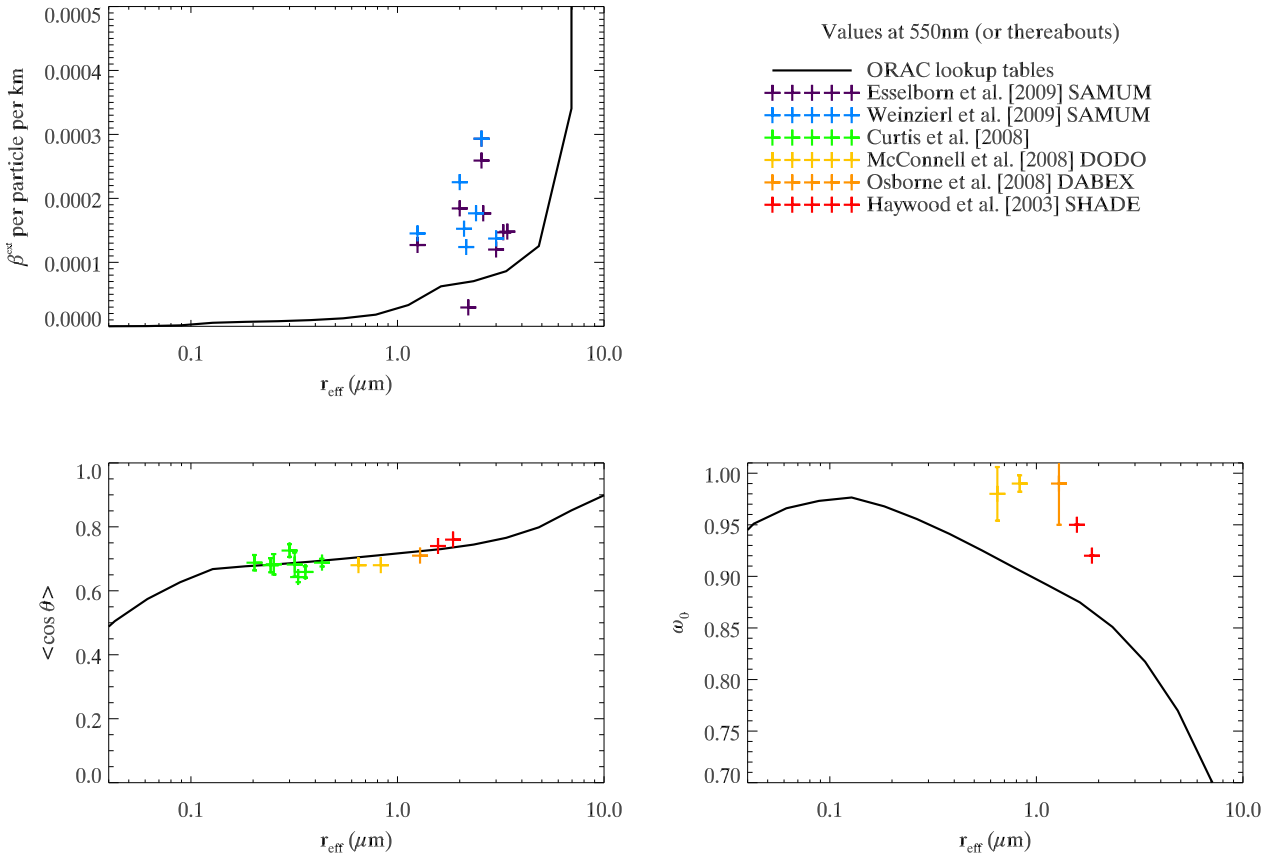

Figure 3.2: Comparing available measurements from field campaigns presented in the literature to the current ORAC optical scattering properties table for $\lambda = 550$ nm. The references from which data were obtained are shown in the legend.

et al. [2009]. Lidar measurements of extinction coefficient are made at 532 nm and calculated by comparing a "background" molecular vertical profile to the current signal. The above points could all contribute errors to the β^{ext} provided in Fig. 3.2.

Curtis et al. [2008] These measurements of r_{eff} and $\langle \cos\theta \rangle$ are taken from measurements of individual types of dust e.g., calcite or gypsum as opposed to a mixture of minerals as would be expected.

McConnell et al. [2008] In this flight campaign, $\bar{\omega}_0$ is measured, and r_{eff} is obtained from values of r_g, S and mixing ratio for four-mode lognormal distributions given in Table 5. It is noted in the table that these size distributions are "Accumulation Mode Only". Also, $\langle \cos\theta \rangle$ is calculated by fitting a best refractive index to the measured size distribution to match the measured $\bar{\omega}_0$, assuming spherical sand particles. Values of k^{ext} (in $m^2\ g^{-1}$), derived from Mie fitting of $\bar{\omega}_0$ were provided, but it was not possible to convert them to β^{ext} values due to lack of coarse mode size distribution data.

Osborne et al. [2008] As McConnell et al. [2008] above, but with a five-mode distribution.

Haywood et al. [2003] As Osborne et al. [2008] above, but with two different five-mode distributions provided. The values of $\langle \cos\theta \rangle$ and $\bar{\omega}_0$ are calculated for the two assumed distributions (but are from the same data).

3.1.3 Other microphysical models used in satellite retrievals

Since microphysical properties of mineral dust have high variability, modelling choices in satellite aerosol retrievals also vary. Table 3.1 presents an outline of the key microphysical assumptions made in the MODIS, and MISR operational retrievals, which are described in depth in this section.

MODIS

Over water, the MODIS aerosol retrieval works identically to the description given in §2.1.4 for the marine aerosol. The fine mode is very similar to the water soluble modes used for the smallest fine mode particles in the ORAC retrieval. The "coarse mode" has the option of two "dust-like" modes, which have similar refractive indices to those used by ORAC (although are less absorbing). The three sand modes used in ORAC are replaced with a single lognormal mode that has a similar effective radius ($r_{\text{eff, coarse dust, MODIS}} = 1.48$ & 2.50 μm; $r_{\text{eff, dust, ORAC}} = 1.76$ μm). A "fine mode fraction", η, determines the relative mixing of the fine (non-dust) mode and coarse mode. The "dust-like" modes are modelled as spheres.

Over land, the MODIS retrieval has both "dust-like" continental aerosol (which uses the OPAC mineral dust RI values in the visible) and a coarse mode non-spherical dust model which uses a combination of spheroids and spheres to model the aerosol shapes. The distribution of non-spherical AR values is taken from retrievals of mineral dust by Dubovik et al. [2006]. Cluster analysis of AERONET data has been used to optimise the size distribution [Omar et al., 2005], which varies as a function of the AOD [§4.3, Levy et al., 2009].

MISR

The MISR team have carried out retrievals that model particle non-sphericity for desert dust aerosol and have non-spherical dust in their operational retrieval. In research retrievals they have used a selection of spheroids, grains, plates (flattened particles), and spheres, based on individual particle analysis using electron microscopy [Kalashnikova and Sokolik, 2004; Kalashnikova et al., 2005]. The operational retrieval has spherical coarse and fine mode dust, but also includes medium sized grains that are modelled with DDA and have increasing non-sphericity with increasing size. Coarse mode spheroids are modelled using the T-matrix method [Kahn et al., 2009].

Both non-spherical modes have less absorbing refractive indices than the ORAC dust model ($m_{670} = 1.51 + 0.001i$). Regarding the size distributions, the fine, "grain" mode has $r_g = 0.5$ μm;

Retrieval	Description	Refractive index @ 670 nm	Nuc. mode r_g	Nuc. mode S	Acc. mode r_g	Acc. mode S	Coarse r_g	Coarse S
ORAC	Spherical	$1.53 + 0.004i$	0.07	1.95	0.39	2.00	1.9	2.15
MODIS (water)	Spherical	$1.53 + 0.000i$	-	-	0.6 0.5	1.8 2.2	-	-
MODIS (land)	Spheres, spheroids	$1.48 + 0.0018i$	0.025	2.13	-	-	0.88	1.74
MISR	Spheres, spheroids, grains	$1.51 + 0.0011i$	-	-	0.5	1.5	1.0	2.0

Table 3.1: Comparing the dust modelling from ORAC, MODIS, and MISR. MODIS data come from Levy et al. [2009]; MISR data come from Kalashnikova et al. [2005]. The MODIS (water) "dust-like" model has two modes available, both of which are shown. The MODIS (land) modes are modelled as spheroids, assuming an optical depth of 1. The MISR accumulation mode are modelled as grains, and the coarse mode as spheroids.

S=1.5, and the spheroidal coarse mode $r_g = 1.0\ \mu$m; S=2.0, compared to ORAC.

3.2 Refractive index

One could suspect that across the world (and indeed within particular regions), variation in the mineralogy of sand and, by extension, the mineralogy of sand aerosol would be significant. Certainly, we would then expect the refractive index (RI) of the mineral dust aerosol to vary. Whether or not this causes unacceptable errors in calculations of optical properties is the next question. Claquin et al. [1998] reported that the imaginary part of refractive index, k, has "natural variability ... [which can] lead to variations of up to $\pm 40\%$ in aerosol forcing calculations", which suggests that these problems cannot be ignored. Looking again, for example, at Fig. 3.2, one could say that comparing the field measurements of $\bar{\omega}_0$ to the ORAC scheme, there is too much absorption in our representation of the optical properties of mineral dust at $\lambda = 550$ nm. This is equivalent to saying that the imaginary part of the refractive index has been over-estimated. Indeed, an evaluation of widely used refractive indices for mineral dust concluded that the OPAC values were higher than those observed in-situ and remotely by numerous investigations of Saharan aerosol [Highwood, 2009].

As a naïve first attempt, the absorption could be "damped" by reducing k by an arbitrary amount.

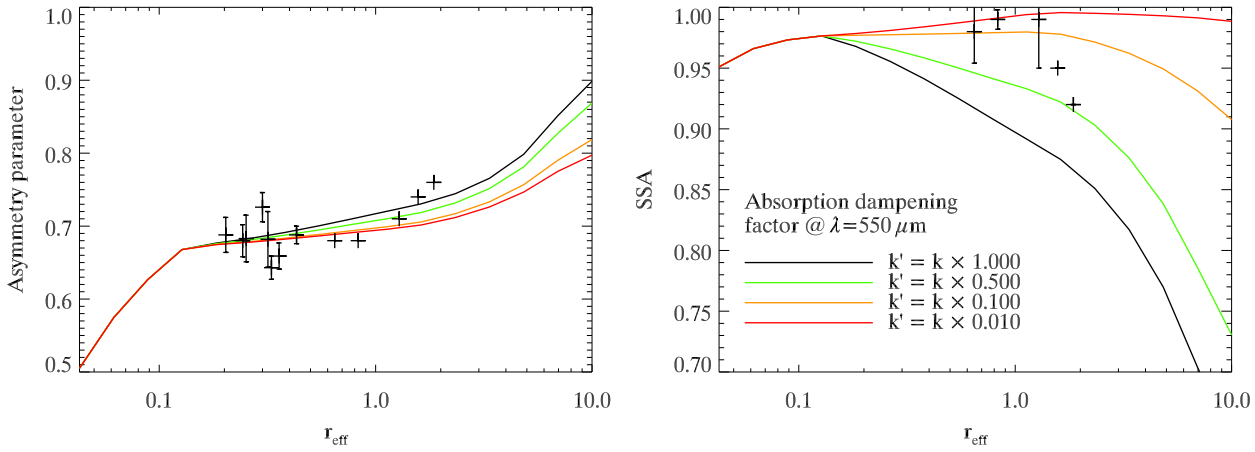

Figure 3.3: "Damping" the imaginary part of refractive index, k, to see its effects on optical properties compared to measured properties as previously shown in Fig. 3.2. (β^{ext}, which has not been shown, is identical for all four cases.)

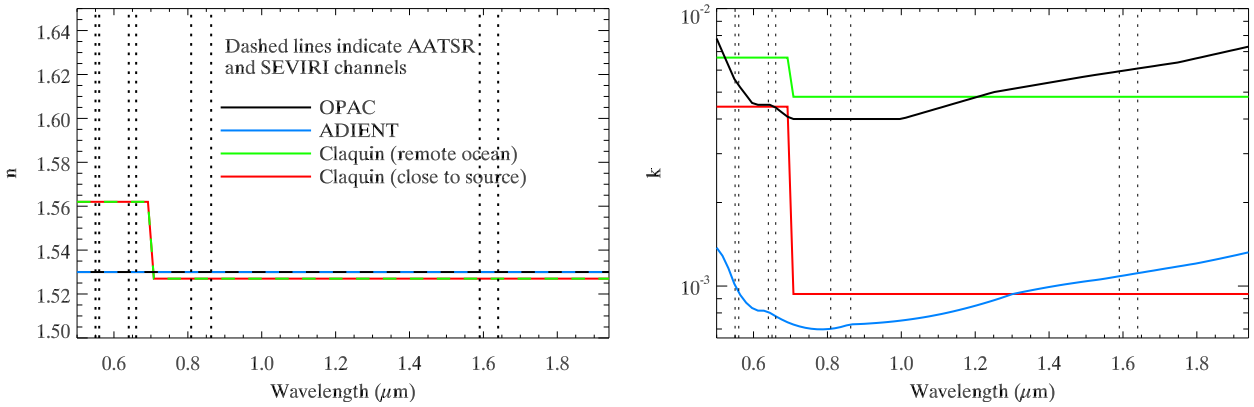

Figure 3.4: Different refractive indices used by the ORAC retrieval, Claquin et al. [1998], and recommended by the ADIENT project [Highwood, 2009].

This is shown in Fig. 3.3. Reducing k to between one half and one tenth of its original value would appear to provide a better fit to $\bar{\omega}_0$ while leaving $\langle \cos\theta \rangle$ similar to before, and β^{ext} unchanged.

This uncertainty in k was also inspected by Claquin et al. [1998] who used two different models of absorption for their mineral dust aerosol: a "close to source" containing more quartz, and "remote oceanic" which was more clay dominant. Fig. 3.4 shows how these two models compare to the ORAC values in the visible channels. It can be seen that using the "close to source" values for k would reduce the absorption over most of the visible spectrum (although only by a small amount at $\lambda = 550$ nm). The optical model used by OPAC appears to have more in common with the "remote"

sand type, which could explain why aircraft measurements taken over the Sahara appear to have less absorption than our model predicts.

In an attempt to better understand and characterise uncertainty in optical properties due to the uncertainty in mineral dust refractive index, a spread of world-wide mineral dust RI was calculated using soil maps as a basis for varying mineralogy.

3.2.1 Method

Obtaining the mean RI was a three step process. First, an approximate soil composition was obtained on a regular grid over the whole earth, built of common minerals. Next, the RI values of the individual minerals were combined for each soil type, giving a picture of how RI varies geographically. Finally, the world-wide spread was reduced to a histogram of RI values. These were weighted using a simple emissions scheme so that only areas where dust was likely to be lofted into the atmosphere contributed to the average.

FAO / UNESCO Digital Soil Map of the World

In order to characterise the spread of world-wide sand RI values, it was decided that soil data would be the most useful starting data set. The FAO[1] / UNESCO[2] Digital Soil Map of the World [FAO / UNESCO, 2003] is a regularly gridded 5×5 arc-minutes resolution map of the world, each cell containing a mix of soil types. These soil types consist in varying proportions of different minerals.

Other world-wide soil maps are very hard to come by and were not readily available. The only other viable candidate would have been the Harmonized World Soil Database[3] (HWSD), which combines the FAO / UNESCO map with regional, more detailed studies allowing for 30×30 arc-second resolution. An intermediate stage in the following calculations involved reducing the resolution to $\frac{1}{4}^\circ \times \frac{1}{4}^\circ$ and so this additional detail seemed unnecessary.

[1] Food and Agriculture Organization of the United Nations
[2] United Nations Educational, Scientific and Cultural Organization
[3] HWSD is available from `http://www.iiasa.ac.at/Research/LUC/External-World-soil-database/`.

FAO textural class		Soil ratio (%)					
		Wet sieving			Dry sieving		
		Clay	Silt	Sand	Clay	Silt	Sand
1	Coarse	9	8	83	0.0	4.2	95.8
1,2	Coarse-Medium	20	20	60	0.4	4.7	94.9
2	Medium	30	33	37	0.7	5.1	94.2
3	Fine	67	17	17	3.6	8.7	87.7

Table 3.2: Showing how selected textural classes can be described in terms of proportions of clay, silt and sand. Wet sieving data are from Zobler [1986, Fig. 2]. Dry sieving data are from Laurent et al. [2008, Table 4]. Notice that fractions of clay particles are much greater when wet sieving techniques are used to analyse the soil.

Claquin et al. [1999, Table 2] provide a list of FAO soil types found in arid areas with the normalised composition by weight of important (sand) minerals, in this case illite, kaolinite, smectite, calcite, quartz, felspath (or felspar), gypsum and hematite. The minerals are divided into those found in clay fraction (< 2 μm) and the larger silt fraction ($2 \rightarrow 50$ μm). There is an even larger, sand fraction ($50 \rightarrow 200$ μm), but this was considered too large to be lofted for extended periods. Unfortunately, the FAO soil map uses 'textures' of soil (coarse, medium or fine) in order to characterise the sizes, so in order to estimate the mineral composition, a method is required to convert soil textures into soil sizes. Data from Zobler [1986] can help by giving approximate compositions for textures, but definitions are from wet sieving techniques which dissolve soluble minerals and dis-aggregate the soil, leading to likely over-representation of the smaller clay particles. Data from dry sieving studies contain much smaller amounts of clay and are said to better represent the actual distribution of mineral dust. Comparisons of size fractions for the two techniques are shown in Table 3.2. It was decided that a size distribution based on dry sieving techniques would be more useful. Since the "coarse sand" class shown above contains no clay particles at all, it was decided to use the next largest, "coarse-medium sand" class which contained a very small fraction of clay (0.4 %).

For each $5' \times 5'$ area of land, the FAO map gives up to 8 soil types which make up a proportion of the land area, each with its own soil texture. Of course, not all of these soils will be suitable for lofting into the air.

Soil type		Clay fraction					Silt fraction				
		Ill	Kao	Sme	Cal	Qua	Qua	Fel	Cal	Hem	Gyp
Qc	30 %	16 %	66 %	5 %	1 %	11 %	82 %	14 %	1 %	4 %	1 %
Ql	20 %	10 %	78 %	3 %	1 %	9 %	70 %	11 %	1 %	7 %	1 %
Re	20 %	32 %	53 %	10 %	1 %	5 %	59 %	38 %	1 %	2 %	1 %
Gc	10 %	Not mineral dust type as defined by Claquin et al. [1999]									
Lk	10 %	Not mineral dust type as defined by Claquin et al. [1999]									
So	10 %	37 %	32 %	17 %	6 %	7 %	71 %	23 %	4 %	2 %	1 %

Table 3.3: An example of north African soil mineralogy as defined by combining FAO/UNESCO digital soil map with data from Claquin et al. [1999]. This soil type is Qc21-1a from north Africa.

Converting soil types into refractive indices

As mentioned above, the mineralogical breakdown of several soils was provided in Claquin et al. [1999, Table 2] who named 24 soils from the FAO soil map which were appropriate arid soil types[4]. An example "cambic arenosol" class, Qc21-1a which is found in North Africa is given in Table 3.3. Non-arid types were ignored in subsequent calculations.

Weighting the RI of each mineral, (using the appropriate clay and silt fractions for each soil type which can be obtained by combining the texture index provided by the soil map with the information from Table 3.2, above) we should then be able to work out the bulk refractive index of soil type Qc21-1a. Non-mineral-dust soil types are not included in the averaging. Initially, refractive indices were combined using mass mixing, but this provided unconvincing results (as had been previously found by Sokolik and Toon [1999]), and so the Bruggeman formula which relates an effective permittivity, ε_{eff}, to the various component phases with permittivities, ε_i, and volume fractions, v_i, [Sihvola, 1999] was used:

$$\sum_i v_i \frac{\varepsilon_i - \varepsilon_{\text{eff}}}{\varepsilon_i + 2\varepsilon_{\text{eff}}} = 0. \tag{3.1}$$

From the literature, RI values in the visible and near infrared were obtained for the minerals mentioned above, out of which Claquin et al. [1999, Table 2] built their sand types. The source for

[4]These appropriate soil types were I, Jc, Je, Qa, Qc, Qf, Ql, Rc, Re, So, Vc, Xh, Xk, Xl, Xt, Xy, Yk, Yl, Yy, Zg, Zo, Zt, sand dunes and salt flats. The details of these FAO soil classifications can be found at `http://www.fao.org/nr/land/soils/key-to-the-fao-soil-units-1974/`

Mineral type	Wavelength (μm) 0.56	0.66	0.863	1.59	10.86	12.05
Illite	Egan and Hilgeman [1979]				Querry [1987]	
Kaolinite	Egan and Hilgeman [1979]				Roush et al. [1991]	
Felspar	Egan and Hilgeman [1979]				No data	
Montmorillonite (Smectite)	Egan and Hilgeman [1979]				Roush et al. [1991]	
Hematite (Iron Ore)	Jacquinet-Husson et al. [2008]					
Quartz	Jacquinet-Husson et al. [2008]					
Calcite	Ghosh [1999]				Long et al. [1993]	
Gypsum	Roush et al. [2007]					

Table 3.4: Source of refractive index values used in this study at the wavelengths of AATSR channels. Calcite values in the visible are assumed non-absorbing ($k = 0$). Calcite and quartz are birefringent. Since we expect any sand particles we observe to be randomly orientated, we combine the o-ray and e-ray values of n and k, with twice the weighting for the o-ray values.

this data is given in Table 3.4. Additionally, the resolution of soil data is reduced from a $5' \times 5'$ grid to a $\frac{1}{4}^\circ \times \frac{1}{4}^\circ$ grid to speed up further computations, reduce statistical noise in RI values, and reduce areas of unknown RI.

Weighting by likelihood of emission

The aim in this final stage is not to obtain a highly complex, detailed view of world-wide mineral dust emission. Instead, a basic scheme is developed which depends on the clay fraction of the mineral dust in a grid box, and a measure of peak wind speed at the same position, and is very quick to calculate with already available data.

The vertical emission flux of fine particles, F, is linearly related to the saltation flux, G (the flux of particles travelling parallel to the soil surface), by the sand blasting efficiency, α, so that we have,

$$F = \alpha G. \tag{3.2}$$

From Laurent et al. [2008], we obtain α using the empirical relation

$$\alpha = 10^{\,(0.134\times\ \%\text{age clay}\ -6)}, \tag{3.3}$$

but the saltation flux is more complex and will be approximated. The full calculation is [Marticorena et al., 1997]:

$$G = E\frac{\rho_a}{g}u^{*3}\int_{D_p}^{\infty}\left(1+\frac{u_t^*(D_p)}{u^*}\right)\left(1+\left[\frac{u_t^*(D_p)}{u^*}\right]^2\right)\delta S(D_p)\,dD_p, \tag{3.4}$$

where E is the erodible fraction of the surface, ρ_a is the air density, g the acceleration due to gravity, u^* the wind friction velocity, $u_t^*(D_p)$ the threshold wind friction velocity which gives the minimum value of u^* needed to lift a particle of diameter D_p from the surface. The size distribution is given by $\delta S(D_p)$.

Since we care about events when the wind speed is large relative to the threshold, we approximate (3.4) to:

$$G = \frac{F}{\alpha} \simeq u^{*3} f(D_p), \tag{3.5}$$

$$\Rightarrow \qquad F \propto u^{*3}\alpha. \tag{3.6}$$

Wind friction velocity can be defined as [Almeida et al., 2006]:

$$u^* = \frac{u(z)\kappa}{\ln\left(\frac{z}{z_0}\right)}, \tag{3.7}$$

where the vertical distance, $z = 10$ m, $\kappa = 0.4$ is the von Karman constant and z_0 is the surface roughness length, which affects emissions, but is not trivial to calculate from the data we have obtained. In the emitting areas of the Sahara, the range of z_0 is from $z_0 = 10^{-3}$ cm to 0.5 cm so can alter u^* by a factor of about 3. Due to the difficulty in obtaining z_0, it was decided to assume that $\ln\left(\frac{z}{z_0}\right)$ was

almost constant relative to $u(z)$, the horizontal wind speed at 10 m.

Peak horizontal wind speed was obtained from a year's worth of ECMWF data. The horizontal wind speed mean and standard deviation were calculated, and peak wind speed was defined as two standard deviations above the mean wind speed for each location.

The final concern is vegetation. If it is present, it all but completely inhibits emission of mineral dust. Tegen and Fung [1995] used a threshold based on the normalised difference vegetation index, NDVI = $\frac{R_{nIR}-R_{red}}{R_{nIR}+R_{red}}$, where R_{nIR} and R_{red} are the reflectances in the near-infrared and red regions respectively. Their approach was to allow emission only for NDVI < 0.07. A value of NDVI above this would suggest a vegetation cover "dense enough to inhibit dust deflation". The AATSR ORAC monthly mean atmospherically corrected NDVI for March 2004 was used as the data set [Sayer, 2008]. It was found that setting the cutoff at NDVI < 0.08 gave a more convincing emissions pattern. The AATSR NDVI product uses different bands for its nIR and red reflectance (which are also much narrower) than the bands from AVHRR used by Tegen and Fung [1995] so this change in threshold is not unreasonable.

Since the NDVI index only shows an absence of vegetation, we must be careful not to mistake other bright areas (such as snow caps) for arid soil locations. Limiting the arid regions to between latitudes of 45°S and 45°N was a simple first step in this.

Fig. 3.5 shows the approximate calculation of relative emissions using the method described above for Saharan Africa, and compares it to a full, far more detailed calculation carried out by Laurent et al. [2008]. Although one could not state that a perfect match has occurred, there are very encouraging features of the stripped down emission scheme. Major known sources, for example along the West Saharan coast, in central Algeria (27° N, 2° W), and the Bodélé depression in Chad (17°55′ N, 19°7′ E) are clearly visible in both representations. Many areas with no emissions at all also match, e.g. (29°N, 2°E), but the region to the east of the Red Sea is disappointing. The simple model predicts quite a few emissions which are completely absent from the full calculation. The most likely reason for this would be soil moisture, which strongly restricts emission [Fécan et al., 1999], but isn't accounted for in this scheme.

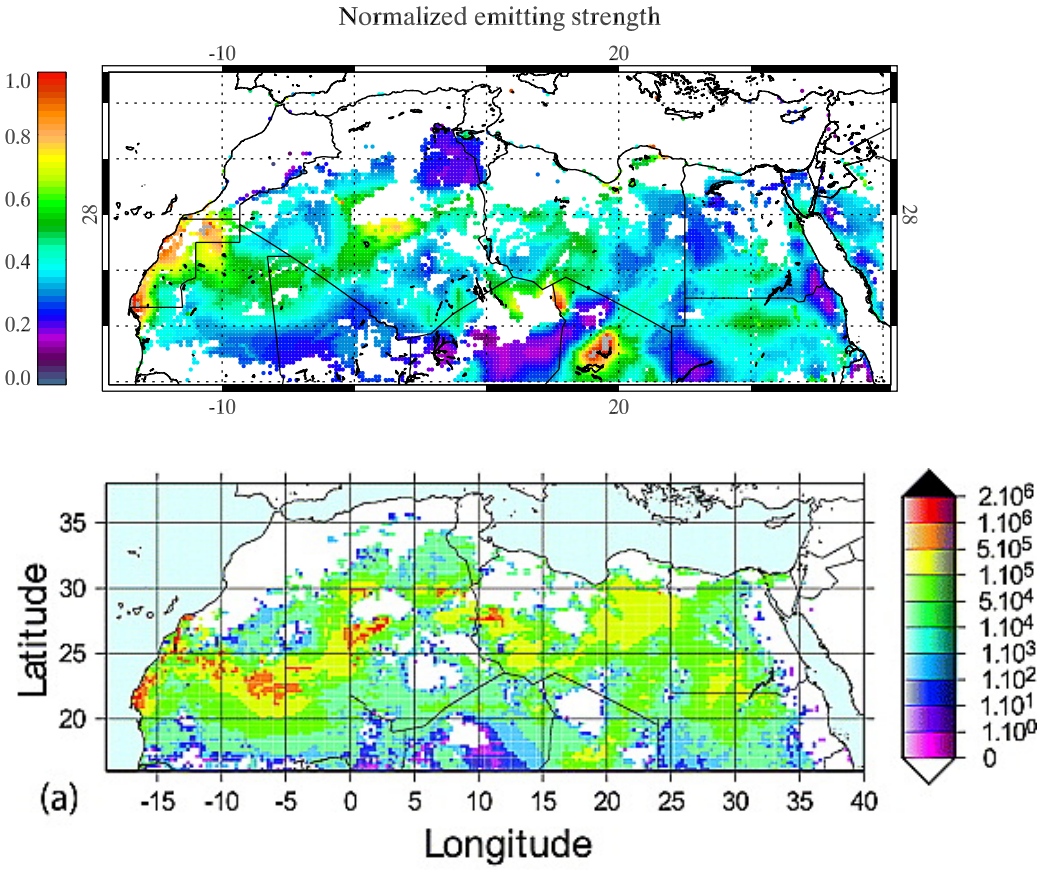

Figure 3.5: Comparing the simple emissions model described in this work (Top) to a full emissions simulation [Laurent et al., 2008, Fig. 3a, reproduced with permission] (Bottom) showing annual dust emissions in Mg (tonnes).

3.2.2 Results

Fig. 3.6 shows predicted emissions for the whole world. Noticeable emitting regions are the Sahara, the Namib desert, central Asia, central Australia, Nevada and the Chilean coast. As well as weighting an area on its emitting strength, because the data are on a latitude-longitude grid, areas close to the equator have greater surface area which must be accounted for. Coastal areas also have to account for loss of ground from which to emit due to parts of the grid being sea. This has all been added to the final calculations shown in Fig. 3.7–3.8 and summarised in Table 3.5 which shows optical characteristics of a mineral dust aerosol class with $r_{\text{eff}} = 1.13\ \mu$m.

The average value of $n_{550} \simeq 1.56$ is slightly larger than previous studies [Highwood, 2009] but the absorbing (imaginary) part centring around $k_{550} =< 10^{-3}$ is slightly less than other studies and far less absorbing than OPAC values. Further inspection shows that areas with high levels of hematite (which has $n_{550} = 3.1$) have the largest (real and imaginary) refractive indices, such as the Sahel region which is known to have minerals with higher proportions of iron oxides [Claquin et al., 1999; McConnell et al., 2010]. Inaccuracies created by such a large number of assumptions about the soil making up our lofted dust (e.g. mapping FAO textural classes to soil types as shown in Table 3.2; the use of data with a low number of sampling points to generate the mineral fractions given by Claquin et al. [1999]) are bound to lead to errors in the calculations of mineral RI, but it is still expected that the spread of values could be a useful indicator of the importance of RI in aerosol light scattering calculations for desert dust.

New optical calculations based on the histograms of RI shown in Fig. 3.7-3.8 show (as one would expect) that with lesser values of k, $\bar{\omega}_0$ is greater than previously. Changes in $\langle \cos\theta \rangle$ are less pronounced, however the phase function can change by significant amounts in the very narrow backscatter direction of $\theta > 160^\circ$. For the backscattered light, $P_{550}(180^\circ)$, relative difference can be as great as 8% which is not a major cause for concern. Very little change is seen in the extinction.

Fig. 3.10 shows the spread of optical properties which is averaged to create Fig. 3.9. The values of k^{ext} (which are not shown) vary only by very small amounts. For larger particles, variation in

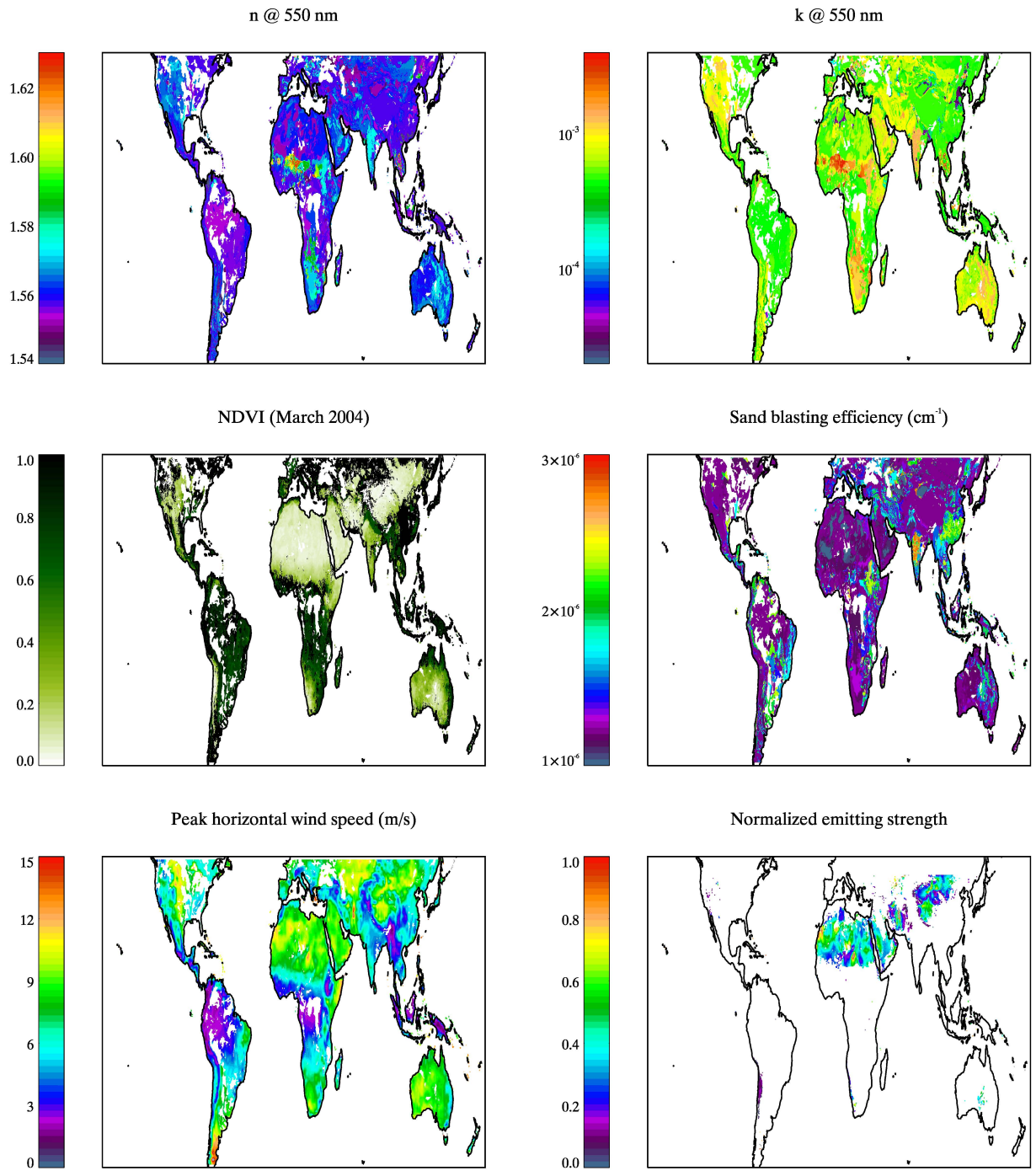

Figure 3.6: The soil refractive index for arid soil types over the earths surface is shown, followed by the various parameters required to calculate the relative emitting strength of an area of the world. NDVI data are the monthly mean from March 2004 AATSR data. An area is only allowed to emit if its NDVI value is less than 0.08. Sand blasting efficiency, α, is only calculated for the soil types which are mineral dust as defined by Claquin et al. [1999] and is obtained as a function of the clay fraction, using eqn (3.3). Peak horizontal wind speed is from ECMWF reanalysis data. The final result, normalised emitting strength, is a function of the previous plots.

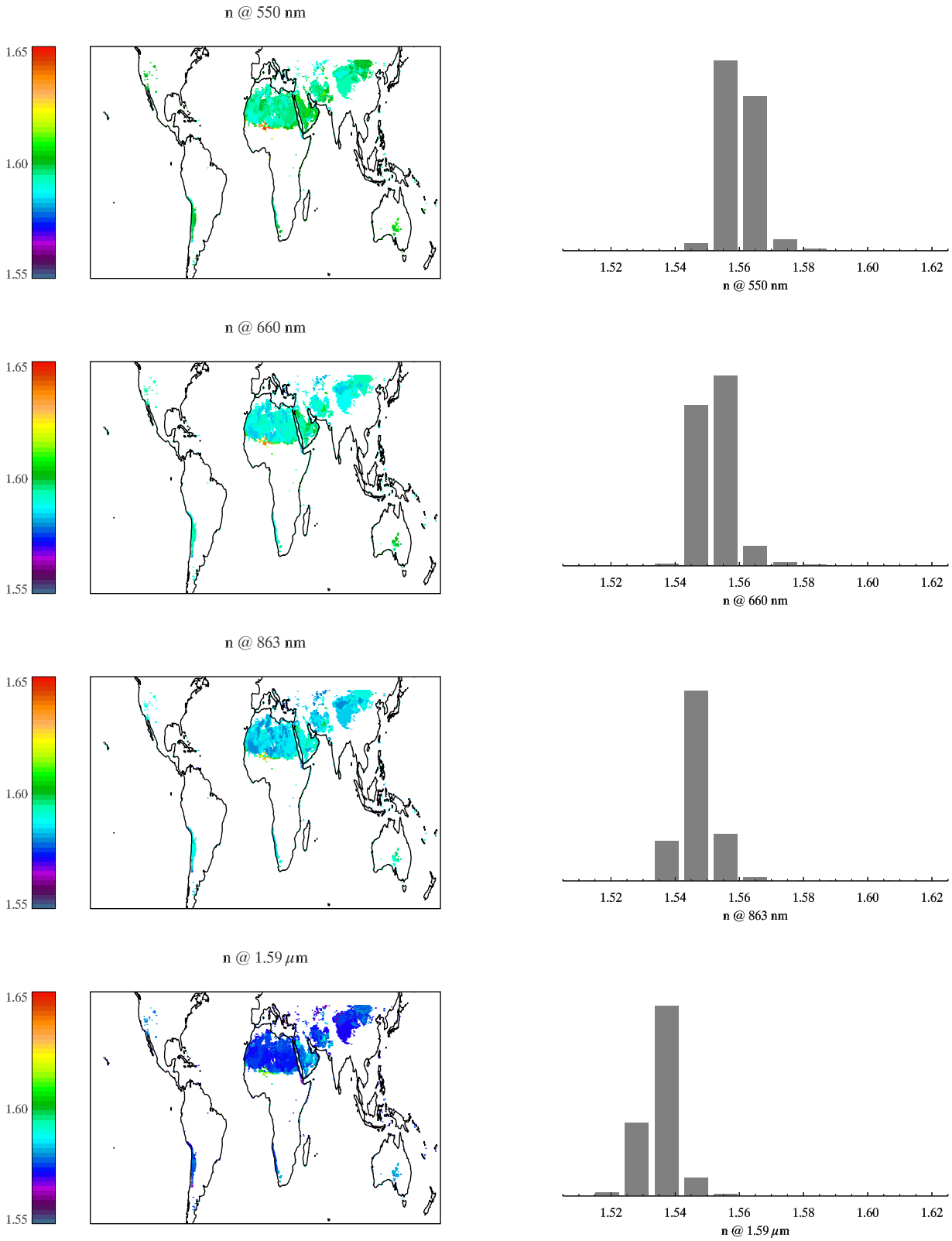

Figure 3.7: Showing the spread of the real part of mineral dust aerosol refractive index for AATSR wavelengths.

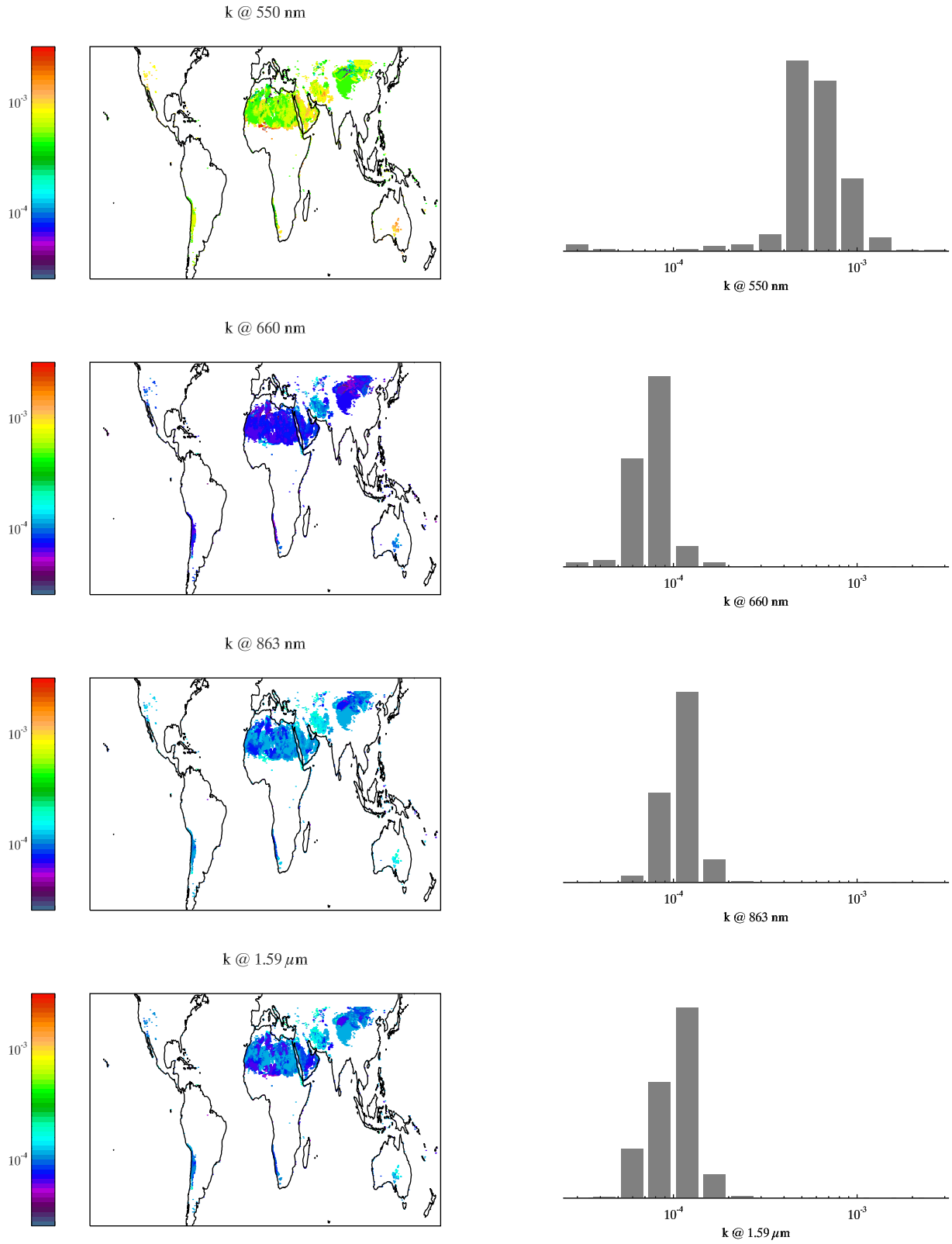

Figure 3.8: Showing the spread of the imaginary part of mineral dust aerosol refractive index for AATSR wavelengths.

$\langle \cos\theta \rangle$ never reaches far above 1 %. Likewise, variation in $\bar{\omega}_0$ can be up to 4 % [5].

Almost all of this variation is caused by the imaginary part of RI. Holding n constant while varying k yields very similar results to allowing the full range of both n and k. Conversely, holding k constant while allowing n to vary reduces greatly the variation in optical properties seen.

The conclusion would be that while imaginary part of refractive index is very important for the correct characterisation of optical properties, particularly $\bar{\omega}_0$, the small variations in the real part (within the range shown by the soil analysis) do not greatly affect most parts of the phase function, or the other optical properties. The variability found in k is not as large as the difference between OPAC values of k and these new calculations. Incorrect characterisation of the imaginary part of refractive index is a greater concern than the natural variability in k seen across different soil types which may be lofted into the atmosphere.

[5] For the purposed of this section, the relative variations reported are defined to be the standard deviation of values as a fraction of their mean value.

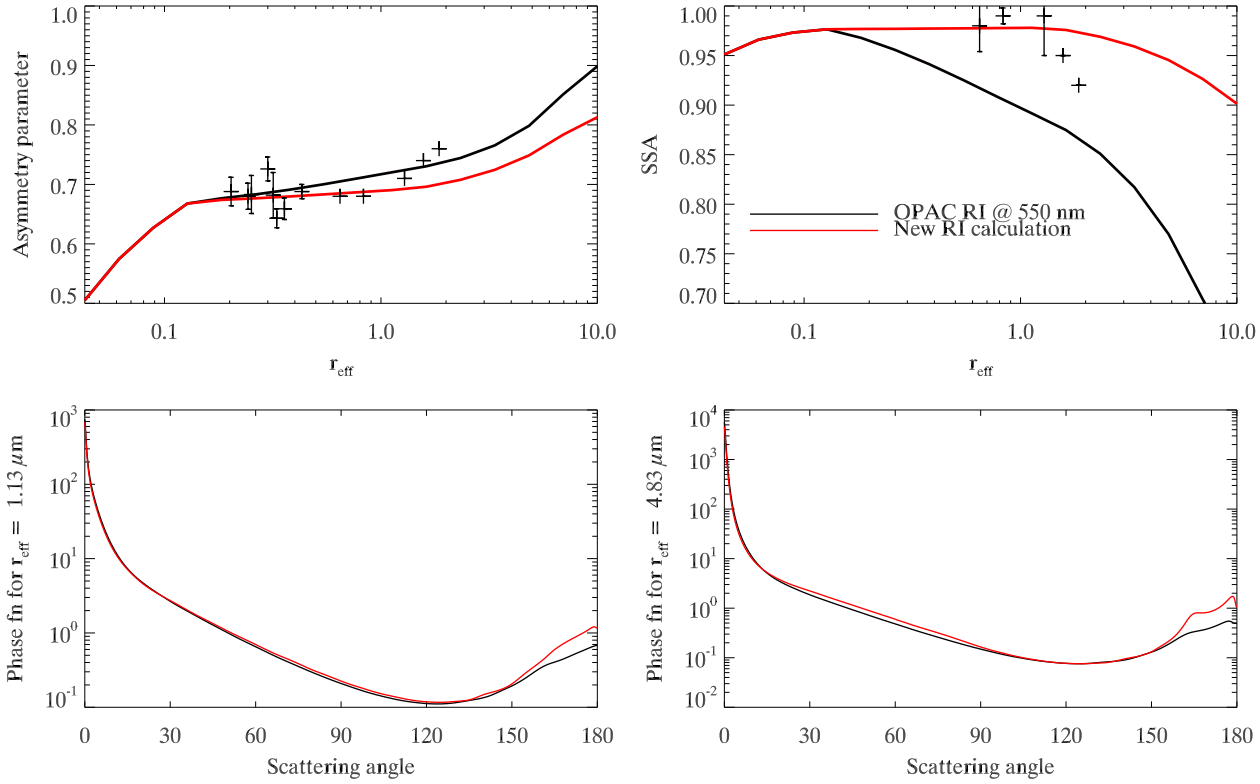

Figure 3.9: Comparing values of $\langle \cos\theta \rangle$ and $\bar{\omega}_0$ at 550 nm, calculated using the OPAC refractive indices, and using a weighted spread of RI from the histograms in Fig. 3.7-3.8. Two example phase functions are also shown. Crosses are the data previously shown in Fig. 3.2. New values of RI appear to better reproduce the SSA.

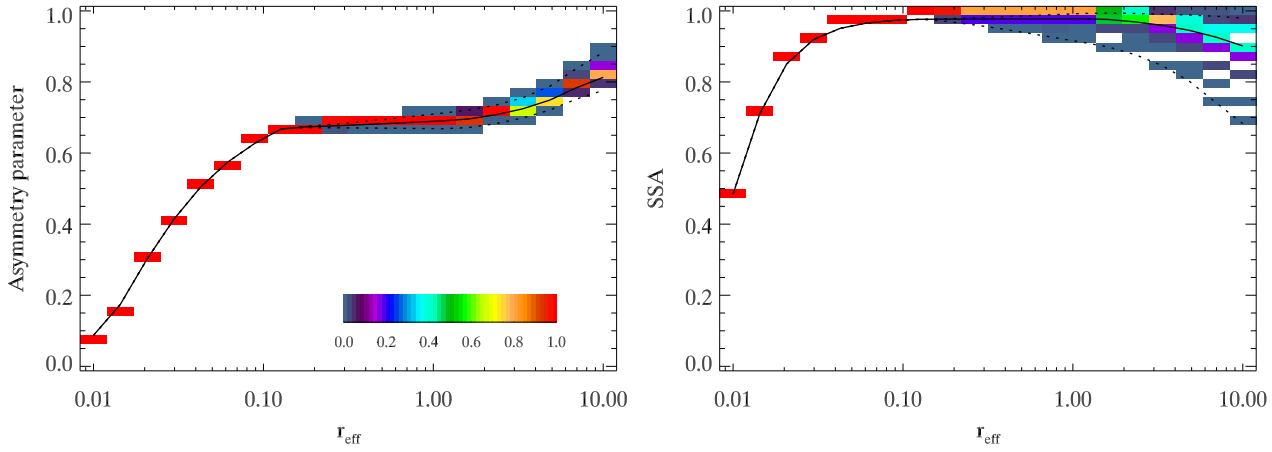

Figure 3.10: Showing the spread of optical properties from the mean value at 550 nm, using the weighted spread of RI from the histograms in Fig. 3.7-3.8. The solid line is the overall scattering as shown in Fig. 3.9 above. The colours show the density of points within a grid box. Dashed lines are the extreme values given by the range of n and k.

WL	Refractive index							
	n				$k \times 10^{-5}$			
(μm)	ORAC	ADIENT	Mean	SD	ORAC	ADIENT	Mean	SD
0.55	1.53	1.53	1.56	0.006	550	100	61.97	27.4
0.66	1.53	1.53	1.55	0.006	440	78	7.56	1.8
0.863	1.53	1.53	1.55	0.005	400	73	10.99	2.3
1.59	1.53	1.53	1.54	0.006	595	108	10.31	2.6

WL	Optical properties for r_{eff} = 1.13 μm															
	$\beta^{\text{ext}} \times 10^{-5}$ [km^{-1}]				$\langle \cos\theta \rangle$				$\bar{\omega}_0$				$P(180^\circ)$			
(μm)	ORAC	Mean	SD	RV	ORAC	Mean	SD	RV	ORAC	Mean	SD	RV	ORAC	Mean	SD	RV
0.55	3.32	3.34	< 0.001	0.10%	0.720	0.690	0.003	0.41%	0.892	0.978	0.008	0.78%	0.680	1.167	0.093	7.94%
0.66	3.17	3.19	< 0.001	0.11%	0.706	0.679	0.002	0.35%	0.913	0.994	0.001	0.06%	0.770	1.210	0.083	6.84%
0.863	3.00	3.02	< 0.001	0.08%	0.694	0.669	0.003	0.37%	0.926	0.992	0.001	0.05%	0.812	1.203	0.072	5.99%
1.59	2.68	2.69	< 0.001	0.30%	0.689	0.670	0.004	0.54%	0.929	0.994	< 0.001	0.04%	0.601	0.815	0.046	5.59%

Table 3.5: RI variation and its affect on the full mineral dust aerosol class. The calculated RI values are compared to the OPAC values currently used by the ORAC retrieval. The class has four modes, but since the smallest mode is the OPAC water soluble mode, it has not been affected by these calculations. The other three modes have had their refractive indices altered to match the results shown in Fig. 3.7-3.8. The relative variances (RV) quoted are the SD divided by the mean.

3.3 Non-sphericity

A great number of studies have investigated the shape of mineral dust aerosol and a great many more, how best to model its light scattering. These studies are summarised, followed by a description of a non-spherical (NS) model for the mineral dust aerosol class. The new scattering model is used as the mineral dust class for a retrieval of a known dust event off the coast of northwest Africa and compared to the standard spherical retrieval.

3.3.1 Other studies

Measurements

If one is interested in the shape of mineral dust aerosols, the best tool at a researchers disposal is scanning and transmission electron microscopy (SEM and TEM). Many campaigns have analysed SEM and TEM images of mineral dust: the output is two dimensional and as such, it is almost always the projected features of a particle onto an image plane that is inspected, and not the full 3D shape.

Generally observed characteristics are of particles with rough edges and aspect ratios of $\sim 1.3 \rightarrow 2.2$ [Buseck et al., 2000; Okada et al., 2001; Reid et al., 2003; Kandler et al., 2007; Chou et al., 2008]. The AR distributions are generally reported to be independent of size, at least for all but the largest particles, where Reid et al. [2003] found that particles with radius > 10 μm were more elongated. Transported Saharan dust, was measured by Kandler et al. [2007], and the distribution of aspect ratios, $n(AR)$, was fitted to a modified lognormal function given by

$$n(AR) = \frac{1}{\sqrt{2\pi}\sigma(AR-1)} \times \exp\left[-\frac{1}{2}\left(\frac{\ln(AR-1)-\mu}{\sigma}\right)^2\right], \tag{3.8}$$

with $\sigma = 0.6579$ and $\mu = -0.4502$ giving a median aspect ratio $AR_{\text{median}} = 1.65$, and $AR_{\text{mode}} = 1.41$.

Similarly for Chinese mineral dust, Okada et al. [2001] fitted the (non-normalised) function

$$n(AR) = \frac{2}{163.9\,e^{-5.76AR} + 0.00133\,e^{3.71AR}}, \tag{3.9}$$

giving $AR_{\text{median}} = 1.36$, and $AR_{\text{mode}} = 1.28$.

Though AR values are found to be mainly size independent, larger particles were generally found to be more "angular" or have "sharper edges" and "rougher surfaces" than those which were smaller [Haywood et al., 2003; Reid et al., 2003; Muñoz et al., 2007; Chou et al., 2008]. These larger particles are sometimes described as "irregular aggregates" with rougher contours [Reid et al., 2003; Chou et al., 2008]. Some sources also commented that a thin coating of sulphate ($\sim$ 60 nm) was found on dust samples [Kandler et al., 2007; Chou et al., 2008].

Modelling

When modelling light scattering by mineral dust, methods employed include Mie theory, the discrete dipole approximation (DDA), T-Matrix theory and ray tracing. The most common non-spherical method of modelling optical properties of mineral dust aerosol is to use T-matrix code [Mishchenko and Travis, 1998] choosing spheroids as the shape of the scatterer (or using look-up tables based on this code, created by Dubovik et al. [2006], which also include ray tracing calculations for larger particles).

Some works pick a single representative aspect ratio, generally with a value of $\sim$1.6 [Yang et al., 2007; Mishra and Tripathi, 2008; Osborne et al., 2008], while others used a distribution of aspect ratios with equal probability [Mishchenko et al., 1997; Wang et al., 2003; Kalashnikova and Sokolik, 2004; Dubovik et al., 2006]. Ray tracing is sometimes used for the more randomly shaped particles, or where the T-matrix method was not possible [Haywood et al., 2003; Dubovik et al., 2006; Yang et al., 2007]. DDA is not used in studies as regularly, probably because it places a strain on computing resources, but was used by Kalashnikova and Sokolik [2004] to model "grain"-like particles which were then used by the MISR retrieval (see §3.1.3). Almost all studies already mentioned conclude

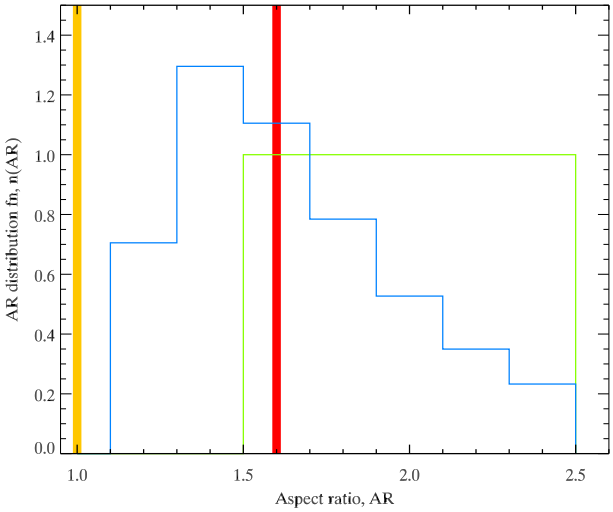

Figure 3.11: Various distributions of spheroid aspect ratios. The yellow delta function is a spherical distribution, which can be calculated using Mie theory. The blue distribution is a discretised version of (3.8), as used by Kandler et al. [2007]; the green is a polydisperse distribution as used by Mishchenko et al. [1997]; the red is mono-disperse in AR.

that including NS components of aerosol in light scattering models improves the agreement of phase functions with those observed. Wang et al. [2003] noted that using only NS aerosol did not give so good an improvement in satellite retrievals as a mixture of spherical and NS particles. Yang et al. [2007] used ray tracing to give larger particles surface roughness.

3.3.2 Method

As in the majority of previous studies on modelling non-sphericity, the T-matrix method is used to calculate the light scattering from spheroid mineral dust particles.

Different distributions

Fig. 3.11 shows four possible aspect ratio distributions we can use to give our best description of aerosol properties in the atmosphere. Our current assumption of sphericity is the yellow distribution. We also looked at other distributions in AR space, as used in previous studies.

- Polydisperse with equal probability of all ARs between 1.5 and 2.5.
- Monodisperse, with AR = 1.6.
- Polydisperse, with log-normal distribution, as given by Kandler et al. [2007] (see eqn. (3.8)).

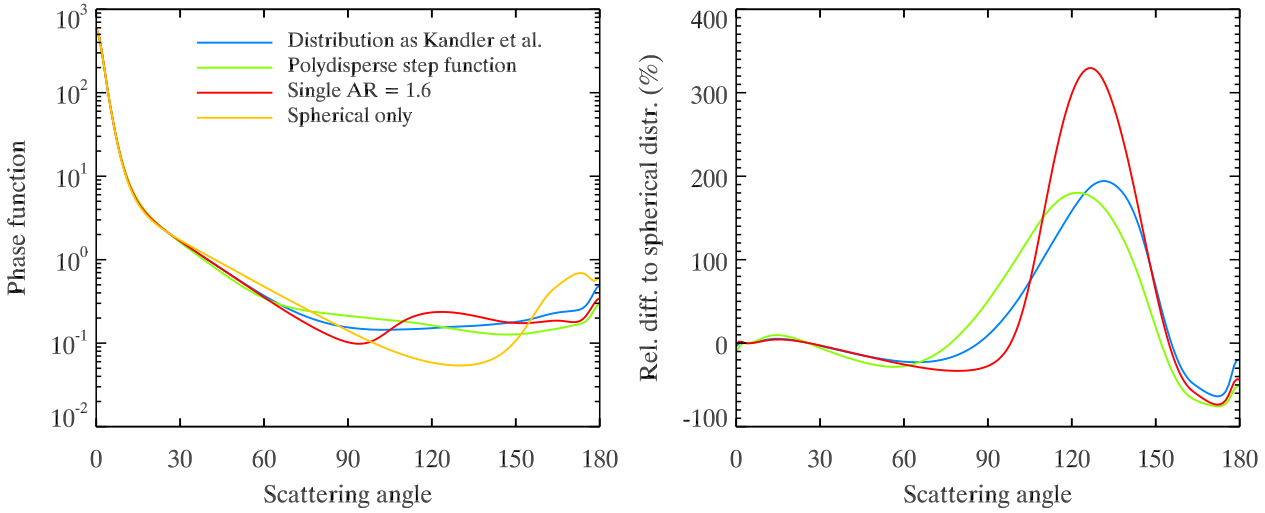

Figure 3.12: Phase functions for spheroid AR distributions (as given in Fig. 3.11) with a log-normal distribution of particle size at λ=550 nm. Relative difference between the spheroid distributions, and a spherical-only distribution are shown in the right-hand figure. Spheroid distributions use equal numbers of oblate and prolate spheroids.

Example phase functions for these aerosols, randomly orientated, with log-normal size distributions are shown in Fig. 3.12. The size distribution has an effective radius of $r_{\text{eff}} = 2.26\ \mu$m (towards the larger end of mineral dust distributions). As usual, a lognormal distribution of sizes is used, and the only difference between the lines are the distributions of non-sphericity. The relative differences between the new, NS models and the spherical case are shown in the right-hand plot. Initial impressions are that the phase function differences are very large in the back scatter direction, while manageable in the forward direction. Additionally, the differences from the spherical distribution are similar for the three NS distributions, that is, all three distributions alter the phase function in a similar way.

3.3.3 Optical calculations

Taking the most physically-justifiable distribution from Fig. 3.11, that of Kandler et al. [2007], we investigate the changes in phase function over a range of effective radii in Fig. 3.13. Most notably, with increasing particle size, the differences between the NS and spherical distributions become

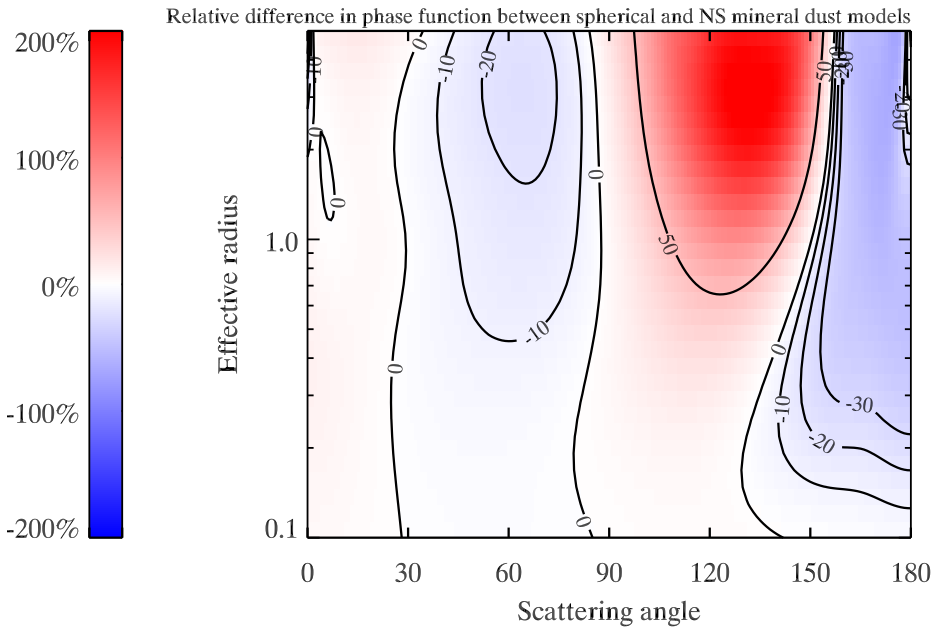

Figure 3.13: Relative difference between NS to spherical phase functions over a range of particle sizes at λ=550 nm. Distribution of NS particles is that of Kandler et al. [2007] as shown in Fig. 3.11.

more pronounced. Biggest differences occur at scattering angles between 100° and 150° and are always positive, agreeing with previous findings by Mishchenko et al. [1997]. For the larger particles, differences between the expected intensity at these angles can be as large as 200 %. In the backscatter direction ($\theta > 150°$), negative differences occur, but generally these are much less than the positive differences at slightly lesser scattering angles. For distributions with effective radii < 1 μm, the mean relative difference in the phase function is less than 10 %.

According to Dubovik et al. [2006], retrieval stability was affected when *only* oblate, or *only* prolate spheroids were used. It was reported that "the assumption of an equal presence [of oblate and prolate spheroids . . .] resulted in improved stability of the retrievals" which suggests either that this is a more accurate representation of the phase function or that there is insufficient information present in AERONET measurements to add additional variables to the state vector. Comparing these individual functions to the full function, Fig. 3.14 shows how oblate-only and prolate-only functions differ substantially from their combined function. The errors shown are mirror images of each other,

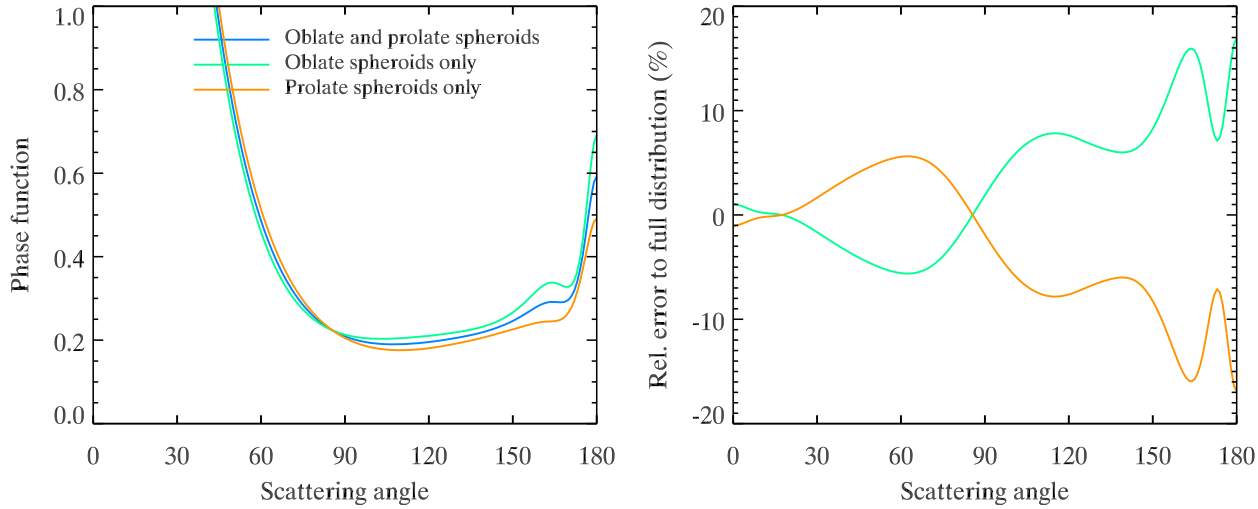

Figure 3.14: Phase functions for lognormal spheroid AR distributions separating the contributions from oblate spheroids, and prolate spheroids. Relative differences between the "oblate only", and "prolate only" spheroid distributions, and an "oblate and prolate" distribution are shown in the right-hand figure.

as the full function is a combination in equal parts of the two other functions. Errors of over 10% in the backscatter direction for these plots are significant enough to be of some concern. It is in no way clear whether oblate or prolate spheroids (or a combination of the two) are the most effective representations for mineral dust. That using one or the other will affect scattering properties so greatly (although not as greatly as with spherical comparisons) leads to an arbitrary choice in this exercise.

3.3.4 Applying the new model to retrievals

A microphysical model with non-spherical dust was created to be tested with ORAC retrievals over the Saharan area. Classes of aerosol are defined as a combination of several aerosol modes, each with their own refractive index, median radius and radius standard deviation. In the mineral dust class (which currently consists of four aerosol modes), the spherical coarse, accumulation and nucleation components of mineral dust in the aerosol tables were replaced with spheroid minerals as shown in the previous section. The final component, a water soluble aerosol, was left spherical.

WL	$\beta^{ext} \times 10^{-5}$ [km^{-1}]			$\langle \cos\theta \rangle$			$\bar{\omega}_0$			$P(180°)$			P(max error)	
[μm]	ORAC	NS	RE	ORAC	NS	RE	ORAC	NS	RE	ORAC	NS	RE	θ	RE
0.55	3.32	3.33	0.38%	0.72	0.71	1.13%	0.89	0.90	0.87%	0.68	0.43	36.8%	125	59.3%
0.66	3.17	3.21	1.17%	0.71	0.71	0.26%	0.91	0.91	0.87%	0.77	0.44	43.0%	172	52.5%
0.863	3.00	3.07	2.04%	0.69	0.70	0.55%	0.93	0.91	1.48%	0.81	0.43	46.8%	173	52.4%
1.59	2.68	2.74	2.10%	0.69	9.69	0.70%	0.93	0.94	0.63%	0.60	0.35	41.8%	175	44.0%
10.86	0.96	0.96	0.61%	0.56	0.57	1.82%	0.49	0.50	1.96%	0.26	0.26	2.1%	90	4.5%
12.05	1.00	1.07	7.34%	0.55	0.55	0.49%	0.34	0.30	12.20%	0.31	0.33	6.0%	161	6.3%

Table 3.6: Showing the variation in optical properties that a partially non-spherical mineral dust class causes.

Scattering examples for the mineral dust class

Fig. 3.15 shows a comparison of phase functions between a new version of the mineral dust aerosol class, incorporating non-spherical components, and the standard, spherical-aerosol-only version. Additionally, the DISORT radiative transfer model (which these optical properties are passed to), does not deal directly with phase functions, but instead, with Legendre coefficients[6]. Although this can lead to errors (if the series is terminated before high order terms are close enough to zero to make them negligible), results here show that errors are very small compared to the differences between spherical and non-spherical (NS) aerosol classes. A mineral dust class effective radius of $r_{\text{eff}} = 1.13$ μm is shown, that size being chosen because it lies in the range of expected r_{eff} values of $1 \rightarrow 2\,\mu$m [Hess et al., 1998].

As discussed previously, the change in aerosol shape has caused the phase function to increase in the backscatter direction, but decrease for scattering angles of $90^\circ \rightarrow 150^\circ$. In the 12 μm channel, differences are much less, since the size parameter for longer wavelengths is, for the most part, less than unity[7].

Errors in the phase function at visible wavelengths peak at over 50 % in this case, at scattering angles of around 120°. This will affect the AATSR nadir view, whose viewing angle is generally in the range $110^\circ \rightarrow 130^\circ$. In the forward view, generally between $70^\circ \rightarrow 90^\circ$, errors are much smaller, suggesting that this view would be less susceptible to errors in retrievals due to spherical assumptions. This is convenient as the two views are affected differently by the non-sphericity.

Although we see large changes in the phase functions between the two versions of mineral dust, the aerosol component, "Water Soluble, 50 % humidity", which is spherical, actually accounts for 87 % of the aerosol in the class at this radius. Additionally, of the sand components, over 50 % of the next most populous mode (the nucleation mode, with 11 % of aerosol) have a size parameter of less than 1. That leaves a very small proportion of particles (maybe 6 %) which are non-spherical, and

[6]Expansion coefficients for the phase function in terms of Legendre polynomials [Arfken and Weber, 1995].

[7]For $\lambda = 12.05$ μm and $r_{\text{eff}} = 1.13\,\mu$m as in the current example, the effective size parameter is $x_{\text{eff}} = 0.59$. This channel is not currently used by the ORAC retrieval, but will be in the near future.

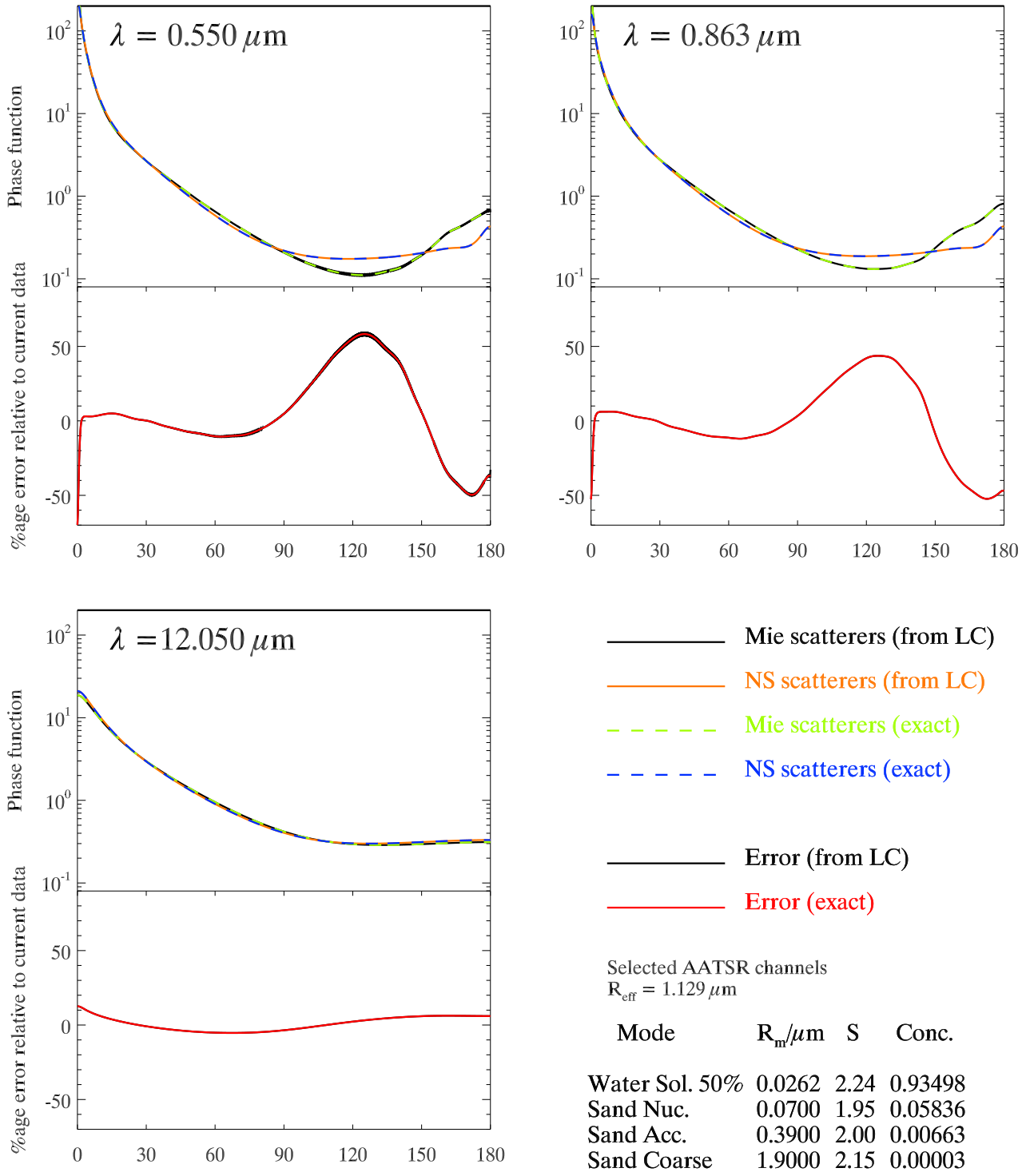

Figure 3.15: Mineral dust class phase functions for three selected AATSR channels. The effective radius in this case is $r_{\text{eff}} = 1.13\,\mu$m. NS and spherical models have been used and compared. In both cases, the refractive index, median radius (r_g), standard deviation of $\ln r$ (S), and external mixing ratios of each aerosol component are kept constant. The exact calculations, and those recalculated from a terminated series of Legendre coefficients, are shown.

are large enough to have phase functions which significantly deviate from the spherical case. This is because the amount by which an individual particle can alter the light patterns with which it interacts is limited by the extinction cross section, which itself is roughly dependant on the cross sectional area $\simeq \pi r^2$ of the particle. Since we are dealing with non-spherical particles, r is some representative radius for the particle in question.

Other effective radii (not shown) indicate the trend is as might be expected. For small particles, the size parameters are smaller and when the wavelength of light becomes much greater than the radius, the shape of the scattering particle becomes unimportant, and errors relative to the spherical case decrease rapidly. Conversely, for larger particles, differences in shape become more pronounced, and errors relative to the spherical case increase accordingly. Additionally, for the larger particles, Legendre coefficients, terminated after 1000 terms (as is currently the case), fail to accurately reproduce the scattering patterns generated for spherical particles. Since the inclusion of non-spherical particles tends to blur the phase functions, making them less variable, this becomes less of a problem, which could add an additional (if physically unsatisfying) advantage to using a non-spherical model.

Retrieval differences

Fig. 3.16 shows the results of an AATSR retrieval off the West African coast from the 10th March, 2006. A large dust plume can clearly be seen in the centre of the image.

The retrieval has found that, in general, within the dust plume, the NS aerosol class provides a lower value of optical depth than the spherical aerosol. The effective radius is a less certain change, with some sections of the plume having larger and some smaller.

The cost difference[8] shows that within the plume, the NS class sometimes has the lower cost, while at other positions, the spherical class wins out. This suggests that the NS class is not significantly better at predicting the scattering from sand than the current spherical model. The clearest

[8]The cost of a retrieval gives a measure of how much the measurements differ from the predicted forward model values, and how much the state we are inferring differs from the a priori information. In order to find our best estimate of a property, we minimise the cost function. The class is selected not only based on the class with minimum cost, but also due to constraints on the radiance and optical depth for the mineral dust class. For example, even if a mineral dust class has the lowest cost, if the optical depth is less than 0.4 it will not be selected.

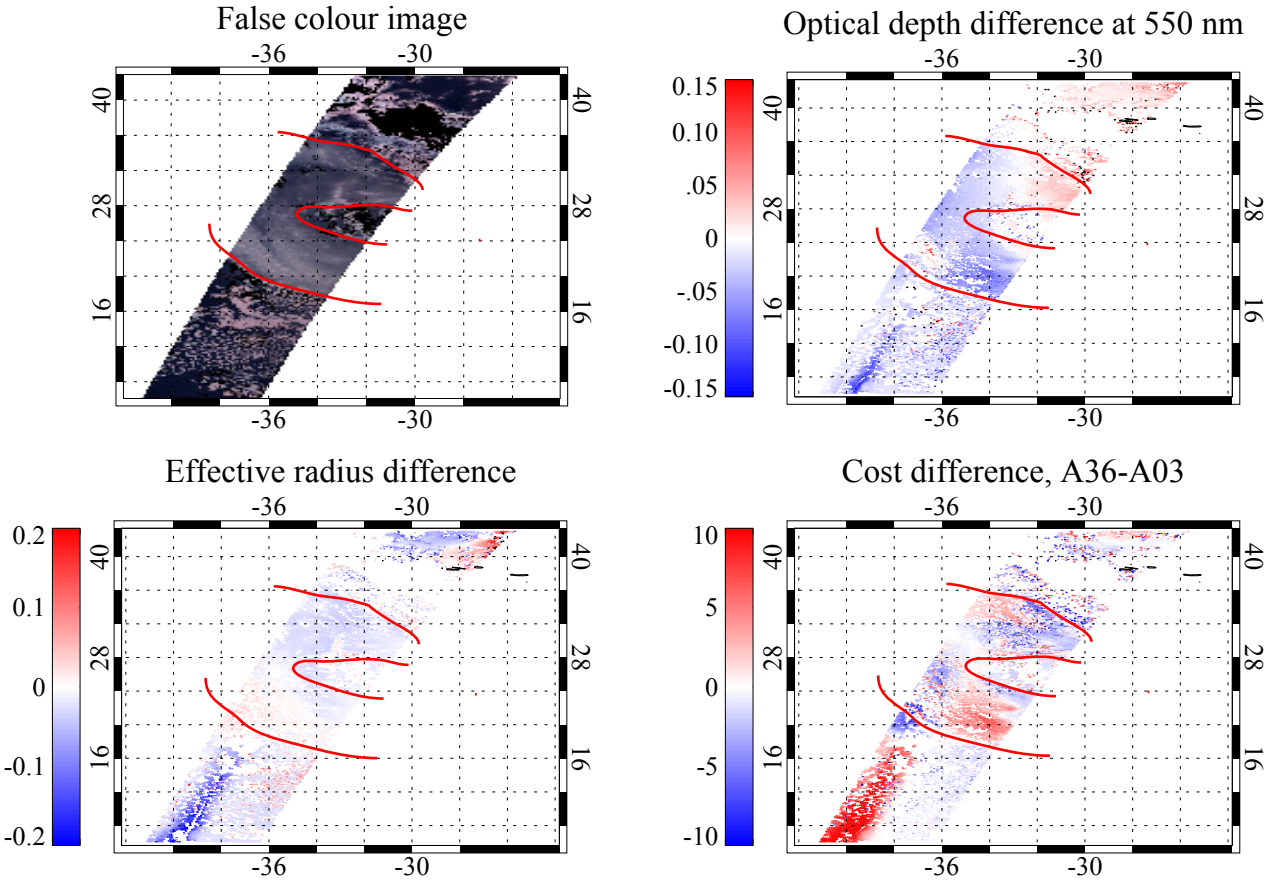

Figure 3.16: Properties from AATSR retrievals of aerosol from 10th March, 2006. Location is over the Atlantic, just off the West African coast. The islands to the top right are part of the Azores archipelago. The false colour image provides a representation of the scene from space. The extremities of the dust event are marked by red lines. The difference in optical depth, effective radius and cost are then shown. In all cases, the spherical result is subtracted from the non-spherical result.

difference in cost occurs over the area south west of the plume, where cost for the NS class is much higher. This is encouraging, as it suggests that retrievals using the NS class will not be as likely to mistake cloud for mineral dust.

While these results provide a first glance at altering the scattering model for a known NS aerosol in a retrieval, there is no way of knowing if they are representative without a more systematic study. Additionally, a particularly prominent dust storm was chosen as the first example. It would be of interest (although computationally expensive) to see how this new dust model alters the overall global statistics for optical depth and effective radius as well as cost. However, the imaginary part of RI is

too high in this aerosol model, and would be expected to be a larger influence on the retrieval than shape, so additional case studies without also altering RI were not a priority.

3.4 Relative humidity

3.4.1 Background

Although areas where one expects mineral dust to be generated are dry, transport can be over thousands of miles, particularly across the Atlantic ocean. As such, one should expect to see mineral dust in a wide variety of humidity conditions. Fig. 3.17 shows average values and variability of relative humidity at surface level. The high variability suggests that an investigation of the scattering properties under changes in RH could be informative.

Previous work, attempting to retrieve aerosol water uptake [Schuster et al., 2009], reported that sand particle changes were not observable, but this relied on bulk mixing of water and desert dust refractive indices, which is not the method used in this work.

3.4.2 Method

Modifications of the mineral dust class were made, aiming to improve optical representation in a humid atmosphere. Several references help to build up a picture of sand composition during the SAMUM campaign. The smallest particles (< 150 nm) were seen to be the most hygroscopic (100 % soluble by volume), and are most likely ammonium sulphate [Kaaden et al., 2009]. It was also observed that above this size range was a "less hygroscopic" regime which was 40 % soluble by volume (assuming the solute was ammonium sulphate). At the upper range of the hygroscopic aerosol, it was noted that smaller particles ($< 0.35 \rightarrow 0.5$ μm) contained "a considerable volatile and hygroscopic fraction" but that the larger particles "were almost entirely non-volatile and showed no significant humidity related particle growth" [Petzold et al., 2009]. These observations were also shown in Weinzierl et al. [2009, Fig. 5]. With this information in mind, the four-mode distribution is altered as

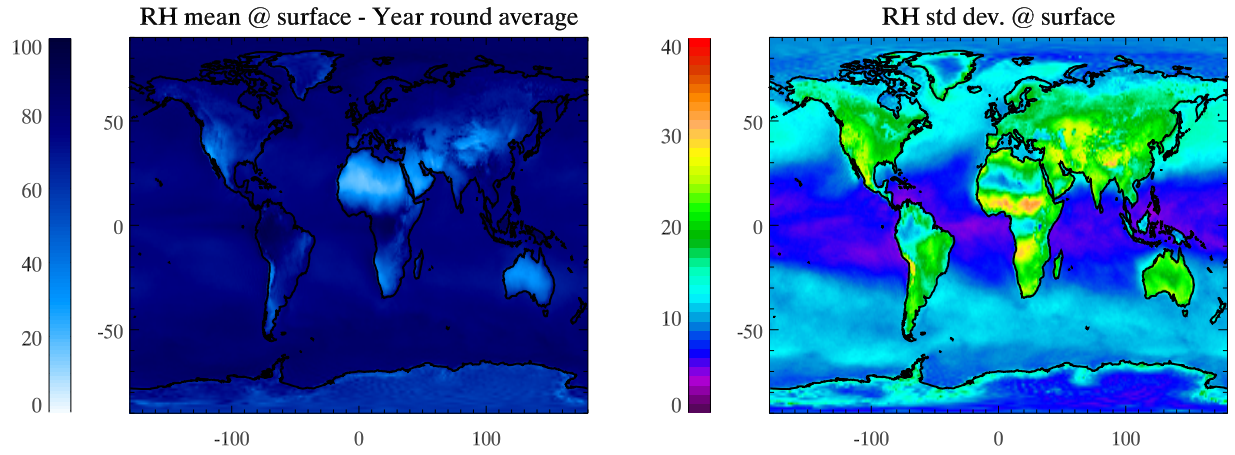

Figure 3.17: Showing ECMWF relative humidity data averaged from April 2006 to March 2007 at surface level. Standard deviation is shown on the right-hand plot.

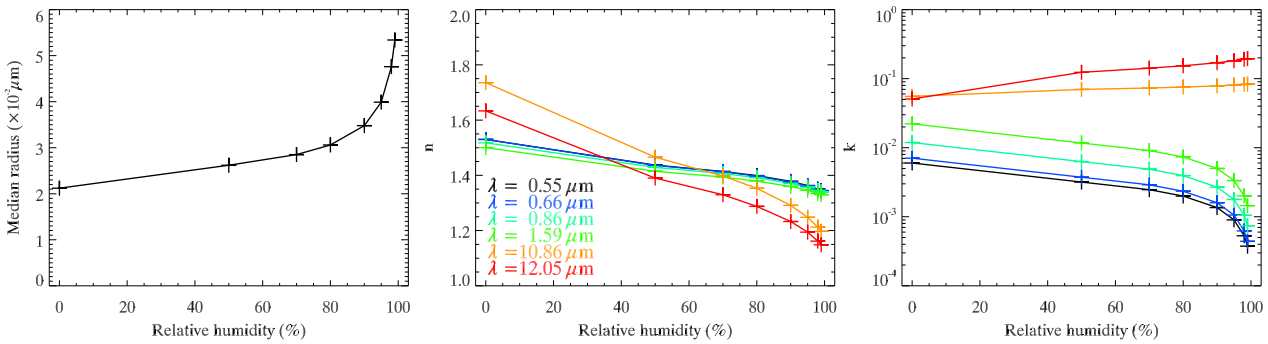

Figure 3.18: Variation of OPAC water soluble aerosol mode properties with relative humidity. Median radius (r_g) is shown in the left-hand plot, real part of refractive index (n) in the centre, and imaginary part (k) on the right. The values n and k are shown at the AATSR channel wavelengths. As RH increases, we see the bulk RI values move towards the values for water.

explained in Table 3.7.

Mode 1 - Fully hygroscopic

The fully hygroscopic mode relies on the OPAC values of refractive index and mode median radius of the water soluble mode as a function of relative humidity. These values are shown in Fig. 3.18. Mie theory is still used for the light scattering calculations since we are looking at a solution which will be spherical and which is small compared to the wavelength. Since r_g changes depending on the humidity, the mode distribution changes slightly from that seen in Fig. 3.1. As one would expect,

Mode	Current model	Relative humidity adjusted model
1	OPAC "Water soluble" mode with 50 % RH at all times	OPAC "Water soluble" mode with varying RH. This also alters the median radius of the mode.
2	OPAC "Mineral dust nucleation" mode (insoluble)	40 % by volume ammonium sulphate, the rest insoluble mineral dust. Scattering modelled as coated spheres. The inner sphere is the insoluble fraction, the outer "coating" is the ammonium sulphate solution. The width of the coating is determined by the relative humidity. When the relative humidity is not sufficient to add a coating to a particle, a single refractive index is chosen for a non-coated sphere.
3	OPAC "Mineral dust accumulation" mode (insoluble)	As mode 2.
4	OPAC "Mineral dust coarse" mode (insoluble)	OPAC "Mineral dust coarse" mode (insoluble).

Table 3.7: Comparing two representations of the desert dust aerosol class.

increased relative humidity causes larger particles, and refractive index tends towards the value for water as the concentration of the solute decreases.

Modes 2 & 3 - Partially hygroscopic

For the partially-hygroscopic particles, modifications of Köhler theory for soluble particles with insoluble fractions were used [Pruppacher and Klett, 1997]:

$$\frac{e_a}{e_{\text{sat},w}} = \exp\left[\frac{2M_w\sigma_{s/a}}{\mathcal{R}T\rho_w a} - \frac{\nu\Phi_s\varepsilon_v M_w\rho_s r_d^3}{M_s\rho_w(a^3 - r_d^3)}\right], \tag{3.10}$$

where:

M_w - Molecular weight of water (= 18.0160 g mol^{-1}).

M_s - Molecular weight of the soluble salt (= 132.14 g mol^{-1} for $(NH_4)_2SO_4$).

$\mathcal{R}$ - Universal gas constant (= 8.314 J mol^{-1} K^{-1}).

a - Wet particle radius.

r_d - Dry particle radius.

ρ_w - Density of water ($= 0.998$ g cm^{-3} at 1 atm, 20 °C).

ρ_s - Density of soluble salt fraction ($= 1.130$ g cm^{-3} for $(NH_4)_2SO_4$).

ε_V - Water soluble volume fraction.

ν - Number of ions into which the salt will disassociate in water (3 for $(NH_4)_2SO_4$).

$\sigma_{s/a}$ - Surface tension of solute / air boundary. Surface tension is a function of molal concentration of salt and temperature. From Pruppacher and Klett [1997], we obtain $\sigma_{s/a}(m,T) = \sigma_{w/a}(T) + Bm$, where $\sigma_{w/a}(T)$ is the temperature-dependant surface tension between a water/air boundary and m is the molal concentration. The gradient, B, can be obtained from Jarvis and Scheiman [1967].

Φ_s - Molal osmotic coefficient of the salt in solution. Characterises the deviation of a solvent from ideal behaviour according to Raoult's law, accounting for behaviour when the concentration of the solute is high. Since this deviation is not great, once an aerosol particle has begun to pick up moisture from the surrounding air, it is set $\Phi_s = 1$.

We are interested in the relationship between a and relative humidity, $\mathrm{RH} = \frac{e_a}{e_{\mathrm{sat},w}}$ given r_d. We rearrange (3.10) to give:

$$\ln\left(\frac{e_a}{e_{\mathrm{sat},w}}\right) = \frac{M_w}{\rho_w}\left[\frac{X}{a} - \frac{Y}{(a^3 - r_d^3)}\right], \tag{3.11}$$

where

$$X = \frac{2\sigma_{s/a}}{\mathcal{R}T}, \qquad Y = \frac{\nu\Phi_s\varepsilon_V\rho_s r_d^3}{M_s}.$$

The Newton-Raphson iterative technique was used to obtain wet radius, a. Values for an initial particle size of $r_d = 0.1$ μm as the relative humidity changes are shown in Fig. 3.19.

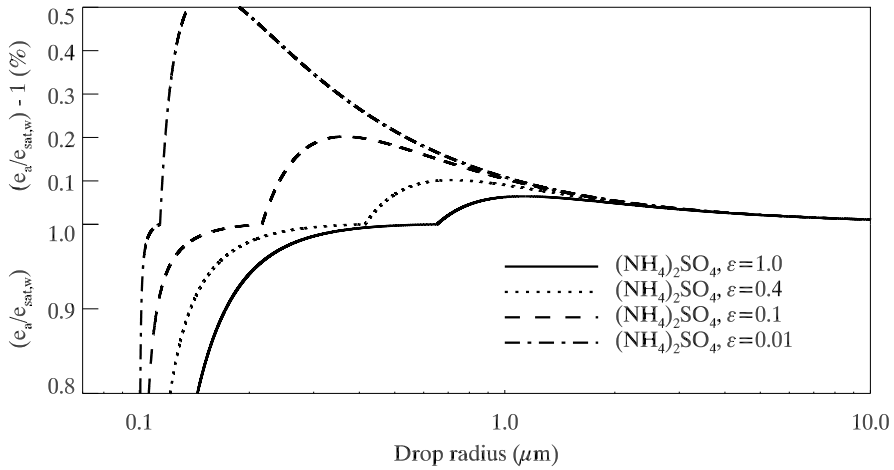

Figure 3.19: Showing how changing the relative humidity over an aqueous solution formed from an aerosol with soluble and insoluble fraction alters the drop radius. The initial dry particle size is $r_d = 0.1$ μm. The four curves show particles with different soluble fractions by volume, ε_V. The upper half of the ordinate shows super-saturation and has a smaller scale. This plot is a reproduction of Fig. 6-3 from Pruppacher and Klett [1997], independently calculated, to test that the method employed was working.

From the above discussion of field measurements, the soluble volume fraction was chosen to be $\varepsilon_V = 40\%$ [Kaaden et al., 2009] and the density of the insoluble mass fraction of mineral dust at the core was chosen to be $\rho_i = 2.65$ g cm^{-3}, which is representative of Saharan sand [Haywood et al., 2001].

After the wet radius has been calculated, further assumptions are required in order to calculate light scattering properties. Since the soluble portion of the mineral dust has now dissolved into solution, the volume of the sand particle core is reduced. To simplify calculations, we assume a coated sphere using a modification of `bhcoat.f` written by Bohren and Huffman [1983] (which was converted to IDL and updated, so that the phase function could also be calculated). Although there is available code to calculate light scattering by non-spherical inclusions to spherical scatterers [Doicu et al., 2006], it was felt that since the shape would be very poorly understood, computer overhead would be significantly greater, and that significant differences would be reduced over a large distribution of sizes, this was an unnecessary complication. Knowing a, r_d and ε_V, the interior

radius, r_{core}, can be easily obtained, by assuming a water / salt solution would take up the same volume as pure water:

$$\begin{aligned} \text{Vol. occupied by insoluble part} &= \tfrac{4}{3}\pi r_{\text{core}}^3 = r_d^3\,(1-\varepsilon_{\text{V}})\,\tfrac{4}{3}\pi, \\ \Rightarrow r_{\text{core}} &= r_d \sqrt[3]{1-\varepsilon_{\text{V}}}. \end{aligned} \tag{3.12}$$

For the case of a dry particle, we calculate a single refractive index, weighted by the mass of the two types of scattering material, the (now dry) ammonium sulphate and the insoluble fraction:

$$m_{\text{dry}} = \frac{(1-\varepsilon_{\text{V}})\,\rho_i m_i + \varepsilon_{\text{V}}\rho_s m_{\text{dry }(\text{NH}_4)_2\text{SO}_4}}{(1-\varepsilon_{\text{V}})\,\rho_i + \varepsilon_{\text{V}}\rho_s}. \tag{3.13}$$

Mode 4 - Hydrophobic

The fourth mode was defined as completely insoluble, so was left in an identical state to that of previous calculations (in terms of relative humidity). Initially, so as to compare as closely as possible with the original dust class, the sand particles in the coarse mode were modelled as spheres, meaning that all differences between the classes were due to the lower 3 modes[9].

Further assumptions

Since the intended application of this method was to improve observed aerosol, it was decided that the distributions should be log-normal for the *wet* radius (since we were observing the particles which were presumed to have a coating). This means that for conditions with heightened relative humidity, one would be observing smaller (dry) sand particles than for a dryer atmosphere with the same aerosol effective radius.

[9] Although, due to the changing size of the smaller modes, mixing ratios between all of the modes altered.

Modifying the model

The final four modes were then combined in an identical method to the standard ORAC routine [Thomas et al., 2005]. The results of this for the AATSR 550 nm channel are shown in Fig. 3.20, along with overlaid data from Fig. 3.2. Here we begin to see a problem emerge, that subsequent retrievals confirmed.

As has been mentioned in other studies (and earlier in §3.4), the OPAC values of k for desert dust, are too high in the visible, leading to optical models of dust which are too absorbing. We see in Fig. 3.20 that as the relative humidity increases, the model appears to become closer to observed values of β^{ext} and $\bar{\omega}_0$. However, this is not due to an improved model of our dust. In fact, the water coating the partially hygroscopic modes 2 & 3 is reducing the absorption of these two distributions. Similarly, the retrievals show lowest cost for the high relative humidity models.

As a result of this, it was decided to reduce the k value of desert dust, using the ADIENT tables provided by Highwood [2009] and plotted previously as Fig. 3.4. This new model is described in Table 3.8 The new optical properties are show in Fig. 3.21. It is no longer the case that increasing the relative humidity *ad infinitum* (or maybe *ad centum*) improves the comparison between our representation of desert dust's optical properties and the observations. As expected, increased RH reduces absorption in the visible. With a more sensible set of optical properties, the retrievals over desert dust scenes are repeated.

3.4.3 Retrievals using variable relative humidity and a non-spherical coarse mode

The AATSR ORAC aerosol state vector, $\mathbf{x}$, has terms for aerosol optical depth, aerosol effective radius, and surface reflectance [Thomas et al., 2011, and also §1.6.3]. Adding additional elements is not feasible, since the limited information given by 8 measurements means the current problem is already under-constrained. The result of this is that we cannot "retrieve" the relative humidity simultaneously with the state vector elements. Instead, we run each relative humidity dust as a

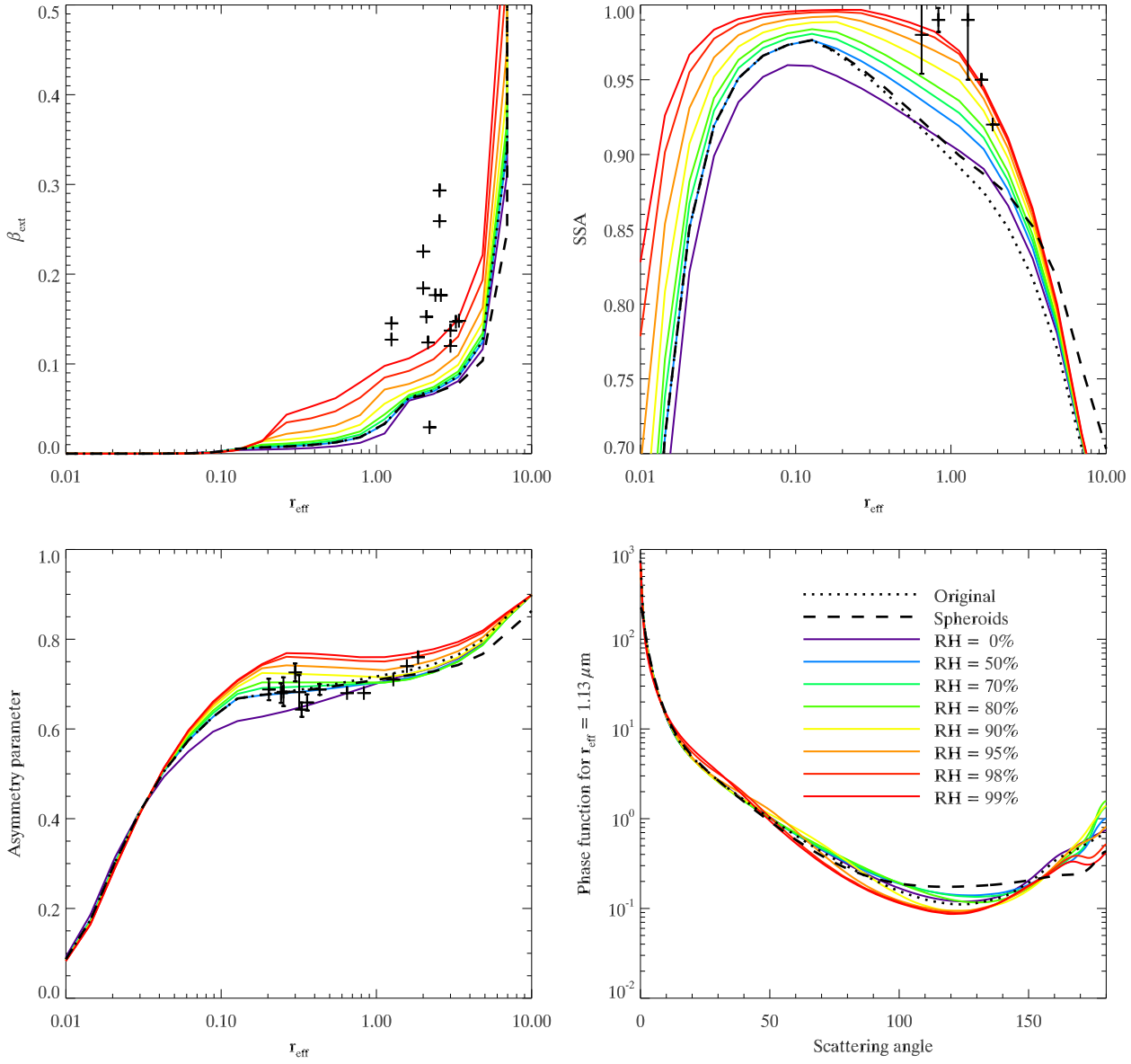

Figure 3.20: Optical properties at $\lambda = 550$ nm from the microphysical models of dust described in §3.4. Overlaid crosses (+) are the measurements previously shown in Fig. 3.2. Also shown are the optical properties of the original spherical model and the spheroid distribution used in §3.3.3.

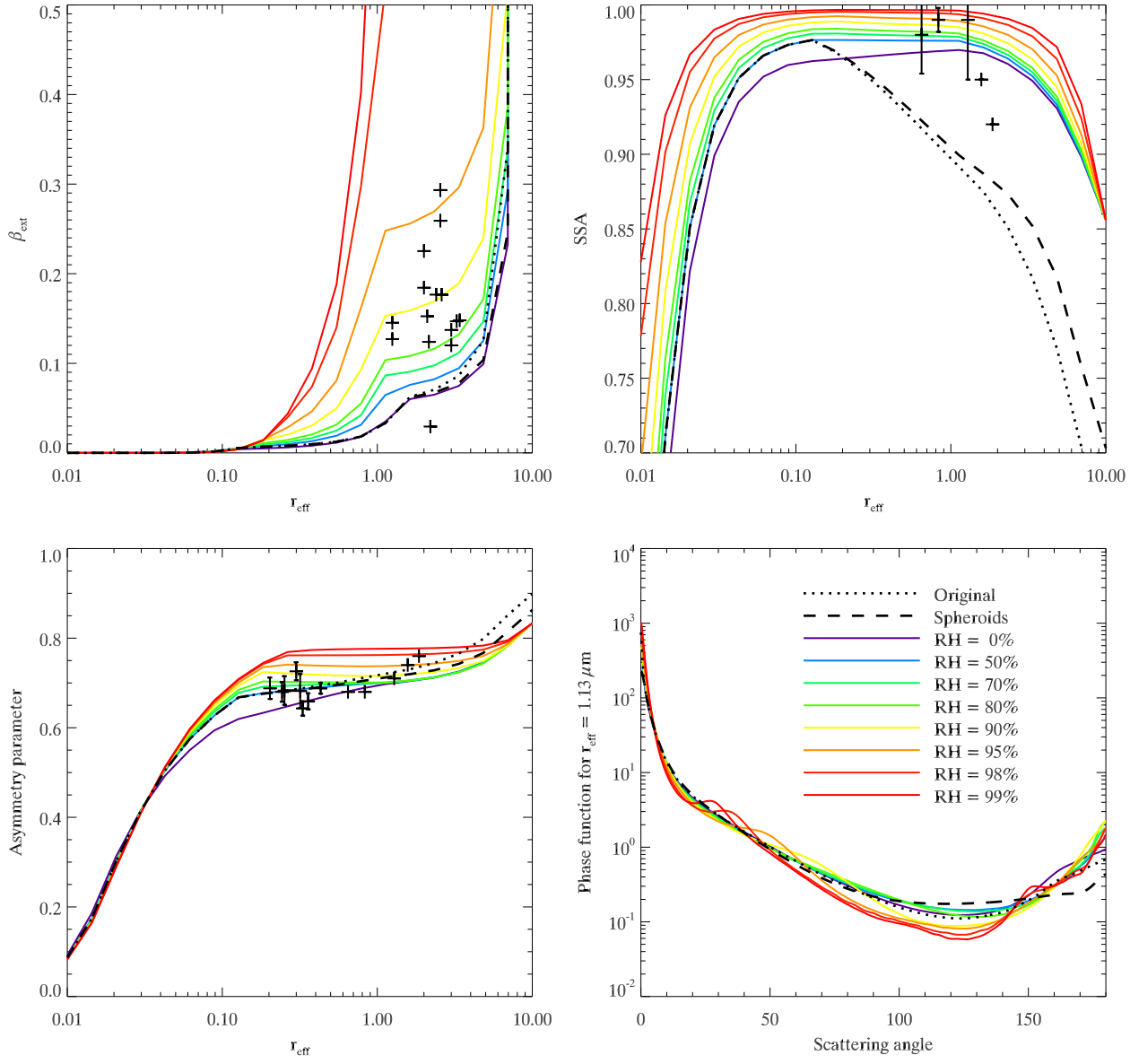

Figure 3.21: Optical properties at $\lambda = 550$ nm of the modified RH dependant dust models described in Table 3.8. The overlaid crosses and lines for original and spheroid models are identical to those shown in Fig. 3.20.

Mode	Second relative humidity adjusted model
1 - "Water soluble"	OPAC "Water soluble" mode with varying RH. This also alters the median radius of the mode.
2 - "Mineral dust nucleation"	40 % by volume ammonium sulphate, the rest insoluble mineral dust. Scattering modelled as coated spheres. The inner sphere is the insoluble fraction, the outer "coating" is the ammonium sulphate solution. The width of the coating is determined by the relative humidity. When the relative humidity is not sufficient to add a coating to a particle, a non-coated sphere is used. **ADIENT desert dust refractive index values are used** for the interior, non-soluble fraction of the aerosol.
3 - "Mineral dust accumulation"	As mode 2.
4 - "Mineral dust coarse"	Spheroidal distribution, as described in §3.3.2. The lognormal distribution in size is defined by the OPAC "Mineral dust coarse" mode. This mode is assumed insoluble and **ADIENT desert dust refractive index values are used.**

Table 3.8: Improved RH dependent desert dust aerosol class, with reduced absorption and non-spherical coarse mode.

separate aerosol class, and look at the end, to see which has the most favourable cost.

Fig. 3.22 shows the same Atlantic AATSR scene shown earlier (in Fig. 3.16) on 10th March 2006, and compares the retrieval cost for 10 different aerosol classes; the "marine" and "desert dust" classes currently used in the operational retrieval, and the relative humidity dependant classes with a non-spherical coarse mode which have just been described. Within the area dominated by the dust cloud, the RH=80 % dust model almost always has the lowest cost of the various desert dust models. In areas outside of the dust event, Fig. 3.22e shows that the optical depth is much lower. At these low values, we would generally assume that this was marine aerosol, so the incoherent muddle of best classes seen at the bottom left of Fig. 3.22c is less of a concern. In the top right of the scene, where Fig. 3.22f shows us that $r_{\text{eff}} \sim 10\ \mu$m it is highly likely that we are looking at clouds. Since the maximum value allowed for retrieved r_{eff} is 10 μm, the aerosol particles cannot be any bigger (and it is extremely unlikely that aerosol particles would have an effective radius this large). It is pleasing that in these areas, the highest relative humidity microphysical models are present.

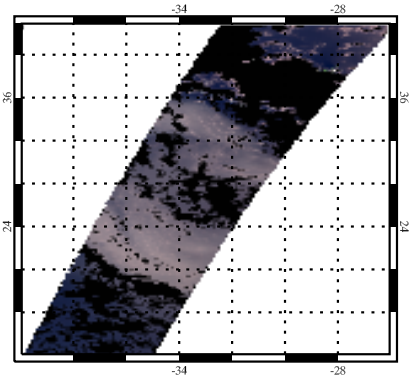

(a) False colour image of the scene

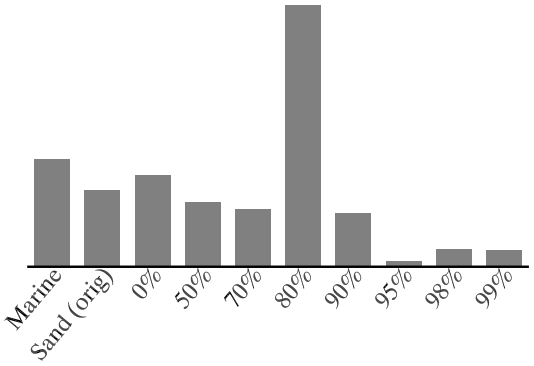

(b) Aerosol class with the lowest cost.

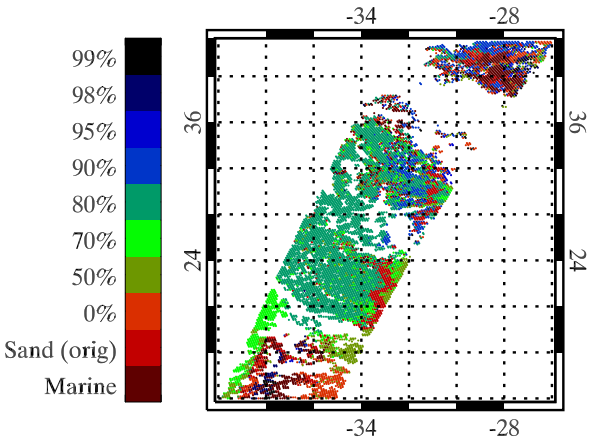

(c) Aerosol class with the lowest cost.

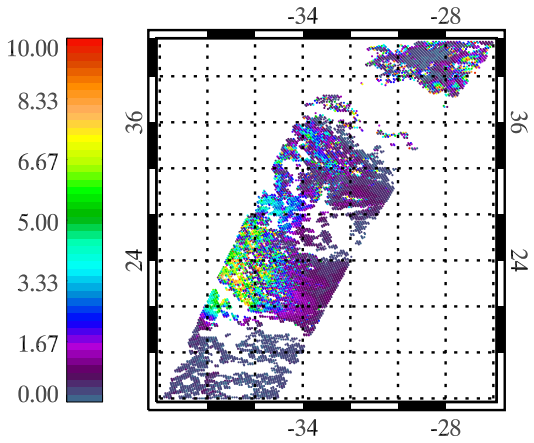

(d) Lowest cost

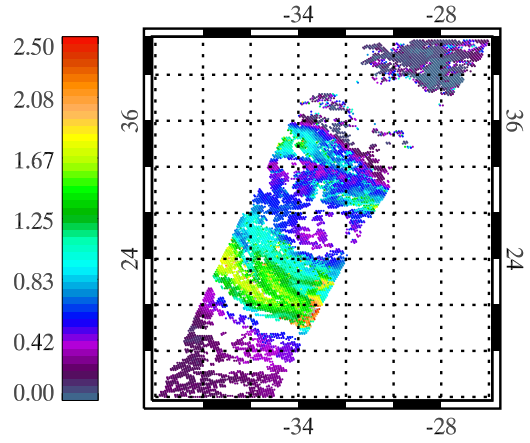

(e) Optical depth at 550 nm for lowest cost class

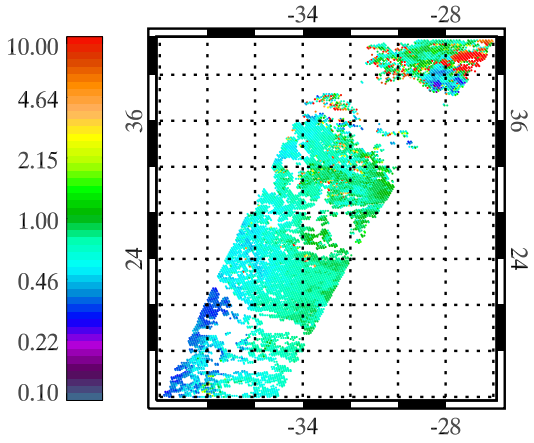

(f) Effective radius (μm) for lowest cost class

Figure 3.22: AATSR retrievals over the Atlantic Ocean on 10th March, 2006. A large dust storm can be seen in the false colour image, (a). The classes in (b & c) defined by a percentage are the RH dependant desert dust models with a hydrophobic, non-spherical coarse mode, as described in §3.4.3.

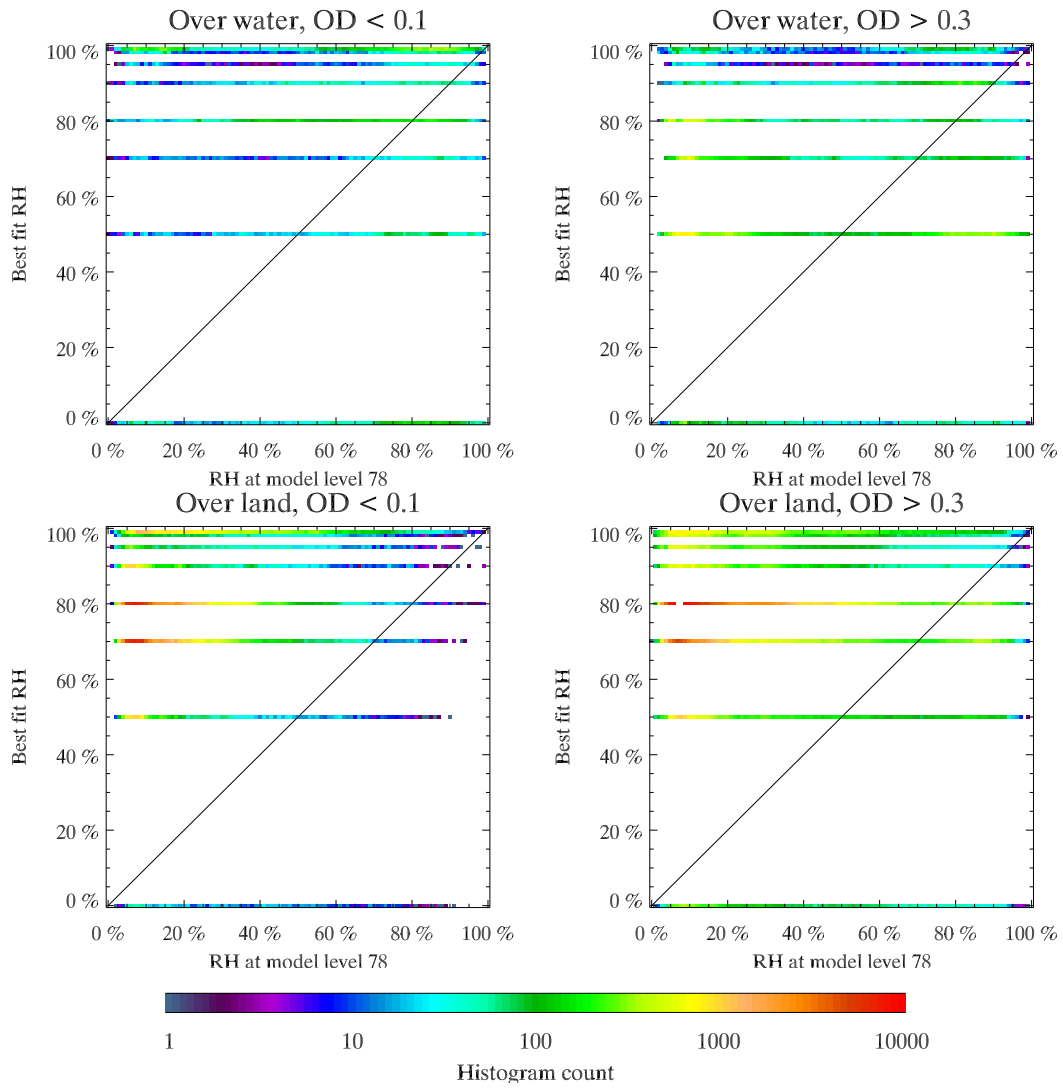

Figure 3.23: 2D histograms of ECMWF relative humidity against RH obtained by finding the RH-variable desert dust class with the lowest cost for each pixel. ECMWF data was interpolated in space and time from the grid points and a pressure level with an average height of $\sim$1 km was selected since the ORAC forward model has places dust in the bottom two layers of the atmosphere, between 0 km and 2 km.

Looking now at statistics for the whole of the month of March 2006, Fig. 3.23 shows a 2D histogram comparing the ECMWF relative humidity at an approximate altitude of $\sim$1 km[10] to a best guess relative humidity, chosen by selecting the lowest cost variable humidity dust model at a pixel. The plots have been divided into low and high optical depths (representing atmospheres that are clean and those likely to contain significant aerosol respectively) over land and water. There is no strong correlation between the ECMWF and retrieval based inferences of local relative humidity, but classes 50 %, 70 %, and 80 % gain the majority of the points (almost regardless of ECMWF values). The one exception to this is the low AOD over water, where high ECMWF relative humidity corresponds to high retrieval AOD. This is almost certainly contamination from marine aerosol, where the highest relative humidity sand model most closely resembles particles consisting mostly of water.

Figure 3.24 shows histograms of retrieval cost and residuals over the Sahara region for the whole of March 2006. Four variations of the sand class are shown: the current sand class, and three of the relative humidity dependent classes defined in this section. It can be clearly seen that the 50 % and 80 % RH NS classes are an improvement on the current model, and also perform better than the higher RH=99 % model. These mid-RH classes have the best centred residuals, implying less systematic bias, and lower overall cost. The bias is not completely removed (as can be seen in the forward view at $\lambda = 670$ nm for example), but relative to the previous microphysical model of dust, the residuals in every channel have been reduced.

Over the Sahara, when optical depth is high (AOD > 1), relative differences between the original ORAC mineral dust and NS RH80 % are regularly more than 100 %, with the original ORAC dust having the smaller AOD.

3.4.4 Comparison with AERONET retrievals

As an independent test of the most appropriate dust class to use, concurrent AERONET measurements were compared to retrieved AATSR aerosol properties. The list of Saharan stations used is

[10]The data are defined on a model level which roughly corresponds to pressure levels, which roughly correspond to altitude.

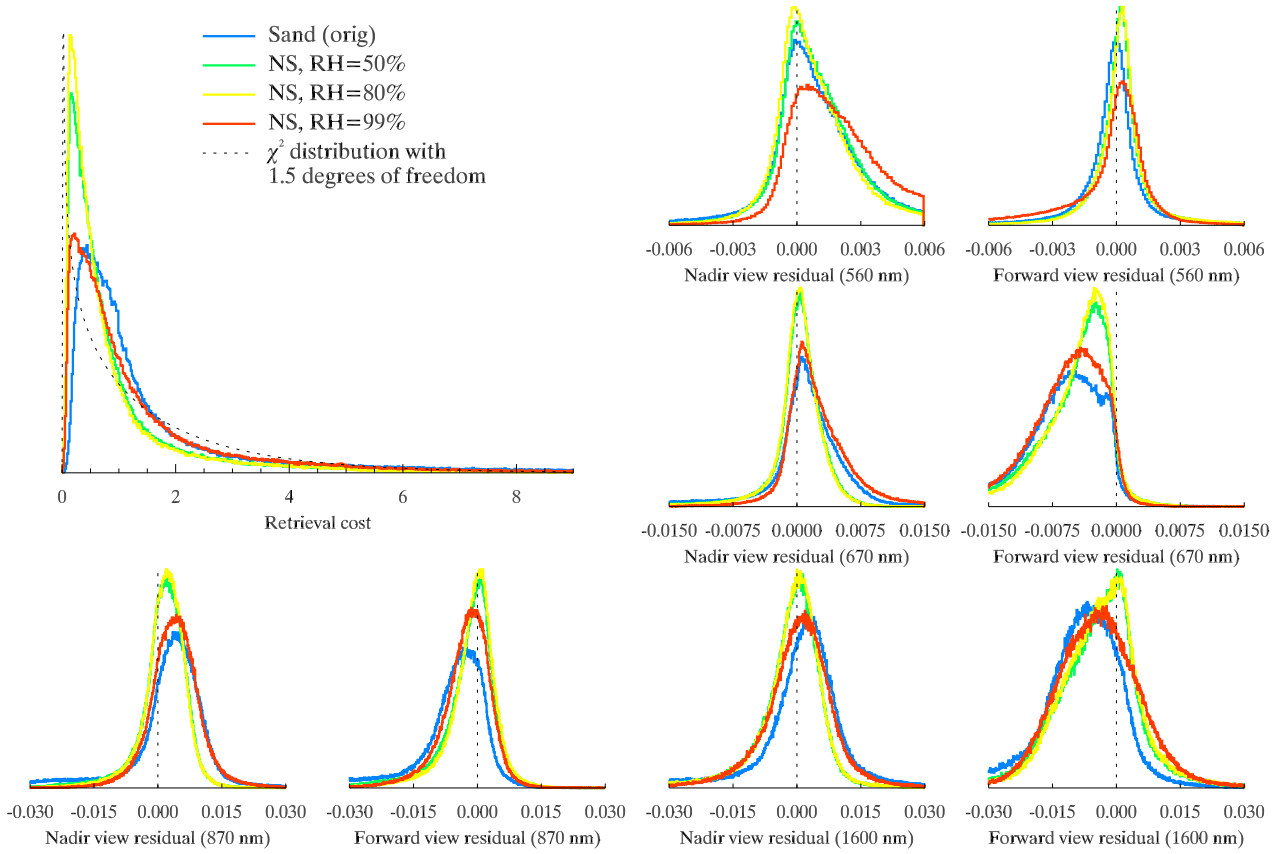

Figure 3.24: Comparing retrieval cost and residuals from various classes representing desert dust aerosol. The current ORAC sand class (spherical, homogeneous) is shown in blue. Comparisons are limited to those over the Sahara region, for the month of March 2006, when the AOD$>$ 0.2.

Site	Location
Agoufou	(15N, 1W)
Banizoumbou	(13N, 2E)
Capo Verde	(16N, 22W)
DMN Maine Soroa	(13N, 12E)
Dakar	(14N, 16W)
Djougou	(9N , 1E)
IER Cinzana	(13N, 5W)
Ilorin	(8N , 4E)
Izana	(28N, 16W)
Lampedusa	(35N, 12E)
Saada	(31N, 8W)
Santa Cruz, Tenerife	(28N, 16W)
Tamanrasset TMP	(22N, 5E)

Table 3.9: List of AERONET sites used in the inter-comparison.

given in Table 3.9. Comparisons were made when satellites passed within 0.1° of a site, within 1 hour of an AERONET measurement. The compared measurement was aerosol optical depth at 870 nm. Assuming a linear relationship, goodness of fit statistics were calculated: the χ^2 statistic with and without measurement errors, and a least total absolute deviation. For measurement error, the retrieval error values were used. The Pearson correlation coefficient was also obtained.

Fig. 3.25 shows the fit statistics. The χ^2 and least absolute deviation should be as small as possible (showing, as they do, the total deviation of individual points from the line of best fit). The correlation coefficient should be as close to 1 as possible. Continuing the trend, the 50–80 % relative humidity dust classes most closely match the AERONET measurements.

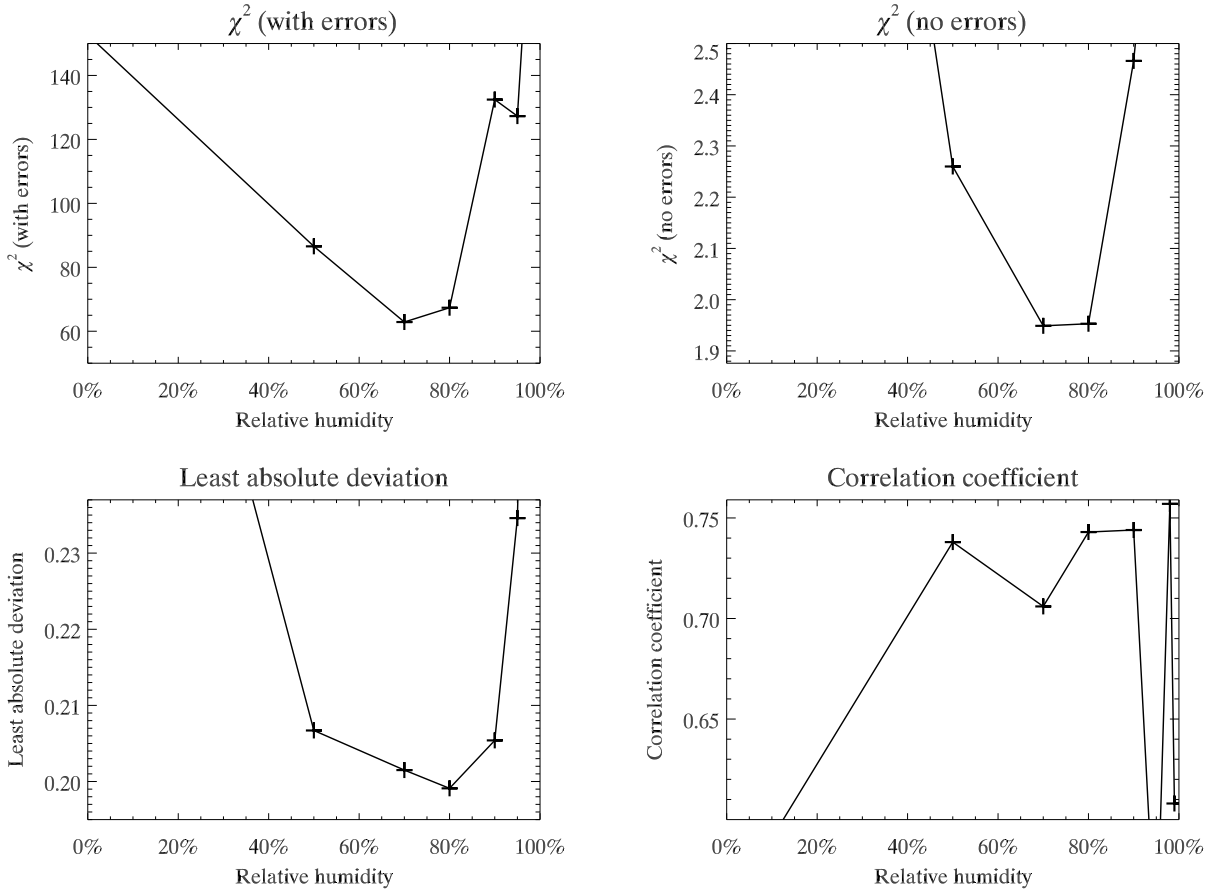

Figure 3.25: Four methods of "scoring" the relationship between AERONET measurements of aerosol optical depth at 870 nm and concurrent retrieved aerosol optical depth from AATSR using various RH dependant desert dust classes. The minimised χ^2 statistics for goodness of fit are presented with and without the measurement errors; minimised least absolute deviation; and correlation coefficient. In the first three plots, we are looking for a minima, and in the final plot of correlation, we want the maxima.

3.5 Conclusions

After reviewing most of the assumptions made by the ORAC desert dust microphysical model, the conclusions about various aspects are presented here.

Size distribution Comparison with measurement campaigns, while not exhaustive, show that our assumptions about size distribution are not unreasonable. Variation of mixing ratios between the different lognormal modes should be the main method of altering r_{eff}.

Refractive index The imaginary part of refractive index, k, currently used for the ORAC retrieval is too large (in the visible), making the desert dust class too absorbing. Reducing k to the values suggested by Highwood [2009] improve agreement with observed optical properties. Natural variation in the mineralogy of desert dusts does not cause huge differences in the optical properties of mineral dust class.

Non-sphericity Numerous previous studies show that desert dust is not spherical. The shapes of individual particles vary dramatically, and calculating scattering tables for an infinite number of shapes (at different wavelengths and possibly refractive indices) is impractical, if not impossible, although Kalashnikova and Sokolik [2004] have generated scattering models for particles defined by a composition-size-shape (CSS) classification. The most immediate improvement that could be made would be to replace spherical particles with ellipsoids with a sensible distribution of aspect ratios [Kandler et al., 2007]. There are three main advantages to this method. Firstly, it is closer to physical reality that our current assumption of sphericity. Secondly, even if the new shapes do not perfectly mirror reality, the effect of the non-spherical particles is to "flatten" the phase function (e.g. Fig. 3.12), a general feature of all non-spherical particles. Finally, the solutions to light scattering by spheroids can be obtained analytically (within size parameter constraints) and what is more, well tested code is available and the results of this code have been tabulated [Dubovik et al., 2006] and so tables can be generated extremely quickly. Retrievals of dust using a spheroidal model did not improve the cost dra-

matically, but a lower optical depth is obtained. Also, the spheroidal models had much higher cost that the spherical models in areas where it was unlikely that we were looking at sand, reducing the likelihood of marine aerosol being mistaken for sand.

Ambient conditions Microphysical models attempting to accurately represent the effect of ambient relative humidity on the dust particles do not show a strong correlation with the actual relative humidity found during a retrieval. This agrees with Kaaden et al. [2009, Fig. 11] who found that the backscatter coefficient measured by lidar at 532 nm had no change as a function of the atmospheric relative humidity. However, the 70 % and 80 % relative humidity models (which also included a non-spherical, hydrophobic coarse mode, and reduced absorption) were consistently the models with the best cost, reduced systematic bias in residuals, and the closest statistical similarity to concurrent AERONET measurements.

Chapter 4

Aerosol from burning

4.1 Background

Burning is the major worldwide source of CO_2 [Solomon et al., 2007] and as such attracts a large amount of attention from policy makers. Recently, focus has also been drawn to the particulate products of incomplete combustion, soot and organic aerosols, with calls for global regulation of their emission[1] [e.g. Jacobson, 2002, 2003; Bond, 2007]. Emissions rates are high [Bond et al., 2004], and have tripled in the last 140 years [Ito and Penner, 2005] although specific regions have not followed this trend. The developed world has reduced emissions while Asian countries have come to dominate carbon aerosol emission [Streets et al., 2003].

Carbonaceous aerosol is separated into two broad categories, black (or elemental) carbon (BC) [Bond and Bergstrom, 2006] which is highly absorbing, and organic carbon (OC) [Jacobson et al., 2000] which is basically all the other carbon based aerosols. Since BC is so absorbing, it is one of the few aerosols that has a positive direct effect on radiative forcing [Jacobson, 2001; Bond, 2007; Bahadur et al., 2011]. Organic carbon aerosols reflect the majority light incident upon them, so give negative forcing. Both BC and OC particles also act as cloud condensation nuclei (CCN) [Kaufman and Fraser, 1997; Hitzenberger et al., 1999, respectively] increasing the indirect effect [Twomey,

[1] Emission of particulate matter is generally regulated on a local or national scale.

1977b].

Additionally, studies have shown that when BC is deposited on snow, the resultant effect of lower surface albedo leads to faster run-off and an additional warming effect [Flanner et al., 2007, 2009; Doherty et al., 2010; Yasunari et al., 2010]. Aside from the positive radiative forcing due to BC, there are considerable negative health effects from fine particulate matter [Dockery et al., 1993; Jansen et al., 2005], of which OC and BC can make up a significant fraction, particularly in urban environments where the highly absorbing refractive index of BC means that there are also issues of poor visibility [Larson et al., 1989].

Attention should be directed at carbonaceous particles by researchers interested in retrieving their properties from satellite measurements as there is significant evidence that they do not exist in the atmosphere as homogeneous spheres, but are almost exclusively modelled as such.

4.1.1 Methods of emitting carbonaceous aerosol

Carbonaceous aerosol is emitted almost entirely as a result of incomplete combustion. There are two principle classes of fuel source, fossil fuels and biomass. Biomass burning (and the burning of biofuels) is estimated to be the larger emitter of carbonaceous aerosol, the majority of it OC. Fossil fuel burning emits far less OC, and around the same amounts of BC [Cooke and Wilson, 1996; Liousse et al., 1996; Bond et al., 2004]. Along with the carbonaceous emissions, combustion processes also emit large amounts of sulphate aerosol [Hegg et al., 1997].

Approximately 80 % of biomass burning occurs in the tropics with the main burning areas being South America and sub-Saharan Africa [Cachier et al., 1996] and of this, 30 % comes from burning of African savanna [Andreae et al., 1996]. Principle biomass combustants are biofuels (renewable fuels from wood and plant and agricultural waste), and vegetation such as forests, crops, and savanna.

Fossil fuel particulate emissions are chiefly the products of the industrial and transportation sectors [Bond, 2007] with coal, coke, diesel, petrol, kerosine, and natural gas the principle combustants. These emissions generally contain a higher proportion of BC and so can be expected to be more

absorbing.

Geographical emissions trends

As mentioned above, the majority of biomass emissions come from the tropics. Studies of global emissions inventories show areas of heightened OC concentrations in Eastern Europe, the East Coast of North America, Brazil, southern and western Africa, India, Indonesia, China, and northern Australia [Liousse et al., 1996, Plate 2]. Of these regions, those that could be described as non-industrial are likely to be producing the vast majority of their OC emissions from biomass. Outside of the tropics, a study from Los Angeles in the 1980s found that the majority of biomass burning aerosol in the region was from fireplace burning and the cooking of meat [Hildemann et al., 1994]. Unger et al. [2010] modelled projected radiative forcings broken down by emissions sectors, and showed that household biofuel was the second biggest worldwide contributer to the negative RF effect of organic aerosol.

Black carbon concentrations are more firmly peaked in urban and industrial areas, but also exist in areas with biomass burning [Cooke and Wilson, 1996]. Transportation is the major source in OECD countries, while in the developing world, industry emits the majority of BC [Bond, 2007].

4.1.2 Physical description of aerosol formation and ageing

Formation

Formation of sub-micron aggregate aerosols from burning is a rapid process involving several stages, some of which are irreversible. Initially, due to very high temperatures, some of the burning fuel vapourises (if it is not already gaseous). If the fuel is something such as coal, the main products could be inorganics and elemental carbon formed from the vapourised ash [Helble et al., 1988; Turns, 2000]. In the case of biomass, this could be organics such as benzene and poly-aromatic hydrocarbons (PAH) [Reid et al., 2005].

Further away from the hottest part of the flame, nucleation of these molecules leads to formation

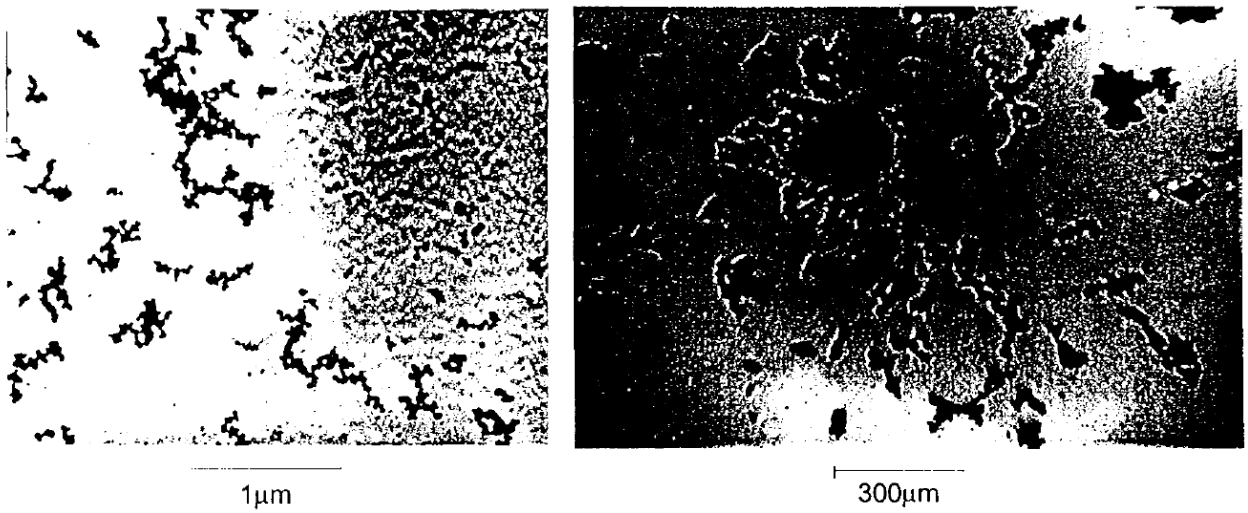

Figure 4.1: TEM image of fractal aggregates formed from the burning of acetylene. Reproduced from Sorensen [2001, Fig. 1] with permission.

of very small particles with diameters of 1–2 nm [Calcote, 1981]. These quickly grow by coagulation and surface condensation to sizes of 10–30 nm. Coagulation is encouraged initially due to a high proportion of hydrocarbon radicals which falls off as the particles age [Homann, 1967; Calcote, 1981]. High resolution TEM images of individual carbonaceous spherules shows them to be haphazardly ordered micro-structures of graphene-like layers [Buseck et al., 1987; Pósfai et al., 1999; Li et al., 2003] with a very narrow range of diameters for a specific flame [Homann, 1967].

After the initial nucleation and coagulation, primary particles can aggregate leading to the fractal soot aerosol often seen [Helble et al., 1988; Katrinak et al., 1993; Lighty et al., 2000; Sorensen, 2001; Abel et al., 2003; Li et al., 2003; Smekens et al., 2007; Zhang et al., 2008]. Examples of these are shown in Fig. 4.1. As the particles pass through the edge of the flame, some will be oxidised, although not completely [Turns, 2000]. Those that make it through the flame without burning are the soot emissions. Flames that burn more intensely have poorer transport of oxygen into the area where the particles are being created, and as a result will emit more particulate matter [Reid et al., 2005].

Volatile organic compounds emitted from the flames condense on any available particles forming the main particulate product of most burning, primary organic matter (POM). Studies show that the POM has often condensed on inorganic matter such as potassium salts [Pósfai et al., 2003] as well as

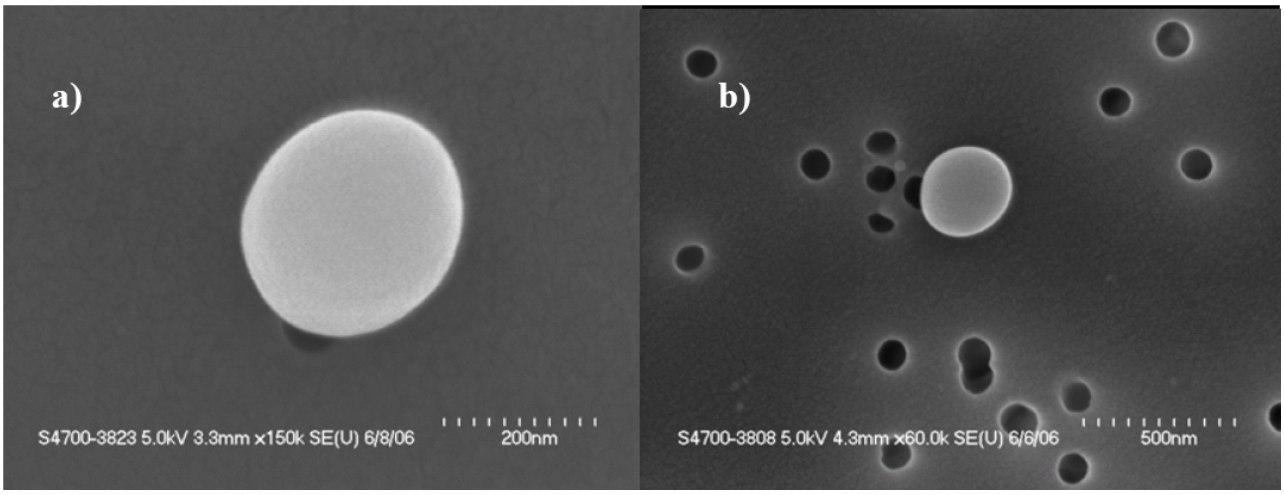

Figure 4.2: SEM images of tar balls from North American duff combustion, duff being the decaying litter of trees. Reproduced from Chakrabarty et al. [2010, Fig. 2] with permission.

BC fractals. These organic aerosols can be water soluble, so are likely to be spherical after spending some time in the atmosphere. In general, potassium salts are more prevalent in emissions from biomass burning than from fossil fuels [Andreae, 1983].

In the last decade, several studies have highlighted tar balls, an additional carbon aerosol product of biomass burning [Pósfai et al., 2003, 2004; Hand et al., 2005; Alexander et al., 2008; Adachi and Buseck, 2011]. These particles are found to be small, homogeneous, hydrophobic, single spheres which do not appear to age dramatically (probably as a result of their aversion to water). It is thought that they form from nucleation of the gaseous organic carbon downwind of burning [Pósfai et al., 2004], although they are generally distinguished from OC aerosol, which are generally described as hydrophilic and less absorbing of visible light. The tar balls are sometimes described as being composed of "brown carbon", due to their light scattering properties, which are less absorbing than BC, but more than OC [Alexander et al., 2008]. Examples of tar balls are shown in Fig. 4.2.

Coarse mode particles are formed (in far lesser numbers) by the fragmentation of large fuel particles which do not vapourise. As a result, some of these residual ash particles more closely resemble large spheres than fractals [Lighty et al., 2000], although many can have irregular shapes. These larger particles have a far shorter residence times in the atmosphere due to their large mass

[Bond et al., 2004].

Ageing

The aggregates created during burning last a very short amount of time, of the order of hours [Martins et al., 1998b], before being irreversibly deformed as the chain-like structures fold up into more spherical clusters [Martins et al., 1998a; Abel et al., 2003]. Although the soot spherules are hydrophobic, their irregular shapes provide active sites where water can be deposited [Zhang et al., 2008]. This change is thought to be due to atmospheric processing of the particles by nucleating water, and the coating of the carbon by nucleating additional products of the burning, e.g. sulphate and OC. This also means that the BC cores become coated in shells of other material which is generally hydrophilic [Popovicheva et al., 2008]. This coating enhances the absorption of the BC core [Fuller et al., 1999; Jacobson, 2001; Bond et al., 2006].

During biomass burning, evolution of the other aerosol components follows a similar path, with nucleation of gaseous and aqueous burning products onto existing aerosol. Mixing of all of the organic and inorganic aerosol components with age leads to a general increase in hygroscopicity and to a more pronounced growth of aerosol size as humidity rises [Reid et al., 2005].

Studies show that with ageing, the sulphate content of aerosols also increases [Pósfai et al., 2003; Reid et al., 2005], being both internally mixed with organic, and on its own. Tar Balls, which do not appear to be altered as relative humidity changes over long periods of time, can become internally mixed with sulphates and OC, allowing them to take on water and consequently making them indistinguishable from these aerosol [Pósfai et al., 2004].

4.1.3 Additional observations of carbonaceous aerosol microphysical properties

Black carbon has an atmospheric residence time of around 40 hrs in rain, and more than a week when dry [Ogren and Charlson, 1983]. Vertical distributions of number concentration measured in remote

	Description	Visible RI		Reference
Organic carbon	Pollution	1.595	$+ 0.049i$	Dinar et al. [2008]
	Wood burning smoke	1.622	$+ 0.048i$	Dinar et al. [2008]
	Rural continental	1.56	$+ 0.003i$	Dinar et al. [2008]
	Swannee River Fulvic Acid	**1.634**	$+$ **0.021i**	Dinar et al. [2008]
	Biomass burning	1.65	$+0.0019i$	Hoffer et al. [2006b]
	OC (in ADRIEX)	1.45	$+ 0.001i$	Kreckov [1993]
	POM (in ECHAM)	1.53	$+0.0055i$	Köpke et al. [1997]
	OC (in HADGEM2)	1.54	$+ 0.006i$	-
Biomass burning	Amazon (from AERONET)	1.47	$+0.0093i$	Dubovik et al. [2002]
	Cerrado, Brazil (AERONET)	1.52	$+ 0.015i$	Dubovik et al. [2002]
	Africa (AERONET)	1.51	$+ 0.021i$	Dubovik et al. [2002]
	Boreal (AERONET)	1.50	$+ 0.009i$	Dubovik et al. [2002]
	Amazon	1.41	$+ 0.013i$	Guyon et al. [2004]
	Amazon	1.5	$+ 0.015i$	Chand et al. [2006]
	Fresh (in HADGEM2)	1.54	$+ 0.029i$	-
	Aged (in HADGEM2)	**1.54**	$+$ **0.018i**	-
	Aged, from Sahel (DABEX)	1.53–1.59	$+ 0.045i$	Johnson et al. [2008]
Secondary OC	HULIS (remote continental)	1.53	$+ 0.003i$	Dinar et al. [2008]
	OC (in HADGEM2)	**1.43**	$+$ **0.000i**	Lund Myhre and Nielsen [2004]

Table 4.1: Refractive index values for various types of organic carbon for $\lambda \sim 550$ μm, RH$= 0$ %, as reported by Highwood [2009]. For each of the defined sub-categories, the recommended value is emphasised in bold font.

areas have been found to be relatively flat throughout the boundary layer [Schwarz et al., 2010]. An exhaustive study of the literature on measurements of BC refractive index in the visible by Bond and Bergstrom [2006] persuasively concluded that common values used repeatedly in the aerosol modelling community were not correct, providing as a replacement a recommended range of values running linearly from "moderately absorbing" BC with $m = 1.75 + 0.63i$ to "strongly absorbing" BC with $m = 1.95 + 0.79i$.

Similarly for OC, the summary of aerosol RI provided for the ADIENT project [Highwood, 2009] provides a comprehensive list of commonly used OC values. Table 4.1 contains the details of this. Generally, fresher OC is more absorbing.

Fresh primary organic matter (POM) and BC from biomass burning have been found to be hydrophyllic. Water uptake is due to presence of inorganics [Hand et al., 2010]. Soot and tar balls do not take up water; mixed organic-inorganics do this, with the inorganic fraction determining hygroscopicity [Semeniuk et al., 2007]. Measurements of of water uptake in Brazil found that organics accept water at low RH. At higher RH, sulphate is more hygroscopic and so grows faster [Kotchenruther and Hobbs, 1998].

4.1.4 How the ORAC retrieval currently models carbonaceous aerosol

Currently, there are two aerosol classes which can represent burning products within the ORAC retrieval scheme, the urban class, and the biomass burning class. The urban class is based on the definition of urban aerosol from Hess et al. [1998, Tables 1c & 4] which is 8 % soot by mass with additional water soluble and insoluble components. The water soluble mode is sulphates and soluble organics, while the insoluble mode is soil and insoluble organics. Soot has been modelled as unphysically small spheres (which are about the size of soot spherules seen in fractal soot structures). As a result, the number concentration of soot aerosol is unfeasible large (82 %) and the class has an extremely low SSA.

Since the urban class has extremely unrealistic light scattering properties, it is almost never selected by the ORAC retrieval as the most likely aerosol type. Additionally, urban plumes are very localised and quickly disperse (and age) into something similar to the continental aerosol class [Thomas et al., 2011] which models water soluble and insoluble modes, but not soot.

The biomass burning aerosol class is based on AERONET retrievals of particulate emitted from the combustion of cerrado in Brazil by Dubovik et al. [2002, Table 1]. Time averaged lognormal volume distributions of fine and coarse mode particles were converted into a two mode lognormal number distribution assuming an optical depth of 1. The retrieved wavelength-independent refractive index of $1.52 + 0.015i$ is used. The particle shape is assumed spherical.

The biomass burning emissions can occur over very large areas and last for significant time peri-

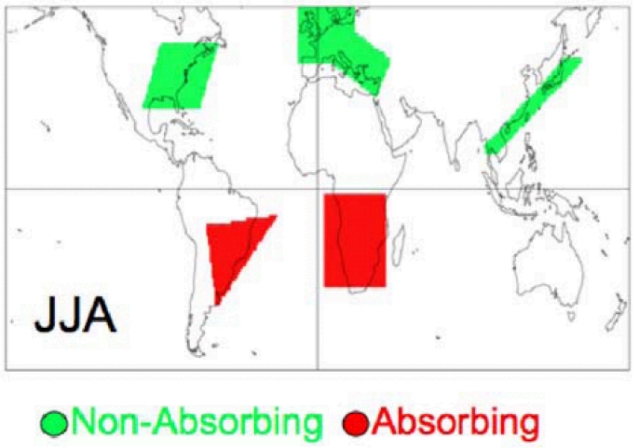

Figure 4.3: Regions where the MODIS operational aerosol retrieval over land assumes that aerosol is absorbing (red), non-absorbing (green), or moderately absorbing (everywhere else) during June, July, and August. Taken from Levy et al. [2007, Fig. 3], reproduced with permission.

ods, making them easier to spot from space. For this reason, biomass burning aerosol will receive more attention in the remainder of this chapter.

4.1.5 Other microphysical models used in satellite retrievals

MODIS

As described in §2.1.4, the MODIS retrieval over oceans models only marine aerosol and dust. Over land, the MODIS aerosol channel uses 3 channels, 0.47 μm, 0.66 μm, and 2.12 μm for its retrieval [Levy et al., 2007, 2009]. Smoke aerosol is split into non-absorbing, moderately absorbing and absorbing types and retrievals are carried out for the type best suited to the geography and season, the aerosol properties being inferred from cluster analysis of AERONET data by Omar et al. [2005]. The regional distinction is shown in Fig. 4.3.

The most absorbing model has refractive index of $1.51+0.02i$ which is very similar to the African biomass burning RI reported by Dubovik et al. [2002]. The two less absorbing models have almost identical RI values which match the hydrated water soluble mode given by Hess et al. [1998].

Each of the three burning models consists of a fine and coarse mode whose size is determined by

the aerosol optical depth. In a similar manner, the fine/coarse volume mixing ratios and imaginary part of aerosol RI is also a function of AOD for the two less absorbing aerosol types. All smoke aerosols are modelled as homogeneous spheres.

MISR

The MISR team have both soot and carbonaceous aerosol in their operational retrieval [Diner et al., 1999]. These modes contribute to the "polluted" aerosol classes, mixing in the same way as is described in §2.1.4. The soot mode is that given by Hess et al. [1998], also used in the ORAC urban class discussed in §4.1.4 .

The carbonaceous mode is defined as a lognormal mode with $r_m = 0.13$ μm; $\sigma = 1.8$; $m = 1.43 + 0.0035i$ at a fixed relative humidity of 97 %. The source of these values was not determined, but could well be the result of calculating the effect of hydrating other biomass burning aerosol data. As in the MODIS and ORAC retrievals, all smoke aerosols are modelled as homogeneous spheres.

MISR researchers have also investigated the sensitivity of their retrievals to varying the properties of their biomass aerosols and concluded that with significant particulate in the line of sight (AOD$\geq$0.5), the MISR instrument would be capable of recovering size and SSA information, provided that the surface reflectance could be well characterised [Chen et al., 2008]. Again, in this study, all aerosols were modelled as homogeneous spheres.

4.2 Fractal modelling of fresh soot

Following the method of Li et al. [2010], a lognormal mode of soot particles is created, but with fixed aerosol spherule size and larger particles created by the aggregation of smaller ones. Comparisons between this model and spherical soot modelling methods are presented.

4.2.1 Method

Fractal aggregate particles are to some extent scale invariant, although cannot have the true scale invariance of a mathematical fractal, which would have infinite extent. Particles are defined by the equation

$$N = k_f \left(\frac{R_g}{a} \right)^{D_f}, \tag{4.1}$$

where N is the number of spherules in the aggregate, a is the radius of an individual spherule in the fractal, D_f is the fractal dimension, k_f is the fractal prefactor, and R_g is the radius of gyration which gives the root-mean-square distance of spherules from the cluster's centre of mass [Sorensen, 2001].

The fractal dimension gives a measure of how "compact" an aggregate is, with lines of particles when $D_f \simeq 1$, "flat" surfaces when $D_f \simeq 2$, and lumpy spherical shapes as $D_f \to 3$ (although due to the individual spherules having non-negligible size, it is not possible to form shapes with no free space between constituent parts). This dependence of shape on D_f will be shown later in Fig. 4.5.

Microphysical properties

Measurements by Köylü and Faeth [1992] of soot from diffusion flames burning various liquid and gaseous fuels[2] found that primary particle radius and fractal dimension were fairly consistent, with $15 < a < 25$ nm, and $1.70 < D_f < 1.8$. However they later recommended that $D_f = 1.82$ should be used for fresh, "fuel-lean soot" [Köylü et al., 1995], just at the outside of the upper range of their previous measurements, but still within experimental error[3]. From theoretical simulations of aggregation, Sorensen and Roberts [1997] also recommended $D_f = 1.82$ along with a fractal prefactor value of $k_f = 1.19$. First Liu and Mishchenko [2005] and then Li et al. [2010] used these parameters when calculating the light scattering by fractal soot.

While Liu and Mishchenko [2005] only investigated mono-disperse numbers of spherules within aggregates (all particles had the same N), Li et al. [2010] used a lognormal distribution of N, centred

[2]Fuels tested were toluene, acetylene, benzene, propylene, ethylene, n-heptane, propane, and isopropanol.

[3]The reason given for the increase in D_f was explained by Köylü et al. [1995] as being due to a slight increase in D_f with increasing N, and a different method of analysis that gave stronger signals from the larger particles.

on $N = 200$ and $\sigma = 2.3$. Converting to a equivalent volume scale with equal distribution of mass, this corresponds to lognormal number distribution with median volume-equivalent radius $r_{m(V)} = 117$ nm and $\sigma_{(V)} = 1.32$, or (using equivalent surface area) $r_{m(SA)} = 283$ nm and $\sigma_{(SA)} = 1.52$, which are physically reasonable, fitting comfortably alongside measurements summarised by Bond et al. [2006, Table 3].

With the size distribution decided, all that remains is to select an appropriate refractive index. Here, we diverge from the previous studies, instead using the midpoint in the range of values recommended by Bond and Bergstrom [2006], $m = 1.85 + 0.71i$, as discussed in §4.1.3. This value was found by Stier et al. [2007] to improve agreement of the ECHAM aerosol-climate model with AERONET stations compared to a previous refractive index value of $m = 1.75 + 0.44i$, the value also used by [Li et al., 2010].

Fractal creation algorithm

Two methods of generating fractal clusters are outlined by Filippov et al. [2000]. Both rely on adding to an initial cluster in such a way as to maintain the fractal relationship given in (4.1) as N increases. The first method, which they name the sequential algorithm, adds additional spherules to the current cluster one-by-one requiring that the newly added particle is a distance X from the centre-of-mass of the current system, and touching (but not overlapping) with at least one particle currently in the cluster, where X is given by:

$$X^2 = \frac{N^2 a^2}{N-1}\left(\frac{N}{k_f}\right)^{2/D_f} - \frac{Na^2}{N-1} - Na^2\left(\frac{N-1}{k_f}\right)^{2/D_f}. \tag{4.2}$$

In (4.2), N is the number of particles in the new cluster. Any location which fulfils the above criteria is an appropriate place to attach the new spherule and the position is selected randomly.

The sequential algorithm has been shown to result in the creation of particles that do not have the correct two-point density-density correlation function as would be expected from calculations of the theoretical fractal properties [Meakin, 1991; Filippov et al., 2000]. Additionally, the appearance of

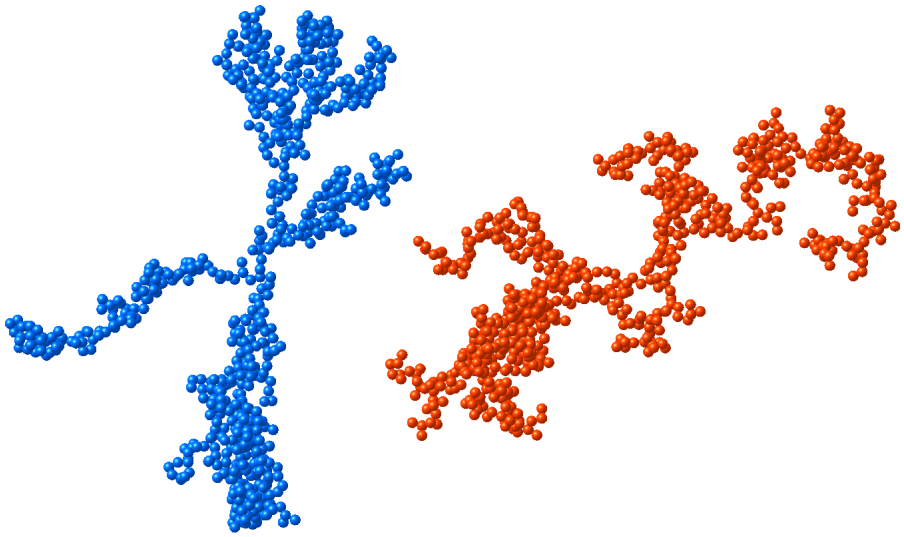

Figure 4.4: Comparing fractals generated using the sequential algorithm (left, blue) and the cluster-cluster algorithm (right, red). Both clusters have $N = 724$, $k_f = 1.3$, and $D_f = 1.8$.

these particles does not match those seen in TEM images, as they generally tend to branch out from a central point (see LHS of Fig. 4.4) .

The second method is an improvement on the sequential algorithm, which repeatedly combines smaller clusters to create the clusters of the required size [Thouy and Jullien, 1994]. This time, instead of defining the distance at which a new spherule should be added in order that (4.1) holds, the distance between the centre of masses of the two smaller clusters, Γ is used:

$$\Gamma^2 = \frac{N_1 + N_2}{N_1 N_2} \left[a^2 (N_1 + N_2) \left(\frac{N_1 + N_2}{k_f} \right)^{2/D_f} - N_1 R_{g,1}^2 - N_2 R_{g,2}^2 \right], \tag{4.3}$$

the subscripts 1 & 2 referring to the two combining aggregates. The very smallest clusters (of less than 7–10 primary spherules) are generated from the sequential algorithm. Clusters are combined by randomly orientating both, placing their centres of mass a distance Γ apart, and then moving one relative to the other until contact occurs (checking that no spherules are overlapping). In the case when we set $N_1 = N - 1$ and $N_2 = 1$, so that $R_{g,2} = a$, we find that substitution into (4.3) leads to $\Gamma = X$ (from 4.2) as would be expected. Comparisons of the cluster-cluster method and the sequential method are shown in Fig. 4.4. Particles created using the cluster-cluster algorithm with increasing

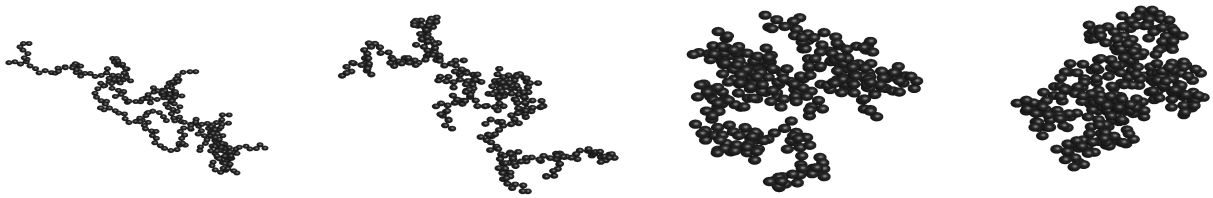

(a) $D_f = 1.5$ (b) $D_f = 1.75$ (c) $D_f = 2.0$ (d) $D_f = 2.25$

Figure 4.5: Fractal aggregates with $N = 300$, $k_f = 1.25$ and varying values of D_f. As the fractal dimension increases, we move from linear to bunched clusters. These aggregates were generated using the cluster-cluster algorithm.

D_f are shown in Fig. 4.5.

Light scattering method

The scattering of light by these fractal clusters can be calculated using the recently released **M**ultiple **S**pheres **T**-**M**atrix Fortran-90 code (MSTM) [Mackowski, 2011] which is based on the theory found in Mackowski and Mishchenko [1996]. This method combines the spherical wave expansions for each spherule (at that spherules origin) in the aggregate, and orientationally averages. The code is extremely robust and, due to very sensible memory allocation and parallelisation, capable of calculating the light scattering properties of large particles that were not previously feasible.

Choosing a specific set of fractal properties, averaged light scatter calculations for the AATSR wavelengths are shown in Fig. 4.6. Since each fractal generated will be different (even though their parameters are the same) it is necessary to take the average of several with identical properties in order to get representative characteristics. Comparisons with volume equivalent spheres show dramatic differences in light scattering properties, but this is not hugely surprising given how different they look. The spread of values in β^{ext}, β^{sca}, and $\bar{\omega}_0$ (not plotted) is extremely small, but can deviate greatly from the spherical volume equivalent case as N increases (generally, all three properties are greatly overestimated in the visible if this assumption is made). The more significant test comes when inspecting distributions of particles, where singular anomalies are smoothed over. For this, we

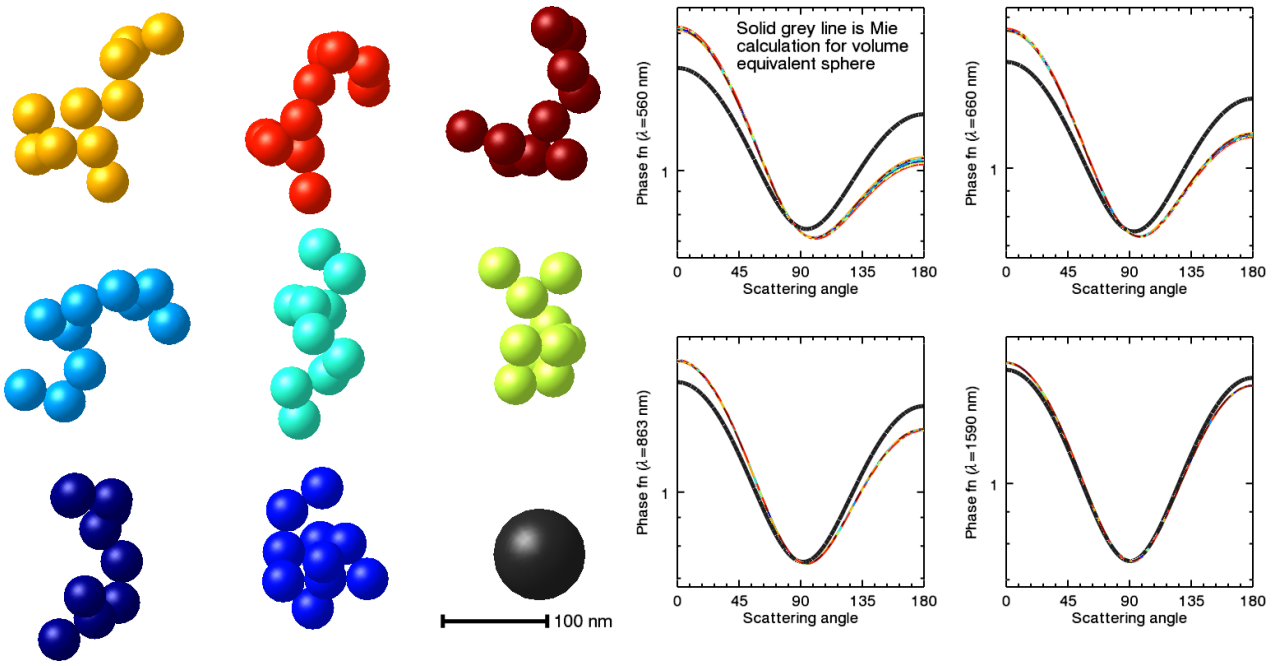

(a) $N = 10$, $r_g = 64.4$ nm.

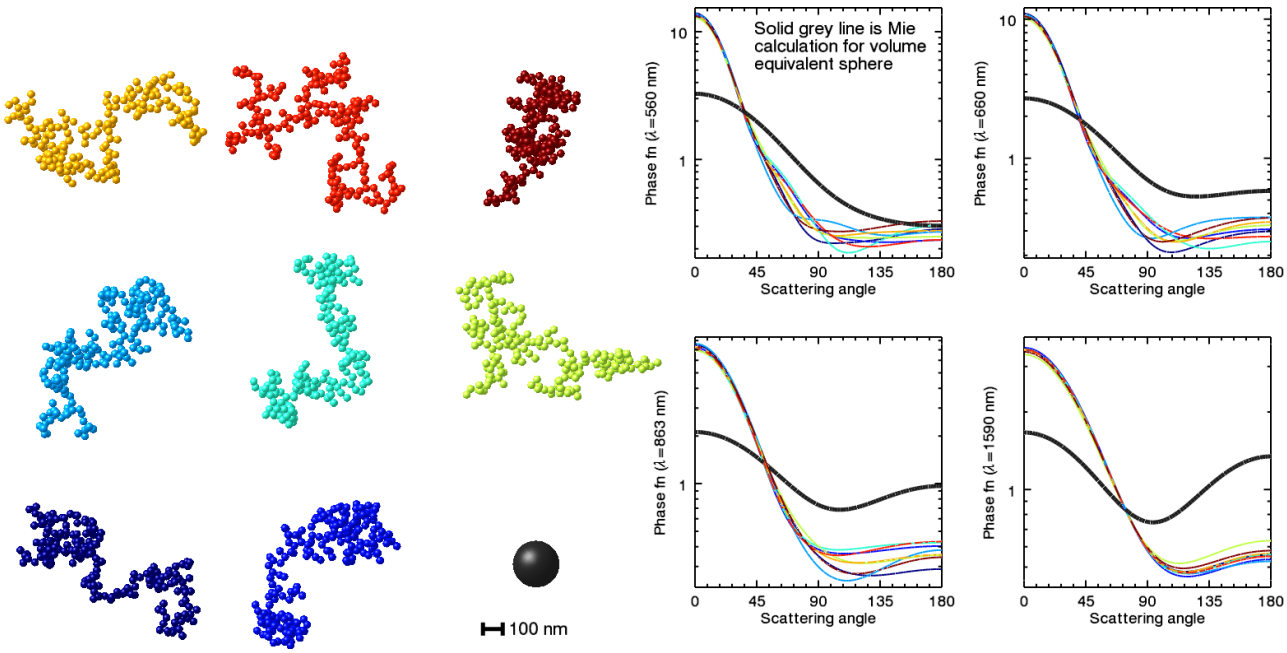

(b) $N = 200$, $r_g = 334$ nm.

Figure 4.6: The light scattering properties of single fractal aggregates. Spherule position was calculated using the cluster-cluster algorithm with $D_f = 1.19$, $k_f = 1.82$, $m = 1.85 + 0.71i$ and primary spherule radius, $a = 20$ nm. Phase functions were calculated using MSTM. The phase functions of a certain colour correspond to the aggregate with matching colour. Comparison with a volume equivalent single sphere (in black) are also shown. Note that in both (a) and (b), the primary spherules are the same size.

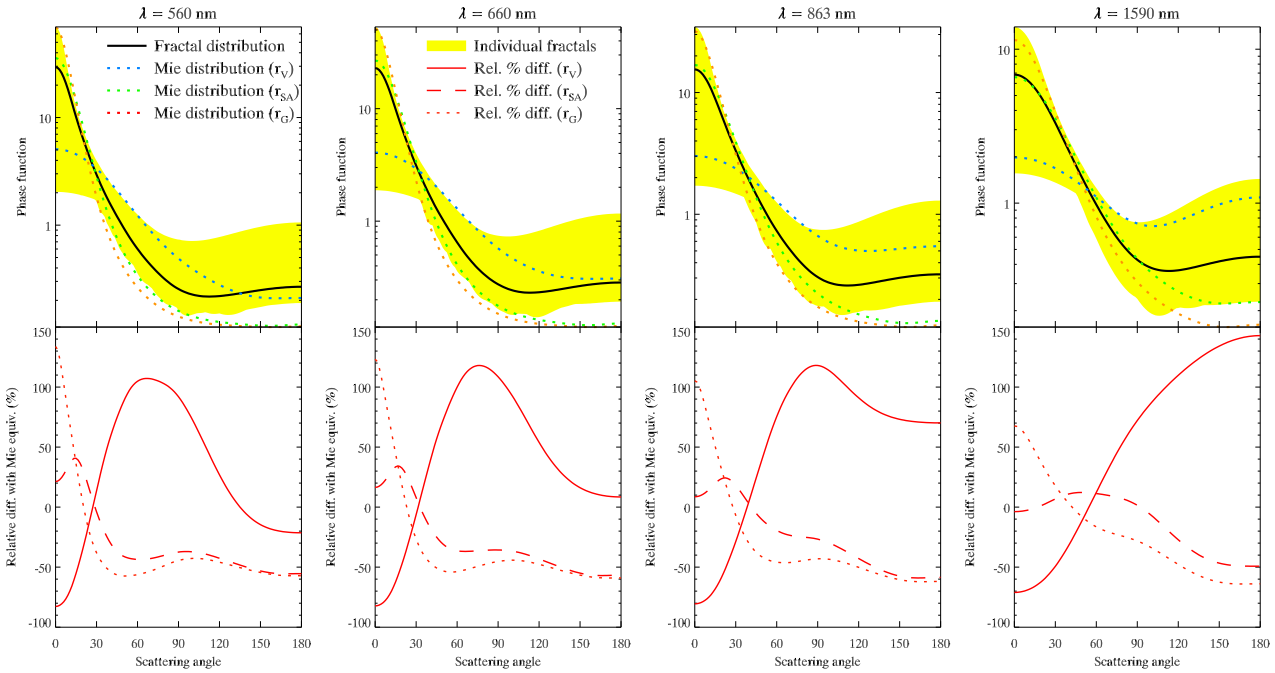

Figure 4.7: Comparing the phase functions of lognormal distributions of fractals to lognormal distributions of spherical scatterers with identical distributions by either volume, surface area, or radius of gyration. The envelope of all phase functions included in the calculation is shown in yellow.

build a distribution of fractal aggregates with the properties described above[4].

Fig. 4.6 reminds us that there is variation in scattering between fractals defined identically due to the randomness of the aggregation process. To take account of this, numerous fractals were generated, and averaged over when sampling in high probability areas of the probability distribution, $n(N)$. In the tail of the distribution ($N > 1000$; the largest 2.5 % of particles), calculation times for MSTM can be as great as 4 days per wavelength per particle, and to conserve resources, the distribution is sampled more sparsely, with one data point for every increase of 10 in N.

The phase functions of the distribution at AATSR wavelengths are shown in Fig, 4.7 along with lognormal distributions of spheres with equivalent volume, surface, and gyration-radius distributions for comparison. The 2nd and 4th panels (for $\lambda = 660$ nm; 1.59 μm, $m = 1.85 + 0.71i$) are very similar to Figures 4 & 5 in Li et al. [2010] (which are for $\lambda = 628$ nm; 1.10 μm, with $m_{628\,\mathrm{nm}} = 1.75 + 0.435i$;

[4]Lognormal distribution of N, $N_g = 200$, $\sigma_g = 2.3$, $D_f = 1.82$, $k_f = 1.19$, $a = 20$ nm, $m = 1.85 + 0.71i$ for all wavelengths.

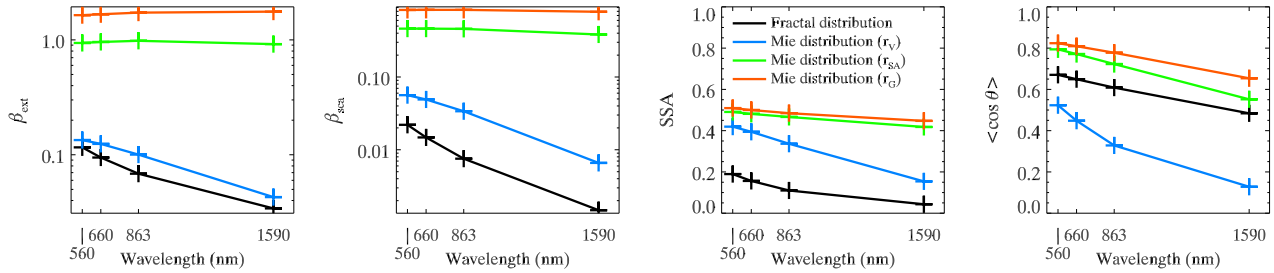

Figure 4.8: Comparing the β^{ext}, β^{sca}, $\bar{\omega}_0$, and $\langle\cos\theta\rangle$ from a lognormal distribution of fractals to lognormal distributions of spherical scatterers with identical distributions by either volume, surface area, or radius of gyration.

$m_{1.10\,\mu m} = 1.82 + 0.60i$, all other parameters identical), which is a reassurance that the calculations have been executed correctly.

Comparing three methods of approximating the fractal distribution to a spherical distribution (equal volume, equal surface area and equal radius of gyration), it appears from Fig. 4.7 that by far the best method of approximating these particles would be with an equal surface area spheres approach. However, looking at other light scattering parameters, namely β^{ext}, β^{sca}, and $\bar{\omega}_0$ from Fig. 4.8, we see that the net light absorption and scattering properties are best represented by the volume equivalent sphere approach. As one would expect based on discussion of the phase function, the fractal $\langle\cos\theta\rangle$ value is most similar to that of the equal surface area distribution. The next step is to replace the existing soot mode with the new fractal model in the urban aerosol class.

4.2.2 A new urban class

From §4.1.4, the current ORAC representation of urban aerosol has completely unrealistic representation of soot particles. In order to maintain the correct mass balance with such small particles, a huge number are required, and these make the urban aerosol extremely absorbing for small values of effective radius.

When replacing these tiny soot particles with the new, larger fractals, the mass ratio between the three modes should be maintained. While replacing the soot mode, it also felt appropriate to improve

		Old urban class				New urban class			
Class	M_i	$r_{m,i}$	σ_i	ρ	N_i	$r_{m,i}$	σ_i	ρ	N_i
Soot	0.079	11.8	2.00	1.00	0.823	117	1.32	1.8	0.0175
Water soluble	0.563	26.2	2.24	1.42	0.177	—— same ——			0.9824
Insoluble	0.358	471.0	2.51	2.00	9.5×10^{-4}	—— same ——			5.3×10^{-5}

Table 4.2: Showing the change in urban aerosol modelling undertaken. M_i and N_i are the mass and number mixing ratios respectively. r_m is lognormal median radius in nm, σ_i is the spread of the lognormal distribution. The density, ρ_i is in g cm^{-3}. Values given in the "Old urban class" section of the table are from Hess et al. [1998].

its density (changing from 1 g cm^{-3} to 1.8 g cm^{-3}) and refractive index (to $m = 1.85 + 0.71i$), both on the advice of Bond and Bergstrom [2006]. The increased density of soot meant that less of it would be needed, even if its median radius and spread had stayed the same. The new number mixing ratios are given in Table 4.2. Rather alarmingly, when soot is modelled with a more physically reasonable size and density, its number mixing ratio drops from 82 % to 2 % of the classes aerosol.

The mass of soot given by Hess et al. [1998] for the "average continental", "polluted continental", and "urban aerosol" is 0.5, 2.1, and 7.8 μg m^{-3} respectively. This agrees well with field measurements which generally range from 0.5 μg m^{-3} for background pollution, to ~ 10 μg m^{-3} for highly polluted urban sources [e.g. Allen et al., 1999; Chen et al., 2001; Alfaro et al., 2003; Latha and Badarinath, 2005; Crosier et al., 2007]. Hence, with more accurate size distribution information (that is very different from the previous assumptions), a more realistic BC density, and plausible values of BC mass loading and total mass loading, the number mixing ratio for soot is very likely to have improved. Unfortunately, since number mixing ratios are generally not reported (mass mixing being of more interest), it is not possible to directly verify that 2 % is a more reasonable value.

As detailed in §1.6.3, the standard ORAC method of obtaining an aerosol distribution with a specific r_{eff} value is to alter the mixing ratios as far as possible. Fig. 4.9 shows how this method works for the old and new urban classes. In the new urban class, because the water soluble mode is no longer larger than the soot mode, it replaces soot as the only aerosol present for small effective radii ($r_{\text{eff}} < 0.18$ μm). There is no mixing at all below these values.

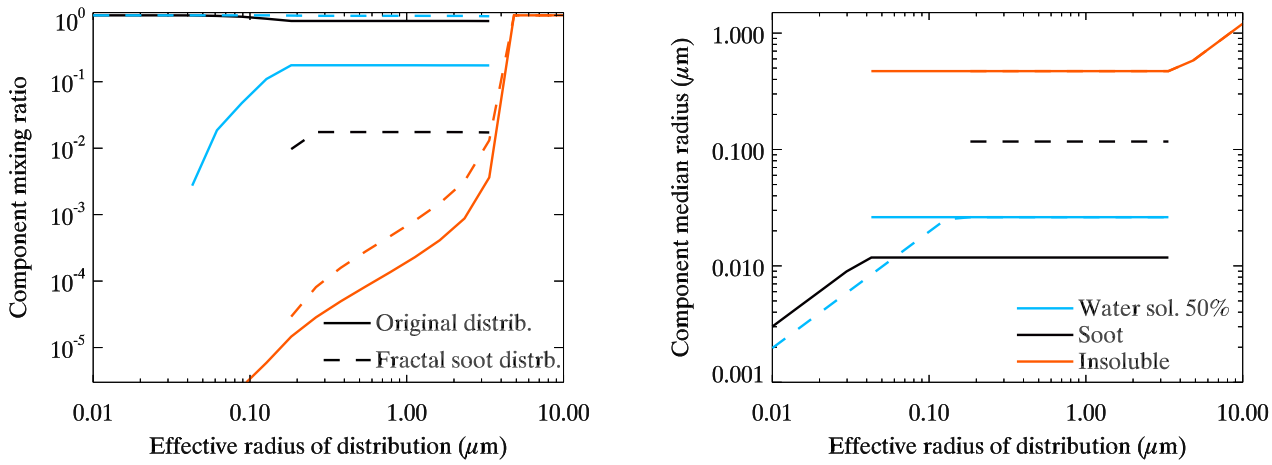

Figure 4.9: Mixing ratios and median radii values for the old and new urban aerosol class aerosol modes. The original distributions are presented with solid lines, and the new urban class, with a fractal soot mode is dashed. Notice that since the smallest particles in the distribution are no longer soot, in order to get the smallest values of r_{eff}, we must turn off the soot mode instead of the water soluble mode.

Dubovik et al. [2002] tabulated properties of urban aerosols obtained from AERONET retrievals located in Maryland, USA, Paris, Mexico City, and the Maldives. Converting their retrieved size distribution at mean optical thickness (distributions were fitted to a linear parameterisation as a function of AOD) to an effective radius gives $r_{\text{eff}} \sim 0.20\ \mu$m. At the nearest ORAC lookup table point ($r_{\text{eff}} = 0.18$), Table 4.3 compares $\bar{\omega}_0$ and $\langle \cos\theta \rangle$ with measured AERONET values.

	$\bar{\omega}_0$		$\langle \cos\theta \rangle$	
λ	660	870	660	870
Old	0.74	0.70	0.65	0.64
New	0.84	0.79	0.66	0.64
AERONET	0.92	0.90	0.62	0.59

Table 4.3: Comparing AERONET and ORAC light scattering properties for urban aerosol.

While these properties are not a stunning endorsement that the new model better represents urban aerosol, at least the values are heading in the right direction (although the class still seems to be far too absorbing). Of more concern is that with an r_{eff} value so close to the cutoff point below which no

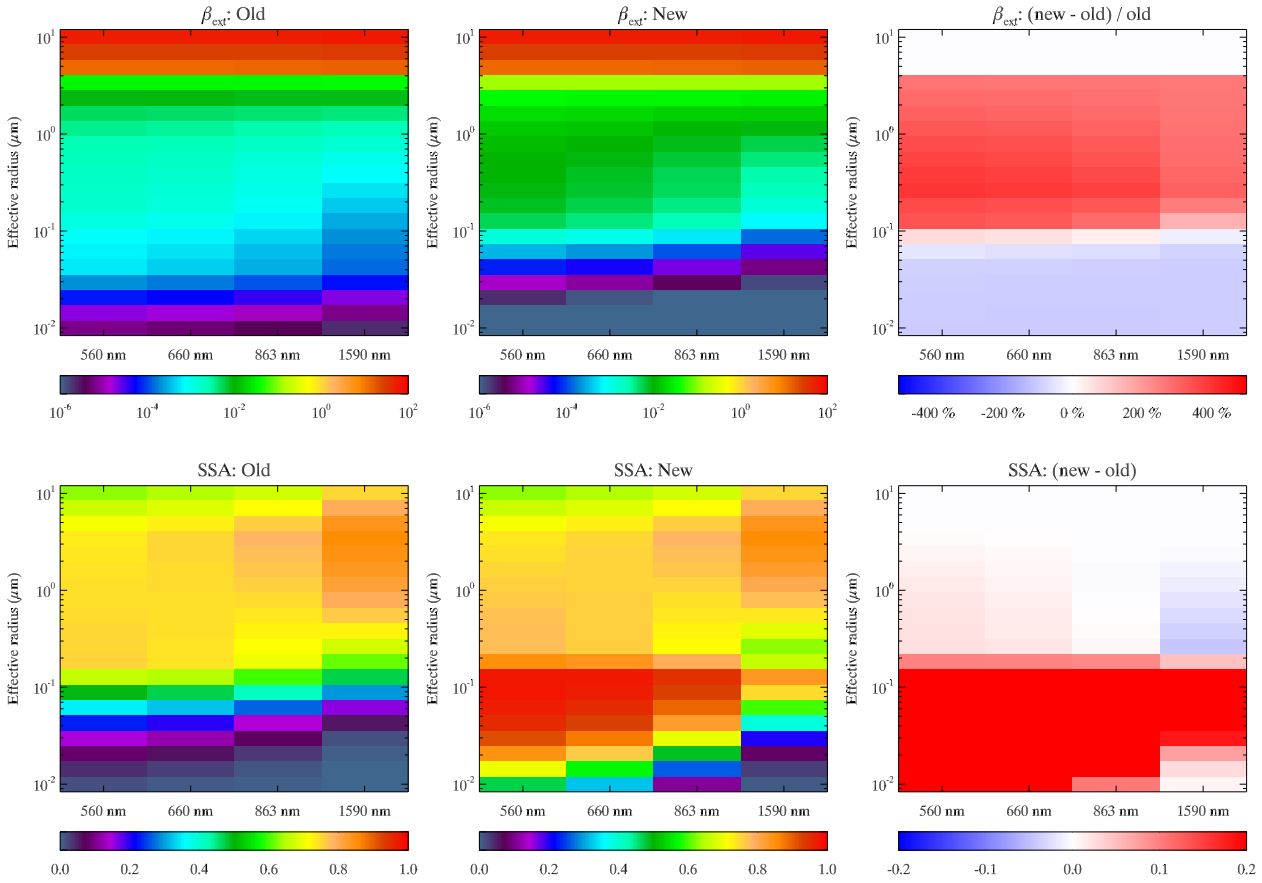

Figure 4.10: Comparing optical properties of the old and new urban aerosol class. The top three plots are for β^{ext}, the bottom three for $\bar{\omega}_0$. The new class has replaced the tiny soot particles previously used with aggregated fractal soot particles which are much larger. In the top three effective radius bins, the distributions are identical, and consist only of the water insoluble class.

soot appears in the mixing, the mixing assumptions, which generally work well for ORAC classes may not be appropriate here.

Fig. 4.10 compares the extinction and single scatter albedo of the new and old description of urban aerosol. The main area of difference is at low values of r_{eff} where the two small modes have been switched round, leading to unreasonably low $\bar{\omega}_0$ (~ 0) in the old model. For the new model, due to the sudden addition of absorbing material as r_{eff} increases, the rapidly increasing $\bar{\omega}_0$ is suddenly curtailed as r_{eff} passes $r_{\text{eff, waso}}$. There is also much more extinction at smaller sizes in the old model. Since extinction is expected to increase with the cross section of the scattering particles, such dramatic

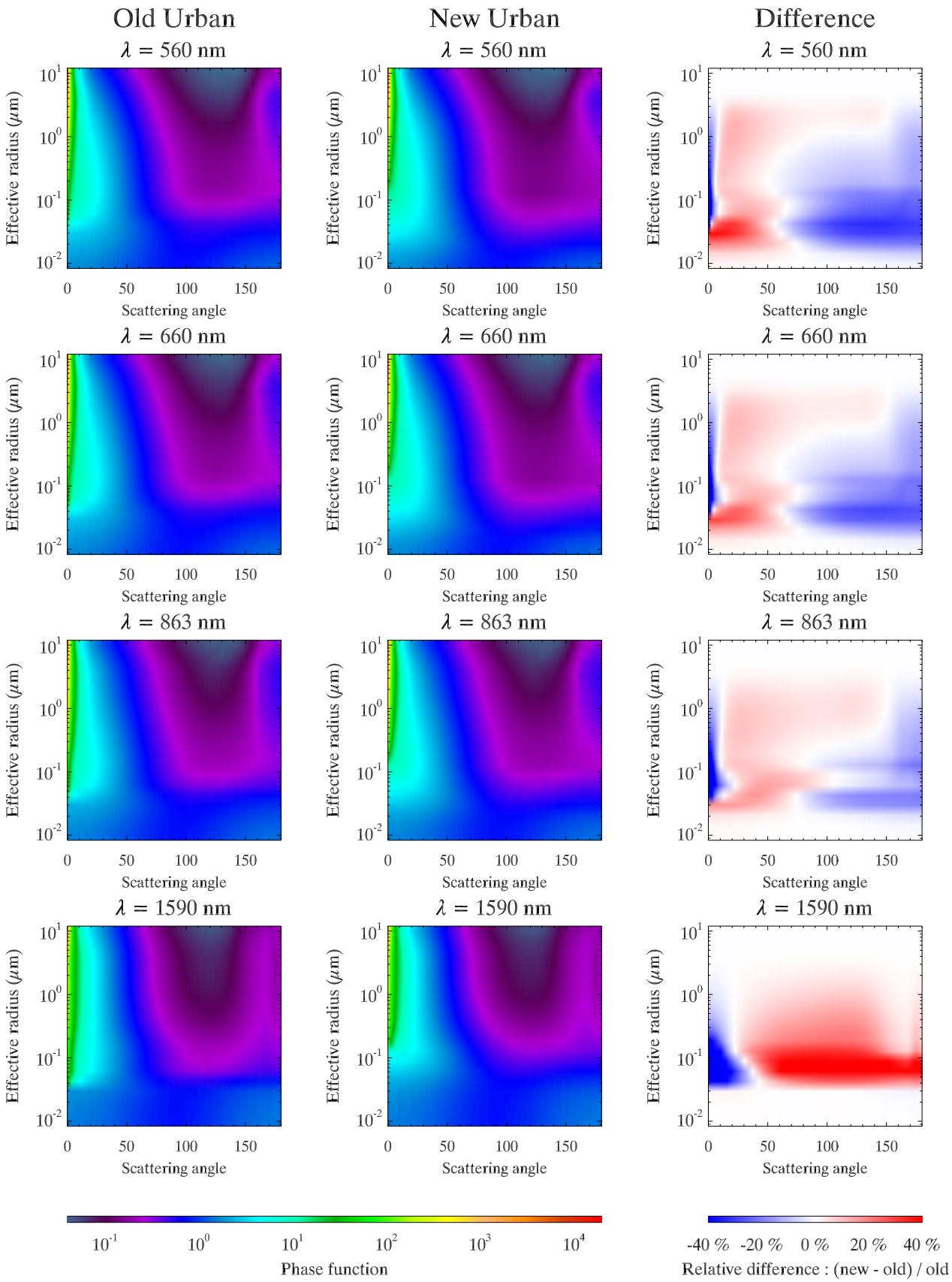

Figure 4.11: Comparing the phase functions of the old and new urban aerosol classes as a function of the class effective radius, r_{eff}.

removal of light at small sizes is extremely unconvincing.

Fig. 4.11 compares the phase function for the four AATSR channels used by the ORAC retrieval. The new model appears to be less strongly peaked in the forward scatter direction, and for $\theta > 90^{\circ}$, visible channels appear to have flatter phase functions but other than this, are not dramatically different. This new urban model was used in retrieval runs which will be discussed in §4.4.

4.3 Modelling biomass burning by age instead of size

Approximately 88 % of carbonaceous aerosol mass originates from biomass combustion [Chakrabarty et al., 2010], so obtaining a good representation of this class is certainly desirable. In the description of biomass burning (§4.1), it is noted that the size range of observed biomass distributions varies very little; certainly not over three orders of magnitude. Additionally, as the smoke plumes age, their microphysical parameters can vary dramatically. As such, it was proposed to construct an aerosol biomass burning class where the second state vector was not effective radius, but some proxy for the age of the aerosol.

Due to the abstraction of the ORAC code, simply defining this new parameter in the state vector element previously occupied by the effective radius state, mapping look up table values of age proxy onto the lookup table values of r_{eff}, and changing the *a priori* assumptions about [r_{eff} / age] should suffice to run the retrieval.

The model of ageing is based roughly on Pósfai et al. [2004], which shows the various components of biomass burning smoke when fresh, aged, and after evolution into a regional haze. The following section explains assumptions made in designing an ageing biomass burning class.

4.3.1 An idealised ageing process

Soot (black carbon), organics, and sulphates are the three main components of the class. The mixture of the various species is defined for fresh smoke, aged smoke, and the regional haze. Moving between these states is done by interpolating between the mixing ratios to some intermediate point. Exact

definitions of the mixing values, and mode properties are given in Table 4.4 and the principle behind these decisions is described in the remainder of this section.

The OC modes are all modelled as homogeneous spheres. The main constituent of the smoke is the OC aerosol which forms from nucleation and grows as time progresses, also becoming more sulphate heavy. The regional haze is the end result of the ageing of biomass burning aerosol, consisting of sulphates and OC. Tar Balls are not numerous at emission, but form downwind, before being broken down by atmospheric processing. Since tar balls are hydrophobic, they do not increase with size as they age, but at some point will cease to exist in the model, where it is assumed they have be coagulated with the aqueous regional haze.

To model the increased size of OC aerosol with age, along with the change in chemical composition, two modes are defined: an OC mode, and a regional haze mode. Increases in size and sulphate content are represented by increasing the mixing of the latter relative to the former. Both the OC and the haze have fine and coarse modes. Aged BC and tar balls are also assumed to have been swallowed up by the haze.

When the smoke is first emitted, we assume it is fractal aggregates of BC, and OC. The aggregates will have the properties of the fractal soot lognormal mode described in §4.2. Rapidly following emission, the soot ages by curling up and becoming coated with organics and sulphates [Jacobson, 2000; Abel et al., 2003]. The final, aged soot is modelled as concentric spheres of BC coated with OC. The mass distribution of soot does not change from fresh to aged BC, but due to the "curling" of the fractals, it will have a smaller radius. Due to the computational overhead for generating additional fractal distributions[5] with increasing D_f, and because these particles would have extremely short lifetimes, it was decided not to model the intermediate stages between fresh and aged BC aerosol. The ageing of the soot would be represented by the changing relative mixing ratios of these two types of BC. As the smoke evolves to a regional haze, most of the BC has either fallen out, or become completely broken down and dissolved, making it an another addition to the general regional haze.

[5]The current mode took nearly two years of processor time to generate.

Mode	Description	Microphysical properties			Mixing ratio (%)		
		r_m (μm)	S	$m_{550\,\mathrm{nm}}$	Fresh	Aged	Haze
Fresh BC	Fractal aggregates following Li et al. [2010], $D_f = 1.82$, $k_f = 1.19$, $a = 20$ nm	0.117[a]	1.32[a]	1.85+0.71i	25	5	0
Aged BC	Concentric spheres: BC coated with OC & sulphate	0.117[b]	1.32[b]	1.85+0.71i [b] 1.63+0.021i [c]	0	5	5
		[Fn of r_{core}][c,d]					
Tar Balls	Hydrophobic, homogeneous spheres	0.080	1.6	1.67+0.27i	5	15	0
OC	Hydrophilic, homogeneous spheres. Coarse and fine modes.	0.100[e] 0.580[f]	1.6[e] 2.203[f]	1.63+0.021i	70	75	30
Haze	Ammonium sulphate and OC. Homogeneous, internally mixed spheres	0.180[e] 0.700[f]	1.6[e] 2.203[f]	1.437+0.003i	0	0	65

[a] Calculations for volume equivalent sphere. [b] Core properties. [c] Coating properties.
[d] See eqn (4.4) for description of coating distribution. [e] Fine mode. [f] Coarse mode.

Table 4.4: An idealised description of biomass aerosol ageing.

Mode	Description / size distrb	Refractive index
Fresh BC	Li et al. [2010]	Bond and Bergstrom [2006]
Aged BC	Jacobson et al. [1994]; Abel et al. [2003]; Bond et al. [2006]; Li et al. [2010]	As BC and OC.
Tar Balls	Pósfai et al. [2003, 2004]; Reid et al. [2005]	Alexander et al. [2008]
OC	Reid et al. [2005]	Highwood [2009]
Haze	Pósfai et al. [1999]; Haywood et al. [2003]	Hess et al. [1998]

Table 4.5: Primary references used in describing the ageing biomass burning aerosol.

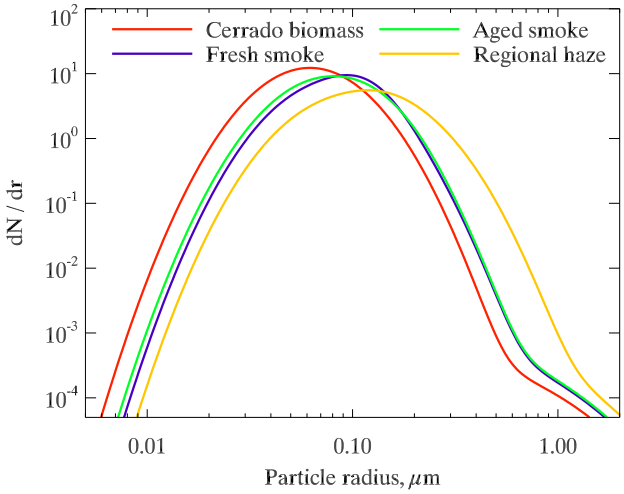

Figure 4.12: Comparing the overall size distribution of various biomass aerosol models. The red distribution is that used in the current ORAC biomass burning model, and is taken from Dubovik et al. [2002, Table 1] (during ORAC retrievals, this size distribution can change as the mixing ration between fine and coarse modes is varied). Ageing from fresh smoke to a regional haze, the effective radius of the distribution increases, additionally, note that more smaller particles appear in the aged smoke as fractal soot from the fresh smoke curls up.

In the aged BC mode, coating radius is defined as a ratio of the core radius. It was decided that this ratio, $t = r_{\text{coat}}/r_{\text{core}}$, should be a normal distribution of plausible thicknesses:

$$p(t) = \frac{1}{\sqrt{2\pi}\,\sigma_t} \exp\left[-\frac{1}{2}\left(\frac{t-t_0}{\sigma_t}\right)^2\right], \tag{4.4}$$

with $t_0 = 1.3$, and $\sigma_t = 0.1$, and cutoff so that $1 < t \leq 1.6$. The values were chosen based on Bond et al. [2006] who stated that particles with $r_{\text{core}} < 1.6\, r_{\text{coat}}$ represent those that had formed "growing by condensation".

Mixing fractions between the various modes for fresh smoke, aged smoke and regional haze were based on those given by Pósfai et al. [2003] whose data was from southern Africa. They found "young smoke" was majority organic aerosols with small quantities (< 35 %) of tar balls and soot. "Aged smoke" had more tar balls, and the regional haze consisted mainly of sulphate and organics mixed with sulphate. Small amounts of soot and tar balls were sometimes present, often mixed with sulphate.

The net aerosol size distributions are shown in Fig. 4.12 and compared to the biomass distribution from Dubovik et al. [2002] on which the current biomass aerosol class is based. The overall increase in size as the aerosol ages can be seen (blue $\rightarrow$ green $\rightarrow$ yellow), as can the slight increase in the number of smaller aerosols in the "aged smoke" (green) as the soot fractals are modelled as coated

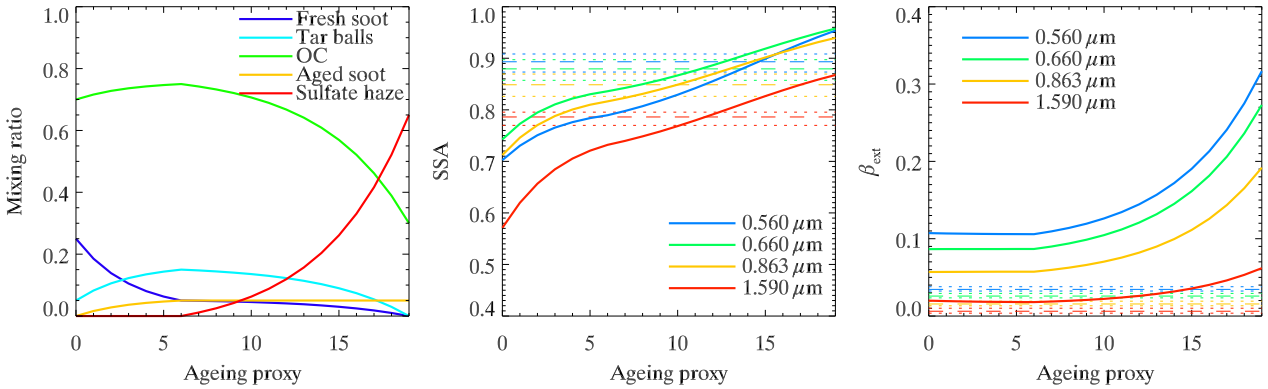

Figure 4.13: Showing the mixing ratios for the various components in the new aerosol biomass burning model. Where in previous models, the x-axis in such plots would be r_{eff}, now we have an arbitrary proxy for age. The single scatter albedo and extinction are also shown for the AATSR wavelengths. Dashed lines indicate the optical properties of the current ORAC biomass model with $0.18 < r_{\text{eff}} < 0.38$ μm.

spheres and assumed to have curled up. The first panel in Fig. 4.13 shows the interpolated ageing process described in Table 4.4.

4.3.2 A comparison of optical properties

The second and third panels in Fig. 4.13 show $\bar{\omega}_0$ and β^{ext} for the new biomass distribution. Overlaid is the spread of these values for the old biomass class, over the range of equivalent r_{eff} possible using the new class ($0.24 < r_{\text{eff}} < 0.36$ μm).

The old class has less extinction, and a comparable value of $\bar{\omega}_0$ to aged biomass. Apart from variations in the size distribution, one of the main differences between the two classes are refractive indices. The old class had a fixed RI value of $m = 1.52 + 0.015i$ for all wavelengths, and for all sizes. In the new model, only the haze component has smaller absorbing part than this, which could explain why, as the haze comes to dominate the mixing, $\bar{\omega}_0$ becomes higher than the old class. Just as the increase in $\bar{\omega}_0$ with age can be explained by a decreasing absorbing component, the increase in β^{ext} with age can be explained by the larger particles present which will increase the cross-sections of the distribution.

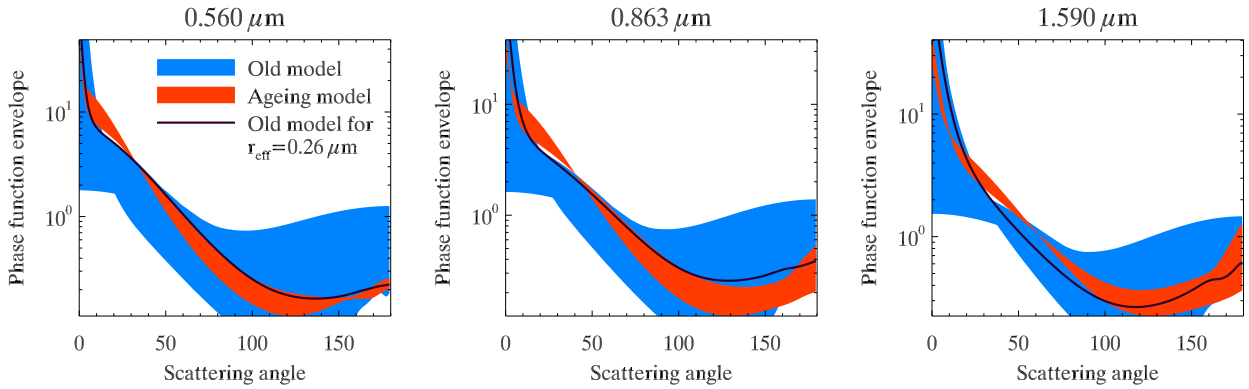

Figure 4.14: Showing envelope of possible phase functions for the old and new biomass burning classes at AATSR wavelengths. The old class has far more variation, as the effective radius varies over 3 orders of magnitude. The plot from the 0.66 μm channel has been omitted as it is very similar to the 0.56 μm channel.

The envelope of possible phase functions for the old biomass model (as r_{eff} varies) is compared to that of the new biomass model (as the aerosol age varies) in Fig. 4.14. Since the shape and composition of the particles are of secondary importance compared to the aerosol size, it is to be expected that the phase function is much more tightly constrained in the new model, where r_{eff} does not vary dramatically. For the old case with a similar r_{eff} to our new model, the phase functions are similar.

Fig. 4.15 shows the ageing phase function in the new biomass burning aerosol. With increased age, a greater proportion of light is scattered in the forward direction, with the phase function less smooth in the backwards directions ($\theta > 90^{\circ}$).

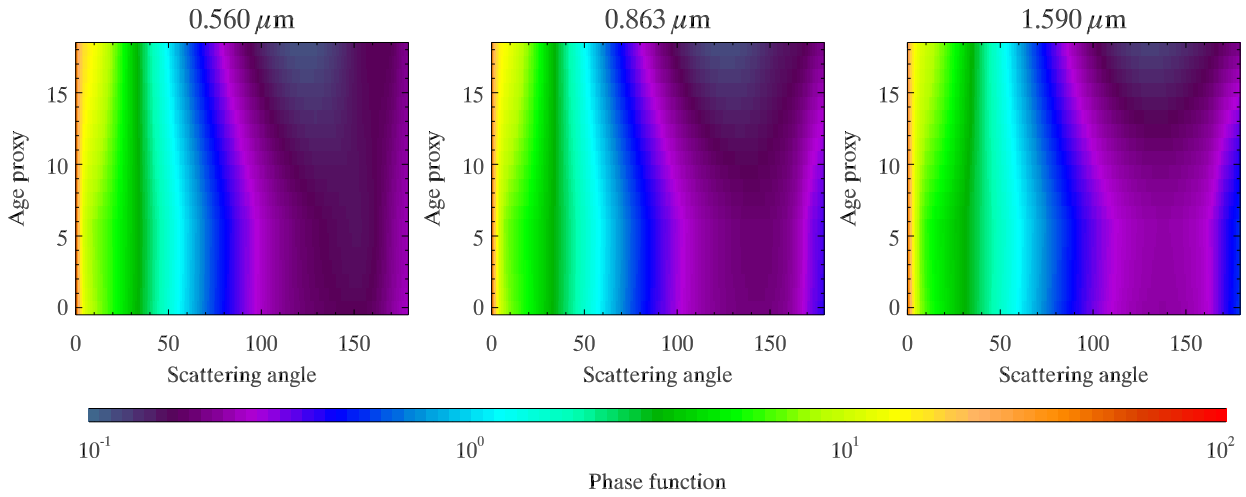

Figure 4.15: Showing the effect of ageing of biomass burning on its phase function. Data from the 0.66 μm channel has been omitted due to its similarity to the 0.56 μm channel.

4.4 Retrievals

To test new aerosol models, a month of AATSR ORAC retrievals were carried out, including the new urban and biomass classes. September 2008 was selected as a preferable month, due to high biomass burning emissions in southern Africa and South America at this time of year [Duncan et al., 2003, Fig. 6] (although far less carbonaceous emissions from China and India, where peak emissions are in March).

The retrievals were carried out between 30° S and 30° N, with analysis of urban retrievals limited to areas of high population within these bounds. Analysis of biomass burning was limited to a smaller area including only southern Africa and South America, as well as the ocean regions to the west of these land masses (30° S, 100° W) to (0° N, 51° E). These regions are shown in Fig. 4.16, a false colour average of the months retrievals. The smaller marked region is the area in which biomass burning was assumed to be the dominant absorbing aerosol.

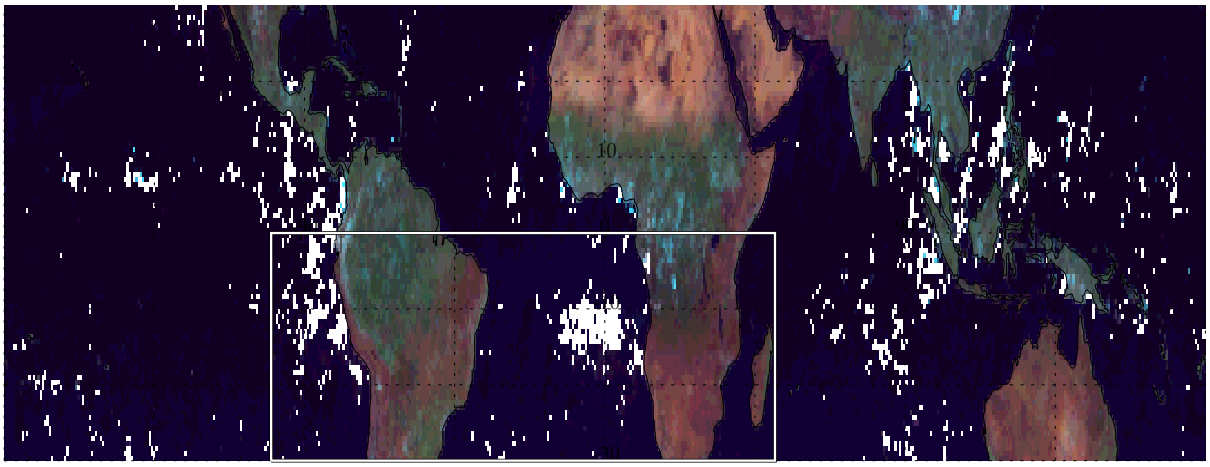

Figure 4.16: False colour image obtained from averaged AATSR forward view radiances for September 2008. The area for interest in biomass burning studies is marked by the box, while analysis of urban locations took place for the entire area shown. The red channel is represented by $\lambda = 1.59$ μm, green by $\lambda = 863$ nm, and blue by $\lambda = 560$ nm. White regions are areas where no retrievals were possible for the entire month, due to cloud contamination.

4.4.1 Urban class

Urban aerosol has never been effectively retrieved in previous versions of ORAC due to the incorrect size distribution, and microphysical properties described previously in §4.2.2. In order to analyse the differences to the retrieval caused by replacing the old urban class, retrieved pixels were only included if they were over an urban extent (defined as settlements of > 5000) obtained from the Global Rural-Urban Mapping Project (GRUMP) [SEDAC, 2005].

Fig. 4.17 shows histograms of the overall retrieval cost, and residuals for individual channels. As well as the urban aerosol models, the "continental" aerosol class has also been included in the comparison, since it is the background aerosol model over land. From the first glance, it is clear that the new urban class has better retrieval statistics than the previous urban class. While the old urban class has a skewed distribution of residuals in the shortest wavelength channels, indicating a systematic bias, the new urban class has on average, lower costs, and residuals in all channels which centre on minimal absolute residual, with little skew. That the residuals at 560 nm are so much more

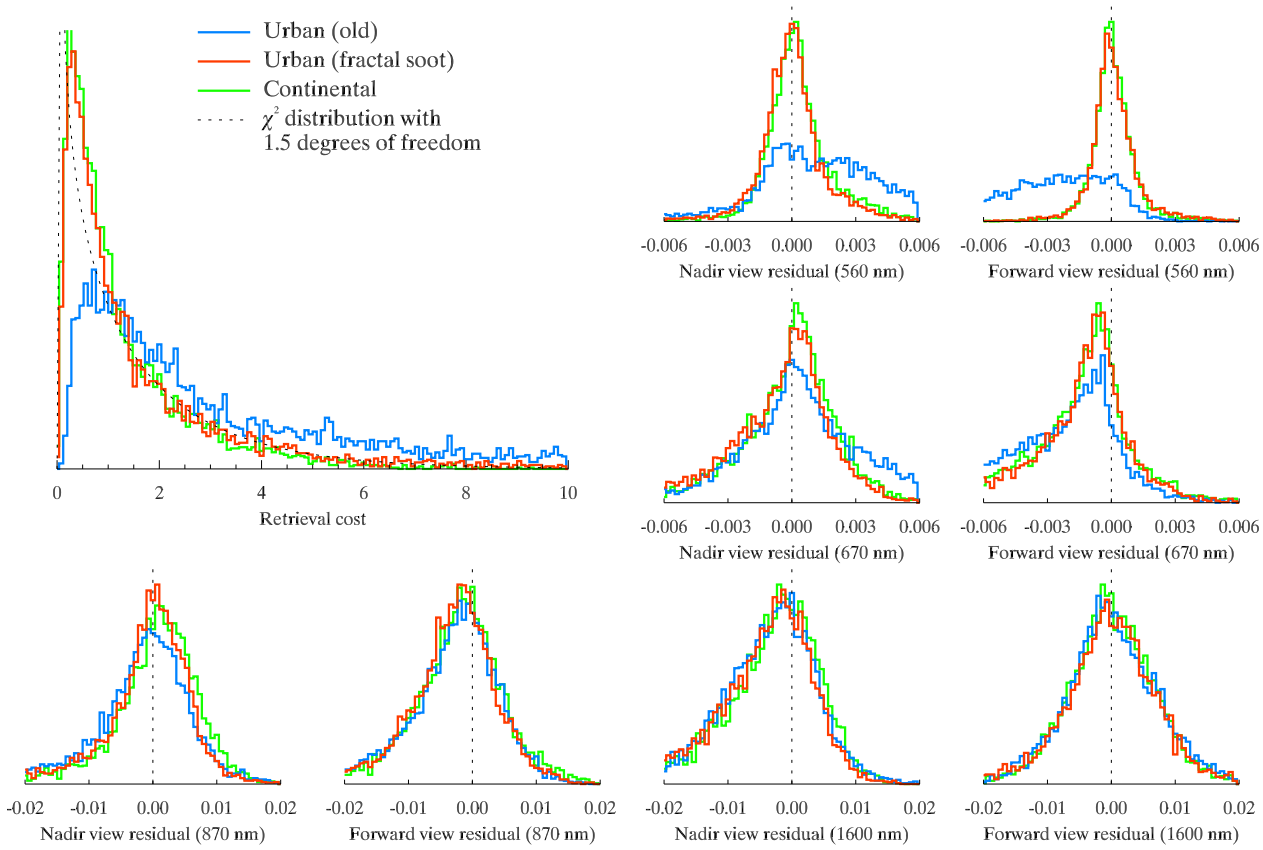

Figure 4.17: Comparing retrieval outputs for the old urban (blue), new urban (red), and continental (green) aerosol classes. Since we are interested in the urban class, comparisons have been limited to cases over urban extents (as defined by SEDAC [2005]), and where $AOD_{550\,nm} > 0.05$. The region tested is between 30°N and 30°S.

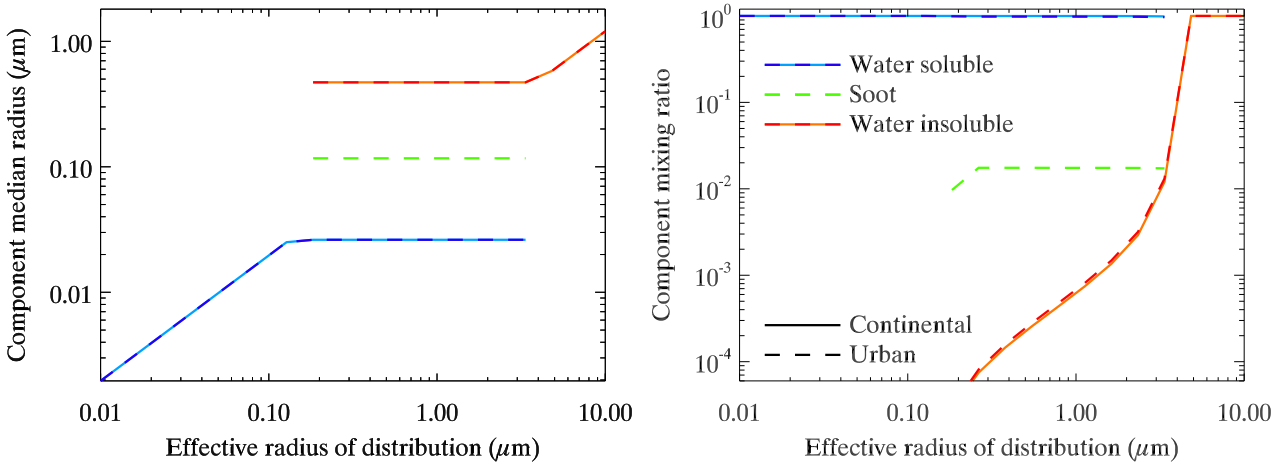

Figure 4.18: Comparing the size distributions of the (new) urban and continental aerosol classes (dashed, and solid lines respectively). The two classes are almost identical, the only difference being the inclusion of a soot mode in the urban mixture. For $r_{\text{eff}} < 0.13$ μm and $r_{\text{eff}} > 4.8$ μm, the two mixtures are identical.

distorted than other channels can be attributed to the huge number of unphysically small particles which would constrain the ability to fit the viewed light scattering at this wavelength.

Unfortunately, comparing the new urban class with the continental class, we see almost identical statistics suggesting little to distinguish between the two modes. This is not particularly strange, since the urban mode, (as described by Hess et al. [1998], on which this work is based) is a polluted version of the continental mode, which has identical relative quantities of water soluble (representing sulphates) and water insoluble (representing soil and insoluble organics) aerosol modes, but an added soot mode. Fig. 4.18 shows these two modes.

Comparing the overall differences in cost, AOD_{550}, and r_{eff}, Fig. 4.19 shows that while the most likely outcome of a retrieval over an urban area is identical costs, the cost of a continental retrieval is generally slightly lower. AOD_{550} is also slightly less for continental aerosol, which is less absorbing. Differences in r_{eff} are peaked about the difference in *a priori* r_{eff}, suggesting that there is very little sensitivity in either continental or urban classes to the size distribution over urban areas. Since urban aerosol is generally considered very fine, this is not unexpected.

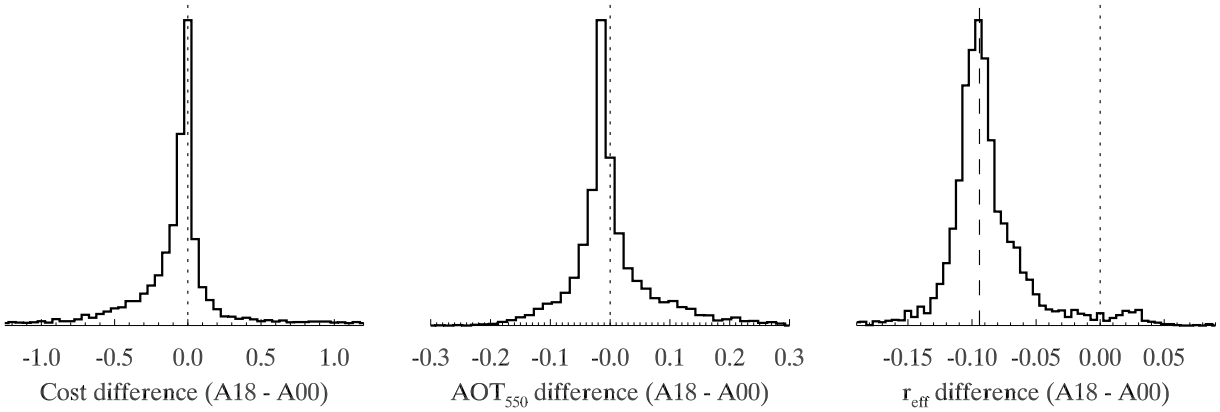

Figure 4.19: Comparing the differences in retrieved values of cost, AOD_{550}, and r_{eff} between new urban, and the continental aerosol classes. Dotted lines indicate no difference, while the dashed line in the final histogram indicates the difference between the *a priori* values of r_{eff} for the two classes.

Comparison with AERONET retrievals

As in previous chapters, comparisons with AERONET retrieved aerosol optical depth were carried out. Stations that were located within urban extents were selected, excluding those in Saharan Africa which were assumed mainly to see dust. Comparisons were made when a satellite overpass made a measurement within 30 km of an AERONET station, and that this AERONET station made a measurement within 30 minutes either side of the overpass. If more than one measurement fulfilled this criteria, averages of the measurements were made.

The old and new urban, and continental classes were compared. Over the course of September 2008, there were 18 available measurements from 10 individual stations that where all of the above conditions were true, and these are shown in Fig. 4.20. There was not sufficient data to obtain meaningful linear lines of best fit, so these have not been plotted. AERONET level 2.0 AOD_{500} and AOD_{870} was compared to ORAC AOD_{560} and AOD_{870}.

All three compared classes perform poorly in the comparison. However, there are so few co-located measurements that no real conclusions can be drawn from this. Since the AERONET measurements are looking up, while satellite measurements are looking down (at surfaces that can have wildly varying reflectances), the AERONET measurements generally have less uncertainty over land.

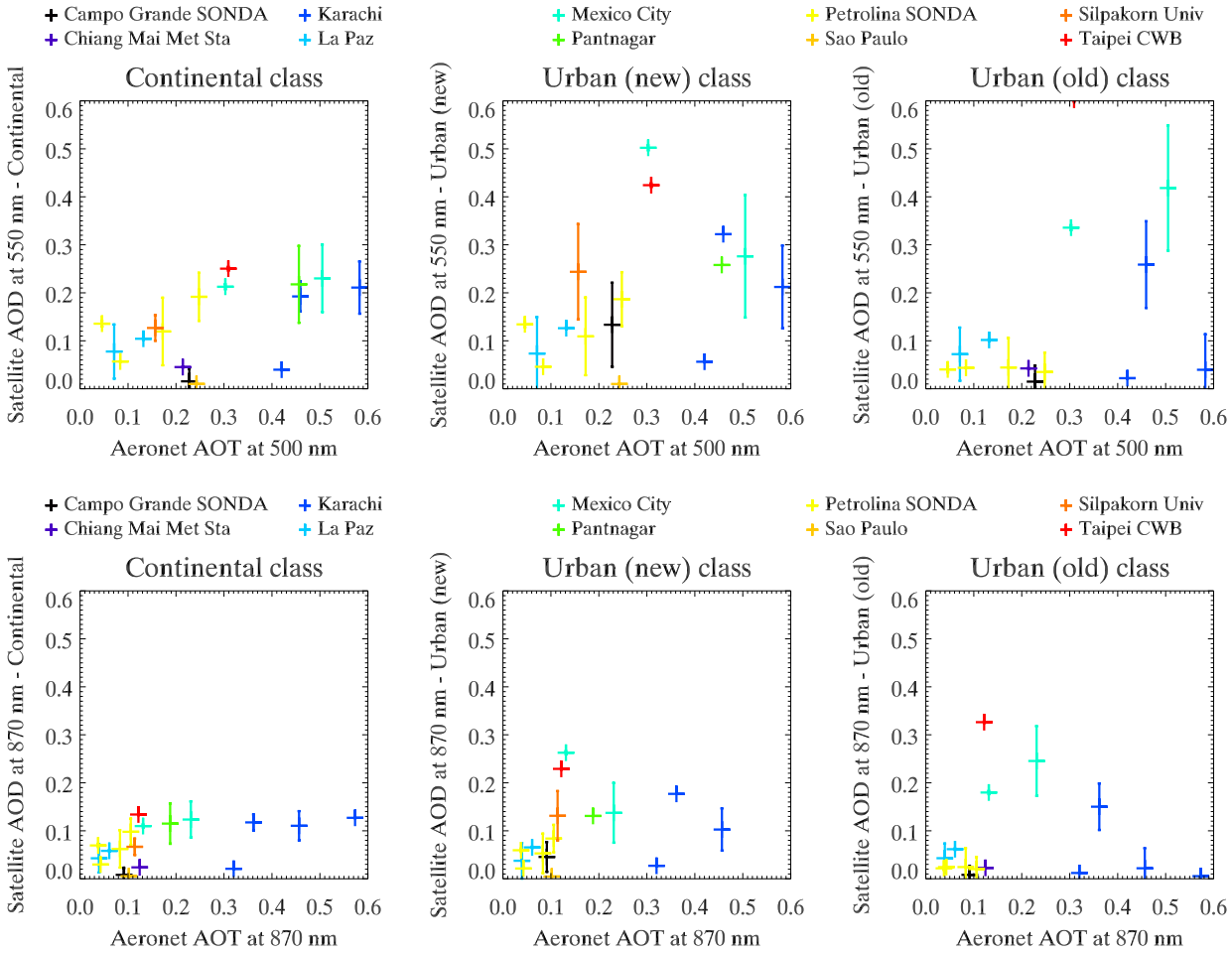

Figure 4.20: Comparing the continental, and urban aerosol classes from the ORAC retrieval to concurrent AERONET retrievals. All measurements are over urban extents, within 30 minutes of each other. Lines of linear best fit are not shown (since removal of random single data points significantly changed the fits). Different coloured crosses indicate measurements from different AERONET stations.

The low bias in Satellite AOD relative to AERONET could be explained by retrieving surface albedos that are more absorbing than is actually the case, leading to more light actually reflected back than would be predicted at the correct AOD.

While the previous urban class used by the ORAC retrieval has been shown completely unfit for purpose, it does not appear that the more physically reasonable model tested here offers significant advantages compared the continental aerosol which is extremely similar.

4.4.2 Biomass burning class

The ageing biomass burning class (BB_{ageing}), and the previous biomass burning class, based on Brazilian cerrado burning ($BB_{cerrado}$) will now be compared over the smaller area previously shown in Fig. 4.16 where this aerosol type would be expected to be prevalent.

The importance of *a priori* values and uncertainties

An initial mistake in the setup of the retrieval runs provided an opportunity to demonstrate the importance of correctly defining *a priori* values and errors. Pointing to the wrong data file containing the state vectors for each class meant that the retrieval using BB_{ageing}were run with the old values of $\mathbf{x}_a$ and $\mathbf{S_x}$ from the $BB_{cerrado}$ class. Since this element of the state vector now represented "age proxy", and not r_{eff}, these assumptions were clearly incorrect, and it would have been lucky chance if the retrieval was optimally set up.

While r_{eff} does not vary much for biomass aerosol, and certainly not through the three orders of magnitude that its state space occupies, age would be expected to vary through a much larger span of its state space. The variance of r_{eff} was quite tightly constrained with $\sigma_{\log_{10}(r)} = 0.3$. This corresponded to an age variance value of $\sigma_{\text{age}} = 1.9$. As a result, the retrieval stuck very closely to the age proxy a priori which turned out to be 7.15. The mistake was clearly obvious upon inspection of the retrieval output, as shown in the left hand panel of Fig. 4.21, where only the most dense aerosol plumes had enough information to convince the retrieval to stray from its *a priori* age.

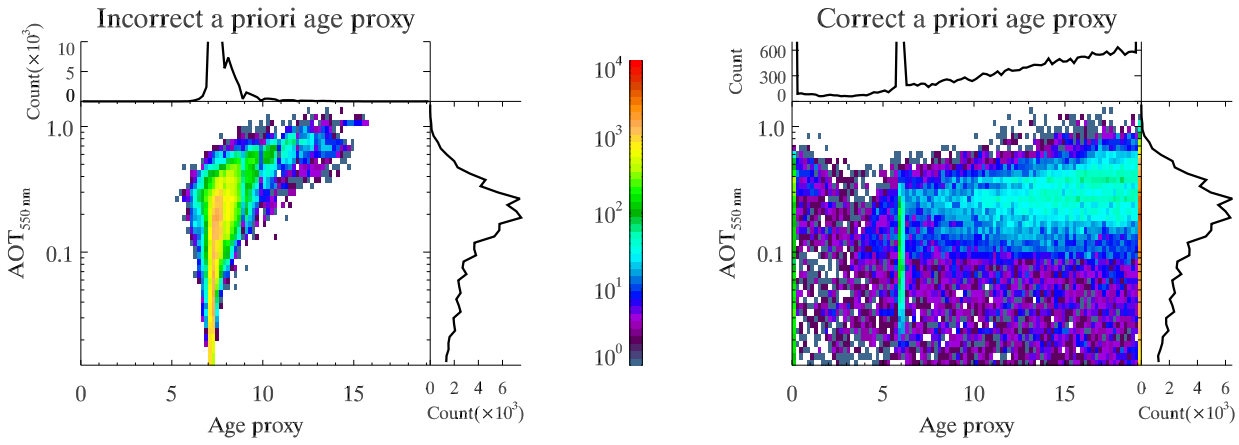

Figure 4.21: Showing the effect of removing constraints on the *a priori* value of aerosol ageing. Two dimensional histograms of AOD against biomass age proxy are shown. Data is only taken from retrievals within the boxed area of Fig. 4.16, over ocean, and where the maritime aerosol was not a more favourable fit to the data. Histograms are on logarithmic scales. In both left and right figures, the a priori age value can be clearly seen as vertical striping at age = 7/6 (in the left/right plots), however in the right hand figure, it is much more likely that the retrieval will depart from this value. Mode AOD values for the second plot are between 0.2 and 0.35.

Since the age of the aerosol plume was assumed to be completely unknown, a very large variance was chosen for the correct retrievals ($\sigma_{age} > 500$), essentially leaving the age completely unconstrained by the *a priori*. Age proxy *a priori* was set to 6 which is a mixture with the ratios of components given by the definition of aged biomass burning aerosol given in Table 4.4. With this implicit assumption that we know nothing about the age of the aerosol, it can be seen that there are still times when the retrieved age "sticks" unnaturally at the *a priori* value (RHS of Fig. 4.21). This corresponds to cases where it is not possible to find a plausible fit using the BB_{ageing} class, and so it is assumed that in these cases, BB_{ageing} is not the optimum aerosol model. There are also many cases where the age proxy is at its minimum or maximum extent. At the minimum age, we are looking at aerosols that are more absorbing than our model predicts. At the maximum, it is likely that a the particles are larger than allowed in this class, and the continental or marine aerosol classes would provide better matches. Screening for the three cases where results are mistrusted, the remaining data shows an increase in number density with increasing age proxy. This makes sense, since as the

age of the aerosols increases, the model tends towards the background aerosol fields, and away from the specific regions where burning takes place. Very little fresh smoke is seen (age proxy < 5) as expected, since it only exists in this form for, at most, a matter of hours. What fresh smoke there is has high AOD_{550}.

Comparison of new and old biomass burning models.

Analysis was limited to measurements where the aerosol was thought to be biomass burning. These cases were chosen by setting a minimum AOD of 0.1, only selecting retrievals where the lowest cost was from either $BB_{cerrado}$ or BB_{ageing}, and only cases where the BB_{ageing} retrieval gave an age which was not the minimum possible, the maximum possible, or the *a priori* value. The logic behind this follows from the discussion above, where it was noted that age proxy was likely to jump to the extremes of the state space, or fix itself at the *a priori* in cases where it could not be well fitted to the observed measurements.

Comparisons of retrieval cost and residuals are shown in Fig. 4.22. BB_{ageing} has residuals that are evenly distributed about the origin for all measurements; $BB_{cerrado}$ does not, although the offsets (which suggest some systematic bias in the class) are not large. $BB_{cerrado}$ residuals for the 1.6 μm channel are much narrower suggesting that the fit to the measurements is better than for BB_{ageing} which contains fewer large particles. Neither of the classes have costs that can be fitted well to a χ^2 distribution, but the expected cost for $BB_{cerrado}$ is slightly smaller.

In cases where retrievals of BB_{ageing} provides an age that is neither the a priori value, or one of the extents of the state space, costs are seen to be lower over land than $BB_{cerrado}$, although this is not the case over water, as shown in Fig. 4.23. In almost all cases, AOD is greater with BB_{ageing} than $BB_{cerrado}$. Since BB_{ageing} is both more absorbing, and has fewer smaller particles (which have a lesser proportion of forward scattered to backscattered light), this is reasonable. Mean over-land AOD difference between $BB_{cerrado}$ and BB_{ageing} is $\Delta AOD = 0.14$. Over the ocean, age of BB_{ageing} is unconvincingly young, but since its cost here is larger than $BB_{cerrado}$ (and other aerosol classes), the class would not generally have been selected in these instances. Mean over-water AOD difference is

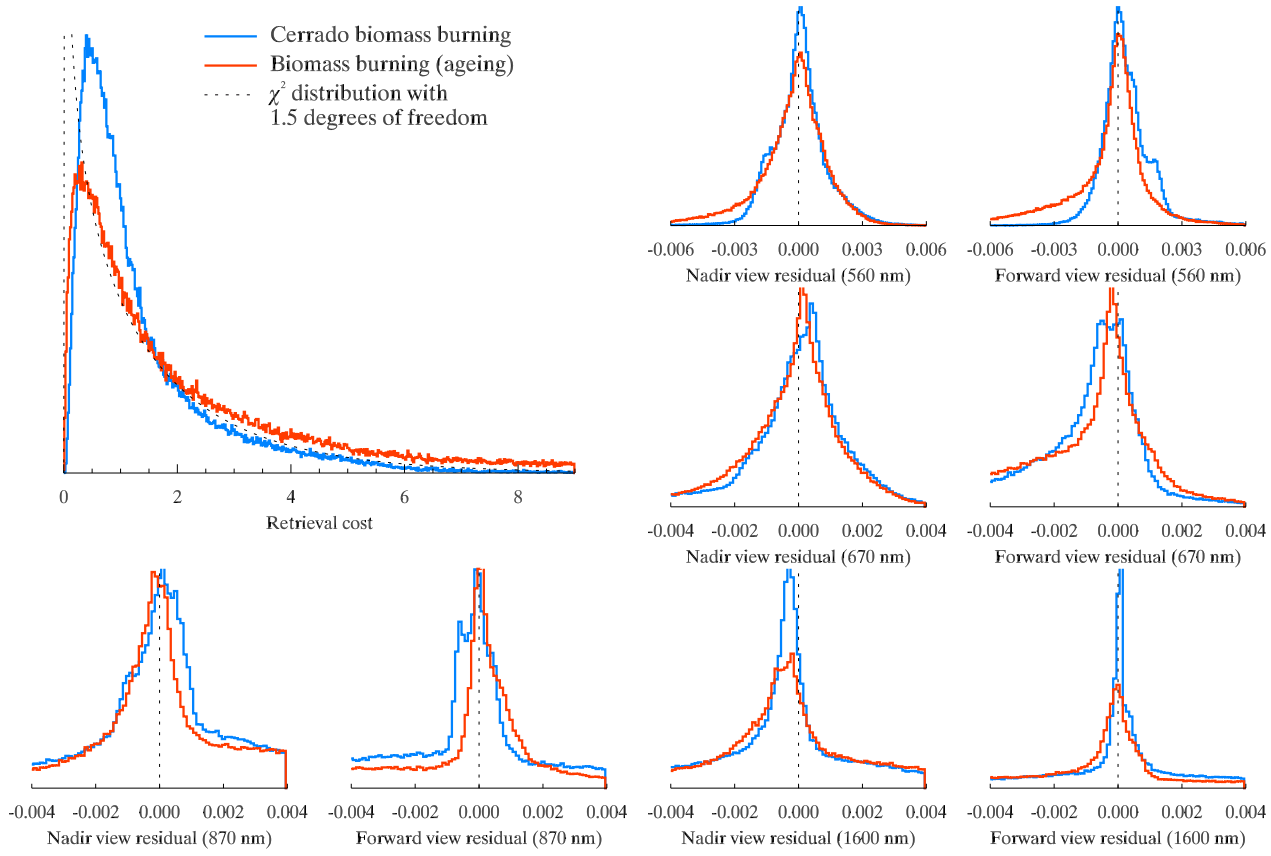

Figure 4.22: Comparing cost, and residuals for old Cerrado biomass burning class (blue) and the new age varying biomass burning class (red). Comparisons have been limited to cases where it is thought likely that we are seeing biomass burning aerosol, and where $AOD_{550\,nm} > 0.1$. Since BB_{ageing} has a tendency to stick to the *a priori* age value, this was excluded, as was the maximum age. At all other values of age, it was assumed that biomass must be present, as was the case when one either $BB_{cerrado}$ or BB_{ageing} had the lowest cost.

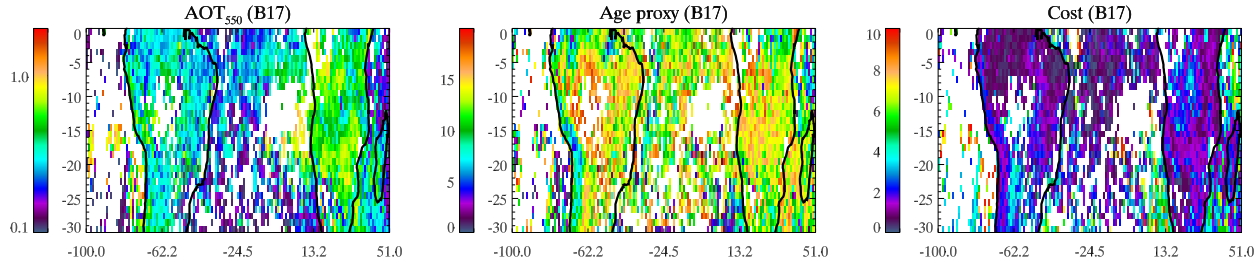

(a) BB_{ageing}

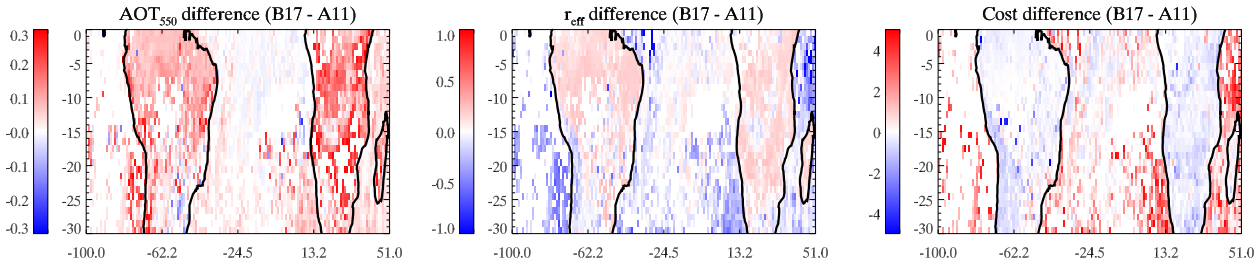

(b) BB_{ageing}- $BB_{cerrado}$.

Figure 4.23: Comparing monthly averages for retrieved values of AOD_{550}, r_{eff}, and cost for $BB_{cerrado}$ and BB_{ageing}. Averaging is carried out in $1^\circ \times 1^\circ$ grid boxes, and only cases where the retrieved age proxy for BB_{ageing} is not at either extent of its state space, or at its *a priori* value are included.

negligible ($\Delta AOD < 0.01$).

For the month of September, Fig. 4.24 shows the majority of biomass burning concentrated between about 25° S and 5° S in Africa and South America. The area of high AOD using BB_{ageing} in southern Africa matches the location of high BB emissions for this time of year given by Duncan et al. [2003, Fig. 6]. In South America, $BB_{cerrado}$ appeared to better represent the biomass aerosol, with a clearer plume showing. The value of BB_{ageing} age proxy varies greatly with the increase corresponding to an increase in particle number.

One reason for the apparent continental differences in effectiveness could be the measurements upon which the two classes are based. $BB_{cerrado}$ is based on measurements of cerrado burning in S. America, while the mixing ratios and particle types of BB_{ageing} were heavily influenced by measurements from Pósfai et al. [2004], taken in southern Africa.

There are retrieval issues when comparing Chile to the rest of S. America. Clear discontinuities can be seen in all aerosol fields when comparing measurements either side of the Andes. Since these

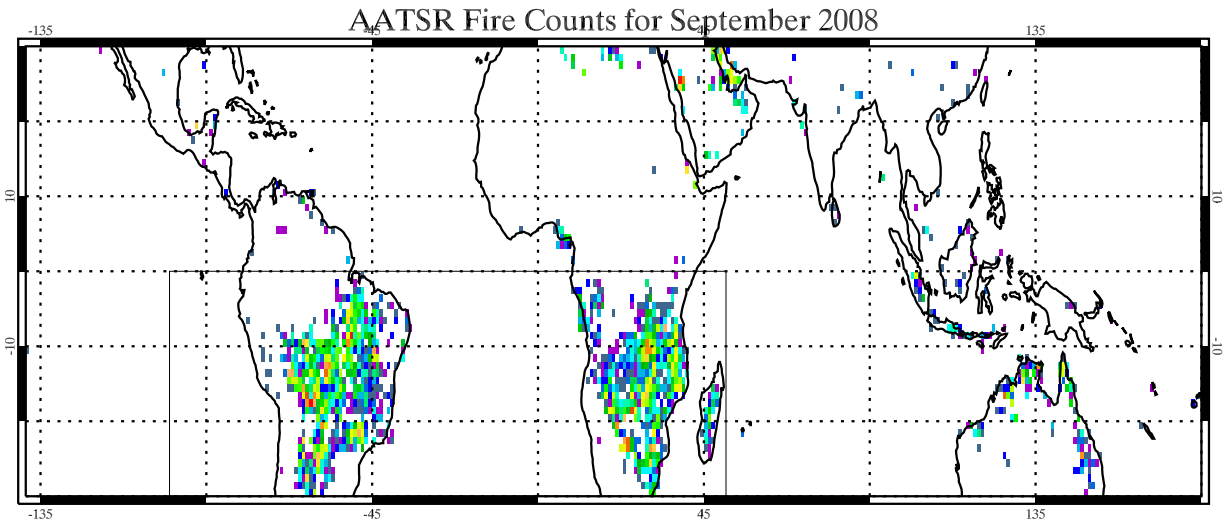

Figure 4.24: Map of fire density measured by AATSR for September 2008. Data is from night time overpasses with high values in thermal channels and was obtained from `http://due.esrin.esa.int/wfa/` (accessed on 29th July, 2011)

issues are evident in all aerosol classes, this was not investigated further, not being due to the aerosol microphysics.

Comparison with AERONET retrievals

From Fig. 4.25, BB_{ageing} has larger error bars on measurements, and worst correlation coefficients with AERONET, but does have lines of best fit that are generally closer to 1:1 line than $BB_{cerrado}$. There were very few cases when matches were found (24 in the month), and not all of these had BB_{ageing} age proxy values which were acceptable (only 16 in the month were accepted).

The continental class appears to be the best fit by far, the conclusion being that the matching AERONET measurements for the month were generally for times with no significant biomass burning aerosol loading.

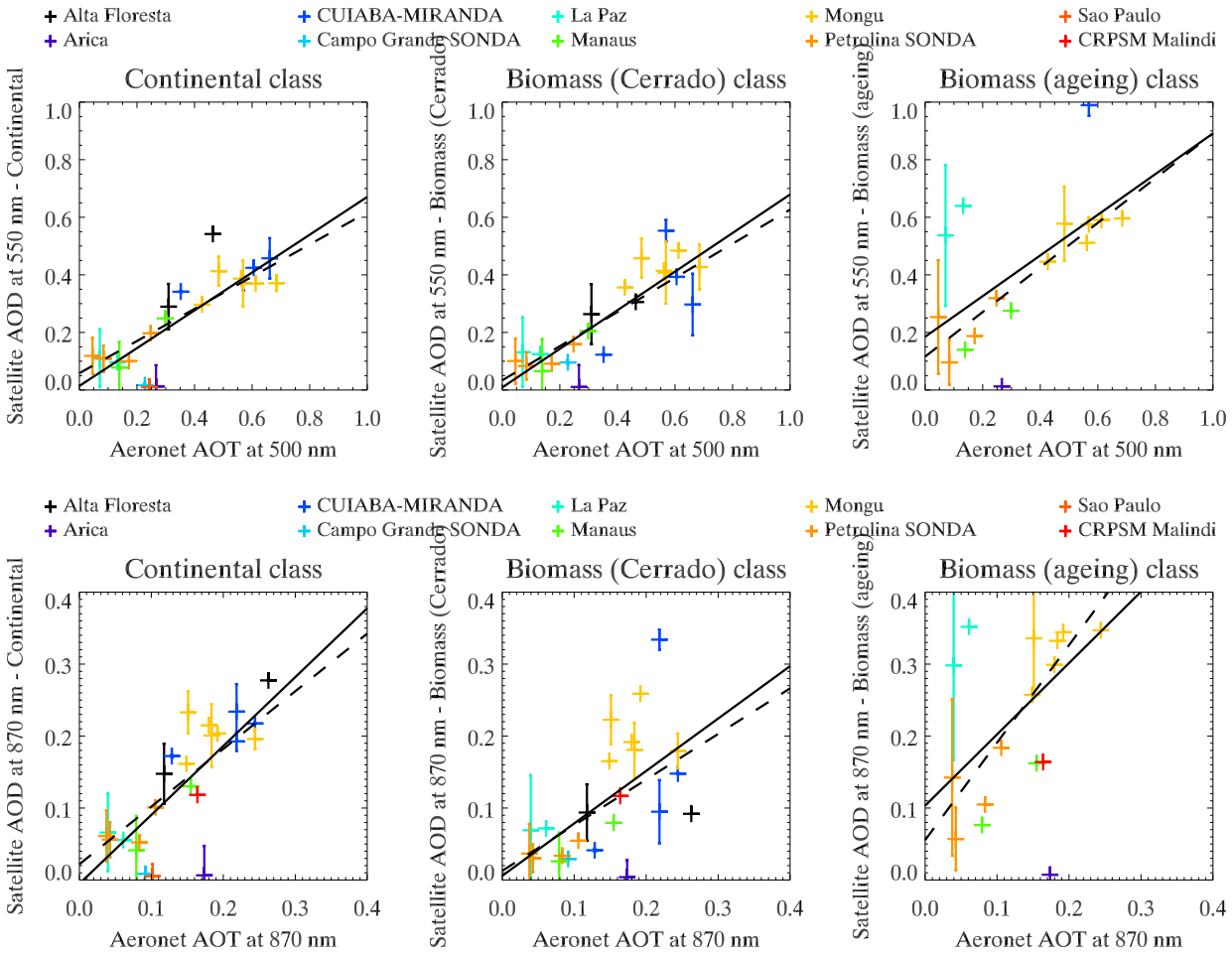

Figure 4.25: Comparing the continental, and biomass aerosol classes from the ORAC retrieval to concurrent AERONET retrievals. All measurements are within 30 minutes of each other. Lines of linear best fit are also shown (least absolute deviation - dashed ; minimum χ^2 statistic - solid). Different coloured crosses indicate measurements from different AERONET stations.

4.5 Summary

There are so many variables in the modelling of carbonaceous aerosol (reflecting the hugely varying methods of production, and ageing) that attempting to distil the microphysical modelling down to one or two free parameters is almost certainly an intractable problem in the context of an operational retrieval. The replacement of the OPAC soot mode with a mode employing fractal aggregates, and with a more physically plausible size distribution can claim to better represent the outflow from urban areas or sites of badly oxidised combustion. As such, the new version of the ORAC urban aerosol model is a legitimate addition to the ORAC aerosol retrieval, which was not true of the previous iteration. Since, as always, the size distribution is the dominant controller of light scattering properties, the pragmatic approach is probably to note that the continental aerosol class is probably adequate in most cases to represent aerosol over land (where desert dust, and biomass burning particulate are not present).

It was pleasing to find that modelling of biomass burning using age of the particles as a state element showed early signs of promise, although further work on this scheme is required. The particular ageing scheme appears to improve on the current cerrado BB model mainly for African BB aerosol. Over ocean, and South America, the current biomass scheme, with two spherical, homogeneous modes seems adequate. This is probably due to the fact that (as well as the current model using data from S. America), the new ageing model was based on work carried out in southern Africa. Here, the burning is more likely to have lower moisture content and contain less tree biomass than that from the cerrado [Eck et al., 2001]. It is also less likely to suffer contamination from forrest burning that cerrado measurements might expect from neighbouring Amazonia where burning would expect to contain more smoke from smouldering phase combustion [Reid et al., 2005].

In the short term, it would be sensible to remain using the $BB_{cerrado}$ model for biomass burning, but there is scope for future development of aged burning, if not for an operational retrieval, then at least for case studies of very large burning events.

Chapter 5

A proposed instrument for the measurement of aerosol properties (SPARCLE)

The SPARCLE detector is based on an earlier prototype detector developed as part of a University of Canterbury, PhD project [Thomas, 2003] designed to be balloon borne, for the measurement of stratospheric aerosol. This gives rise to the acronym SPARCLE, a contraction of "Stratospheric Aerosol Composition and Loading Experiment". Using a laser beam, individual aerosol particles are illuminated, and the scattered light collected by a linear diode array (LDA) and a photo-multiplier tube (PMT). It is expected that by measuring a significant amount of the total scattered light (using the PMT), and the structure of the scattered phase function at high resolution (using the LDA), there is enough information to infer the particle's size and complex refractive index (assuming that the scattering particle is spherical).

This chapter describes work done optimising the placement of the PMT and LDA, after completion of the basic design of the instrument. This design is outlined in §5.1, followed by a description of the forward model used in §5.2. Using the tools of optimal estimation (see §1.6.2 and Rodgers [2000]), §5.3 describes the method of selecting the best detector placement using the number of degrees of freedom, d_s as a metric.

5.1 Instrument design

The basic design of the detector has been fixed and is described by Peters et al. [2009]. A simplified layout is shown in Fig. 5.1. Incoming laser light (λ = 405 nm) travels into the measuring volume along the x-axis and, at the origin, crosses the path of injected aerosol particles which are travelling within a sheath flow from an air inlet at right angles to the laser beam (into the page, as shown in Fig. 5.1). Due to engineering issues, the detectors must be placed parallel to the incoming beam, but can be displaced along the x-axis in order to sample different parts of the phase function. Since the detectors are protected by sheets of glass, some light will be reflected at the boundaries between air and glass and the amount of transmitted light will be angularly dependant.

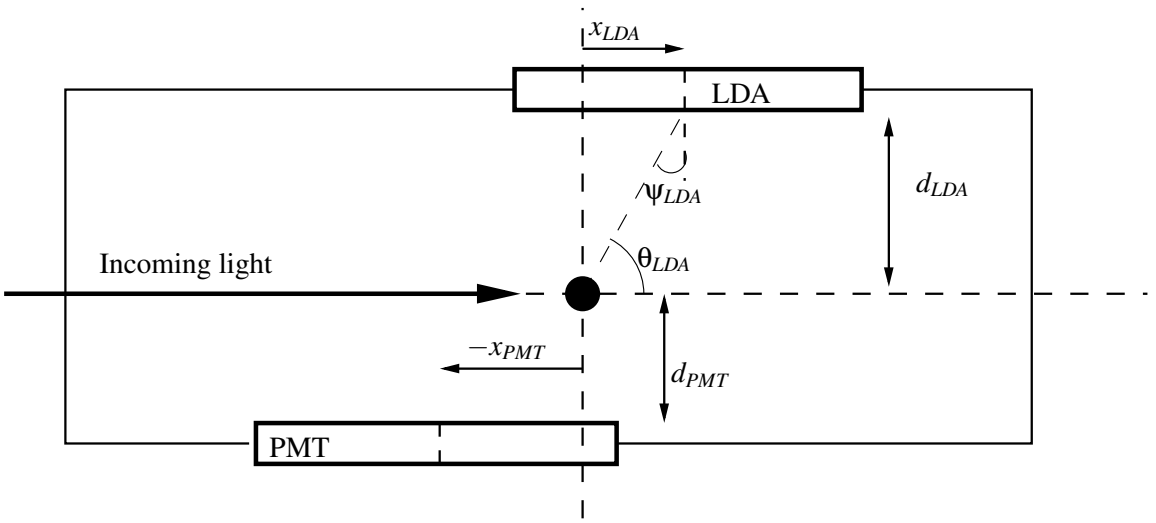

Figure 5.1: New model of SPARCLE. Detectors are fixed parallel to the incoming light, a distance d from the scattering source and are positioned to measure different parts of the phase function by moving a distance x along the side of the detector. The light scattering angle is θ_i and the incident angle at the detector is ψ_i. Scattering particles travel into the plane of the page.

	Thorn-EM1 9124B PMT	LDA
No. of elements	1	3000
Element active area	2.8×10^{-4} m^2	1.4×10^{-9} m^2
Distance from scattering plane	4.5 mm	10.2 mm
Efficiency (η)	0.206	0.1541

Table 5.1: Properties of the PMT and LDA. Any values with spectral dependence are defined at the laser wavelength of 405 nm.

5.2 Forward model

The forward model is our best representation of how light scattered by a known particle will be measured by our defined system. In the case of the LDA, this means the number of photons detected by each pixel (giving a 3000 element array); in the case of the PMT, we measure the current induced by detected photons in the instrument. The first stage of the model is to define the detector geometry.

5.2.1 Geometry

Incoming light travels along the x-axis, meeting the scattering aerosol at the origin. For an arbitrary detector, we define a set of elements, $\mathbf{d}_i$, each with associated areas, a_i, placed in the y-z plane as shown in Fig. 5.2a. The whole detector is defined by the collective set of points $\mathbf{D} = (\mathbf{d}_1, \mathbf{d}_2, \ldots)$ with areas $\mathbf{A} = (a_1, a_2, \ldots)$. In the case of the PMT, because of the wide angular view, the detector signal is simulated by summing of the light signals from a large number of points. Due to the small collection area of individual pixels, the LDA only requires one scattering angle to define each pixel, but of course has 3000 individual pixels.

Once a detector is defined, it must be moved from the origin to a useful position. This is done using a series of matrix transformations (rotations and a translation) which can place a detector at any position, in any orientation (Fig. 5.2b). These are, from an initial position at the origin:

1. Rotate an angle φ_x about the x-axis.

2. Rotate an angle φ_y about the y-axis.

3. Rotate an angle φ_z about the z-axis.

4. Translate a distance L along the x-axis.

5. Rotate an angle ϕ about the y-axis.

6. Rotate an angle θ about the x-axis.

The final detector element position, $\mathbf{d}'_i$ can then be written as:

$$\mathbf{d}'_i = \mathbf{R}_\theta \mathbf{R}_\phi \left(\mathbf{R}_z \mathbf{R}_y \mathbf{R}_x \mathbf{d}_i + \mathbf{t}\right), \tag{5.1}$$

where $\mathbf{R}$ are appropriate rotation matrices and $\mathbf{t} = (L, 0, 0)$ is a translation. The angular position of an element, (θ_i, ϕ_i), can be recovered by:

$$\cos\theta_i = \frac{x_i}{\sqrt{x_i^2 + y_i^2}}, \qquad \text{and} \qquad \cos\phi_i = \sqrt{\frac{x_i^2 + y_i^2}{x_i^2 + y_i^2 + z_i^2}}. \tag{5.2}$$

The scattering angle, θ'_i, between an incident beam along the x-axis, and detector element, as required in light scattering calculations, can be obtained by:

$$\cos\theta'_i = \cos\theta_i \times \cos\phi_i. \tag{5.3}$$

Solid angle subtended by scattered light

For any flat detector surface element with small area, the solid angle subtended from the origin to an element is,

$$d\Omega = \frac{\hat{\mathbf{n}} \cdot d\mathbf{A}}{r^2}, \tag{5.4}$$

where $\hat{\mathbf{n}}$ is the direction from the origin to that element, $d\mathbf{A}$ is the element surface area, in the direction normal to the plane, and r is the distance from the origin to the element. Fig. 5.3 shows

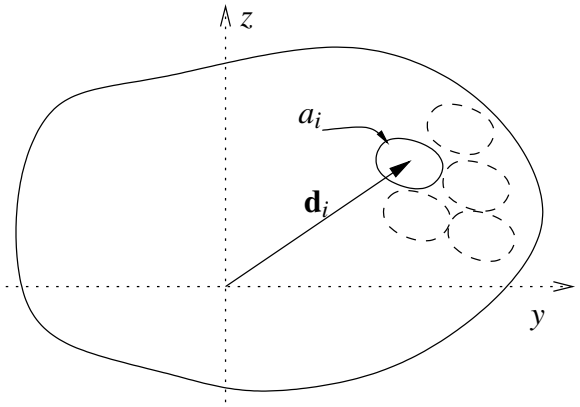

(a) Defining the detector in the y-z plane. Each element of detector, i, is given a position, $\mathbf{d}_i$, and an area, a_i.

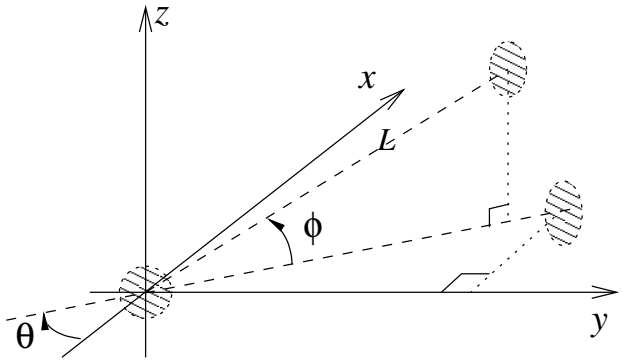

(b) Placement of the detector - Once orientated, the detector is moved a distance L from the light scattering particle. It is then rotated an angle θ in the x-y plane, then ϕ out of the x-y plane.

Figure 5.2: Positioning the detector.

such a detector plane, S', with the transformed origin ($\mathbf{0} \rightarrow \mathbf{0}'$) and an arbitrary transformed detector point, $\mathbf{d}'_i$. Using (5.4), it can be seen that in this case, with $\hat{\mathbf{n}} = \hat{\mathbf{d}}'_i$ and $r = |\mathbf{d}'_i|$ the transformed solid angle is given by:

$$d\Omega_i = \frac{\mathbf{d}'_i}{|\mathbf{d}'_i|^3} \cdot d\mathbf{S}'_i \,. \tag{5.5}$$

The missing value, $d\mathbf{S}'_i$ is the normal to the surface, S', multiplied by the predefined area of the element, a_i. To obtain the normal, we define vectors, $\mathbf{d}'_0$, $\mathbf{d}'_y$, $\mathbf{d}'_z$ as

$$\mathbf{d}_0 = \mathbf{0} = \begin{pmatrix} 0 \\ 0 \\ 0 \end{pmatrix} ; \mathbf{d}_y = \begin{pmatrix} 0 \\ 1 \\ 0 \end{pmatrix} ; \mathbf{d}_z = \begin{pmatrix} 0 \\ 0 \\ 1 \end{pmatrix},$$

and transform them to the new plane, using (5.1). Taking the cross product of any two non-parallel vectors on the plane S' will give us the surface normal, so we can say

$$d\mathbf{S}'_i = a_i \frac{(\mathbf{d}'_y - \mathbf{d}'_0) \wedge (\mathbf{d}'_z - \mathbf{d}'_0)}{|(\mathbf{d}'_y - \mathbf{d}'_0) \wedge (\mathbf{d}'_z - \mathbf{d}'_0)|},$$

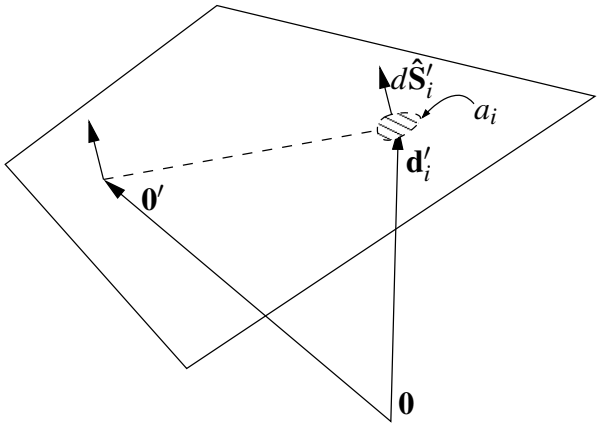

Figure 5.3: Showing the plane of the detector, S', after being rotated and moved from the origin, $\mathbf{0}$.

which immediately leads to

$$d\Omega'_i = a_i \frac{\mathbf{d}'_i \cdot \left[(\mathbf{d}'_y - \mathbf{d}'_0) \wedge (\mathbf{d}'_z - \mathbf{d}'_0)\right]}{|\mathbf{d}'_i|^3 |(\mathbf{d}'_y - \mathbf{d}'_0) \wedge (\mathbf{d}'_z - \mathbf{d}'_0)|}. \tag{5.6}$$

5.2.2 Polarisation

There are three logical sets of polarisation reference frames in the system. Starting with the laser beam and working through to the final detector position, the first is that determined by the rotation of the laser beam which enters along the x-axis. Second, is the polarisation in the plane of scattering[1], defined parallel and perpendicular to this plane and given the polarisation basis vectors $\mathbf{p}_1$ and $\mathbf{p}_2$ where the numbers correspond to the 1st and 2nd intensity functions of Mie theory which are for light polarised perpendicular and parallel respectively in this plane [Bohren and Huffman, 1983]. Finally, at the detector element, there is the polarisation direction required to calculate the Fresnel coefficients in the plane on refraction, and perpendicular to the plane of refraction (here called $\mathbf{p}_p$ and $\mathbf{p}_s$ respectively).

[1]The plane of scattering is the plane which includes the incoming light and the outgoing scattered light directions.

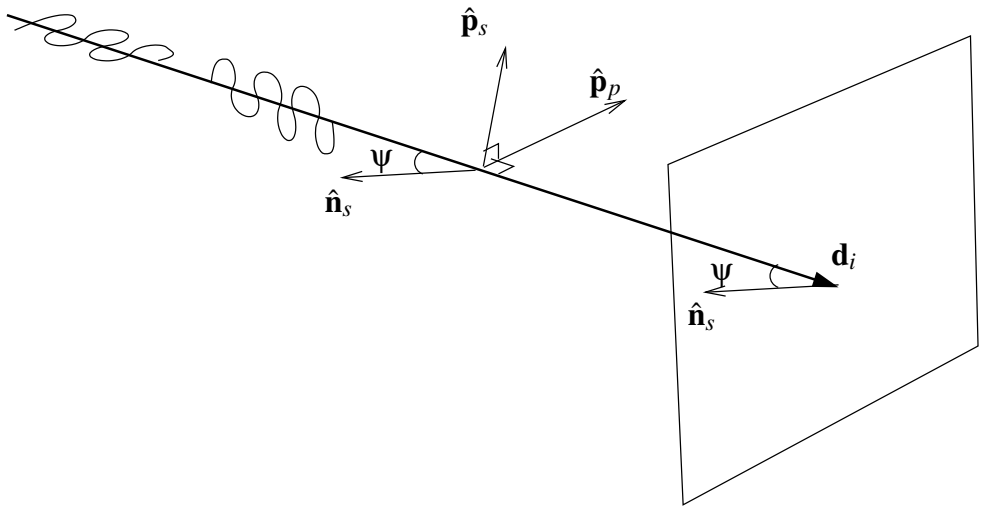

Figure 5.4: Showing the two orthogonal polarisation states $\hat{\mathbf{p}}_p$ and $\hat{\mathbf{p}}_s$ which are parallel and perpendicular respectively to the plane of refraction of incoming light to the detector glass surface. The surface has normal $\hat{\mathbf{n}}_s$ and the incident angle with surface normal is ψ.

For the polarisation of the laser beam, we assume linear polarisation, and define the basis vector

$$\hat{\mathbf{p}}_{\text{laser}} = \hat{\mathbf{e}}_z \cos\zeta + \hat{\mathbf{e}}_y \sin\zeta. \tag{5.7}$$

The orientation of the laser being defined by the rotation about the x-axis of ζ from

The incoming direction of light is $\hat{\mathbf{e}}_x$, the outgoing direction $\hat{\mathbf{d}}'_i$, and the normal to the surface is calculated above in (5.6) and shall be called $\hat{\mathbf{n}}_s$. From here we can define

$$\hat{\mathbf{p}}_1 = \frac{\hat{\mathbf{e}}_x \wedge \mathbf{d}'_i}{\left|\hat{\mathbf{e}}_x \wedge \mathbf{d}'_i\right|}. \tag{5.8}$$

The second state is perpendicular to the scattered light and the first state, so can be defined

$$\hat{\mathbf{p}}_2 = \frac{\hat{\mathbf{p}}_1 \wedge \mathbf{d}'_i}{\left|\hat{\mathbf{p}}_1 \wedge \mathbf{d}'_i\right|}. \tag{5.9}$$

The directions of the polarisation states in the detector plane can be defined from $\mathbf{d}_i$ and $\hat{\mathbf{n}}_s$. This can

also be used to calculate the incident angle of light striking the detector glass, ψ.

$$\hat{\mathbf{p}}_p = \frac{\hat{\mathbf{n}}_s \wedge \mathbf{d}'_i}{|\hat{\mathbf{n}}_s \wedge \mathbf{d}'_i|}, \qquad \hat{\mathbf{p}}_s = \frac{\hat{\mathbf{p}}_p \wedge \mathbf{d}'_i}{|\hat{\mathbf{p}}_p \wedge \mathbf{d}'_i|}, \qquad \cos\psi = \frac{\mathbf{d}'_i \cdot \hat{\mathbf{n}}_s}{|\mathbf{d}'_i|}. \tag{5.10}$$

Now that the two sets of orthogonal polarisation states have been defined, converting between the two is trivial, using the square of the dot product between the two basis vectors[2].

5.2.3 Passage of scattered light through instrument windows

Both of the the detectors have glass windows separating themselves from the aerosol cavity. The windows have much greater thickness than the wavelength of light, so this is a problem of geometric optics. The change in refractive index at these boundaries divert the course of the scattered light (from Snell's law) and reduce transmission (from the Fresnel equations). For this reason, the polarisation directions of the light incident on the detector glass are required.

In the case of the PMT, offsets in the beam's direction are not important: any light that is transmitted through the glass face of the detector is assumed detected (with a probability defined by the collection efficiency, η). More problematically, deviations of light to the LDA could well offset the signal into a new detector element than that predicted without a glass shield (the width of each element is 7 μm). As a result, the scattering angles of light to LDA elements must be recalculated.

Transmission

Reflection coefficients at a boundary between two mediums is given by the Fresnel equations. They are [Bohren and Huffman, 1983]:

$$r_\perp = \frac{\cos\theta_i - m\cos\theta_t}{\cos\theta_i + m\cos\theta_t} \;; \qquad r_\parallel = \frac{\cos\theta_t - m\cos\theta_i}{\cos\theta_t + m\cos\theta_i}. \tag{5.11}$$

[2]Since the polarisation is of the electric field, not the irradiance

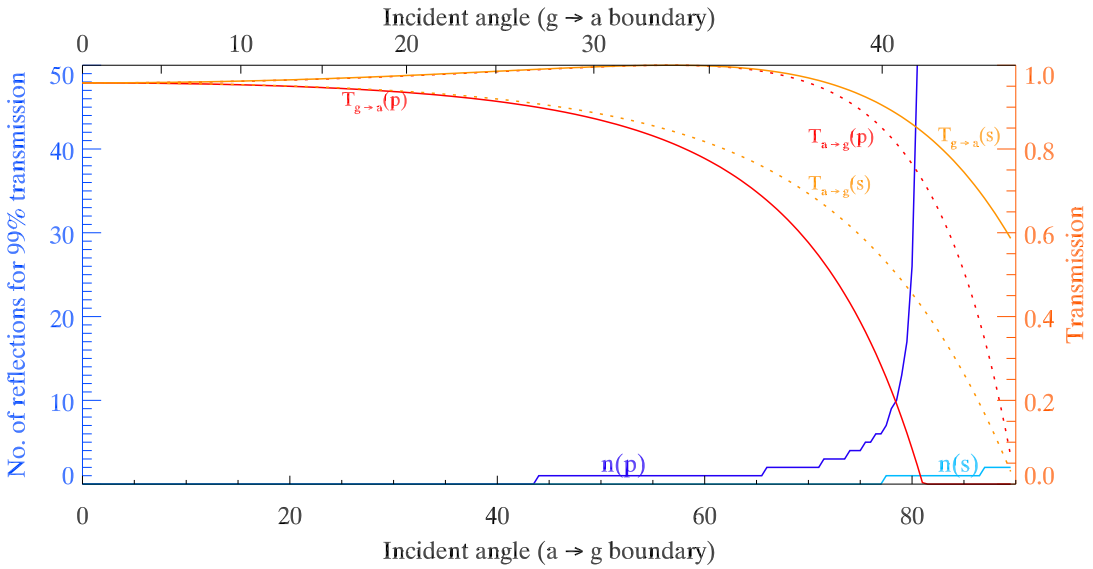

Figure 5.5: Calculations of transmitted light (red lines) for the air→glass (dashed) and glass→air (solid) boundaries. At the glass→air boundary, the incident angle is such that it corresponds to the transmitted angle at the air→glass boundary. This means the total transmitted intensity (excluding multiple internal reflections) is $T_{a\to g} \times T_{g\to a}$. The number of internal reflections required to transmit 99 % of the total transmitted light (calculated as the limit of the geometric series) are shown in blue. Light polarised perpendicular to the plane of refraction is labelled (s); light polarised in the plane of refraction is labelled (p).

The glass is assumed non-absorbing, so any light that is not reflected is assumed transmitted. Given the incident angle of the light on the glass, we can therefore calculate the transmission through the medium and then out of the other side. Fig. 5.5 shows transmission at the two interfaces (air→glass and glass→air) for light polarised parallel (p) and perpendicular (s) to the plane of refraction. The p-polarised light undergoes more reflections within the glass. At incident angles of 45° more than 1 % of the light has a second (and third) reflection before reaching the detector. With the s-polarised light, almost all of the detected light will be detected without repeated reflections within the glass up to angles of 77°. This is not to say that 100 % of the light incident on the glass would be transmitted, but rather that of the light which eventually will pass through both boundaries (calculated as the sum of the geometric progression for repeated reflections and transmissions), 100 % will be transmitted without reflections further deviating its journey.

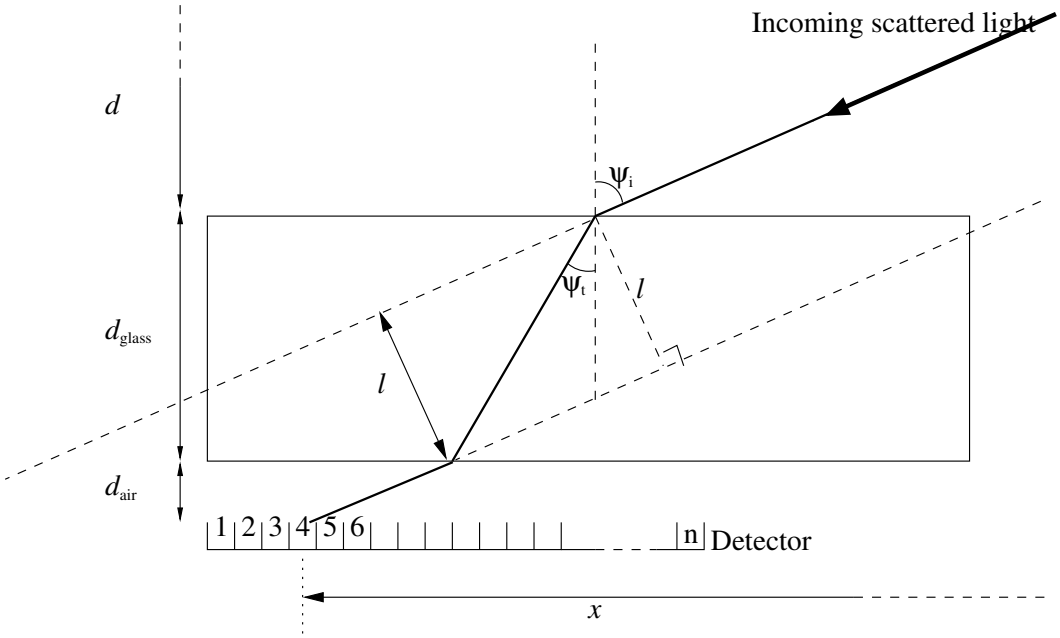

Figure 5.6: Showing the displacement of incoming light to an LDA detector element. Light which would have not been detected has there been no glass present has been diverted into detector element #4.

As a result of this, it is recommended that the laser is orientated to optimise s-polarised light reaching the detector glass, instead of p-polarised light. This has the effect of simplifying the forward model as repeated reflections within the glass can be omitted. In order to obtain this polarisation, we require the laser to be orientated so that it is linearly polarised in the direction $\hat{\mathbf{e}}_y$.

Light deviation in LDA calculations

As shown in Fig 5.6, light incident on the glass plate placed before the LDA detector diverts its path from that expected if the glass were not there. Since we know the values of d, d_{glass}, d_{air} and x for each element, the scattering angles can be obtained using geometry. Because the PMT is a more blunt instrument with respect to phase function, in that case, the following calculations are unnecessary.

Since the detectors are placed at right-angles to the laser direction, the incident angle, ψ_i is related

to the scattering angle, θ, by:

$$\theta = \begin{cases} \frac{\pi}{2} - \psi_i & \text{if } x < 0 \\ \frac{\pi}{2} + \psi_i & \text{if } x \geq 0 \end{cases}. \tag{5.12}$$

The relationship between l and ψ_i can be deduced from Fig 5.6 by:

$$l = \frac{d_{\text{glass}}}{\cos(\psi_t)} \cdot \sin(\psi_i - \psi_t) = \frac{d_{\text{glass}}}{\cos\psi_t} (\sin\psi_i \cos\psi_t - \cos\psi_i \sin\psi_t), \tag{5.13}$$

and using Snell's law: $\sin\psi_i = m \sin\psi_t$

$$l = d_{\text{glass}} \sin\psi_i \left[1 - \frac{\cos\psi_i}{\sqrt{m^2 - \sin^2\psi_i}} \right]. \tag{5.14}$$

The relationship between x and l can be obtained by further inspection:

$$|x| + \frac{l}{\cos\psi_i} = (d + d_{\text{glass}} + d_{\text{air}}) \tan\psi_i, \tag{5.15}$$

and substituting l from (5.14) above:

$$|x| + \tan\psi_i \, d_{\text{glass}} \left[1 - \frac{\cos\psi_i}{\sqrt{m^2 - \sin^2\psi_i}} \right] = (d + d_{\text{glass}} + d_{\text{air}}) \tan\psi_i,$$

$$|x| = \tan\psi_i \left[d_{\text{air}} + d + \frac{d_{\text{glass}} \cos\psi_i}{\sqrt{m^2 - \sin^2\psi_i}} \right]. \tag{5.16}$$

which, while there is an analytic solution for ψ_i, was solved numerically using a bisection method [Press et al., 1992]. From (5.16), it is easily verified that upon removing the glass (either by setting $d_{\text{glass}} = 0$ or $m = 1$), the solution simplifies to the non-glass case. The new scattering angles of light and their deviations from the non-glass case are shown in Fig. 5.7.

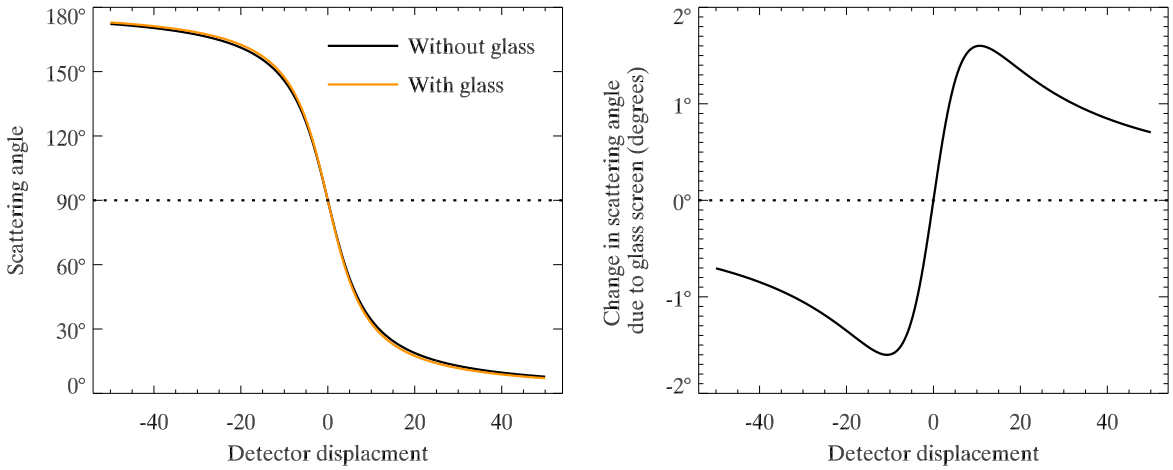

Figure 5.7: Deviation of light scattering angle caused by glass screen.

5.3 Optimisation

To place the detector in the most sensible position, optimal estimation techniques are employed (see §1.6.2). The instrument provides measurements which are collated into the measurement vector, $\mathbf{y}$, with measurement error characterised by a covariance matrix, $\mathbf{S_y}$. Degrees of freedom, d_s, gives a measure of the number of independent elements of the state vector, $\mathbf{x}$, that could theoretically be resolved, given the current error estimates and *a priori* constraints. Since SPARCLE is designed to retrieve radius, and both real and imaginary parts of refractive index, the range of values in this case is $0 \leq d_s \leq 3$. It is defined:

$$d_s = \mathrm{tr}\left(\mathbf{A}\right), \tag{5.17}$$

where $\mathbf{A}$ is the averaging kernel, defined [Rodgers, 2000] as:

$$\mathbf{A} = \left(\mathbf{S}_{\mathbf{x}_a}^{-1} + \mathbf{K}_\mathbf{x}^\mathrm{T}\,\mathbf{S}_\mathbf{y}^{-1}\,\mathbf{K}_\mathbf{x}\right)^{-1}\mathbf{K}_\mathbf{x}^\mathrm{T}\,\mathbf{S}_\mathbf{y}^{-1}\,\mathbf{K}_\mathbf{x}. \tag{5.18}$$

Here, $\mathbf{S}_{\mathbf{x}_a}$ is the covariance of the *a priori* state and $\mathbf{K}_\mathbf{x}$ is the weighting function.

Over a range of parameters (see Table 5.2), d_s was calculated and the results for each particle type (defined by its radius and refractive index) was given equal weighting in an average value of

Parameter	Min	Max	Number of steps	
Radius (μm)	5 nm	5 μm	41	(logarithmic)
$\Re$(refractive index)	1.3	1.8	6	(linear)
$\Im$(refractive index)	5×10^{-4}	0.5	7	(logarithmic)
Detector position (both PMT and LDA)	-30 mm	+30 mm	15	(linear)
Polarisation angle (from perp. to x-y plane)	0, $\pi/2$			

Table 5.2: Parameters used in SPARCLE optimisation runs.

d_s for each detector position (and polarisation angle). The results of these calculations are shown in Fig. 5.8 and Fig. 5.9 which also show d_s at the optimum detector position.

The main conclusions of these calculations are that the best positioning of the LDA would be with its centre at the y-axis. This placement catches the largest percentage of the phase function (since as the detector moves further from $x = 0$ at a constant perpendicular distance from the origin), it subtends a smaller solid angle from the scattering particle). Additionally, at the origin, the incident angle of incoming light with the glass surface normal is minimised, increasing the amount of light transmitted to the detector elements.

Changing the PMT position has very little influence while the LDA is in its optimal position. This also makes sense as the PMT does not measure in detail the phase function, but more the total light scattered within a large solid angle. That is not to say that having a PMT in this design set up is redundant. The PMT can be used to trigger LDA detection (since it has much greater temporal resolution), and can help to better characterise the scattering cross section.

The lower right sections of the figures show that for particles with radii below 0.1 μm, there is very little chance of resolving more than one piece of information from the state vector. Inspection of the averaging kernel shows that only radius can be resolved. For particles with radii below 0.01 μm, there is very little chance of obtaining any information about the particle (although it could still be counted).

Conveniently, from §5.2.3, it was recommended that the laser was linearly polarised in the direction $\hat{\mathbf{e}}_y$ and as can be seen in the lower right plot of Fig. 5.9, particle information can be resolved for smaller particles than in Fig. 5.8.

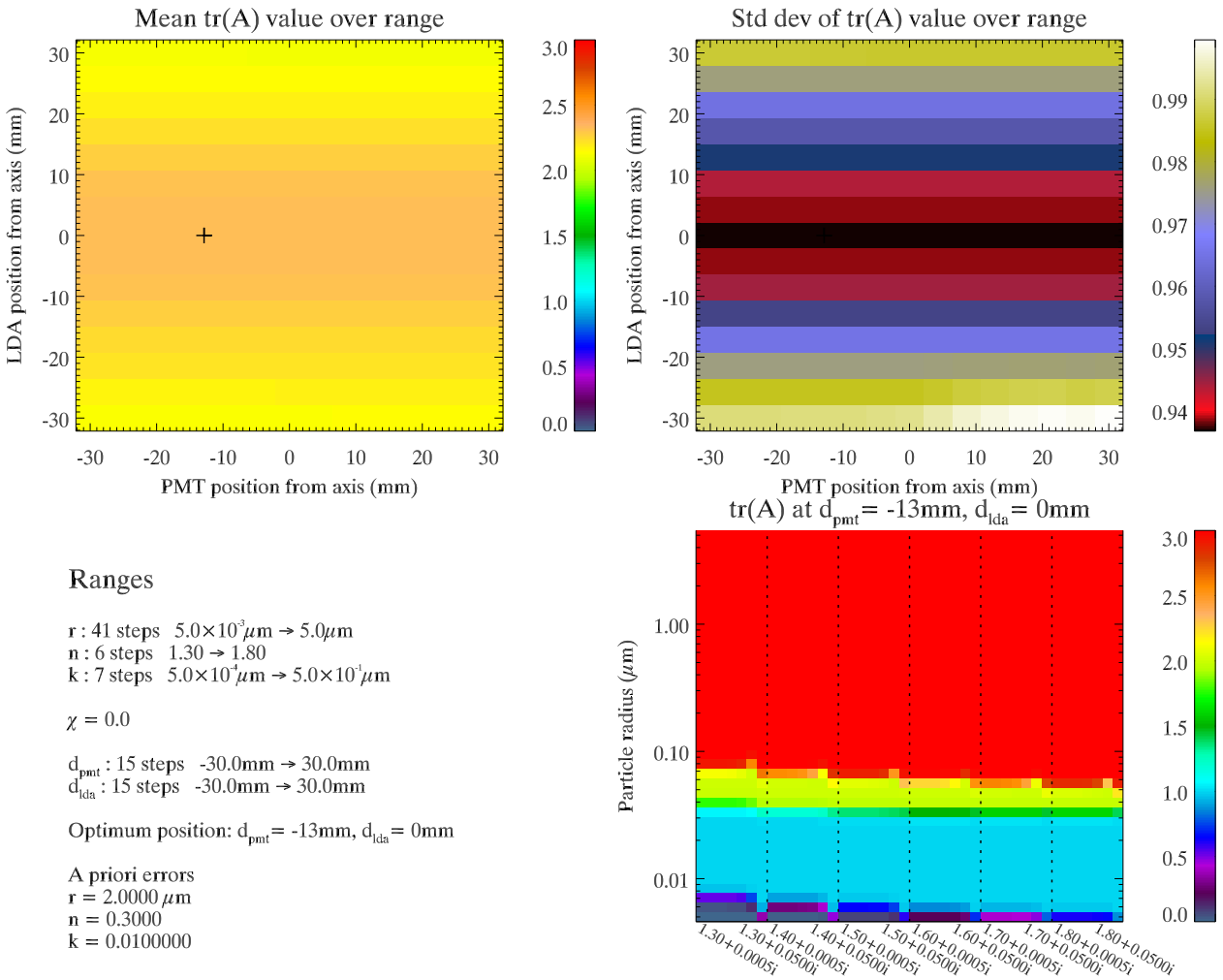

Figure 5.8: Optimisation calculations for SPARCLE detector with laser beam linearly polarised perpendicular to the *x*-*y* plane. Optimum detector positions are marked with a cross (+) and all of the values of d_s going into the average at this point are shown in the lower right plot.

5.4 Summary

Based on the calculations above, it is recommended that if the detector SPARCLE were to be built with the current specifications, the optimum detector placement would be for both LDA and PMT to be placed at $x = 0$ as shown in Fig. 5.1. The laser should be linearly polarised parallel to the plane of light scattering, the *x*-*y* plane.

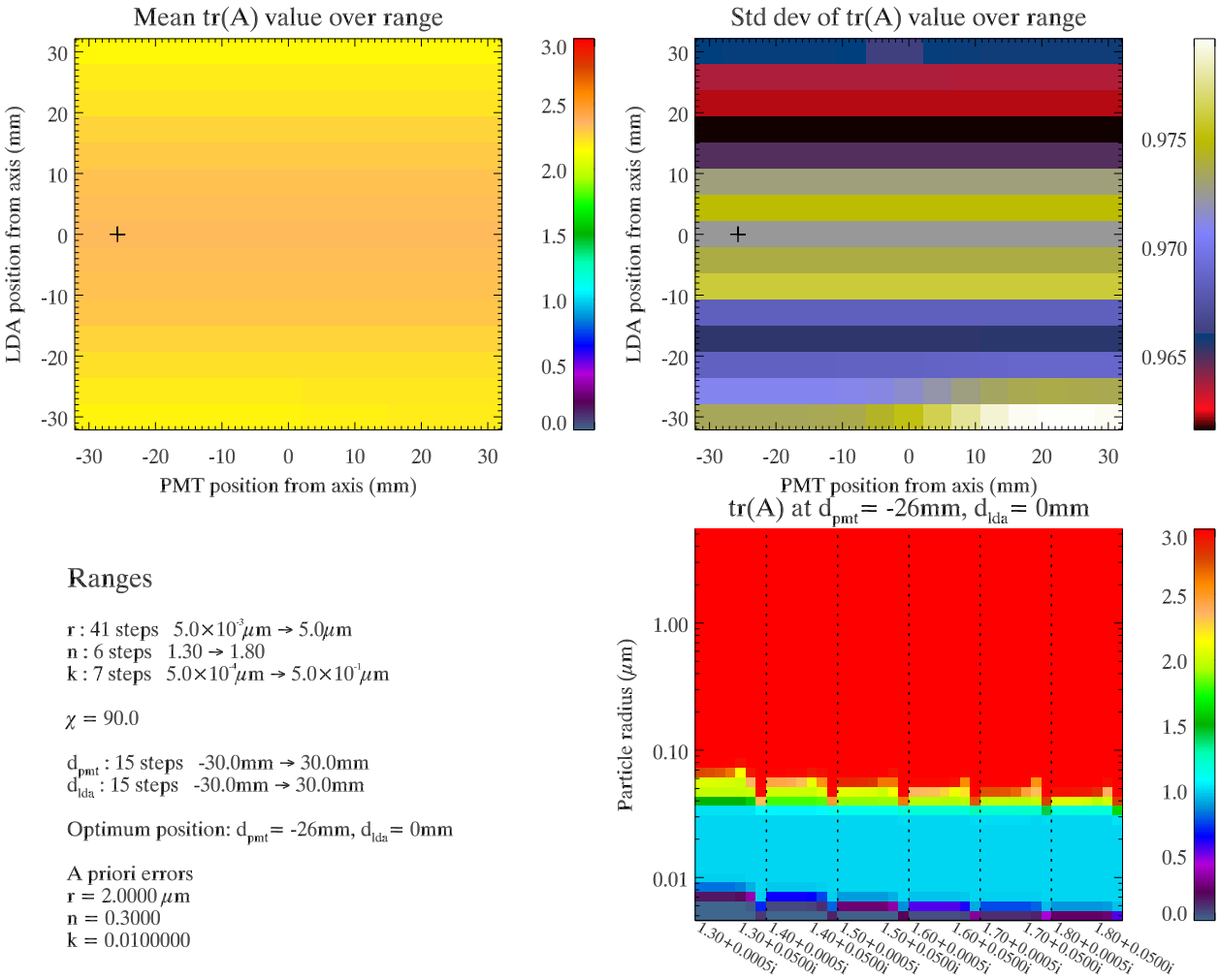

Figure 5.9: Optimisation calculations for SPARCLE detector with laser beam linearly polarised parallel to the x-y plane. Optimum detector positions are marked with a cross (+) and all of the values of d_s going into the average at this point are shown in the lower right plot.

Chapter 6

Conclusions and future work

6.1 Summary and general conclusions

Following in the order of increasing complexity, four of the microphysical models of aerosol used by the ORAC retrieval scheme have been investigated. The intention was to improve the overall output of the aerosol product. It is now possible to add non-spherical particles, coated particles, and fractal aggregate particles to size distributions within ORAC, which was not previously the case.

The most important parameters in the microphysical models are (in order) the size distribution, and the refractive index. In the case of the size distribution, this is since it determines the length scales of light scattering, and so which wavelengths of incoming light are likely to be most perturbed by interaction with the particles. The imaginary part of refractive index determines the absorption of light by the aerosol, and so is the second major predictor of how much light a particle would remove by the time incoming solar radiation has travelled through the atmosphere and been reflected back towards space.

The other general rule to emerge is that if a certain particle type has a parameter with large spatial variability, and variation of this parameter significantly changes the light scattering properties (that we choose not to vary in the microphysical model), it is unlikely that it will be possible to adequately model this aerosol type in a global, operational aerosol retrieval. This explains why the desert dust

class (which has significant non-sphericity, but low worldwide variation) can be improved by the addition of non-spherical modelling, but fresh carbonaceous aerosols proved much more difficult.

A more minor issue, that could be easily dealt with is the range of allowed values of effective radius. The current ORAC allowed range is 10 nm $\leq r_{\text{eff}} \leq$ 10 μm. For the minimum value, although individual particles can have sizes this small, the likelihood of an aerosol distribution having an such a small value of r_{eff} is negligible. For the upper limit, atmospheric aerosol distributions will again not get anywhere near this large (although a retrieved value of r_{eff} =10 μm is a good indicator that one is in fact looking at clouds). Coarse mode particles would drop out at too fast a rate to make this observable. Reducing the range (to say 0.1 μm $\leq r_{\text{eff}} \leq$ 5 μm) would have two major benefits:

- Assuming that the same number of data points would be included in the look-up tables, a higher resolution set of forward model values along the r_{eff} axis could provide a better r_{eff} retrieval.

- Since the largest particles would be smaller, optical properties would take less time to calculate.

Finally, a study was also undertaken to improve the information capture of an individual aerosol analyser (SPARCLE), designed to build up a picture aerosol properties in a specific region. Although the conclusions obtained in this work were specific, the general method employed is applicable to the development of similar instruments.

6.2 Comments on the modelling of specific aerosol classes

Maritime

The current method of modelling maritime aerosol is generally fine, but increasing the modelled atmospheric relative humidity from 50 % to 80 % would be more physically realistic (although this would not dramatically alter the results of retrievals). Increasing the relative humidity leads to aerosol optical depths that are, on average, 5 % larger. The effective radius is unchanged.

Dust

Modifications to the sand mode have been shown to improve the overall quality of both the microphysical model, and the resulting retrieval. Some of the modifications have been incorporated into the new versions of the ORAC retrieval. The main findings confirm that imaginary part of refractive index is too low, and that the addition of non-sphericity to the mineral dust modes are the dominant improvers of the retrieval (as had been found previously by other science teams). The worldwide spread of refractive indices of various mineral dusts was found to not be a dominant factor in modelling the light scattering properties.

A microphysical model which defined the accumulation mineral dust particles as inorganic-coated and hygroscopic, with a relative humidity of 80 % improved retrieval systematic biases, suggesting a better representation of dust. Unfortunately, RH this high is not a reasonable assumption over the Sahara desert. Indeed it was not possible to find a strong correlation between ambient RH (taken from ECMWF re-analysis data) and the optimum non-spherical, relative humidity dependent desert dust class. This improved model gives AOD values that can be 100 % larger over the Sahara, while having smaller residuals in all channels.

The naturally produced aerosols (this comment also applies to the maritime class) are well represented by the mixing rules that determine their effective radius, i.e. the mixing between different modes, while keeping the size distributions the same is the correct method to obtain natural aerosol distributions with different overall sizes.

Carbonaceous particles

Soot aerosol has been redefined, moving away from the OPAC description. It now has physically reasonable values of RI, size, and shape (none of which were previously the case). As a result, the urban aerosol class has now been improved to the point of being a working member of the ORAC aerosol classes, which the old version certainly was not. However, its similarity to normal continental aerosol, and the small spatial extent over which it is expected to be visible before morphing into the

continental regional haze make it unlikely to be regularly spotted by satellite measurements. None the less, it exists, and contains fractally aggregated soot particles.

An attempt to model biomass burning ageing was undertaken, and shows promise, although there is still more work to be done in this category. The current biomass model, which is based on AERONET measurements of biomass burning is reasonably good, so should be retained at the current time. Over land, the ageing BB model reported AOD values that were around 0.14 larger than the current model.

It would be interesting to undertake investigation of specific biomass burning aerosol plumes using the ageing model, but the representation is not suitable for the operational retrieval at this time.

6.3 Future work

Several tasks are still to be carried out before this work can be completed satisfactorily. The list has been ordered so that higher priorities are placed first.

Retrieval using all of the new aerosol types simultaneously The most obvious next step is to see how the new maritime, dust, and urban models behave when all combined into the same retrieval instead of one at a time as was shown in the analysis sections of previous chapters. This should provide a more accurate picture of global aerosol distributions (particularly of aerosol type), given that the new models are better representations of the atmospheric particles, and thus better for comparison with models that partition different aerosol types.

It is unlikely that major conflicts could arise during this implementation. Changes in individual aerosol types lead to incremental improvements of the retrieval (with the exception of the urban class). The aerosol retrievals are in any case carried out independently of each other for each pixel. It is up to the user to select which of the retrieved classes is the most appropriate to use for any pixel. Normally, this is done by comparison of cost, and based on geographical considerations e.g. it is unlikely to be continental aerosol in the remote ocean. With regards

to the urban class, its new similarity to the continental class may make it likely to give very similar retrieved parameters. However, this is not a problem since if the optical depth, effective radius, and cost are essentially identical, one needn't particularly worry about the nomenclature. Proximity to an urban extent might be a better method of flagging this aerosol.

The biomass burning class (in its current form) would not be suitable for comparison at this time.

Longer analysis periods (yearly, or seasonal) Current analysis of the new microphysical model retrievals has been limited to single months for each aerosol type. This obviously does not include seasonal, or year-on-year variations, both of which could affect the findings of this work. All of the modified classes have seasonal cycles. The increase in measurements would also provide far more co-located pixels for comparisons with model runs, and measurements such as AERONET or the Maritime Aerosol Network.

Extension to other satellites The ORAC retrieval can also be run using data from ATSR-2, SEVERI, and MODIS with relatively moderate alterations to the light scattering code, principally involving altering the channel wavelengths. The additional coverage afforded by these instruments would result in better temporal resolution of aerosol measurements from a consistent algorithm. However the variation in calibration and observing wavelengths inevitably leads to systematic biases between the measurements which would have to be accounted for.

Addition of further IR channels Current work within the Earth Observation Data Group includes the addition of the 11 and 12 μm channels to AATSR aerosol retrievals. In order for these retrievals to function, the lookup tables of aerosol optical properties will have to be extended. Some of the classes are already at this stage, for example the maritime class, but the fractal calculations for carbonaceous aerosol will be extremely time consuming to extend, as will non-spherical dust calculations. For the dust case, the refractive indices required are outside the range of those pre-calculated by Dubovik et al. [2006], and so would have to be calculated in-house.

The addition of these channels can be used either to further constrain the retrieval, or to add an

extra element to the state vector, the height of the aerosol plume. There is no sensitivity to aerosol height in the visible, but an IR forward model can take account of the temperature at the altitude of the plume.

Modelling volcanic ash aerosol Recent work took measurements of volcanic ash refractive index, which have been incorporated into ORAC retrievals [Carboni, 2011, priv. comm.]. However, the shape and size distribution of the aerosols have not been given full attention. Since the grounding of aircraft after the eruption of the Icelandic Eyjafjallajökull volcano in April 2010, a great deal of interest in reliable, near real-time volcanic ash products has developed. Ash can be harder to spot than SO_2 due to inconsistent shape, size, and RI values between different eruptions. It is also not always co-located with the gaseous emissions. In cases when it is, comparison with other retrievals such as SO_2 retrievals from IASI or OMI would be beneficial.

Continue modification of the biomass burning aerosol class Ageing of BB is a promising avenue for study of individual events. The model developed for this project is by no means complete, and currently based very much on studies focussed on African biomass burning. Comparing the current ageing model to one based on measurements from S. America, where the burning can tend to be more smouldering, would be an interesting exercise as would be comparisons of the ageing scheme with ageing of aerosol inside a box model, or even a full aerosol transport model.

Multiple aerosol layers It is possible to place aerosols in different atmospheric layers when calculating atmospheric transmission with the ORAC forward model. This could apply to situations where lofted mineral dust is blown over the Atlantic from west Africa at altitudes of 2–5 km [e.g. Otto et al., 2009], and we would expect marine aerosol in the lower levels of the atmosphere.

Another area of research within the ORAC group involves modelling clouds and aerosols within the same scene. Accurately modelling this and managing to retrieve the properties at the other end is extremely non-trivial but would hopefully help to resolve cloud flagging issues, which can be a strong source of error in ORAC retrievals, outside the scope of this project. In this manner, it

would be hoped that aerosol retrievals from AATSR would be able to gain better spatial coverage.

Further development of SPARCLE The development of SPARCLE continues, and changes to the specifications of the instrument may require additional optimisation calculations. The completed instrument would be used to characterise aerosol plumes, probably at ground level, and most likely from of urban aerosol. Field tests of aircraft emissions were previously carried out in this manner with an early prototype of the instrument, before optimisation.

The SPARCLE work has been placed last in the list of priorities, mainly because the timetable for additional work is controlled by other researchers.

Bibliography

Abel, S. J., J. M. Haywood, E. J. Highwood, J. Li, and P. R. Buseck, 2003: Evolution of biomass burning aerosol properties from an agricultural fire in southern Africa. *Geophysical Research Letters*, **30**(15):1783, doi:10.1029/2003GL017342.

Ackerman, S. A. and S. K. Cox, 1989: Surface weather observations of atmospheric dust over the southwest summer monsoon region. *Meteorology and Atmospheric Physics*, **41**:19–34, doi:10.1007/BF01032587.

Adachi, K. and P. R. Buseck, 2011: Atmospheric tar balls from biomass burning in Mexico. *Journal of Geophysical Research*, **116**(D5):D05204, doi:10.1029/2010JD015102.

Albrecht, B. A., 1989: Aerosols, Cloud Microphysics, and Fractional Cloudiness. *Science*, **245**:1227–1230, doi:10.1126/science.245.4923.1227.

Alexander, D. T. L., P. A. Crozier, and J. R. Anderson, 2008: Brown Carbon Spheres in East Asian Outflow and Their Optical Properties. *Science*, **321**(5890):833–836, doi:10.1126/science.1155296.

Alfaro, S. C., G. L., R. J. L., S. Lafon, A. Gaudichet, B. Chatenet, M. Maille, G. Cautenet, F. Lasserre, H. Cachier, and X. Y. Zhang, 2003: Chemical and optical characterization of aerosols measured in spring 2002 at the ACE-Asia supersite, Zhenbeitai, China. *Journal of Geophysical Research*, **108**:8641, doi:10.1029/2002JD003214.

Allen, G. A., J. Lawrence, and P. Koutrakis, 1999: Field validation of a semi-continuous method for aerosol black carbon (aethalometer) and temporal patterns of summertime hourly black carbon measurements in southwestern PA. *Atmospheric Environment*, **33**(5):817–823, doi:10.1016/S1352-2310(98)00142-3.

Almeida, M. P., J. José S. Andrade, and H. J. Herrmann, 2006: Aeolian Transport Layer. *Physical Review Letters*, **96**(1):018001, doi:10.1103/PhysRevLett.96.018001.

Andreae, M. O., 1983: Soot Carbon and Excess Fine Potassium: Long-Range Transport of Combustion-Derived Aerosols. *Science*, **220**(4602):1148–1151, doi:10.1126/science.220.4602.1148.

Andreae, M. O., E. Atlas, H. Cachier, W. R. Coffer, III, G. W. Harris, G. Helas, R. Koppmann, J.-P. Lacaux, and D. E. Ward, 1996: Trace Gas and Aerosol Emissions from Savanna Fires. *Biomass Burning and Global Change*, J. S. Levine, ed., The MIT Press, Cambridge. Massachusetts, volume 1, chapter 27, 278–295.

Arfken, G. B. and H. J. Weber, 1995: *Mathematical Methods for Physicists*. Academic Press, 4th edition, associated Legendre polynomials pp722–735; Bessel functions pp627–692.

Bagnold, R. A., 1941: *The Physics of Blown Sand and Desert Dunes*. Chapman and Hall, Methuen Inc.; Halsted Press.

Bahadur, R., Y. Feng, L. M. Russell, and V. Ramanathan, 2011: Impact of California's air pollution laws on black carbon and their implications for direct radiative forcing. *Atmospheric Environment*, **45**(5):1162–1167, doi:10.1016/j.atmosenv.2010.10.054.

Barnaba, F. and G. P. Gobbi, 2001: Lidar estimation of tropospheric aerosol extinction, surface area and volume: Maritime and desert-dust cases. *Journal of Geophysical Research*, **106**(D3):3005–3018, doi:10.1029/2000JD900492.

Bates, T., B. Huebert, J. Gras, F. Griffiths, and P. Durkee, 1998: International Global Atmospheric Chemistry (IGAC) project's first aerosol characterization experiment (ACE 1): Overview. *Journal of Geophysical Research*, **103**(D13):16297–16318, doi:10.1029/97JD03741.

Bates, T. S., D. J. Coffman, D. S. Covert, and P. K. Quinn, 2002: Regional marine boundary layer aerosol size distributions in the Indian, Atlantic, and Pacific Oceans: A comparison of INDOEX measurements with ACE-1, ACE-2, and Aerosols99. *Journal of Geophysical Research*, **107**(D19):8026, doi:10.1029/2001JD001174.

Bates, T. S., P. K. Quinn, D. S. Covert, D. J. Coffman, J. E. Johnson, and A. Wiedensohler, 2000: Aerosol physical properties and processes in the lower marine boundary layer: A comparison of shipboard sub-micron data from ACE-1 and ACE-2. *Tellus B*, **52**(2):258–272, doi:10.1034/j.1600-0889.2000.00021.x.

Berg, O. H., E. Swietlicki, and R. Krejci, 1998: Hygroscopic growth of aerosol particles in the marine boundary layer over the Pacific and Southern Oceans during the First Aerosol Characterization Experiment (ACE 1). *Journal of Geophysical Research*, **103**(D13):16535–16545, doi:10.1029/97JD02851.

Bhutiyani, M. R., V. S. Kale, and N. J. Pawar, 2007: Long-term trends in maximum, minimum and mean annual air temperatures across the Northwestern Himalaya during the twentieth century. *Climatic Change*, **85**(1):159–177, doi:10.1007/s10584-006-9196-1.

Bigg, E. K., J. L. Gras, and C. Evans, 1984: Origin of Aitken particles in remote regions of the Southern Hemisphere. *Journal of Atmospheric Chemistry*, **1**:203–214, doi:10.1007/BF00053841.

Blanchard, D. C., A. H. Woodcock, and R. J. Cipriano, 1984: The vertical distribution of the concentration of sea salt in the marine atmosphere near Hawaii. *Tellus B*, **36B**(2):118–125, doi:10.1111/j.1600-0889.1984.tb00233.x.

Bluth, G. J. S., S. D. Doiron, C. C. Schnetzler, A. J. Krueger, and L. S. Walter, 1992: Global Tracking of the SO_2 Clouds from the June, 1991 Mount Pinatubo Eruptions. *Geophysical Research Letters*, **19**(2):151–154, doi:10.1029/91GL02792.

Bohren, C. F. and D. R. Huffman, 1983: *Absorption and Scattering of Light by Small Particles*. Wiley-VCH, doi:10.1002/9783527618156.

Bond, T. C., 2007: Can warming particles enter global climate discussions? *Environmental Research Letters*, **2**(4):045030, doi:10.1088/1748-9326/2/4/045030.

Bond, T. C. and R. W. Bergstrom, 2006: Light Absorption by Carbonaceous Particles: An Investigative Review. *Aerosol Science and Technology*, **40**(1):27–67, doi:10.1080/02786820500421521.

Bond, T. C., G. Habib, and R. W. Bergstrom, 2006: Limitations in the enhancement of visible light absorption due to mixing state. *Journal of Geophysical Research*, **111**(D20):D20211, doi:10.1029/2006JD007315.

Bond, T. C., D. G. Streets, K. F. Yarber, S. M. Nelson, J.-H. Woo, and Z. Klimont, 2004: A technology-based global inventory of black and organic carbon emissions from combustion. *Journal of Geophysical Research*, **109**(D14):D14203, doi:10.1029/2003JD003697.

Buseck, P. R., B. Huang, and L. P. Keller, 1987: Electron microscope investigation of the structures of annealed carbons. *Energy & Fuels*, **1**(1):105–110, doi:10.1021/ef00001a020.

Buseck, P. R., D. J. Jacob, M. Posfai, J. Li, and J. R. Anderson, 2000: Minerals in the air: An environmental perspective. *International Geology Review*, **42**(7):577–593, doi:10.1080/00206810009465101, Symposium Honoring the Contributions of Professor Konrad Krauskopf, Stanford, CA, December, 1999.

Cachier, H., C. Liousse, M.-H. Pertuisot, A. Gaudichet, F. Echalar, and J.-P. Lacaux, 1996: African Fire Particulate Emissions and Atmospheric Influence. *Biomass Burning and Global Change*, J. S. Levine, ed., The MIT Press, Cambridge. Massachusetts, volume 1, chapter 41, 428–440.

Calcote, H. F., 1981: Mechanisms of soot nucleation in flames–A critical review. *Combustion and Flame*, **42**:215–242, doi:10.1016/0010-2180(81)90159-0.

Campmany, E., R. G. Grainger, S. M. Dean, and A. M. Sayer, 2009: Automatic detection of ship tracks in ATSR-2 satellite imagery. *Atmospheric Chemistry and Physics*, **9**(6):1899–1905, doi:10.5194/acp-9-1899-2009.

Capes, G., B. Johnson, G. McFiggans, P. I. Williams, J. Haywood, and H. Coe, 2008: Aging of biomass burning aerosols over West Africa: Aircraft measurements of chemical composition, microphysical properties, and emission ratios. *Journal of Geophysical Research*, **113**(D23):D00C15, doi:10.1029/2008JD009845.

Cavalli, F., M. C. Facchini, S. Decesari, M. Mircea, L. Emblico, S. Fuzzi, D. Ceburnis, Y. J. Yoon, C. D. O'Dowd, J.-P. Putaud, and A. Dell'Acqua, 2004: Advances in characterization of size-resolved organic matter in marine aerosol over the North Atlantic. *Journal of Geophysical Research*, **109**(D24):D24215, doi:10.1029/2004JD005137.

Chakrabarty, R. K., H. Moosmüller, L.-W. A. Chen, K. Lewis, W. P. Arnott, C. Mazzoleni, M. K. Dubey, C. E. Wold, W. M. Hao, and S. M. Kreidenweis, 2010: Brown carbon in tar balls from smoldering biomass combustion. *Atmospheric Chemistry and Physics*, **10**(13):6363–6370, doi:10.5194/acp-10-6363-2010.

Chand, D., P. Guyon, P. Artaxo, O. Schmid, G. P. Frank, L. V. Rizzo, O. L. Mayol-Bracero, L. V. Gatti, and M. O. Andreae, 2006: Optical and physical properties of aerosols in the boundary layer and free troposphere over the Amazon Basin during the biomass burning season. *Atmospheric Chemistry and Physics*, **6**(10):2911–2925, doi:10.5194/acp-6-2911-2006.

Charlson, R. J., J. E. Lovelock, M. O. Andreae, and S. G. Warren, 1987: Oceanic phytoplankton, atmospheric sulphur, cloud albedo and climate. *Nature*, **326**(6114):655–661, doi:10.1038/326655a0.

Chen, L.-W. A., B. G. Doddridge, R. R. Dickerson, J. C. Chow, P. K. Mueller, J. Quinn, and W. A. Butler, 2001: Seasonal variations in elemental carbon aerosol, carbon monoxide and sulfur dioxide: Implications for sources. *Geophysical Research Letters*, **28**(9):1711–1714, doi:10.1029/2000GL012354.

Chen, W.-T., R. A. Kahn, D. Nelson, K. Yau, and J. H. Seinfeld, 2008: Sensitivity of multiangle imaging to the optical and microphysical properties of biomass burning aerosols. *Journal of Geophysical Research*, **113**(D10):D10203, doi:10.1029/2007JD009414.

Chou, C., P. Formenti, M. Maille, P. Ausset, G. Helas, M. Harrison, and S. Osborne, 2008: Size distribution, shape, and composition of mineral dust aerosols collected during the African Monsoon Multidisciplinary Analysis Special Observation Period 0: Dust and Biomass-Burning Experiment field campaign in Niger, January 2006. *Journal of Geophysical Research*, **113**:D00C10, doi:10.1029/2008JD009897.

Clapp, M. L., D. R. Worsnop, and R. E. Miller, 1995: Frequency-dependent optical constants of water ice obtained directly from aerosol extinction spectra. *The Journal of Physical Chemistry*, **99**(17):6317–6326, doi:10.1021/j100017a010.

Claquin, T., M. Schülz, and Y. J. Balkanski, 1999: Modeling the mineralogy of atmospheric dust sources. *Journal of Geophysical Research*, **104**(D18):22,243–22,256, doi:10.1029/1999JD900416.

Claquin, T., M. Schülz, Y. J. Balkanski, and O. Boucher, 1998: Uncertainties in assessing radiative forcing by mineral dust. *Tellus B*, **50**(5):491–505, doi:10.1034/j.1600-0889.1998.t01-2-00007.x.

Clarke, A. D., D. Davis, V. N. Kapustin, F. Eisele, G. Chen, I. Paluch, D. Lenschow, A. R. Bandy, D. Thornton, K. Moore, L. Mauldin, D. Tanner, M. Litchy, M. A. Carroll, J. Collins, and G. Albercook, 1998: Particle Nucleation in the Tropical Boundary Layer and Its Coupling to Marine Sulfur Sources. *Science*, **282**(5386):89–92, doi:10.1126/science.282.5386.89.

Clarke, A. D. and V. N. Kapustin, 2002: A Pacific Aerosol Survey. Part I: A Decade of Data on Particle Production, Transport, Evolution, and Mixing in the Troposphere. *Journal of the Atmospheric Sciences*, **59**(3):363–382, doi:10.1175/1520-0469(2002)059<0363:APASPI>2.0.CO;2.

Colbeck, I., ed., 1998: *Physical and Chemical Properties of Aerosols*. Blackie Academic & Professional, 1st edition.

Cook, J. and E. J. Highwood, 2004: Climate response to tropospheric absorbing aerosols in an intermediate general-circulation model. *Quarterly Journal of the Royal Meteorological Society*, **130**(596):175–191, doi:10.1256/qj.03.64.

Cooke, W. F. and J. J. N. Wilson, 1996: A global black carbon aerosol model. *Journal of Geophysical Research*, **101**(D14):19395–19409, doi:10.1029/96JD00671.

Crosier, J., J. D. Allan, H. Coe, K. N. Bower, P. Formenti, and P. I. Williams, 2007: Chemical composition of summertime aerosol in the Po Valley (Italy), northern Adriatic and Black Sea. *Quarterly Journal of the Royal Meteorological Society*, **133**(S1):61–75, doi:10.1002/qj.88. http://dx.doi.org/10.1002/qj.88

Cruzan, O. R., 1962: Translational addition theorems for spherical vector wave functions. *Quarterly of Applied Mathmatics*, **20**:33–40.

Curtis, D. B., B. Meland, M. Aycibin, N. P. Arnold, V. H. Grassian, M. A. Young, and P. D. Kleiber, 2008: A laboratory investigation of light scattering from representative components of mineral dust aerosol at a wavelength of 550 nm. *Journal of Geophysical Research*, **113**:D08210, doi:10.1029/2007JD009387.

Dinar, E., A. A. Riziq, C. Spindler, C. Erlick, G. Kiss, and Y. Rudich, 2008: The complex refractive index of atmospheric and model humic-like substances (HULIS) retrieved by a cavity ring down aerosol spectrometer (CRD-AS). *Faraday Discussions*, **137**:279–295, doi:10.1039/B703111D.

Diner, D. J., W. A. Abdou, T. Ackerman, K. Crean, H. R. Gordon, R. A. Kahn, J. V. Martonchik, S. McMuldroch, S. Paradise, B. Pinty, M. Verstraete, M. Wang, and R. A. West, 2008: MISR Level 2 Aerosol Retrieval. Algorithm Theroretical Basis Document JPL D-11400, Rev. G, Jet Propulsion Laboratory, California Institute of Technology. http://eospso.gsfc.nasa.gov/eos_homepage/for_scientists/atbd/viewInstrument.php?instrument=19

Diner, D. J., W. A. Abdou, H. R. Gordon, R. A. Kahn, Y. Knyazikhin, J. V. Martonchik, D. McDonald, S. McMuldroch, R. Myneni, and R. A. West, 1999: MISR Level 2 Ancillary Products and Datasets. Algorithm Theroretical Basis Document JPL D-13402, Rev. B, Jet Propulsion Laboratory, California Institute of Technology. http://eospso.gsfc.nasa.gov/eos_homepage/for_scientists/atbd/viewInstrument.php?instrument=19

Dockery, D. W., C. A. Pope, X. Xu, J. D. Spengler, J. H. Ware, M. E. Fay, B. G. Ferris, and F. E. Speizer, 1993: An Association between Air Pollution and Mortality in Six U.S. Cities. *New England Journal of Medicine*, **329**(24):1753–1759, doi:10.1056/NEJM199312093292401.

Doherty, S. J., S. G. Warren, T. C. Grenfell, A. D. Clarke, and R. E. Brandt, 2010: Light-absorbing impurities in Arctic snow. *Atmospheric Chemistry and Physics*, **10**(23):11647–11680, doi:10.5194/acp-10-11647-2010.

Doicu, A., T. Wriedt, and Y. A. Eremin, 2006: *Light Scattering by Systems of Particles: Null-Field Method with Discrete Sources - Theory and Programs*, volume 124 of *Optical Sciences*. Springer-Verlag, Berlin Heidelberg.

Draine, B. T. and P. J. Flatau, 1994: Discrete-dipole approximation for scattering calculations. *Journal of the Optical Society of America A*, **11**(4):1491–1499, doi:10.1364/JOSAA.11.001491.

Dubovik, O., B. Holben, T. F. Eck, A. Smirnov, Y. J. Kaufman, M. D. King, D. Tanre, and I. Slutsker, 2002: Variability of absorption and optical properties of key aerosol types observed in worldwide locations. *Journal of the Atmospheric Sciences*, **59**(3):590–608, doi:10.1175/1520-0469(2002)059<0590:VOAAOP>2.0.CO;2.

Dubovik, O. and M. D. King, 2000: A flexible inversion algorithm for retrieval of aerosol optical properties from Sun and sky radiance measurements. *Journal of Geophysical Research*, **105**(D16):20,673–20,696, doi:10.1029/2000JD900282.

Dubovik, O., A. Sinyuk, T. Lapyonok, B. N. Holben, M. Mishchenko, P. Yang, T. F. Eck, H. Volten, O. Munoz, B. Veihelmann, W. J. van der Zande, J.-F. Leon, M. Sorokin, and I. Slutsker, 2006: Application of spheroid models to account for aerosol particle nonsphericity in remote sensing of desert dust. *Journal of Geophysical Research*, **111**:D11208, doi:10.1029/2005JD006619.

Duncan, B. N., R. V. Martin, A. C. Staudt, R. Yevich, and J. A. Logan, 2003: Interannual and seasonal variability of biomass burning emissions constrained by satellite observations. *Journal of Geophysical Research*, **108**(D2):4100, doi:10.1029/2002JD002378.

Eck, T. F., B. N. Holben, D. E. Ward, O. Dubovik, J. S. Reid, A. Smirnov, M. M. Mukelabai, N. C. Hsu, N. T. O'Neill, and I. Slutsker, 2001: Characterization of the optical properties of biomass burning aerosols in Zambia during the 1997 ZIBBEE field campaign. *Journal of Geophysical Research*, **106**(D4):3425–3448, doi:10.1029/2000JD900555.

Egan, W. G. and T. W. Hilgeman, 1979: *Optical Properties of Inhomogeneous Materials : Applications to Geology, Astronomy, Chemistry, and Engineering*. Academic Press, New York.

Esselborn, M., M. Wirth, A. Fix, B. Weinzierl, K. Rasp, M. Tesche, and A. Petzold, 2009: Spatial distribution and optical properties of Saharan dust observed by airborne high spectral resolution lidar during SAMUM 2006. *Tellus B*, **61**(1):131–143, doi:10.1111/j.1600-0889.2008.00394.x.

FAO / UNESCO, 2003: Digital Soil Map of the World and Derived Soil Properties. CD-ROM, ISBN: 9789251048955. `http://www.fao.org/icatalog/search/dett.asp?aries_id=103540`

Fécan, F., B. Marticorena, and G. Bergametti, 1999: Parametrization of the increase of the aeolian erosion threshold wind friction velocity due to soil moisture for arid and semi-arid areas. *Annales Geophysicae*, **17**(1):149–157, doi:10.1007/s00585-999-0149-7.

Fiebig, M., C. Stein, F. Schrder, P. Feldpausch, and A. Petzold, 2005: Inversion of data containing information on the aerosol particle size distribution using multiple instruments. *Journal of Aerosol Science*, **36**(11):1353–1372, doi:10.1016/j.jaerosci.2005.01.004.

Filippov, A. V., M. Zurita, and D. E. Rosner, 2000: Fractal-like Aggregates: Relation between Morphology and Physical Properties. *Journal of Colloid and Interface Science*, **229**(1):261–273, doi:10.1006/jcis.2000.7027.

Fischer-Bruns, I., J. Feichter, S. Kloster, and A. Schneidereit, 2010: How present aerosol pollution from North America impacts North Atlantic climate. *Tellus A*, **62**(4):579–589, doi:10.1111/j.1600-0870.2010.00446.x.

Fitzgerald, J. W., 1991: Marine aerosols: A review. *Atmospheric Environment. Part A. General Topics*, **25**(3-4):533–545, doi:10.1016/0960-1686(91)90050-H.

Flanner, M. G., C. S. Zender, P. G. Hess, N. M. Mahowald, T. H. Painter, V. Ramanathan, and P. J. Rasch, 2009: Springtime warming and reduced snow cover from carbonaceous particles. *Atmospheric Chemistry and Physics*, **9**(7):2481–2497, doi:10.5194/acp-9-2481-2009.

Flanner, M. G., C. S. Zender, J. T. Randerson, and P. J. Rasch, 2007: Present-day climate forcing and response from black carbon in snow. *Journal of Geophysical Research*, **112**(D11):D11202, doi:10.1029/2006JD008003.

Fuller, K. A., W. C. Malm, and S. M. Kreidenweis, 1999: Effects of mixing on extinction by carbonaceous particles. *Journal of Geophysical Research*, **104**(D13):15941–15954, doi:10.1029/1998JD100069.

Gao, Y., S. B. Chen, and L. E. Yu, 2007: Efflorescence relative humidity of airborne sodium chloride particles: A theoretical investigation. *Atmospheric Environment*, **41**(9):2019–2023, doi:10.1016/j.atmosenv.2006.12.014.

Ghosh, G., 1999: Dispersion-equation coefficients for the refractive index and birefringence of calcite and quartz crystals. *Optics Communications*, **163**(1-3):95–102, doi:10.1016/S0030-4018(99)00091-7.

Giannini, A., M. Biasutti, and M. M. Verstraete, 2008: A climate model-based review of drought in the Sahel: Desertification, the re-greening and climate change. *Global and Planetary Change*, **64**(3-4):119–128, doi:10.1016/j.gloplacha.2008.05.004.

Gong, S. L. and L. A. Barrie, 2003: Simulating the impact of sea salt on global nss sulphate aerosols. *Journal of Geophysical Research*, **108**(D16):4516, doi:10.1029/2002JD003181.

Gong, S. L., L. A. Barrie, and M. Lazare, 2002: Canadian Aerosol Module (CAM): A size-segregated simulation of atmospheric aerosol processes for climate and air quality models. 2. Global sea-salt aerosol and its budgets. *Journal of Geophysical Research*, **107**(D24):4779, doi:10.1029/2001JD002004.

Grainger, R. G. and E. J. Highwood, 2003: Changes in stratospheric composition, chemistry, radiation and climate caused by volcanic eruptions. *Volcanic Degassing*, C. Oppenheimer, D. M. Pyle, and J. Barclay, eds., Geological Society, volume 123 of *Special Publications*, 329–347.

Grainger, R. G., J. Lucas, G. E. Thomas, and G. B. Ewen, 2004: Calculation of Mie derivatives. *Applied Optics*, **43**(28):5386–5393, doi:10.1364/AO.43.005386.

Gras, J. L. and G. P. Ayers, 1983: Marine Aerosol at Southern Mid-Latitudes. *Journal of Geophysical Research*, **88**(C15):10661–10666, doi:10.1029/JC088iC15p10661.

Guyon, P., B. Graham, G. C. Roberts, O. L. Mayol-Bracero, W. Maenhaut, P. Artaxo, and M. O. Andreae, 2004: Sources of optically active aerosol particles over the Amazon forest. *Atmospheric Environment*, **38**(7):1039–1051, doi:10.1016/j.atmosenv.2003.10.051.

Gwaze, P., O. Schmid, H. J. Annegarn, M. O. Andreae, J. Huth, and G. Helas, 2006: Comparison of three methods of fractal analysis applied to soot aggregates from wood combustion. *Journal of Aerosol Science*, **37**(7):820–838, doi:10.1016/j.jaerosci.2005.06.007.

Hand, J. L., D. E. Day, G. M. McMeeking, E. J. T. Levin, C. M. Carrico, S. M. Kreidenweis, W. C. Malm, A. Laskin, and Y. Desyaterik, 2010: Measured and modeled humidification factors of fresh smoke particles from biomass burning: role of inorganic constituents. *Atmospheric Chemistry and Physics*, **10**(13):6179–6194, doi:10.5194/acp-10-6179-2010.

Hand, J. L., W. C. Malm, A. Laskin, D. Day, T. Lee, C. Wang, C. Carrico, J. Carrillo, J. P. Cowin, J. J. Collett, and M. J. Iedema, 2005: Optical, physical, and chemical properties of tar balls observed during the Yosemite Aerosol Characterization Study. *Journal of Geophysical Research*, **110**(D21):D21210, doi:10.1029/2004JD005728.

Hänel, G., 1976: The properties of atmospheric aerosol particles as functions of the relative humidity at thermodynamic equilibrium with the surrounding moist air. *Advances in Geophysics*, **19**:74–188, doi:10.1016/S0065-2687(08)60142-9.

Hansen, J., M. Sato, and R. Ruedy, 1997: Radiative forcing and climate response. *Journal of Geophysical Research*, **102**(D6):6831–6864, doi:10.1029/96JD03436.

Haywood, J. M., P. N. Francis, M. D. Glew, and J. P. Taylor, 2001: Optical properties and direct radiative effect of Saharan dust: A case study of two Saharan dust outbreaks using aircraft data. *Journal of Geophysical Research*, **106**(D16):18,417–18,430, doi:10.1029/2000JD900319.

Haywood, J. M., P. N. Francis, S. R. Osborne, M. D. Glew, N. Loeb, E. J. Highwood, D. Tanré, G. Myhre, P. Formenti, and E. Hirst, 2003: Radiative properties and direct radiative effect of Saharan dust measured by the C-130 aircraft during SHADE: 1. Solar spectrum. *Journal of Geophysical Research*, **108**(D18):8577, doi:10.1029/2002JD002687.

Haywood, J. M., J. Pelon, P. Formenti, N. Bharmal, M. Brooks, G. Capes, P. Chazette, C. Chou, S. Christopher, H. Coe, J. Cuesta, Y. Derimian, K. Desboeufs, G. Greed, M. Harrison, B. Heese, E. J. Highwood, B. Johnson, M. Mallet, B. Marticorena, J. Marsham, S. Milton, G. Myhre, S. R. Osborne, D. J. Parker, J. L. Rajot, M. Schülz, A. Slingo, D. Tanré, and P. Tulet, 2008: Overview of the Dust and Biomass-burning Experiment and African Monsoon Multidisciplinary Analysis Special Observing Period-0. *Journal of Geophysical Research*, **113**:D00C17, doi:10.1029/2008JD010077.

Haywood, J. M. and K. P. Shine, 1995: The effect of anthropogenic sulfate and soot aerosol on the clear sky planetary radiation budget. *Geophysical Research Letters*, **22**(5):603–606, doi:10.1029/95GL00075.

Hecht, E., 2002: *Optics*. Addison Wesley, San Francisco, 4th edition.

Hegg, D. A., J. Livingston, P. V. Hobbs, T. Novakov, and P. Russell, 1997: Chemical apportionment of aerosol column optical depth off the mid-Atlantic coast of the United States. *Journal of Geophysical Research*, **102**(D21):25293–25303, doi:10.1029/97JD02293.

Heintzenberg, J., 2009: The SAMUM-1 experiment over Southern Morocco: overview and introduction. *Tellus B*, **91**(1):2–11, doi:10.1111/j.1600-0889.2008.00403.x.

Heintzenberg, J., W. Birmili, A. Wiedensohler, A. Nowak, and T. Tuch, 2004: Structure, variability and persistence of the submicrometre marine aerosol. *Tellus B*, **56**(4):357–367, doi:10.1111/j.1600-0889.2004.00115.x.

Helble, J., M. Neville, and A. F. Sarofim, 1988: Aggregate formation from vaporized ash during pulverized coal combustion. *Symposium (International) on Combustion*, **21**(1):411–417, doi:10.1016/S0082-0784(88)80268-6.

Henyey, L. G. and J. L. Greenstein, 1941: Diffuse radiation in the Galaxy. *The Astrophysical Journal*, **93**:70–83, doi:10.1086/144246.

Hess, M., P. Koepke, and I. Schult, 1998: Optical Properties of Aerosols and Clouds: The Software Package OPAC. *Bulletin of the American Meteorological Society*, **79**(5):831–844, doi:10.1175/1520-0477(1998)079<0831:OPOAAC>2.0.CO;2.

Highwood, E. J., 2009: Suggested refractive indices and aerosol size parameters for use in radiative effect calculations and satellite retrievals. ADIENT / APPRAISE CP2 technical report, Department of Meteorology, University of Reading, 2nd Draft. `http://www.reading.ac.uk/adient/refractiveindices.html`

Hildemann, L. M., D. B. Klinedinst, G. A. Klouda, L. A. Currie, and G. R. Cass, 1994: Sources of Urban Contemporary Carbon Aerosol. *Environmental Science & Technology*, **28**(9):1565–1576, doi:10.1021/es00058a006.

Hitzenberger, R., A. Berner, H. Giebl, R. Kromp, S. M. Larson, A. Rouc, A. Koch, S. Marischka, and H. Puxbaum, 1999: Contribution of carbonaceous material to cloud condensation nuclei concentrations in European background (Mt. Sonnblick) and urban (Vienna) aerosols. *Atmospheric Environment*, **33**(17):2647–2659, doi:10.1016/S1352-2310(98)00391-4.

Hoffer, A., A. Gelencsér, M. Blazsó, P. Guyon, P. Artaxo, and M. O. Andreae, 2006a: Diel and seasonal variations in the chemical composition of biomass burning aerosol. *Atmospheric Chemistry and Physics*, **6**(11):3505–3515, doi:10.5194/acp-6-3505-2006.

Hoffer, A., A. Gelencsér, P. Guyon, G. Kiss, O. Schmid, G. P. Frank, P. Artaxo, and M. O. Andreae, 2006b: Optical properties of humic-like substances (HULIS) in biomass-burning aerosols. *Atmospheric Chemistry and Physics*, **6**(11):3563–3570, doi:10.5194/acp-6-3563-2006.

Holben, B. N., T. F. Eck, I. Slutsker, D. Tanré, J. P. Buis, A. Setzer, E. Vermote, J. A. Reagan, Y. J. Kaufman, T. Nakajima, F. Lavenu, I. Jankowiak, and A. Smirnov, 1998: AERONET – A Federated Instrument Network and Data Archive for Aerosol Characterization. *Remote Sensing of Environment*, **66**(1):1–16, doi:10.1016/S0034-4257(98)00031-5.

Homann, K. H., 1967: Carbon formation in premixed flames. *Combustion and Flame*, **11**(4):265–287, doi:10.1016/0010-2180(67)90017-X.

Hoppel, W. A., J. W. Fitzgerald, G. M. Frick, R. E. Larson, and E. J. Mack, 1989: Atmospheric Aerosol Size Distributions and Optical Properties Found in the Marine Boundary Layer Over the Atlantic Ocean. NRL Report 9188, Naval Research Laboratory, Washington D. C.

Hoppel, W. A., G. M. Frick, J. W. Fitzgerald, and R. E. Larson, 1994: Marine boundary layer measurements of new particle formation and the effects nonprecipitating clouds have on aerosol size distribution. *Journal of Geophysical Research*, **99**(D7):14443–14459, doi:10.1029/94JD00797.

Irshad, R., R. G. Grainger, D. M. Peters, R. A. McPheat, K. M. Smith, and G. Thomas, 2009: Laboratory measurements of the optical properties of sea salt aerosol. *Atmospheric Chemistry and Physics*, **9**(1):221–230, doi:10.5194/acp-9-221-2009.

Ito, A. and J. E. Penner, 2005: Historical emissions of carbonaceous aerosols from biomass and fossil fuel burning for the period 1870–2000. *Global Biogeochemical Cycles*, **19**(2):GB2028, doi:10.1029/2004GB002374.

Jacobson, M. C., H.-C. Hansson, K. J. Noone, and R. J. Charlson, 2000: Organic atmospheric aerosols: Review and state of the science. *Reviews of Geophysics*, **38**(2):267–294, doi:10.1029/1998RG000045.

Jacobson, M. Z., 2000: A physically-based treatment of elemental carbon optics: Implications for global direct forcing of aerosols. *Geophysical Research Letters*, **27**(2):217–220, doi:10.1029/1999GL010968.

— 2001: Strong radiative heating due to the mixing state of black carbon in atmospheric aerosols. *Nature*, **409**(6821):695–697, doi:10.1038/35055518.

— 2002: Control of fossil-fuel particulate black carbon and organic matter, possibly the most effective method of slowing global warming. *Journal of Geophysical Research*, **107**(D19):4410, doi:10.1029/2001JD001376.

— 2003: Reply to comment by J. E. Penner on "Control of fossil-fuel particulate black carbon and organic matter, possibly the most effective method of slowing global warming". *Journal of Geophysical Research*, **108**(D24):4772, doi:10.1029/2003JD003403.

Jacobson, M. Z., R. P. Turco, E. J. Jensen, and O. B. Toon, 1994: Modeling coagulation among particles of different composition and size. *Atmospheric Environment*, **28**(7):1327–1338, doi:10.1016/1352-2310(94)90280-1.

Jacquinet-Husson, N., N. A. Scott, A. Chédin, L. Crèpeau, et al., 2008: The GEISA spectroscopic database: Current and future archive for Earth and planetary atmosphere studies. *Journal of Quantitative Spectroscopy & Radiative Transfer*, **109**:1043–1059, doi:10.1016/j.jqsrt.2007.12.015. `http://munk.ipsl.jussieu.fr/etherTypo/?id=1060`

Jansen, K. L., T. V. Larson, J. Q. Koenig, T. F. Mar, C. Fields, J. Stewart, and M. Lippmann, 2005: Associations between Health Effects and Particulate Matter and Black Carbon in Subjects with Respiratory Disease. *Environmental Health Perspectives*, **113**(12):1741–1746, doi:10.1289/ehp.8153.

Jarvis, N. L. and M. A. Scheiman, 1967: Surface Potentials of Aqueous Electrolyte Solutions. NRL Formal Reports FR-6583, Naval Research Laboratory, Washington, D.C.

Jeong, S.-J., C.-H. Ho, M. E. Brown, J.-S. Kug, and S. Piao, 2011: Browning in desert boundaries in Asia in recent decades. *Journal of Geophysical Research*, **116**(D2):D02103, doi:10.1029/2010JD014633.

Johnson, B. T., S. R. Osborne, J. M. Haywood, and M. A. J. Harrison, 2008: Aircraft measurements of biomass burning aerosol over West Africa during DABEX. *Journal of Geophysical Research*, **113**(D23):D00C06, doi:10.1029/2007JD009451.

Kaaden, N., A. Massling, A. Schladitz, T. Müller, K. Kandler, L. Schütz, B. Weinzierl, A. Petzold, M. Tesche, S. Leinert, C. Deutscher, M. Ebert, S. Weinbruch, and A. Wiedensohler, 2009: State of mixing, shape factor, number size distribution, and hygroscopic growth of the Saharan anthropogenic and mineral dust aerosol at Tinfou, Morocco. *Tellus B*, **61**(1):51–63, doi:10.1111/j.1600-0889.2008.00388.x.

Kahn, R., A. Petzold, M. Wendisch, E. Bierwirth, T. Dinter, M. Esselborn, M. Fiebig, B. Heese, P. Knippertz, D. Müller, A. Schladitz, and W. V. Hoyningen-huene, 2009: Desert dust aerosol air mass mapping in the western Sahara, using particle properties derived from space-based multi-angle imaging. *Tellus B*, **61**(1):239–251, doi:10.1111/j.1600-0889.2008.00398.x.

Kalashnikova, O. V., R. Kahn, I. N. Sokolik, and W.-H. Li, 2005: Ability of multiangle remote sensing observations to identify and distinguish mineral dust types: Optical models and retrievals of optically thick plumes. *Journal of Geophysical Research*, **110**(D18):D18S14, doi:10.1029/2004JD004550.

Kalashnikova, O. V. and I. N. Sokolik, 2004: Modeling the radiative properties of nonspherical soil-derived mineral aerosols. *Journal of Quantitative Spectroscopy & Radiative Transfer*, **87**(2):137–166, doi:10.1016/j.jqsrt.2003.12.026.

Kaluza, P., A. Kölzsch, M. T. Gastner, and B. Blasius, 2010: The complex network of global cargo ship movements. *Journal of The Royal Society Interface*, **7**(48):1093–1103, doi:10.1098/rsif.2009.0495.

Kandler, K., N. Benker, U. Bundke, E. Cuevas, M. Ebert, P. Knippertz, S. Rodriguez, L. Schuetz, and S. Weinbruch, 2007: Chemical composition and complex refractive index of Saharan Mineral Dust at Izana, Tenerife (Spain) derived by electron microscopy. *Atmospheric Environment*, **41**(37):8058–8074, doi:10.1016/j.atmosenv.2007.06.047.

Katoshevski, D., A. Nenes, and J. H. Seinfeld, 1999: A study of processes that govern the maintenance of aerosols in the marine boundary layer. *Journal of Aerosol Science*, **30**(4):503–532, doi:10.1016/S0021-8502(98)00740-X.

Katrinak, K. A., P. Rez, P. R. Perkes, and P. R. Buseck, 1993: Fractal geometry of carbonaceous aggregates from an urban aerosol. *Environmental Science & Technology*, **27**(3):539–547, doi:10.1021/es00040a013.

Kaufman, Y. J. and R. S. Fraser, 1997: The Effect of Smoke Particles on Clouds and Climate Forcing. *Science*, **277**(5332):1636–1639, doi:10.1126/science.277.5332.1636.

Kaufman, Y. J., I. Koren, L. A. Remer, D. Tanré, P. Ginoux, and S. Fan, 2005: Dust transport and deposition observed from the Terra-Moderate Resolution Imaging Spectroradiometer (MODIS) spacecraft over the Atlantic Ocean. *Journal of Geophysical Research*, **110**(D10):D10S12, doi:10.1029/2003JD004436.

Köpke, P., M. Hess, I. Schult, and E. P. Shettle, 1997: Global Aerosol Data Set. Technical Report 243, Max Planck Institut für Meteorologie, Bundesstrasse 55, D-20146, Hamburg, Germany. `http://www.mpimet.mpg.de/en/wissenschaft/publikationen/mpi-report-1987-2004.html`

Kotchenruther, R. A. and P. V. Hobbs, 1998: Humidification factors of aerosols from biomass burning in Brazil. *Journal of Geophysical Research*, **103**(D24):32081–32089, doi:10.1029/98JD00340.

Köylü, U. O. and G. M. Faeth, 1992: Structure of overfire soot in buoyant turbulent diffusion flames at long residence times. *Combustion and Flame*, **89**(2):140–156, doi:10.1016/0010-2180(92)90024-J.

Köylü, U. O., G. M. Faeth, T. L. Farias, and M. G. Carvalho, 1995: Fractal and projected structure properties of soot aggregates. *Combustion and Flame*, **100**(4):621–633, doi:10.1016/0010-2180(94)00147-K.

Kreckov, G. M., 1993: Models of atmospheric aerosols. *Aerosol Effects on Climate*, S. G. Jennings, ed., University of Arizona Press, Tucson, Arizona.

Larson, S. M., G. R. Cass, and H. A. Gray, 1989: Atmospheric Carbon Particles and the Los Angeles Visibility Problem. *Aerosol Science and Technology*, **10**(1):118–130, doi:10.1080/02786828908959227.

Latha, K. M. and K. V. S. Badarinath, 2005: Seasonal variations of black carbon aerosols and total aerosol mass concentrations over urban environment in India. *Atmospheric Environment*, **39**(22):4129–4141, doi:10.1016/j.atmosenv.2005.04.004.

Laurent, B., B. Marticorena, G. Bergametti, J. F. Leon, and N. M. Mahowald, 2008: Modeling mineral dust emissions from the Sahara desert using new surface properties and soil database. *Journal of Geophysical Research*, **113**:D14218, doi:10.1029/2007JD009484.

Levy, R. C., L. A. Remer, and O. Dubovik, 2007: Global aerosol optical properties and application to Moderate Resolution Imaging Spectroradiometer aerosol retrieval over land. *Journal of Geophysical Research*, **112**(D13):D13210, doi:10.1029/2006JD007815.

Levy, R. C., L. A. Remer, D. Tanré, Y. J. Kaufman, C. Ichoku, B. N. Holben, J. M. Livingston, P. B. Russell, and H. Maring, 2003: Evaluation of the Moderate-Resolution Imaging Spectroradiometer (MODIS) retrievals of dust aerosol over the ocean during PRIDE. *Journal of Geophysical Research*, **108**(D19):8594, doi:10.1029/2002JD002460.

Levy, R. C., L. A. Remer, D. Tanré, S. Mattoo, and Y. J. Kaufman, 2009: Algorithm for remote sensing of tropospheric arerosol over dark targets from MODIS. Algorithm Theoretical Basis Document MOD04/MYD04, NASA Goddard Space Flight Center. `http://modis-atmos.gsfc.nasa.gov/MOD04_L2/atbd.html`

Lewis, E. R. and S. E. Schwartz, 2004: *Sea Salt Aerosol Production: Mechanisms, Methods, Measurements, and Models—A Critical Review*, volume 152 of *Geophysical Monograph*. American Geophysical Union, 2000 Florida Avenue, N. W., Washington, DC 20009.

— 2006: Comment on 'Size distribution of sea-salt emissions as a function of relative humidity'. *Atmospheric Environment*, **40**(3):588–590, doi:10.1016/j.atmosenv.2005.08.043.

Li, H., C. Liu, L. Bi, P. Yang, and G. W. Kattawar, 2010: Numerical accuracy of "equivalent" spherical approximations for computing ensemble-averaged scattering properties of fractal soot aggregates. *Journal of Quantitative Spectroscopy & Radiative Transfer*, **111**(14):2127–2132, doi:10.1016/j.jqsrt.2010.05.009.

Li, J., M. Pósfai, P. V. Hobbs, and P. R. Buseck, 2003: Individual aerosol particles from biomass burning in southern Africa: 2. Compositions and aging of inorganic particles. *Journal of Geophysical Research*, **108**(D13):8484, doi:10.1029/2002JD002310.

Lighty, J. S., J. M. Veranth, and A. F. Sarofim, 2000: Combustion Aerosols: Factors Governing Their Size and Composition and Implications to Human Health. *Journal of the Air & Waste Management Association*, **50**(9):1565–1618. `http://secure.awma.org/journal/Abstract.aspx?id=232`

Liousse, C., J. E. Penner, C. Chuang, J. J. Walton, H. Eddleman, and H. Cachier, 1996: A global three-dimensional model study of carbonaceous aerosols. *Journal of Geophysical Research*, **101**(D14):19411–19432, doi:10.1029/95JD03426.

Liu, L. and M. I. Mishchenko, 2005: Effects of aggregation on scattering and radiative properties of soot aerosols. *Journal of Geophysical Research*, **110**(D11):D11211, doi:10.1029/2004JD005649.

Long, L. L., M. R. Querry, R. J. Bell, and R. W. Alexander, 1993: Optical properties of calcite and gypsum in crystalline and powdered form in the infrared and far-infrared. *Infrared Physics*, **34**(2):191–201, doi:10.1016/0020-0891(93)90008-U.

Lund Myhre, C. E. and C. J. Nielsen, 2004: Optical properties in the UV and visible spectral region of organic acids relevant to tropospheric aerosols. *Atmospheric Chemistry and Physics*, **4**(7):1759–1769, doi:10.5194/acp-4-1759-2004.

Mackowski, D. W., 2011: *MSTM - A multiple sphere T-matrix FORTRAN code for use on parallel computer clusters. Version 2.1*. Department of Mechanical Engineering, Auburn University, Auburn, AL 36849, USA. `http://eng.auburn.edu/users/dmckwski/scatcodes`

Mackowski, D. W. and M. I. Mishchenko, 1996: Calculation of the T-matrix and the scattering matrix for ensembles of spheres. *Journal of the Optical Society of America A.*, **13**(11):2266–2278, doi:10.1364/JOSAA.13.002266.

Marticorena, B., G. Bergametti, B. Aumont, Y. Callot, C. N'Doum, and M. Legrand, 1997: Modeling the atmospheric dust cycle. 2. Simulation of Saharan dust sources. *Journal of Geophysical Research*, **102**(D4):4387–4404, doi:10.1029/96JD02964.

Martins, J. V., P. Artaxo, C. Liousse, J. S. Reid, P. V. Hobbs, and Y. J. Kaufman, 1998a: Effects of black carbon content, particle size, and mixing on light absorption by aerosols from biomass burning in Brazil. *Journal of Geophysical Research*, **103**(D24):32,041–32,050, doi:10.1029/98JD02593.

Martins, J. V., P. V. Hobbs, R. E. Weiss, and P. Artaxo, 1998b: Sphericity and morphology of smoke particles from biomass burning in Brazil. *Journal of Geophysical Research*, **103**(D24):32,051–32,057, doi:10.1029/98JD01153.

McConnell, C. L., P. Formenti, E. J. Highwood, and M. A. J. Harrison, 2010: Using aircraft measurements to determine the refractive index of Saharan dust during the DODO Experiments. *Atmospheric Chemistry and Physics*, **10**(6):3081–3098, doi:10.5194/acp-10-3081-2010.

McConnell, C. L., E. J. Highwood, H. Coe, P. Formenti, B. Anderson, S. Osborne, S. Nava, K. Desboeufs, G. Chen, and M. A. J. Harrison, 2008: Seasonal variations of the physical and optical characteristics of Saharan dust: Results from the Dust Outflow and Deposition to the Ocean (DODO) experiment. *Journal of Geophysical Research*, **113**:D14S05, doi:10.1029/2007JD009606.

Meakin, P., 1991: Fractal aggregates in geophysics. *Reviews of Geophysics*, **29**(3):317–354, doi:10.1029/91RG00688.

Mergenthaler, J. L., J. B. Kumer, and A. E. Roche, 1995: CLAES observations of Mt. Pinatubo stratospheric aerosol. *Geophysical Research Letters*, **22**(24):3497–3500, doi:10.1029/95GL02787.

Mie, G., 1908: Beiträgge zur Optik trüber Medien, speziell kolloidaler Metallösungen. *Annalen der Physik*, **25**(3):377–445, a translation can be found at `http://diogenes.iwt.uni-bremen.de/vt/laser/papers/RAE-LT1873-1976-Mie-1908-translation.pdf` (accessed on 15/3/2011).

Mishchenko, M., L. Travis, R. Kahn, and R. West, 1997: Modeling phase functions for dustlike tropospheric aerosols using a shape mixture of randomly oriented polydisperse spheroids. *Journal of Geophysical Research*, **102**(D14):16831–16847, doi:10.1029/96JD02110.

Mishchenko, M. I., J. W. Hovenier, and L. D. Travis, eds., 2000: *Light Scattering by Nonspherical Particles: Theory, Measurements, and Applications*. Academic Press.

Mishchenko, M. I. and L. D. Travis, 1998: Capabilities and limitations of a current FORTRAN implementation of the T-matrix method for randomly oriented, rotationally symmetric scatterers. *Journal of Quantitative Spectroscopy & Radiative Transfer*, **60**(3):309–324, doi:10.1016/S0022-4073(98)00008-9.

Mishra, S. K. and S. N. Tripathi, 2008: Modeling optical properties of mineral dust over the Indian Desert. *Journal of Geophysical Research*, **113**(D23):D23201, doi:10.1029/2008JD010048.

Monahan, E. C. and I. O. Muircheartaigh, 1980: Optimal Power-Law Description of Oceanic Whitecap Coverage Dependence on Wind Speed. *Journal of Physical Oceanography*, **10**(12):2094–2099, doi:10.1175/1520-0485(1980)010<2094:OPLDOO>2.0.CO;2.

Moorthy, K. K. and S. K. Satheesh, 2000: Characteristics of aerosols over a remote island, Minicoy in the Arabian Sea: Optical properties and retrieved size characteristics. *Quarterly Journal of the Royal Meteorological Society*, **126**(562):81–109, doi:10.1002/qj.49712656205.

Mulcahy, J. P., C. D. O'Dowd, and S. G. Jennings, 2009: Aerosol optical depth in clean marine and continental northeast Atlantic air. *Journal of Geophysical Research*, **114**(D20):D20204, doi:10.1029/2009JD011992.

Muñoz, O., H. Volten, J. W. Hovenier, T. Nousiainen, K. Muinonen, D. Guirado, F. Moreno, and L. B. F. M. Waters, 2007: Scattering matrix of large Saharan dust particles: Experiments and computations. *Journal of Geophysical Research*, **112**:D13215, doi:10.1029/2006JD008074.

Murphy, D. M., J. R. Anderson, P. K. Quinn, L. M. McInnes, F. J. Brechtel, S. M. Kreidenweis, A. M. Middlebrook, M. Posfai, D. S. Thomson, and P. R. Buseck, 1998: Influence of sea-salt on aerosol radiative properties in the Southern Ocean marine boundary layer. *Nature*, **392**(6671):62–65, doi:10.1038/32138.

Nair, P. R., K. Parameswaran, A. Abraham, and S. Jacob, 2005: Wind-dependence of sea-salt and non-sea-salt aerosols over the oceanic environment. *Journal of Atmospheric and Solar-Terrestrial Physics*, **67**(10):884–898, doi:10.1016/j.jastp.2005.02.008.

Nicolas, M., M. Ndour, O. Ka, B. DAnna, and C. George, 2009: Photochemistry of Atmospheric Dust: Ozone Decomposition on Illuminated Titanium Dioxide. *Environmental Science & Technology*, **43**(19):7437–7442, doi:10.1021/es901569d.

O'Connor, T. C., S. G. Jennings, and C. D. O'Dowd, 2008: Highlights of fifty years of atmospheric aerosol research at Mace Head. *Atmospheric Research*, **90**(2-4):338–355, doi:10.1016/j.atmosres.2008.08.014, 17th International Conference on Nucleation and Atmospheric Aerosols - ICNAA07.

O'Dowd, C. D., E. Becker, and M. Kulmala, 2001: Mid-latitude North-Atlantic aerosol characteristics in clean and polluted air. *Atmospheric Research*, **58**:167–185, doi:10.1016/S0169-8095(01)00098-9.

O'Dowd, C. D. and G. de Leeuw, 2007: Marine aerosol production: a review of the current knowledge. *Philosophical Transactions of the Royal Society A: Mathematical, Physical and Engineering Sciences*, **365**(1856):1753–1774, doi:10.1098/rsta.2007.2043.

O'Dowd, C. D., M. C. Facchini, F. Cavalli, D. Ceburnis, M. Mircea, S. Decesari, S. Fuzzi, Y. J. Yoon, and J.-P. Putaud, 2004: Biogenically driven organic contribution to marine aerosol. *Nature*, **431**(7009):676–680, doi:10.1038/nature02959.

O'Dowd, C. D. and M. H. Smith, 1993: Physicochemical Properties of Aerosols Over the Northeast Atlantic: Evidence for Wind-Speed-Related Submicron Sea-Salt Aerosol Production. *Journal of Geophysical Research*, **98**(D1):1137–1149, doi:10.1029/92JD02302.

O'Dowd, C. D., M. H. Smith, I. E. Consterdine, and J. A. Lowe, 1997: Marine aerosol, sea-salt, and the marine sulphur cycle: A short review. *Atmospheric Environment*, **31**(1):73–80, doi:10.1016/S1352-2310(96)00106-9.

Ogren, J. A. and R. J. Charlson, 1983: Elemental carbon in the atmosphere: cycle and lifetime. *Tellus B*, **35B**(4):241–254, doi:10.1111/j.1600-0889.1983.tb00027.x.

Okada, K., J. Heintzenberg, K. J. Kai, and Y. Qin, 2001: Shape of atmospheric mineral particles collected in three Chinese arid-regions. *Geophysical Research Letters*, **28**(16):3123–3126, doi:10.1029/2000GL012798.

Omar, A. H., J.-G. Won, D. M. Winker, S.-C. Yoon, O. Dubovik, and M. P. McCormick, 2005: Development of global aerosol models using cluster analysis of Aerosol Robotic Network (AERONET) measurements. *Journal of Geophysical Research*, **110**(D10):D10S14, doi:10.1029/2004JD004874.

Osborne, S. R., B. T. Johnson, J. M. Haywood, A. J. Baran, M. A. J. Harrison, and C. L. McConnell, 2008: Physical and optical properties of mineral dust aerosol during the Dust and Biomass-burning Experiment. *Journal of Geophysical Research*, **113**:D00C03, doi:10.1029/2007JD009551.

Otto, S., E. Bierwirth, B. Weinzierl, K. Kandler, M. Esselborn, M. Tesche, A. Schladitz, M. Wendisch, and T. Trautmann, 2009: Solar radiative effects of a Saharan dust plume observed during SAMUM assuming spheroidal model particles. *Tellus B*, **61**(1):270–296, doi:10.1111/j.1600-0889.2008.00389.x.

Peters, D., R. G. Grainger, and A. J. A. Smith, 2009: Local Air Quality - Characterising near surface aircraft PM. Technical report, Omega. `omega.mmu.ac.uk/characterising-near-surface-aircraft-particulate-emissions.htm`

Petters, M. D., J. R. Snider, B. Stevens, G. Vali, I. Faloona, and L. M. Russell, 2006: Accumulation mode aerosol, pockets of open cells, and particle nucleation in the remote subtropical Pacific marine boundary layer. *Journal of Geophysical Research*, **111**(D2):D02206, doi:10.1029/2004JD005694.

Petzold, A., K. Rasp, B. Weinzierl, M. Esselborn, T. Hamburger, A. Dörnbrack, K. Kandler, L. Schütz, P. Knippertz, M. Fiebig, and A. Virkkula, 2009: Saharan dust absorption and refractive index from aircraft-based observations during SAMUM 2006. *Tellus B*, **61**(1):118–130, doi:10.1111/j.1600-0889.2008.00383.x.

Pham, M., J.-F. Müller, G. P. Brasseur, C. Granier, and G. Mégie, 1995: A three-dimensional study of the tropospheric sulfur cycle. *Journal of Geophysical Research*, **100**(D12):26061–26092, doi:10.1029/95JD02095.

Phinney, L., W. R. Leaitch, U. Lohmann, H. Boudries, D. R. Worsnop, J. T. Jayne, D. Toom-Sauntry, M. Wadleigh, S. Sharma, and N. Shantz, 2006: Characterization of the aerosol over the sub-arctic north east Pacific Ocean. *Deep Sea Research Part II: Topical Studies in Oceanography*, **53**(20-22):2410–2433, doi:10.1016/j.dsr2.2006.05.044.

Pincus, R. and M. B. Baker, 1994: Effect of precipitation on the albedo susceptibility of clouds in the marine boundary layer. *Nature*, **372**(6503):250–252, doi:10.1038/372250a0.

Popovicheva, O., N. M. Persiantseva, N. K. Shonija, P. DeMott, K. Koehler, M. Petters, S. Kreidenweis, V. Tishkova, B. Demirdjian, and J. Suzanne, 2008: Water interaction with hydrophobic and hydrophilic soot particles. *Physical Chemistry Chemical Physics*, **10**:2332–2344, doi:10.1039/b718944n.

Pósfai, M., J. R. Anderson, P. R. Buseck, and H. Sievering, 1999: Soot and sulfate aerosol particles in the remote marine troposphere. *Journal of Geophysical Research*, **104**(D17):21685–21693, doi:10.1029/1999JD900208.

Pósfai, M., A. Gelencsér, R. Simonics, K. Arató, J. Li, P. V. Hobbs, and P. R. Buseck, 2004: Atmospheric tar balls: Particles from biomass and biofuel burning. *Journal of Geophysical Research*, **109**(D6):D06213, doi:10.1029/2003JD004169.

Pósfai, M., R. Simonics, J. Li, P. V. Hobbs, and P. R. Buseck, 2003: Individual aerosol particles from biomass burning in southern Africa: 1. Compositions and size distributions of carbonaceous particles. *Journal of Geophysical Research*, **108**(D13):8483, doi:10.1029/2002JD002291.

Press, W. H., B. P. Flannery, S. A. Teukolsky, and W. T. Vetterling, 1992: *Numerical Recipes in Fortran 77: The Art of Scientific Computing*. Cambridge University Press, 2nd edition. `http://www.nrbook.com/fortran/`

Pruppacher, H. R. and J. D. Klett, 1997: *Microphysics of clouds and precipitation*. Kluwer Academic Publishers, 2nd edition.

Querry, M. R., 1987: Optical Constants of Minerals and Other Materials from the millimeter to the ultraviolet. Technical Report CRDEC-CR-88009, Chemical Research Development and Engineering Center, Aberdeen Proving Ground, MD 21010-5423. `http://oai.dtic.mil/oai/oai?verb=getRecord&metadataPrefix=html&identifier=ADA192210`

Quinn, P. K., W. E. Asher, and R. J. Charlson, 1992: Equilibria of the marine multiphase ammonia system. *Journal of Atmospheric Chemistry*, **14**:11–30, doi:10.1007/BF00115219.

Quinn, P. K. and D. J. Coffman, 1998: Local closure during the First Aerosol Characterization Experiment (ACE 1): Aerosol mass concentration and scattering and backscattering coefficients. *Journal of Geophysical Research*, **103**(D13):16575–16596, doi:10.1029/97JD03757.

Quinn, P. K., D. J. Coffman, V. N. Kapustin, T. S. Bates, and D. S. Covert, 1998: Aerosol optical properties in the marine boundary layer during the First Aerosol Characterization Experiment (ACE 1) and the underlying chemical and physical aerosol properties. *Journal of Geophysical Research*, **103**(D13):16547–16563, doi:10.1029/97JD02345.

Reid, E. A., J. S. Reid, M. M. Meier, M. R. Dunlap, S. S. Cliff, A. Broumas, K. Perry, and H. Maring, 2003: Characterization of African dust transported to Puerto Rico by individual particle and size segregated bulk analysis. *Journal of Geophysical Research*, **108**(D19):8591, doi:10.1029/2002JD002935.

Reid, J. S., H. H. Jonsson, M. H. Smith, and A. Smirnov, 2001: Evolution of the vertical profile and flux of large sea-salt particles in a coastal zone. *Journal of Geophysical Research*, **106**(D11):12039–12053, doi:10.1029/2000JD900848.

Reid, J. S., R. Koppmann, T. F. Eck, and D. P. Eleuterio, 2005: A review of biomass burning emissions part II: Intensive physical properties of biomass burning particles. *Atmospheric Chemistry and Physics*, **5**(3):799–825, doi:10.5194/acp-5-799-2005.

Remer, L. A., Y. J. Kaufman, D. Tanré, S. Mattoo, D. A. Chu, J. V. Martins, R.-R. Li, C. Ichoku, R. C. Levy, R. G. Kleidman, T. F. Eck, E. Vermote, and B. N. Holben, 2005: The MODIS Aerosol Algorithm, Products, and Validation. *Journal of the Atmospheric Sciences*, **62**(4):947–973, doi:10.1175/JAS3385.1.

Rinaldi, M., M. C. Facchini, S. Decesari, C. Carbone, E. Finessi, M. Mircea, S. Fuzzi, D. Ceburnis, M. Ehn, M. Kulmala, G. de Leeuw, and C. D. O'Dowd, 2009: On the representativeness of coastal aerosol studies to open ocean studies: Mace Head a case study. *Atmospheric Chemistry and Physics*, **9**(24):9635–9646, doi:10.5194/acp-9-9635-2009.

Rodgers, C. D., 2000: *Inverse methods for atmospheric sounding: Theory and practice*, volume 2 of *Atmospheric, Oceanic and Planetary Physics*. World Scientific Publishing Co.

Roush, T., J. Pollack, and J. Orenberg, 1991: Derivation of midinfrared (5-25 μm) optical constants of some silicates and palagonite. *Icarus*, **94**(1):191–208, doi:10.1016/0019-1035(91)90150-R.

Roush, T. L., F. Esposito, G. R. Rossman, and L. Colangeli, 2007: Estimated optical constants of gypsum in the regions of weak absorptions: Application of scattering theories and comparisons to independent measurements. *Journal of Geophysical Research*, **112**:E10003, doi:10.1029/2007JE002920.

Sayer, A. M., 2008: *Aerosol Remote Sensing Using AATSR*. Ph.D. thesis, Atmospheric, Oceanic and Planetary Physics, University of Oxford.

Sayer, A. M., G. E. Thomas, and R. G. Grainger, 2010: A sea surface reflectance model for (A)ATSR, and application to aerosol retrievals. *Atmospheric Measurement Techniques*, **3**(4):813–838, doi:10.5194/amt-3-813-2010.

Schuster, G. L., B. Lin, and O. Dubovik, 2009: Remote sensing of aerosol water uptake. *Geophysical Research Letters*, **36**(3):L03814, doi:10.1029/2008GL036576.

Schwarz, J. P., J. R. Spackman, R. S. Gao, L. A. Watts, P. Stier, M. Schulz, S. M. Davis, S. C. Wofsy, and D. W. Fahey, 2010: Global-scale black carbon profiles observed in the remote atmosphere and compared to models. *Geophysical Research Letters*, **37**(18):L18812, doi:10.1029/2010GL044372.

SEDAC, 2005: Global Rural-Urban Mapping Project (GRUMP), Alpha Version. Socioeconomic Data and Applications Center (SEDAC), Columbia University. `http://sedac.ciesin.columbia.edu/gpw/`

Seinfeld, J. H. and S. N. Pandis, 2006: *Atmospheric Chemisty and Physics, From Air Pollution to Climate Change*. John Wiley & Sons, Inc., 2nd edition.

Sellegri, K., C. D. O'Dowd, Y. J. Yoon, S. G. Jennings, and G. de Leeuw, 2006: Surfactants and submicron sea spray generation. *Journal of Geophysical Research*, **111**(D22):D22215, doi:10.1029/2005JD006658.

Semeniuk, T., M. Wise, S. Martin, L. Russell, and P. Buseck, 2007: Hygroscopic behavior of aerosol particles from biomass fires using environmental transmission electron microscopy. *Journal of Atmospheric Chemistry*, **56**:259–273, doi:10.1007/s10874-006-9055-5.

Shettle, E. P. and R. W. Fenn, 1979: Models for the Aerosols of the Lower Atmosphere and the Effects of Humidity Variations on their Optical Properties. Technical Report AFGL-TR-79-0214, Air Force Geophysics Lab, Hanscom Air Force Base, MA 01731. `http://handle.dtic.mil/100.2/ADA085951`

Sihvola, A., 1999: *Electromagnetic mixing formulas and applications*, volume 47 of *IEE Electromagnetic Waves Series*. The Institution of Electrical Engineers, London.

Smekens, A., R. Godoi, M. Vervoort, P. van Espen, S. Potgieter-Vermaak, and R. van Grieken, 2007: Characterization of Individual Soot Aggregates from Different Sources using Image Analysis. *Journal of Atmospheric Chemistry*, **56**:211–223, doi:10.1007/s10874-006-9050-x.

Smirnov, A., B. N. Holben, Y. J. Kaufman, O. Dubovik, T. F. Eck, I. Slutsker, C. Pietras, and R. N. Halthore, 2002: Optical Properties of Atmospheric Aerosol in Maritime Environments. *Journal of the Atmospheric Sciences*, **59**(3):501–523, doi:10.1175/1520-0469(2002)059<0501:OPOAAI>2.0.CO;2.

Smirnov, A., B. N. Holben, I. Slutsker, D. M. Giles, C. R. McClain, T. F. Eck, S. M. Sakerin, A. Macke, P. Croot, G. Zibordi, P. K. Quinn, J. Sciare, S. Kinne, M. Harvey, T. J. Smyth, S. Piketh, T. Zielinski, A. Proshutinsky, J. I. Goes, N. B. Nelson, P. Larouche, V. F. Radionov, P. Goloub, K. K. Moorthy, R. Matarrese, E. J. Robertson, and F. Jourdin, 2009: Maritime Aerosol Network

as a component of Aerosol Robotic Network. *Journal of Geophysical Research*, **114**:D06204, doi:10.1029/2008JD011257.

Smirnov, A., Y. Villevalde, N. T. O'Neill, A. Royer, and A. Tarussov, 1995: Aerosol optical depth over the oceans: Analysis in terms of synoptic air mass types. *Journal of Geophysical Research*, **100**(D8):16639–16650, doi:10.1029/95JD01265.

Smirnov, V., 2006: Nature and evolution of ultrafine aerosol particles in the atmosphere. *Izvestiya Atmospheric and Oceanic Physics*, **42**(6):663–687–687, doi:10.1134/S0001433806060016.

Sokolik, I. N. and O. B. Toon, 1999: Incorporation of mineralogical composition into models of the radiative properties of mineral aerosol from UV to IR wavelengths. *Journal of Geophysical Research*, **104**(D8):9423–9444, doi:10.1029/1998JD200048.

Solomon, S., D. Qin, M. Manning, R. Alley, T. Berntsen, N. Bindoff, Z. Chen, A. Chidthaisong, J. Gregory, G. Hegerl, M. Heimann, B. Hewitson, B. Hoskins, F. Joos, J. Jouzel, V. Kattsov, U. Lohmann, T. Matsuno, M. Molina, N. Nicholls, J. Overpeck, G. Raga, V. Ramaswamy, J. Ren, M. Rusticucci, R. Somerville, T. Stocker, P. Whetton, R. Wood, and D. Wratt, 2007: *Climate Change 2007: The Physical Science Basis*. Cambridge University Press, contribution of Working Group I to the Fourth Assessment Report of the Intergovernmental Panel on Climate Change. `http://www.ipcc.ch/publications_and_data/publications_ipcc_fourth_assessment_report_wg1_report_the_physical_science_basis.htm`

Sorensen, C. M., 2001: Light Scattering by Fractal Aggregates: A Review. *Aerosol Science and Technology*, **35**(2):648–687, doi:10.1080/02786820117868.

Sorensen, C. M. and G. C. Roberts, 1997: The Prefactor of Fractal Aggregates. *Journal of Colloid and Interface Science*, **186**(2):447–452, doi:10.1006/jcis.1996.4664.

Stamnes, K., S.-C. Tsay, W. Wiscombe, and K. Jayaweera, 1988: Numerically stable algorithm for discrete-ordinate-method radiative transfer in multiple scattering and emitting layered media. *Applied Optics*, **27**(12):2502–2509, doi:10.1364/AO.27.002502.

Stier, P., J. H. Seinfeld, S. Kinne, and O. Boucher, 2007: Aerosol absorption and radiative forcing. *Atmospheric Chemistry and Physics*, **7**(19):5237–5261, doi:10.5194/acp-7-5237-2007.

Streets, D. G., T. C. Bond, G. R. Carmichael, S. D. Fernandes, Q. Fu, D. He, Z. Klimont, S. M. Nelson, N. Y. Tsai, M. Q. Wang, J.-H. Woo, and K. F. Yarber, 2003: An inventory of gaseous and primary aerosol emissions in Asia in the year 2000. *Journal of Geophysical Research*, **108**(D21):8809, doi:10.1029/2002JD003093.

Swietlicki, E., J. Zhou, O. H. Berg, B. G. Martinsson, G. Frank, S.-I. Cederfelt, U. Dusek, A. Berner, W. Birmili, A. Wiedensohler, B. Yuskiewicz, and K. N. Bower, 1999: A closure study of sub-micrometer aerosol particle hygroscopic behaviour. *Atmospheric Research*, **50**(3-4):205–240, doi:10.1016/S0169-8095(98)00105-7.

Tang, I. N., 1997: Thermodynamic and optical properties of mixed-salt aerosols of atmospheric importance. *Journal of Geophysical Research*, **102**(D2):1883–1893, doi:10.1029/96JD03085.

Tanré, D., J. M. Haywood, J. Pelon, J. F. Léon, B. Chatenet, P. Formenti, P. Francis, P. Goloub, E. J. Highwood, and G. Myhre, 2003: Measurement and modeling of the Saharan dust radiative impact: Overview of the Saharan Dust Experiment (SHADE). *Journal of Geophysical Research*, **108**(D18):8574, doi:10.1029/2002JD003273.

Tegen, I. and I. Fung, 1995: Contribution to the atmospheric mineral aerosol load from land surface modification. *Journal of Geophysical Research*, **100**(D9):18,707–18,726, doi:10.1029/95JD02051.

Thomas, G. E., 2003: *A New Instrument for Atmospheric Aerosol Measurement*. Ph.D. thesis, University of Canterbury, Christchurch, New Zealand. `http://www-atm.physics.ox.ac.uk/group/eodg/theses/Thomas.pdf`

Thomas, G. E., S. M. Dean, E. Carboni, R. G. Grainger, C. A. Poulsen, R. Siddans, and B. J. Kerridge, 2005: GlobAEROSOL Data User Elements - Aerosol Extraction Algorithm Definition. Algorithm theoretical basis document, Atmospheric, Oceanic and Planetary Physics, Oxford University. `http://www.globaerosol.info/docs/aatsr_atbd_v1p0.pdf`

Thomas, G. E., C. A. Poulsen, R. Siddans, E. Carboni, A. M. Sayer, and R. G. Grainer, 2011: ORAC v3 Dual-view aerosol retrieval from (A)ATSR. AOPP Memorandum 2011.1, Atmospheric, Oceanic and Planetary Physics, Oxford University, Parks Rd, Oxford. OX1 3PU, UK. `http://www-atm.physics.ox.ac.uk/main/Science/technical.html`

Thouy, R. and R. Jullien, 1994: A cluster-cluster aggregation model with tunable fractal dimension. *Journal of Physics A: Mathematical and General*, **27**(9):2953, doi:10.1088/0305-4470/27/9/012.

Tsang, L., J. A. Kong, and R. T. Shin, 1985: *Theory of Microwave Remote Sensing*. Wiley Series in Remote Sensing, John Wiley & Sons, Inc.

Turns, S. R., 2000: *An Introduction to Combustion - Concepts and Applications*. McGraw-Hill, 2nd edition.

Twomey, S., 1977a: *Atmospheric Aerosols*, volume 7 of *Developments in Atmospheric Science*. Elsevier Scientific Publishing Company.

— 1977b: The Influence of Pollution on the Shortwave Albedo of Clouds. *Journal of the Atmospheric Sciences*, **34**(7):1149–1152, doi:10.1175/1520-0469(1977)034<1149:TIOPOT>2.0.CO;2.

Unger, N., T. C. Bond, J. S. Wang, D. M. Koch, S. Menon, D. T. Shindell, and S. Bauer, 2010: Attribution of climate forcing to economic sectors. *Proceedings of the National Academy of Sciences*, **107**(8):3382–3387, doi:10.1073/pnas.0906548107.

van de Hulst, H. C., 1957: *Light Scattering by Small Particles*. John Wiley & Sons.

Vignati, E., M. Facchini, M. Rinaldi, C. Scannell, D. Ceburnis, J. Sciare, M. Kanakidou, S. Myriokefalitakis, F. Dentener, and C. O'Dowd, 2010: Global scale emission and distribution of sea-spray aerosol: Sea-salt and organic enrichment. *Atmospheric Environment*, **44**(5):670–677, doi:10.1016/j.atmosenv.2009.11.013.

Volten, H., O. Muñoz, J. F. de Haan, W. Vassen, and J. W. Hovenier, 2001: Scattering matrices of mineral aerosol particles at 441.6 nm and 632.8 nm. *Journal of Geophysical Research*, **106**(D15):17,375–17,401, doi:10.1029/2001JD900068.

Wang, J., X. Liu, S. Christopher, J. Reid, E. Reid, and H. Maring, 2003: The effects of non-sphericity on geostationary satellite retrievals of dust aerosols. *Geophysical Research Letters*, **30**(24):2293, doi:10.1029/2003GL018697.

Washington, R., M. C. Todd, G. Lizcano, I. Tegen, C. Flamant, I. Koren, P. Ginoux, S. Engelstaedter, C. S. Bristow, C. S. Zender, A. S. Goudie, A. Warren, and J. M. Prospero, 2006: Links between topography, wind, deflation, lakes and dust: The case of the Bodélé Depression, Chad. *Geophysical Research Letters*, **33**:L09401, doi:10.1029/2006GL025827.

Waterman, P. C., 1969: New Formulation of Acoustic Scattering. *The Journal of the Acoustical Society of America*, **45**(6):1417–1429, doi:10.1121/1.1911619.

— 1973: Numerical Solution of Electromagnetic Scattering Problems. *Computer Techniques for Electromagnetics*, R. Mittra, ed., Pergamon Press, chapter 3, 97–157.

— 1976: Matrix theory of elastic wave scattering. *The Journal of the Acoustical Society of America*, **60**(3):567–580, doi:10.1121/1.381130.

— 1979: Matrix methods in potential theory and electromagnetic scattering. *Journal of Applied Physics*, **50**(7):4550–4566, doi:10.1063/1.326562.

Weinzierl, B., A. Petzold, M. Esselborn, M. Wirth, K. Rasp, K. Kandler, L. Scütz, P. Koepke, and M. Fiebig, 2009: Airborne measurements of dust layer properties, particle size distribution and mixing state of Saharan dust during SAMUM 2006. *Tellus B*, **61**(1):96–117, doi:10.1111/j.1600-0889.2008.00392.x.

Wentzel, M., H. Gorzawski, K. H. Naumann, H. Saathoff, and S. Weinbruch, 2003: Transmission electron microscopical and aerosol dynamical characterization of soot aerosols. *Journal of Aerosol Science*, **34**(10):1347–1370, doi:10.1016/S0021-8502(03)00360-4.

Whitby, K. T. and B. K. Cantrell, 1976: Atmospheric Aerosols: Characteristics and Measurement. *International Conference on Environmental Sensing and Assessment (ICESA)*, Institute of Electrical and Electronic Engineers (IEEE), ICESA, Las Vegas, NV, number 29–1, 6.

Wiscombe, W. J. and G. W. Grams, 1976: The Backscattered Fraction in Two-Stream Approximations. *Journal of the Atmospheric Sciences*, **33**(12):2440–2451, doi:10.1175/1520-0469(1976)033<2440:TBFITS>2.0.CO;2.

Xu, Y. and B. Å. S. Gustafson, 2001: A generalized multiparticle Mie-solution: further experimental verification. *Journal of Quantitative Spectroscopy & Radiative Transfer*, **70**(4–6):395–419, doi:10.1016/S0022-4073(01)00019-X.

Yang, P., Q. Feng, G. Hong, G. W. Kattawar, W. J. Wiscombe, M. I. Mishchenko, O. Dubovik, I. Laszlo, and I. N. Sokolik, 2007: Modeling of the scattering and radiative properties of nonspherical dust-like aerosols. *Journal Of Aerosol Science*, **38**(10):995–1014, doi:10.1016/j.jaerosci.2007.07.001.

Yasunari, T. J., P. Bonasoni, P. Laj, K. Fujita, E. Vuillermoz, A. Marinoni, P. Cristofanelli, R. Duchi, G. Tartari, and K.-M. Lau, 2010: Estimated impact of black carbon deposition during pre-monsoon season from Nepal Climate Observatory Pyramid data and snow albedo changes over Himalayan glaciers. *Atmospheric Chemistry and Physics*, **10**(14):6603–6615, doi:10.5194/acp-10-6603-2010.

Yia, L., Y. L. Koganb, and D. B. Mechemc, 2008: An idealized modeling study of the effect of continental air mass aerosol parameters on marine stratocumulus. *Atmospheric Research*, **88**(2):157–167, doi:10.1016/j.atmosres.2007.10.010.

Yurkin, M. A. and A. G. Hoekstra, 2007: The discrete dipole approximation: An overview and recent developments. *Journal of Quantitative Spectroscopy & Radiative Transfer*, **106**(1-3):558–589, doi:10.1016/j.jqsrt.2007.01.034, IX Conference on Electromagnetic and Light Scattering by Non-Spherical Particles.

Zhang, R., A. F. Khalizov, J. Pagels, D. Zhang, H. Xue, and P. H. McMurry, 2008: Variability in morphology, hygroscopicity, and optical properties of soot aerosols during atmospheric processing. *Proceedings of the National Academy of Sciences of the United States of America*, **105**(30):10291–10296, doi:10.1073/pnas.0804860105.

Zhou, J., E. Swietlicki, O. H. Berg, P. P. Aalto, K. Hämeri, E. D. Nilsson, and C. Leek, 2001: Hygroscopic properties of aerosol particles over the central Arctic Ocean during summer. *Journal of Geophysical Research*, **106**(D23):32111–32123, doi:10.1029/2000JD900426.

Zobler, L., 1986: A World Soil File for Global Climate Modeling. Technical Memorandum 87802, NASA, Goddard Institute for Space Studies, New York, NY 10025. `http://ntrs.nasa.gov/search.jsp?Ntk=Report%20-%20Patent%20Number&Ntt=87802`